Experimental and Numerical Analysis of Forming, Fracture and Wrinkling Limit Diagrams for Inconel 718 Alloy at Elevated Temperatures

THESIS

submitted in partial fulfillment
of the requirements for the degree of

DOCTOR OF PHILOSOPHY

by

GAURI RAJENDRA MAHALLE

ID No: 2016PHXF0415H

under the supervision of

Dr. NITIN RAMESHRAO KOTKUNDE

&

Co- supervision of

Prof. AMIT KUMAR GUPTA

BIRLA INSTITUTE OF TECHNOLOGY AND SCIENCE, PILANI, HYDERABAD CAMPUS
2021

BIRLA INSTITUTE OF TECHNOLOGY AND SCIENCE, PILANI

HYDERABAD CAMPUS

CERTIFICATE

This is to certify that the thesis entitled "**Experimental and Numerical Analysis of Forming, Fracture and Wrinkling Limit Diagrams for Inconel 718 Alloy at Elevated Temperatures**" and submitted by **Gauri Rajendra Mahalle** ID.No **2016PHXF0415H** for award of Ph.D. of the Institute embodies original work done by him under my supervision.

Signature of the Supervisor

Name in capital letters: **Dr. NITIN RAMESHRAO KOTKUNDE**

Designation: **Assistant Professor**

Mechanical Engineering Department

BITS-Pilani, Hyderabad Campus

Date: **18/07/2021**

Signature of the Co-supervisor

Name in capital letters: **Prof. AMIT KUMAR GUPTA**

Designation: **Professor**

Mechanical Engineering Department

BITS-Pilani, Hyderabad Campus

Date: **18/07/2021**

BIRLA INSTITUTE OF TECHNOLOGY AND SCIENCE, PILANI

HYDERABAD CAMPUS

DECLARATION

I, Gauri Rajendra Mahalle, declare that

a. The work contained in this thesis is original and has been done by myself under the general supervision of my supervisors.
b. The work has not been submitted to any other Institute for any degree or diploma.
c. I have followed the guidelines provided by the Institute in writing the thesis.
d. I have conformed to the norms and guidelines given in the Ethical Code of Conduct of the Institute.
e. Whenever I have used materials (data, theoretical analysis, and text) from other sources, I have given due credit to them by citing them in the text of the thesis and giving their details in the references.
f. Whenever I have quoted written materials from other sources, I have put them under quotation marks and given due credit to the sources by citing them and giving required details in the references.

Signature of the Student

Name in capital letters: GAURI RAJENDRA MAHALLE

Date: **18/07/2021**

Acknowledgement

I would like to express my genuine and immense gratitude to my supervisor Dr. Nitin R. Kotkunde, for his incredible patience, comprehensive guidance, and continuous support in the completion of this research work. He has not only provided endless encouragement and tremendous help for research but also motivated during the whole Ph.D. study. I would like to thank him for teaching me persistence, exquisite logical thinking, and research enthusiasm. Thank you for being my inspiration and well-wisher.

I would like to extend my sincere gratitude to my co-supervisor, Prof. Amit Kumar Gupta, for offering substantial guidance and assistance during this research. I would like to give special thanks for his scientific advice and practical instruction during my Ph.D. research. Thank you for carefully reviewing the manuscripts & thesis and providing detailed and constructive comments. My deep gratitude to Dr. Swadesh Kumar Singh, Professor, Mechanical Engineering Department, GRIET, Hyderabad, for the kind cooperation, encouragement, unceasing guidance, and moral support. Thank you for providing an opportunity to avail the lab facility at GRIET, Hyderabad.

I am thankful to my doctoral advisory committee members, Dr. Pavan Kumar P. and Dr. Ravi Shanker Vidyarthy for their encouragement and valuable advice during semester reviews. I am grateful for their insightful comments and suggestion helps to bring this thesis into final form. I thank Prof. Souvik Bhattacharyya, former Vice-Chancellor, BITS-Pilani, and Prof. G. Sundar, Director, BITS-Pilani, Hyderabad Campus, for providing a research environment to enhance my research interest.

I am extremely grateful to all the faculty and staff of the Department of Mechanical Engineering, BITS-Pilani, Hyderabad Campus. Special thanks to Workshop staff for providing the unstinting cooperation and help. Also, I thank Ahsan Ul Haq and Mahesh technical staff at GRIET for their corporation and help during the experimentation.

I thank the Science and Engineering Research Board (SERB–DST ECR) Government of India, ECR/2016/001402, for financially supporting this research work. In addition, I am thankful to the Department of Physics, Osmania University, Hyderabad, India, for availing the Scanning Electron Microscope (SEM) facility for fractography studies and Department of Metallurgical Engineering and Material Science, Indian Institute of Technology Bombay, India, for availing the OIM facility for Electron Backscatter Diffraction (EBSD) studies.

I heartily thank all my co-authors of published papers. Their valuable input and kind assistance helped me to publish the manuscript in reputed international journals and conferences. I am obliged to Omkar Salunke and Ayush Morchhale for their support and technical assistance. My sincere appreciations also go to my friends. They helped a lot and supported me during tough times.

Lastly, I would like to express my deepest gratitude to my parents and brother Gaurav, for their endless support and understanding; without them accomplishment of this work might be impossible.

Gauri Rajendra Mahalle

Abstract

Inconel 718 alloy is an indispensable material in various high-temperature applications. The major formability challenges of this alloy are very high forming loads, high elastic recovery, and considerable wrinkling tendency. One of the popular alternatives to overcome these issues is elevated temperature forming.

This research work is mainly focused on experimental and numerical studies of forming, fracture, and wrinkling limit diagrams for Inconel 718 alloy at elevated temperatures. Firstly, uniaxial tensile tests have been performed at different temperatures (RT-700ºC, at an interval of 100ºC) and quasi-static strain rates (10^{-4}-$10^{-1}s^{-1}$). The Portevin–Le Chatelier effect is reported from 400°C-700°C at all the strain rate conditions. Mainly, B and combination of A + B type of serrations are observed at different temperatures and strain rates. Subsequently, various empirical relationships, namely, Holloman, Swift, Ludwick, and Voce, have been used to define the two-stage work hardening behavior of Inconel 718 alloy. Further, the fractographs indicate a ductile-brittle fracture due to nucleation and micro-void growth phenomena. Electron Backscatter Diffraction (EBSD) studies revealed that the dynamic recrystallization mechanism starts at relatively lower testing temperatures, i.e., 300°C.

Furthermore, different uniaxial constitutive models, namely m-CS, m-JC, KHL, m-ZA, and integrated JC-ZA model, have been developed. Among these models, the JC-ZA model shows good agreement in terms of the highest correlation coefficient (98.73%) and the least average absolute error (2.44%). Anisotropic yield criteria, namely, Hill'48 and Barlat'89 are weighed based on experimental yield strength points, variation in yield stress, and anisotropic coefficients. Barlat’89 yield criterion exhibited better prediction over a range of strain rate, temperature, and sheet orientations.

Experimental FLDs and FFLDs are plotted using the Nakazima test. The various qualitative aspects of stretch forming such as strain distribution, thickness distribution, LDH have been investigated. It has been found that the material failed without a substantial prior hint of the necking particularly, in the tension-tension region, no necking tendency has been seen at room temperature condition. However, necking tendency can be identified properly at higher temperatures (700ºC) because of the increase in flowablity and ductility of the material. Hence, it is not reliable to consider necking limits to plot the FLD for this material at lower temperatures. Thus, FFLDs are also evaluated at different temperatures.

Afterward, Marciniak-Kuaynski (MK) model coupled with Hill'48-r and Hill'48–σ model has been implemented to predict FLDs. The predicted FLDs with Barlat'89 yield

criterion displayed a good correlation with experimentally FLDs with the least RMSE (<0.058) and AAE (<0.031). Furthermore, failure limit strains were predicted by using B-W model coupled with Hill'48-r, Hill'48-σ, Barlat'89 yield criteria and compared with the experimental values for the onset of fracture. B-W model with Barlat'89 yield criterion gave the best prediction of experimental fracture strains with a least RMSE (< 0.02) and AAE (< 0.028). Later, the FE analysis of the stretch forming process has been carried out using ABAQUS software. The predicted LDHs and thickness distribution are observed within 0.5 – 3.0% error range.

Finally, an integrated experimental and numerical approach has been used for the prediction of strain-based wrinkling limit curves (ε-WLCs) of Inconel 718 alloy at different temperatures. The in-plane principal strains have been transferred to effective plastic strain (EPS) vs. triaxiality (η) space to differentiate the transformation between safe and wrinkling instability. The complete forming behavior of alloy is represented by means of forming, fracture, and wrinkling limit curves.

Keywords: Inconel 718 Alloy, Deformation Behavior, Material Properties, Dynamic Strain Ageing, Microstructural Characteristics, Uniaxial Constitutive Models, Yield Criteria, FLDs, FFLDs, WLCs, FE Analysis

Contents

List of Tables

List of Figures

List of Abbreviations

ASTM	American Society for Testing and Materials
AAE	Average Absolute Error
ANN	Artificial neural network
BCC	Body centered cubic crystal structure
B-W	Bao and Wierzbicki
COF	Coefficient of friction
CNC	Computerized numerical control
DMM	Dynamic Material Model
DMV	Donnell-Mushtari-Vlasov
DSA	Dynamic Strain Ageing
EDS	Energy dispersive spectroscopy
EBSD	Electron Backscatter Diffraction
FCC	Face centered cubic crystal structure
FEM	finite element method
FLD	Forming limit diagram
FLC	Forming limit curve
FLD_o	plane strain forming limit
FFLD	Fracture Forming limit diagram
GTN	Gursone-Tvergaarde-Needleman
HCP	Hexagonal close packed crystal structure
HSS	High-speed steel
JC	Johnson Cook model
KHL	Khan–Huang–Liang
LDR	Limiting draw ratio
LDH	Limiting dome height
MGGP	multi-gene genetic programming
M-K	Marciniak-Kuaynski
MSE	Mean Square Error
MTS	Mechanical threshold model
m-CS	Modified Cowper–Symonds
m-FB	Modified Fields- Backofen model
m-Arr.	Modified Arrhenius model
m-ZA	Modified Zerilli Armstrong model
NADDRG	North American Deep Drawing Research Group
OSUFT	Ohio State University Formability Test
PLC	Portevin Le Chatelier
RT	Room temperature
RMSE	Root Mean Square Error
SEM	Scanning electron microscope
SFE	Stack Fault Energy

SMF	Sheet Metal Forming
UTM	Universal testing machine
WLD	Wrinkling limit diagram
YBT	Yoshida buckling test

List of Symbols

Symbol	Meaning	Unit
$e_{1,2}$	Major and minor engineering strains	-
$\varepsilon_{1,2}$ & $\acute{\varepsilon}_{1,2}$	True and corrected limiting surface strains	-
ε_0 & $\varepsilon_f/\overline{\varepsilon_f}$	Strain at yield and fracture in uniaxial tensile test	-
$\varepsilon_1^A/\varepsilon_1^{A*}$ & ε_1^B	Principal/Limiting strain in region A and B	-
$d\overline{\varepsilon_A}$ & $d\overline{\varepsilon_B}$	Equivalent strain in region A and B	-
ε_{1exp} & $\bar{\varepsilon}_{1pre}$	Experimental and Predicted major true strains	-
α	Strain ratio ($\alpha = \frac{d\varepsilon_2}{d\varepsilon_1} = -\frac{\bar{r}}{1-\bar{r}}$ by volume consistency theorem)	-
$\sigma_{1,2,3}$, σ_b & σ_m	Major, minor, biaxial and hydrostatic true stress	MPa
σ_0 /σ_y, Y & σ_{uts}	Yield and Ultimate tensile strength along Rolling Direction (RD)	MPa
$\bar{\sigma}_B$ & $\bar{\sigma}_H$	Effective stress by Barlat'89 and Hill'48 yield functions	MPa
k_1, k_2	Invariants of stress tensors	
$\sigma_{\theta_i}^{exp}$ & $\sigma_{\theta_i}^{pre}$	Experimental and Predicted uniaxial yield strength along θ_i	MPa
ρ	Stress ratio ($\rho = \frac{\sigma_2}{\sigma_1}$)	-
η	Stress triaxiality, $\eta = \frac{\sigma_m}{\bar{\sigma}}$, where $\sigma_m = \frac{\sigma_1+\sigma_2+\sigma_3}{3}$	-
R_n	Punch curvature/radius	mm
t_o & t_f	Initial and Instantaneous thickness of sheet	mm
% elong.	% Elongation	-
m	Strain rate sensitivity	-
r_0, r_{45}, r_{90} & r_b	Lankford anisotropy coefficients at 0°, 45º, 90º to RD and balanced biaxial condition	-
$r_{\theta_i}^{exp}$ & $r_{\theta_i}^{pre}$	Experimental and Predicted anisotropy coefficients along θ_i	-
$\bar{r}$	Normal anisotropy/ avg. plastic strain ($\bar{r} = \frac{r_0+2r_{45}+r_{90}}{4}$).	-
ΔR	Planer anisotropy	-
p	An exponent defining crystallographic structure of material (p = 8 for FCC structure)	-
a, c & h	Anisotropy ratio functions in Barlat'89 yield criteria	-
ω	Global accuracy index	-
φ	Accuracy index for predictability of the yield locus shape in principal stresses plane	-
γ	Accuracy index for predictability of planar anisotropic coefficients	-
δ	Accuracy index for predictability of distribution of uniaxial stress	
$d^2(P_i, Q_i)$	Square of distance from P_i (experimental value) to Q_i (its projection) in predicted yield locus	mm
j	Total number of experimental points	-
θ_i	Angle measured from RD	° (deg.)

$\Delta_{improve}$ (%)	% Improvement in the limiting strains (RT value as datum)	-
f_0	Inhomogeneity factor	-
$t_{A,B}$	Uniform thickness in region A and B	mm
W, b	An integer/Constant	-
M	Number of strain paths selected (M=6)	-
Δ_{avg}	Average absolute error	-
s	Root mean square error	-
L_p	Lode parameter	-
F, G, H, N, P´, Q´, R´ & S´	Anisotropic material constants define anisotropy of a material	-

1. Introduction

Sheet Metal Forming (SMF) is a popular and important manufacturing technology used in various industries to fabricate intricate and complex shape components (Banabic et al. 2010). Different modern techniques for forming high strength, low ductility, difficult-to-form materials, and complex-shaped parts are developed in the past decades (Banabic 2000). Sheet metal formed parts are widely used in automobiles, aviation, aerospace, nuclear reactors, marine, domestic and medical applications (Kennedy 2005; Reed 2006). Some of these applications are shown in Figure 1.1.

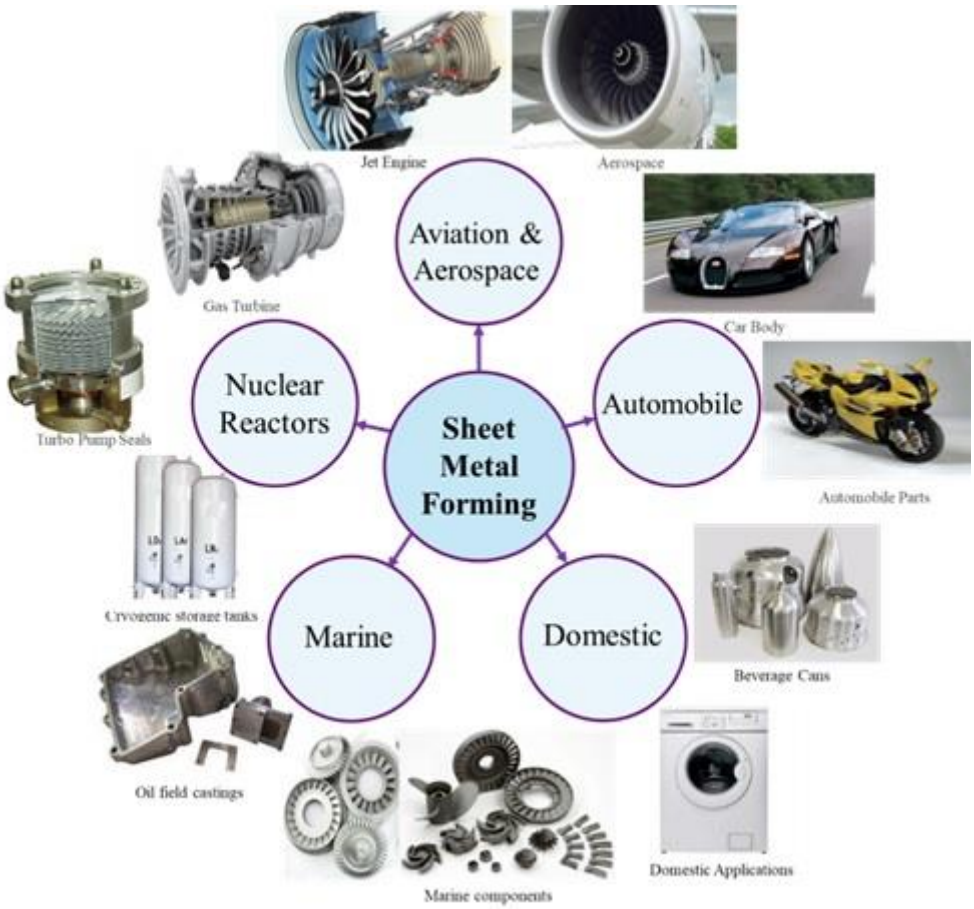

Figure 1.1 Common applications of SMF processes (Kennedy 2005; Reed 2006)

Sheet metal formed components/products facilitated considerable material saving compared to other traditional manufacturing processes, which significantly achieve cost-effectiveness and higher productivity (Reed 2006). The sustainability and environment concern recently forced various industries to use high strength materials as an alternative for traditional materials (Bassoli et al. 2019). Therefore, 'alternative' materials were studied to replace conventional materials to improve the critical applications' performance. For this purpose,

various high-strength alloys such as Nickel-based superalloys and Titanium alloy are gaining special attention (Luo and Qian 2018; Prasad et al. 2017; Zhang and Lu 2019).

1.1 Introduction to Ni-based Superalloys

Since the introduction of Ni-based superalloys in the early 1960s, these alloys in a relatively short time become indispensable materials for aircraft structures, rocket engines, nuclear reactors, gas turbines, pressure vessels, and marine applications (Kennedy 2005). These high-performance superalloys exhibit excellent heat resistance due to outstanding mechanical strength, creep strength, and ductility, high fatigue strength and typically superior corrosion and oxidation resistance at elevated temperature.

The Ni-based superalloy contains major constituent elements such as Nickel (Ni), Iron (Fe), Chromium (Cr), Molybdenum (Mo), and Cobalt (Co) with some minor elements like Aluminum (Al), Titanium (Ti), Tungsten (W) and so on. These alloying elements enhance the mechanical characteristics. Where, Ni stabilizes alloy structure and properties at elevated temperatures. Co, Mo, and W increase strength at elevated temperature, Cr, Al, Si enhances oxidation resistance and elevated temperature corrosion resistance, and Carbon (C) increases creep strength. Ni-based superalloys can also be broadly classified according to grade under the distinct groups (Group A, Group B, Group C, and Group D) as presented in Figure 1.2.

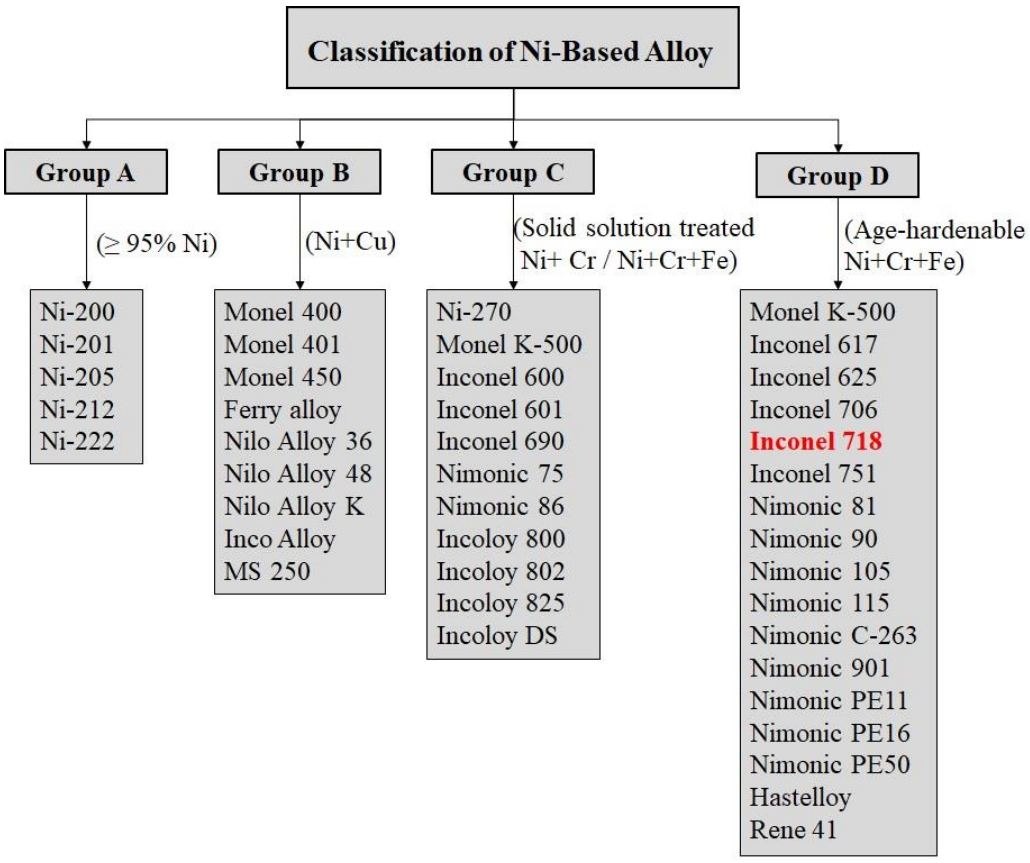

Figure 1.2 Classification of Ni-based superalloy (Reed 2006)

Group A contains more than 95% of Nickel. These alloys have high toughness as well as moderate mechanical strength. These alloys are used for electronic parts in domestic application and in corrosion resistance applications, such as handling foods and alkaline solutions. Group B contains Nickel and Copper as major constituents. These alloys have slightly lower toughness and higher strength than Group A. These alloys are used in a marine application, namely marine fixtures, piping systems pumps, and valves. Whereas Group C contains a large amount of solution treated Ni-Cr and Ni-Cr-Fe elements. These alloys are extensively used in aerospace applications, namely for exhaust systems, ducting, combustors, and thrust reversers. Further, Group D contains primarily of age hardenable alloys. These alloys can also be subdivided into unaged and aged alloys. These aged hardenable/ precipitate hardenable alloys have high strength and hardness compared to other groups. These alloys are used in high-performance conditions, namely combustor parts in jet engines, gas turbine engine components, and nuclear reactors.

Mainly, Inconel 718, in Ni-based alloy, is an indispensable alloy for various components, namely, castings of a jet engine, high-speed airframe parts such as impellers, wheels, casings, blades, discs, rings shafts, oil field casting, nuclear reactor component, land-based gas turbine, rocket motor, pumps cryogenics and elevated temperature bolts and fastener (Schafrik, Ward, and Groh 2001; Thaller and Zimmerman 2003). Inconel 718 is a Nickel-Iron-Chromium based precipitate-hardenable alloy with the secondary precipitation of Ni-Al/Ti/Nb (i.e., γ'' and γ' phases) into a metal matrix (Reed 2006). These help in achieving an excellent combination of mechanical properties such as high tensile strength (700-1250 MPa), excellent strain hardening, and sufficient ductility (Thomas et al. 2006). A combination of these precipitates is highly resistant towards corrosion (mostly pitting and crevice corrosion), oxidation, and stable in extreme working conditions the significant amount of Cr, Nb, and Mo contents (Prasad et al. 2017). Some of the Inconel 718 parts in aerospace and medical applications are shown in Figure 1.3.

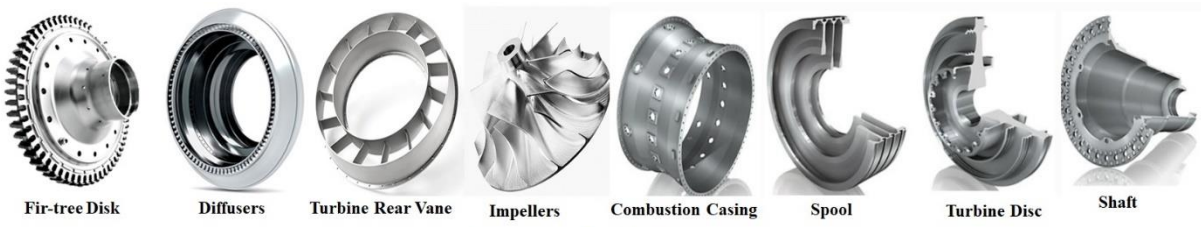

Figure 1.3 Aerospace and medical applications of Inconel 718 alloy (Schafrik et al. 2001)

1.2 Sheet Metal Forming

Metal forming is a crucial manufacturing process to produce complex and critical components in the aerospace and automotive industries (Lin, Balint, and Pietrzyk 2012). SMF processes include stretching, drawing, bending, roll forming, or various combinations of these basic processes. Some of these basic tests are as shown in Figure 1.4. Deep drawing and stretch forming are most popular in SMF industries. In deep drawing, circular metal blank is stretched by downward drawing force into the desired part, commonly circular or square shape parts. Here, metal sheet plastically deformed into a cup shaped part by applied the tensile force. Whereas in bending, a sheet metal piece is bend to an angle to form a desired shape. Here plastic deformation mainly occur along the axis. Generally, sequence of operation has been performed to produce a complex shape part, similar to the roll forming. In roll forming, the operation is carried out on a roll forming line, which involves feeding sheet metal material through a sequence of roll stations. Sheet metal is forced through these roll stations to plastically deform and bend to desired shape.

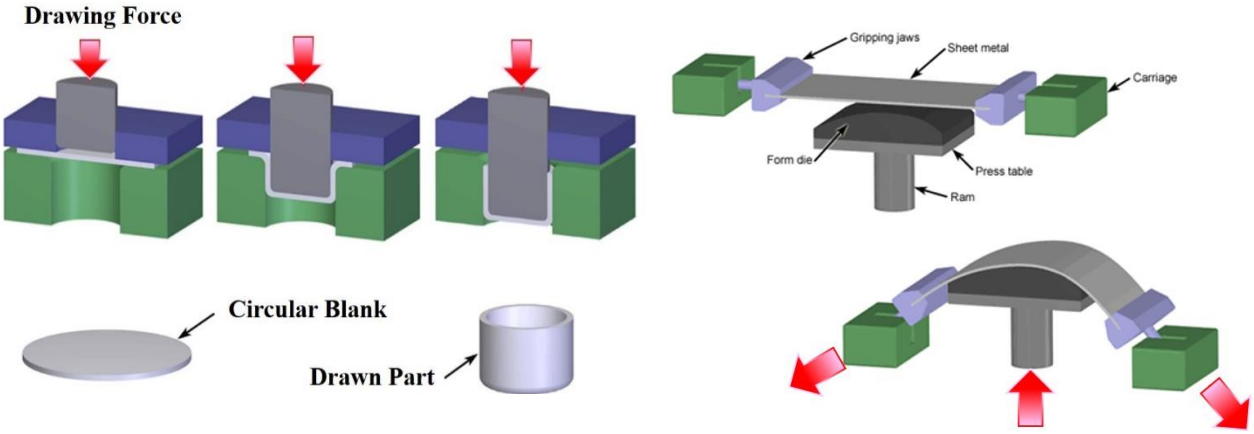

(a) (b)

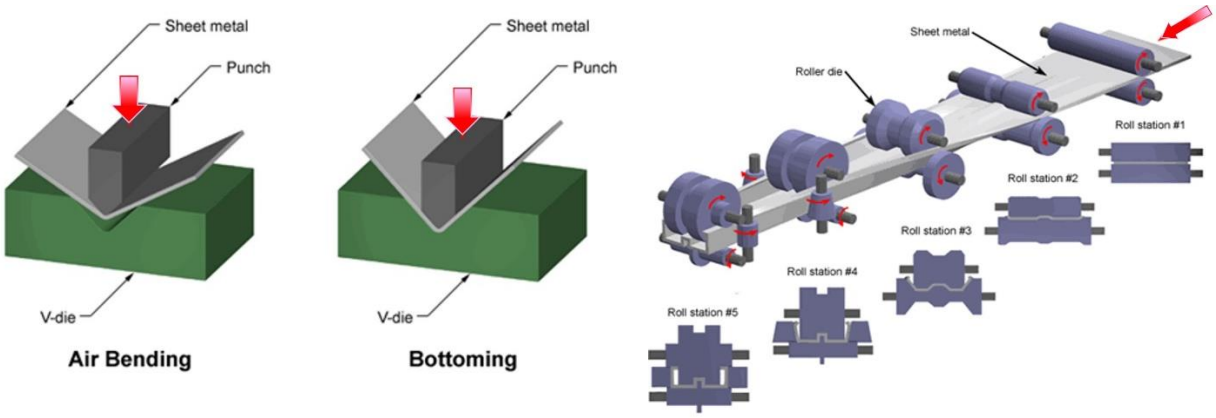

(c) (d)

Figure 1.4 Schematic of (a) circular deep drawing (b) stretch forming (c) Bending processes and (d) Roll Forming [Courtesy from www.custompartnet.com/wu/sheet-metal-forming]

Stretch forming is one of the fundamental process for formability testing in sheet metal forming. According to Schuler Metal Forming Handbook (1998), it is defined as forming by using tensile forces to stretch the sheet material over a tool or form a component or block. In stretch forming, first, sheet metal is clamped at its circumference/ circumferential edges over the die cavity, then punch was brought down to deform the sheet metal and forced to take the shape of the die. As sheet edges were clamped, sheet metal deformed due to radial strain. Stretch-formed shapes vary from a simple curved surface to complex non-uniform cross-sections. The stretch forming process is capable of stretching/shaping parts with very high accuracy and smooth surfaces. But stretch forming is influenced by various process parameters: sheet thickness, velocity of die, circumferential clamping force or blank holding force, lubricant used etc. (Banabic 2000). The complexity of stretch forming further increased with rise temperature. Thus, it is essential to know of plastic deformation process, formability measures, and particular factors limiting sheet formability while monitoring the formability issues.

1.2.1 Material Properties and Flow Stress Determination

Understanding the deformation behavior and material properties are key prerequisites to optimize the process parameters and to produce quality form products. The deformation behavior of material varies due to the base metal, alloying elements present, processing or heat treatment history (Banabic et al. 2010). The response to plastic deformation manifests itself through different phenomena, such as hardening and softening, failure and fracture. These phenomena are significantly influenced by many factors such as strain, strain-rate, and temperature. During the hot forming process, for a given combination of thermo-mechanical parameters, microstructure of the alloy changes which affect the mechanical characteristics. Therefore, it may deeply affect the behavior of the sheet metal. Hence, knowledge of the

deformation behaviors of metals and alloys have a significant importance for designers of metal forming processes because of its effective role on metal flow pattern as well as the kinetics of metallurgical transformation.

1.2.2 Experimental Formability Evaluation

Formability is the ability of a given metal workpiece to undergo plastic deformation without being damaged. Formability depends on the consequence of material properties and the complex tool- sheet interactions (Schafrik et al. 2001). Figure 1.5 shows the numerous process parameters that influence the formability. The complexity may even further increase at elevated temperature. Formability is evaluated based on standard parameters, namely, Limiting Dome Height (LDH), Limiting Drawing Ratio (LDR), and Forming Limit Diagram (FLD) (Ayres, Brazier, and Sajewski 1978; Basak and Panda 2019a; Kuroda and Tvergaard 2000). Among all these parameters, FLD provides a comprehensive picture of material deformation capability and limiting strains. Hence, it has been extensively used as the formability measure. FLD represents the maximum extent of the deformation of sheet metal until plastic instability occurs in a material. FLDs are established by experiments that provide pairs of values of the limit strains ε_1 and ε_2 obtained for various loading patterns (equibiaxial, biaxial, uniaxial etc.) as shown in Figure 1.6. The limit strains are measured by marking of circular grids on the sheet specimen. The precise and accurate measurement of deformed grid is one of the critical issues to get accurate limiting strains in the FLD.

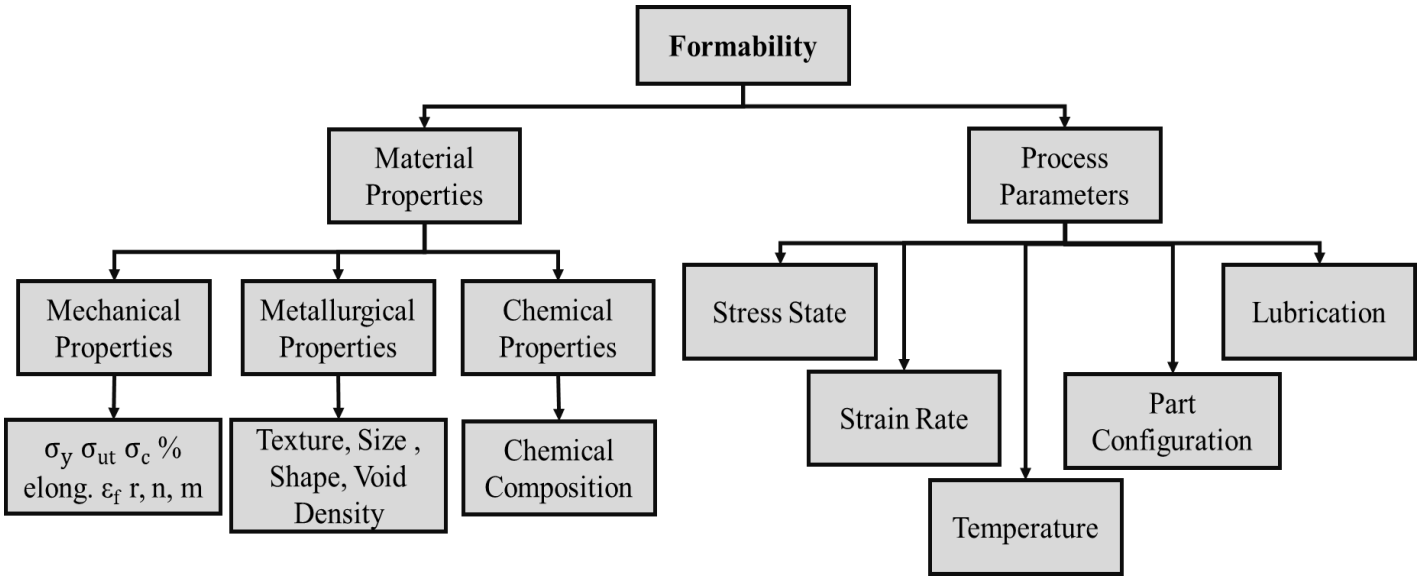

Figure 1.5 Parameters influencing sheet metal formability (Banabic 2010b)

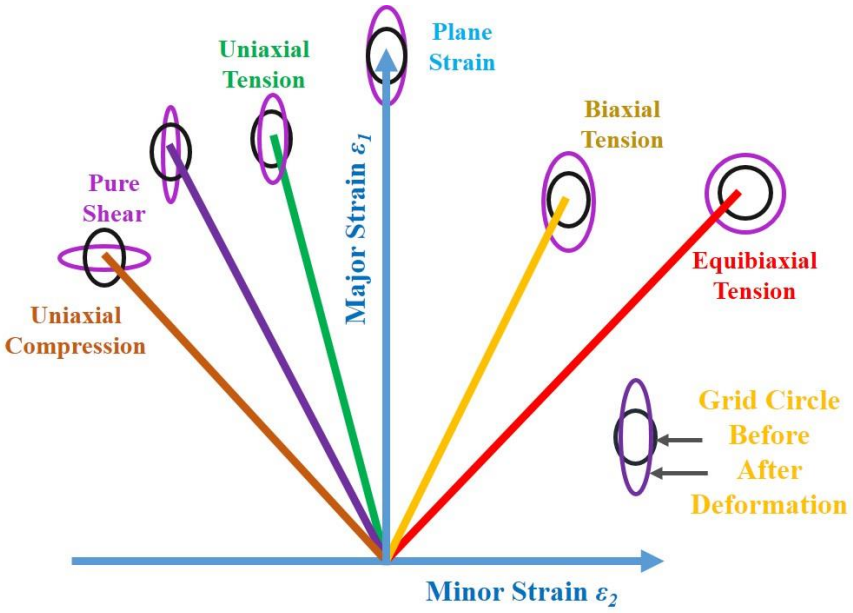

Figure 1.6 Various loading patterns for limit strains determination (Banabic 2000)

In most of the high performance/strength materials, many times, it is challenging to define the forming limit at onset of the necking, as fracture takes place without a noticeable necking in the blank specimen (Jafarian et al. 2018; Kuroda and Tvergaard 2000; Prasad et al. 2017). Recently, researchers considered fracture forming limit diagrams (FFLDs) to define material fracture limiting strains. These FFLDs were developed to evaluate the fracture limits in a minor (ε_2) and major (ε_1) strains space from uniaxial compression (T-C) to biaxial tension (T-T) region (Basak and Panda 2019a; Basak, Panda, and Zhou 2015; Bruschi et al. 2014; Güler and Efe 2018; Prasad et al. 2018b). Accurate determination of failure limits is one of the key issues for reliable FLD prediction. The formed parts are rejected because of necking, excessive thinning, wrinkling, or insufficient stretching. While manufacturing a component by SMF, it is necessary to consider the other failure conditions also. Therefore, FLDs need to be determined based on necking, fracture, wrinkling limits of a material. The details of different zones of a FLD are illustrated Figure 1.7.

Necking is noticed as the failure mode in tension, while wrinkling occurs in compression. The locus of limiting strains measured at onset of necking of the material is considered as Forming Limit Curve (FLC). FLC is strongly influenced by strain path change and the least limiting strain value is observed at plane strain condition loading. Usually, a safe forming limit zone is considered as 10% below the FLC as shown in Figure 1.7. A locus of in-plane strains delimiting the onset of wrinkling in SMF is considered as the Wrinkling Limit Curve (WLC) by measuring the circumferential and radial strains (Won et al. 2019). The WLC is situated in the lower left-hand of the second quadrant of the principal strain space.

Furthermore, the introduction of advanced high strength (AHS) grades of material with reduced ductility brought up an issue concerning shear fracture which could not be accurately predicted by the conventional FLC. It is exceedingly difficult to capture the accurate necking limits with limited ductility of the material. Therefore, fracture forming limit curve (FFLC) is used to predict failure of sheet materials where fracture or tearing were observed without noticeable necking. Generally, FFLC is observed above FLC (Basak and Panda 2019a).

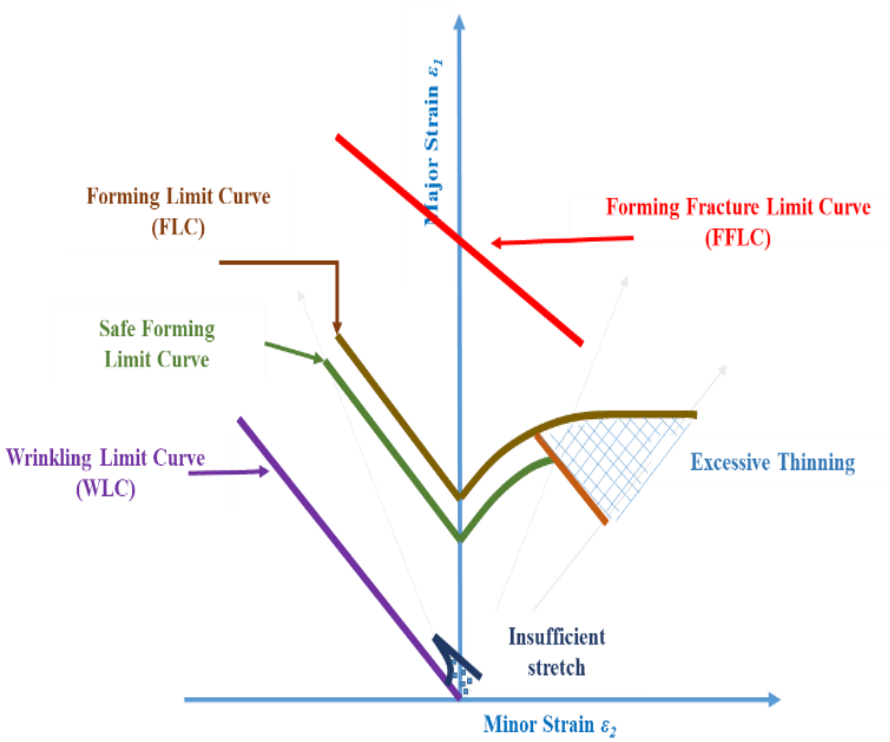

Figure 1.7 Forming, Fracture and Wrinkling Limit Diagram (Paul 2016)

It was reported that maximum permissible limiting strains are affected by several factors such as work-hardening, plastic anisotropy (induced in rolling process) and strain rate sensitivity (Dewang, Panthi, and Hora 2019; Satish, Feyissa, and Kumar 2017; Seyedkashi et al. 2018). Further, it was observed that the FLC is even sensitive to pre-formed conditions of the sheet material, particularly in non-linear paths during the deformation process (Dilmec et al. 2013). In many engineering applications, complex workpieces are manufactured by undergoing sequential processes. Where, experimental FLC prediction requires tedious experimental work, complex calculation, and advanced computational analysis, which is incredibly challenging, costly, and time-consuming (Su et al. 2019). Therefore, prediction of FLC by theoretical and numerical models was gaining special attention.

1.2.3 Need of Warm Forming

Forming of high strength alloy is incredibly challenging due to its high strength and limited ductility at room temperature. Also, high strength materials require excessive

deformation load during the forming processes which in turn increase the tendency of elastic recovery, wrinkling and sudden failure tendency. In literature, warm/elevated temperature forming is proposed as one of the proven techniques to produce complex shapes of high strength alloy. The elevated temperature forming facilitates easy flow of material in a die cavity, with less deformation resistance (Panicker et al. 2015). As expected, hot forming makes a material softer and ductile, which helps to form product (Satish, Kumar, and Merklein 2017; Wu and Koo 1997). Hot forming of any sheet metal permits maximum deformation, reduces spring back and increases its formability with proper care of overheating (Banabic 2010b; Kuhlmann-Wilsdorf 1989). But, forming at elevated temperature also have some drawbacks such as, high tooling cost, special heating setup and more precautions need to be taken during and post forming operations.

1.2.4 Numerical Investigation of Formability

Nowadays, Finite Element (FE) simulations are extensively used to reduce inaccurate and expensive tryouts in sheet metal industries. The prediction capabilities have significantly reduced the time consuming and costly die tryouts. FE simulation is widely used in the sheet forming industries, where the technology has contributed to a better understanding of preferred forming processes. The FE technology and CAE tools make a complete virtual process development. Many nonlinearities such as anisotropic behavior, complex geometries with large deformation, contact issues, elevated temperature interactions are involved in FE simulations of sheet forming processes. Nowadays, many advanced FE software such as ABAQUS/DYNAFORM/ LSDYNA/ AUTOFORM are available to handle these nonlinearities efficiently. Thus, it is necessary to investigate the various aspects of FE simulations for limiting strain predictions.

The trustworthiness of the numerical modeling depends on the used input material models and correctness of the input material data to evaluate the several aspects of the material response to deformation (Banabic et al. 2010). Input material properties namely tensile strength (yield and ultimate), strain hardening exponent (n) anisotropic parameter/Lankford coefficient (r) and strain rate sensitivity parameter (m) play a significant role in understanding the plastic deformation during the sheet metal formability. A large variety of experiments are available to define the sheet metal flow behavior, categorized by different abstraction levels, from material testing-type to physical simulation experiments, which aim by reproducing process testing conditions more closely (Bruschi et al. 2014). As experimental results depend on the number of process parameters, it cannot assure transferability other than one it to replicate. The uniaxial

tensile test is nowadays the most widely used to determine sheet metal behavior, due to its intrinsic simplicity of execution.

To characterize the flow behavior and initiation of plastic deformation of sheet metal under various forms of loading, appropriate selection of material models is essential for accurate numerical models. This can be achieved by study of two elements namely,

1. **A Hardening/Constitutive model**, to describe complicated deformation behavior of different alloys by process variables like strain, strain rate and temperature.

   Material deformation under thermal processing is characterized by a constitutive model for flow stress. It relates the effective flow stress to strain, strain rate and temperature. These mathematical governing equations are calculated by set of experimental outcomes in the plastic deformation domain. The data collected from uniaxial tensile test at quasi-static strain rate provides the basis for the material parameters identification in constitutive models especially for forming applications. An ideal constitutive model for material should describe the test temperature and strain rate dependency, pre-strain and strain-rate dependency, strain hardening behavior. However, it is exceedingly difficult to cover all phenomena in a single model.

2. **A Yield criterion**, to describe states of stress that will cause yielding.

   Yield criterion is a hypothesis defining the elasticity limit in a material and onset of plastic deformation for any stress combination. In SMF experiment, plane stress condition ($\sigma_3 = 0$) is assumed. In sheet metal forming, sheet metal is considered as anisotropic in nature (properties of sheet are different in different directions). Hence, well-known Von Mises or Tresca yield functions are inadequate to describe the plastic behavior of Inconel alloys. Therefore, it is essential to investigate the correctness of constitutive models and anisotropic yield criteria, to describe the plastic anisotropic behavior of sheet metal.

1.3 Organization of the Thesis

This research work is presented in seven chapters as:

Chapter – 1: This chapter covers the background and introduction of Ni-based alloy in sheet metal forming. It also discussed the need of formability studies for Inconel 718 alloy. The chapter confers about the thesis organization.

Chapter – 2: This chapter presents an extensive literature review for various aspects of the SMF process. Various aspects of experimental, theoretical, and numerical for warm SMF have

been discussed. Research gaps based on extensive literature review, objectives for the thesis, and the adopted methodology, have been recognized.

Chapter – 3: This chapter deals with the experimental investigations about the uniaxial tensile flow behavior of Inconel 718 alloy at elevated temperature (RT-700ºC). The required uniaxial anisotropic material properties, flow stress, and strain hardening behaviors have been studied at various test temperatures (RT-700ºC, at an interval of 100ºC) and quasi-static strain rates (0.0001-0.1 /s). The fractography and EBSD studies of post tensile test specimens have been carefully studied.

Chapter – 4: This chapter involves development and comparative evaluation of various constitutive models and anisotropic yield criteria for Inconel 718 alloy at a wide range of temperatures. The detailed procedures to determine material constants for each constitutive model and anisotropic yield criteria have been discussed.

Chapter – 5: This chapter focused on the experimental and theoretical investigation of forming, fracture, and wrinkling limit diagram of Inconel 718 alloy. The experimental forming and fracture limit diagrams have been determined using the Nakazima test. The detailed fracture morphology of stretch-formed specimens has been examined. Theoretical forming and fracture limit diagrams were predicted by M-K and B-W Models, respectively. Further different qualitative aspects of the stretch forming process by FE analysis have been investigated and validated with experimental and theoretical outcomes.

Chapter – 6: This chapter is focused on a systematic investigation of modified YBT to define the occurrence of wrinkling instability in the SMF process. Finally, forming, fracture, and wrinkling limit curves of Inconel 718 have been estimated to understand the complete formability behavior at elevated temperatures.

Chapter – 7: This chapter covers major conclusions and specific contributions to scientific and technical research. Further scope of research is also discussed.

Thus, the next chapter discussed the detailed literature review on the formability of the SMF process.

2. Literature Review

This chapter covers an extensive literature review on major aspects of warm sheet metal forming. The material testing, flow stress behavior, and strain hardening behavior of Inconel 718 alloy have been discussed in detail. Further, experimental and numerical aspects of SMF have been discussed thoroughly. Based on a thorough literature survey, the research gaps have been identified. The objectives and research methodology have been formulated.

2.1 Challenges in Forming Inconel 718 Alloy

Inconel 718 alloy is an indispensable material for various critical applications due to its excellent blend of material properties. Despite the above advantages, Inconel 718 alloy has a narrow forming temperature range, more deformation resistance, and complex microstructures. Inconel 718 alloy is more difficult to deform and often has less predictable forming characteristics than other commonly used metallic alloys such as steel and aluminum at room temperature (Roamer et al. 1997). From the literature, it is observed that the Inconel 718 alloy can be formed at RT but requires an excessively high forming load. Also, high strength-to-weight ratio requires excessive deformation force to form the product, which increases the tendency of elastic recovery during forming processes; this phenomenon is popularly known as spring-back. Thus, it requires compensation either during bending or post-bend treatment (Prasad et al. 2017; Roamer et al. 1997). It was stated that noticeable localized necking or thinning tendency was not observed during the stretch forming process of Inconel alloy. Thus, it is challenging to define the forming limit at onset of the necking (Jafarian et al. 2018; Kuroda and Tvergaard 2000; Prasad et al. 2017).

Another major challenge with Inconel alloy is considerable wrinkling tendency due to high deformation force (Reed 2006). The wrinkling in the final sheet metal component seriously affects the final product's functional requirements and aesthetic appeal (Banabic 2000). Wrinkling instability on contact surfaces can negatively influence the part assembly and its function. Also, other post-processing operations such as welding, machining affect drastically due to wrinkle defects in the sheet components. It may damage the tooling due to the critical wrinkling tendency (Ameziane-Hassani and Neale 1991). Therefore, prevention and prediction of wrinkling instability is essential to have hassle-free wrinkling operations for quality sheet metal components.

One of the prominent solutions to overcome these issues is forming at elevated temperature either hot forming ($0.44Tm < T < 0.55T_{m)}$ or warm forming ($0.3T_m < T < 0.5T_m$)

condition. As expected, hot forming makes a material softer, which helps to form a product with less deformation resistance (Wu and Koo 1997). Hot forming of any sheet metal permits maximum deformation reduces spring back and permits maximum deformation with minimum annealing between forming operations by proper care of overheating (Banabic 2010b; Kuhlmann-Wilsdorf 1989). But, forming at elevated temperature also has some drawbacks such as high tooling cost, special heating setup, and more precautions that need to be taken during and post-forming operations.

Additionally, the most important aspect of any hot working is controlling the temperature of the workpiece. Usually, 90% of the energy imparted into the workpiece is converted into heat. Therefore, the deformation process should be quick enough to instantly raise the temperature of the workpiece instantly, which will not occur in usual practice. Some of the heat is lost through the surface of the workpiece to the cold tooling. One of the prominent solutions to this problem is to heat the tooling setup. Thus, less heat loss occurs with heated tooling. But it reduces the overall tool life (Bruschi et al. 2014). The following sections discussed the various important literature aspects of material testing, deformation behavior and material modeling for warm/hot behavior of sheet metal.

2.2 Mechanical Properties Determination

Accurate determination of mechanical properties is the most critical issue to analyze the plastic deformation behavior of sheet metals. Thorough knowledge of deformation behavior helps to optimize the process parameters and produce quality form products. Additionally, the overall process becomes more complicated during the hot forming processes, the microstructure of the alloy may change, which affects the mechanical behavior of a material. Particularly, yield strength (σ_y), ultimate tensile strength (σ_{ut}), compression strength (σ_c), biaxial tensile strength (σ_b), ductility (% elongation), fracture strain, uniaxial and biaxial Lankford/anisotropy coefficient (r), strain rate coefficient (n), and strain rate sensitivity (m) have the considerable influences on formability (Banabic et al. 2010).

A large variety of standardized tests/techniques are available to describe the flow stress behavior and to evaluate the material properties of sheet metal. These tests are divided into three main groups, namely (i) uniaxial tests, (ii) multi-axial tests, and (iii) cyclic tests, for material properties determination, as listed in Figure 2.1. The material data collected for the above tests provide the basic for material parameter identification in various material models (constitutive model + yield function), required for numerical simulations of sheet metal

forming. In uniaxial tests, the various established techniques are uniaxial tensile, layer compression, uniaxial tests at elevated temperature, and uniaxial tests at high strain rates.

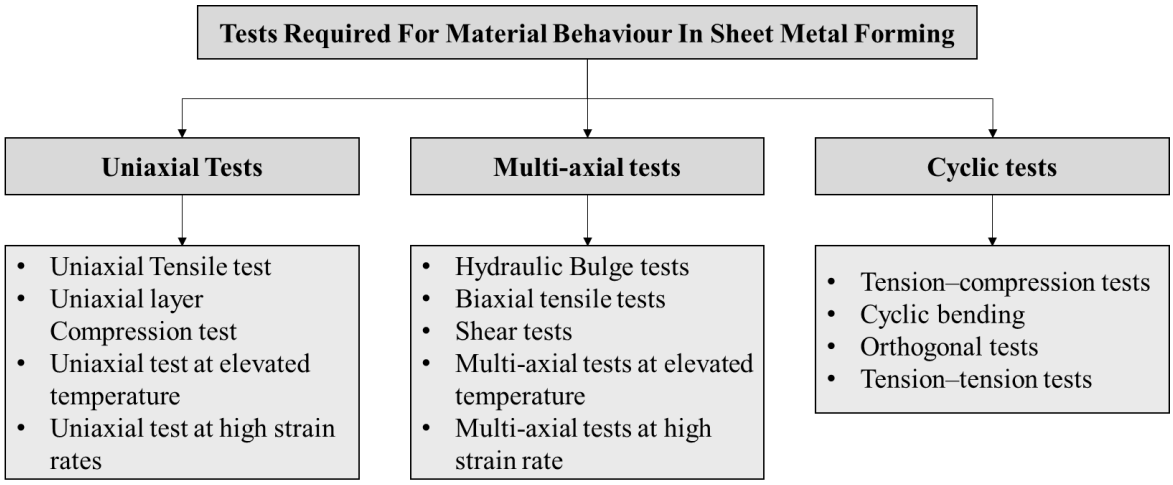

Figure 2.1: Standardized tests available for material properties determination in sheet metals (Bruschi et al. 2014)

The uniaxial tensile test, according to the ASTM E8 standard, is the most popular and widely used testing method to determine yield/ ultimate strength, % elongation, fracture strain, strain hardening exponent (n) and strain rate sensitivity (m). Tensile strength defines the load-bearing capacity of the material during uniaxial loading. Whereas % elongation defines the ductility of the material. The dependence of flow stress on strain level is defined by strain hardening exponent (n). In materials, a high n-value indicates the good workability of material. Also strain hardening exponent assistances for high elongation under slow strain rate (Dieter 2011).

The dependence of flow stress on strain rate measured by strain rate sensitivity (m). It is experimentally determined by two methods. The two methods are graphically illustrated in Figure 2.2. In the first methods, the stress levels at different strain rates and at the fixed strain of two tensile tests were compared at a particular test temperature (Banabic 2000). In other methods, the strain rate is changed suddenly during a test and compares the levels of stress immediately before and after the change (Banabic 2000). This method is usually called as a jump test or rate-change test. The first method, continuous stress-strain curves give larger m-value than the second test (Hedworth and Stowell 1971). In the continuous stress-strain curves method, for each strain rate, a separate specimen is required, whereas in jump test, single specimen can be used for quite a few strain rate changes (Marciniak, Duncan, and Hu 2002).

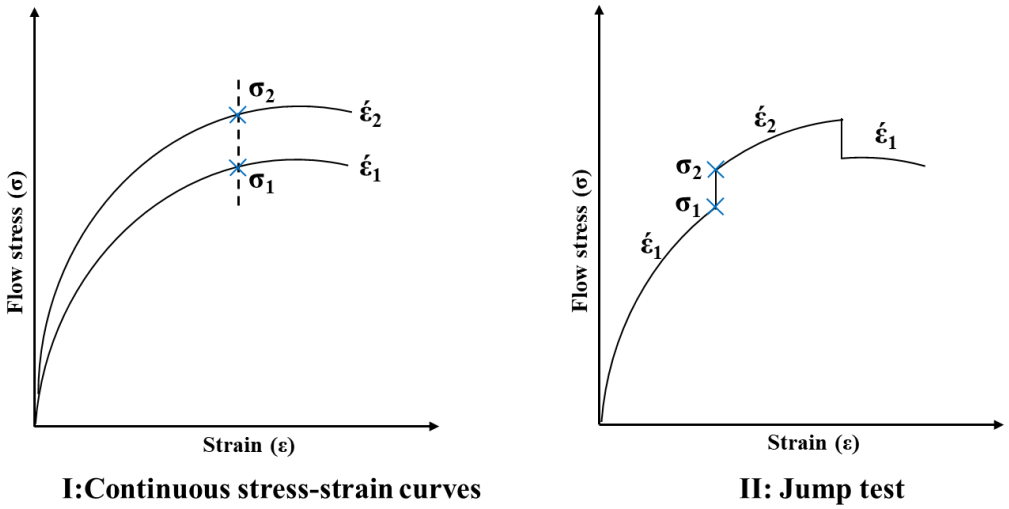

Figure 2.2 Methods used for strain-rate sensitivity measurement (Banabic 2000)

Sheet metal is manufactured by either cold/hot rolling process; grain elongates severely in the strained direction. This directionality of properties of metal is called anisotropy (Banabic 2010b). Flow characteristics of metal, with respect to the axial loading direction, are highly dependent on sheet texture in SMF processes. Plastic anisotropy of a rolled sheet metal is typically characterized in terms of strain ratio by Lankford coefficient (r). This parameter defines the resistance of the material to thickness change. Lankford coefficients can be determined by uniaxial tensile tests with a sheet strip specimen as per ASTM 517-00:2010. It is reported in the literature that the determination of r -value is extremely sensitive (Banabic 2010b). Three Lankford coefficients are considered in three loading directions to sheet metal i.e., rolling direction (0º), diagonal to rolling direction (45º), and transverse direction to rolling direction (90º) as illustrated in Figure 2.3.

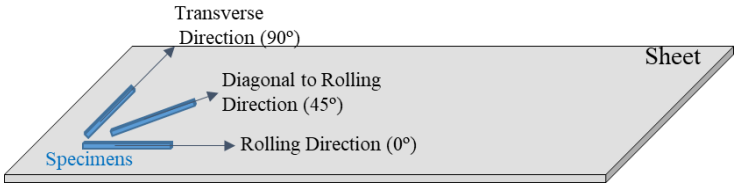

Figure 2.3 Specimen orientations with respect to the sheet rolling direction

Usually, average or normal anisotropy and planer anisotropy are considered for defining the anisotropy in sheet metal forming. Normal anisotropy ($\bar{R}$) is the main influencing parameter of the maximum drawability of the sheet. During a deep-drawing operation, metal with high ($\bar{R}$) experiences less thinning than metal with small ($\bar{R}$) with the same metal flow characteristics (Banabic 2010b). Therefore, for smooth contoured parts (e.g., automotive/ aerospace panels) a high $\bar{R}$-value, larger than unity, is desirable (Wang and Cao 2000). The planar anisotropy (ΔR) is expressed by the difference of strain ratio in three orientations of the sheet. It is responsible

for formation of ears in drawn cups and uneven thinning. A Smaller value of ΔR indicates a lesser possibility of formation of earing. This also reduces the defect of wrinkling/ripples and tearing in part. To reduce the asymmetric stretching and earing, material should have a smaller value of ΔR (Wang and Cao 2000). The other alternative parameters, such as in-plane anisotropy (A_{IP}) and the anisotropic index (δ) also play a significant role in defining anisotropy in terms of yield stress variation and % elongation of material (Jata, Hopkins, and Rioja 1996; Wu and Koo 1997). An increase in the values of A_{IP}, indicates an increase in the extent of anisotropic nature. Also, the presence of low value of anisotropic index (δ) indicate very less elongation anisotropy of the material.

A layer compression test, proposed by Pawelski (1967) and modified from the standard compression test (Merklein and Kuppert 2009), is commonly used to determine the biaxial compression strength (σ_c), biaxial Lankford/anisotropy coefficient (r_b), and time dependency of anisotropic behavior of sheet metal. In this test, a stack of circular blanks is compressed between two coplanar tool panels/ pull rods. The uniaxial pressure loading leads to an equi-biaxial tensile load in the layered and compressed specimen. The stress-strain curve, recorded by the layer compression test, shows maximum achievable strain values up to 0.7, greater than attainable in uniaxial tensile tests (Merklein and Kuppert 2009). The stress-strain measurement is highly influenced by overall friction at the contact interface (tool plates and stacked blanks specimen). It is advisable to use Teflon foils at contact to avoid a 3D stress state and stacked blanks oriented along rolling direction.

The forming behavior is overly sensitive towards to its process parameters i.e., temperature, strain rate, and sheet orientation. It is reported that elevated temperature forming with lower strain rate is more favorable condition for high strength alloy difficult to form material like Inconel alloy, Titanium alloy (Lin et al. 2012; Wu and Koo 1997). Commonly, an isothermal/elevated temperature uniaxial tensile test is used to determine the flow stress curves and evaluate material properties at elevated temperatures. In the isothermal tensile test, first sheet metal sample is heated to test temperature and heat preserve for 5-6 minutes to ensure a uniform temperature prior to loading and then the test is performed at a certain strain rate and constant temperature. Split furnace covering test specimen is attached to Universal Testing Machine (UTM).

Since strain rate or deforming speed plays a significant role during evaluation of mechanical properties. Figure 2.4 illustrates the distinction between strain rate regions and techniques used to attain these strain rates. Conventional cross head devices, especially uniaxial testing machine is widely used to evaluate flow behavior at quasi-static strain rates. The uniaxial

testing machine has a limitation and cannot provide testing at extremely high speed. Also, the total duration of a typical tensile test varies from seconds to hours depending upon the material under investigation. The negligible inertia effect is not able to be exploited in these test durations. Split hopkinson pressure bars (SHPBs), Taylor impact, and drop towers are widely used to evaluate the flow stress behavior at intermediate strain rates (10^2-10^5). Whereas, plate impact test was used at higher strain rates (>10^5). The flow behavior of a material is extremely sensitive to high strain rate values. It is mentioned in the literature that mechanical properties of the material tested at quasi-static strain rates are more consistent than tested at higher strain rates (Bruschi et al. 2014; Field et al. 2004). Also, material tested at higher strain rate shows higher strength values compared to the static one. Figure 2.5(a) gives the representative comparison of flow stress curves for duplex steel A900 tested at quasi-static and higher/dynamic strain rates.

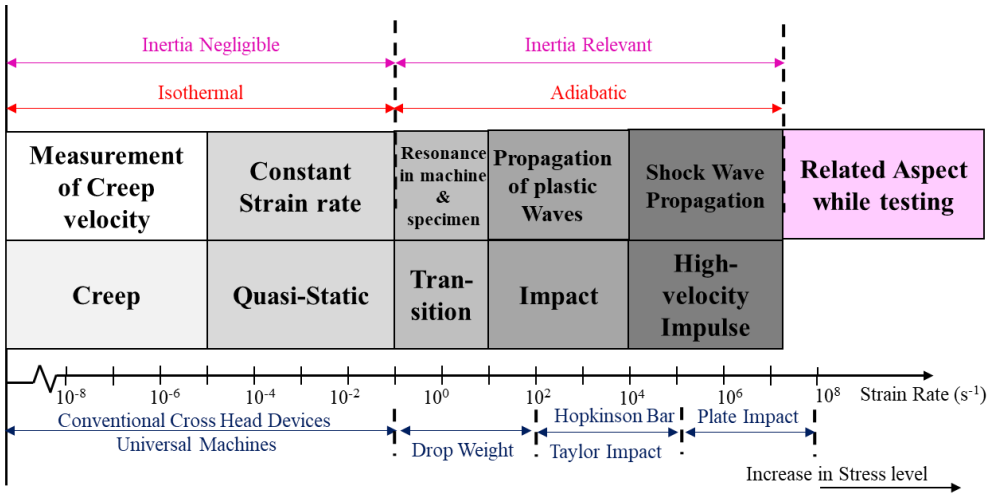

Figure 2.4: Classification of the strain rate regions and techniques (Bruschi et al. 2014)

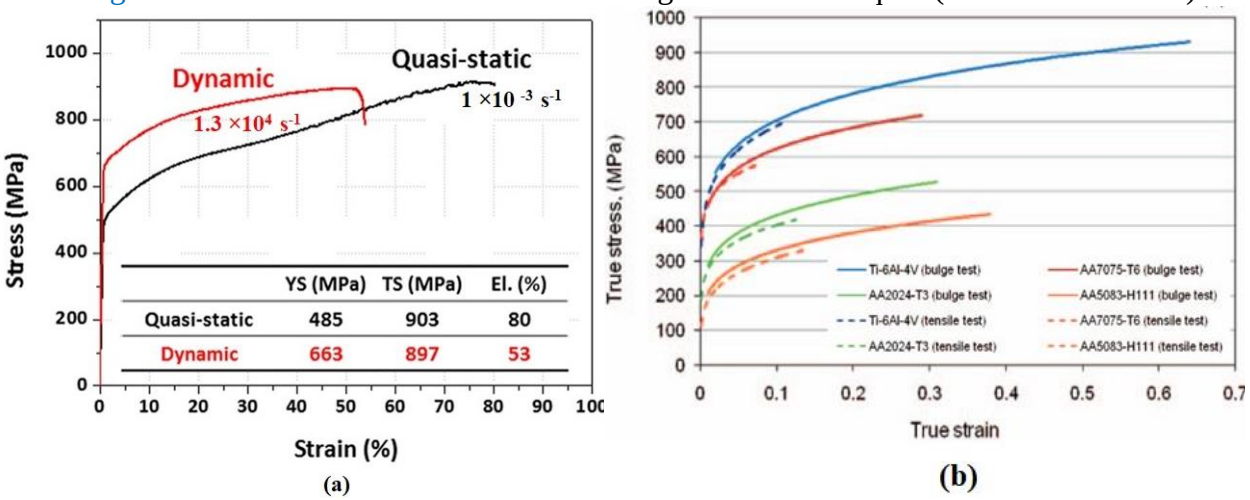

Figure 2.5: Comparison of stress–strain curves (a) tested at quasi-static and dynamic strain rates (b) from tensile and bulge test (Janbakhsh, Djavanroodi, and Riahi 2013; Park et al. 2017).

Evaluation of sheet metal behavior under uniaxial and monotonic loading conditions is still most widely used in industrial practice since it provides a quick tool for gaining material data. Due to its simplicity of execution, a direct understanding of the obtainable data is possible. Most of the input parameters of material modeling i.e., constitutive modeling (especially for flow stress prediction) and yield criteria in commercially available finite element packages, are identified through a uniaxial tensile test. Thus, the accuracy of most of the numerical simulations is highly dependent on these input parameters. However, one of the major drawbacks of these experimental procedures is conducting tests at the high strain rates or temperatures. It is difficult to keep strain rate and/or temperature constant during the test. This leads to difficulty in obtaining flow curves at constant strain rate and temperature. Further, during actual service conditions, a biaxial state of tensile/compression stress was experienced. Thus, it is necessary to assess nonlinear stress-strain relationships, mostly experienced during complex multiaxial loading in formed part lifetime. Hence, biaxial tests or multiaxial tests are designed for more accurate properties for predicting sheet metal behavior.

The main advantages of biaxial tests are that maximum achievable values of strain are between 0.5 and 0.8, depending on the material. Figure 2.5(b) gives the comparison of uniaxial and biaxial tensile test data for different alloys. In the biaxial test, a testing setup suitable for determining the stress–strain curve under a biaxial stress state with influence of friction is neglected. Numerous tests, namely dome test/ bulge test (Hydraulic bulge test or viscous pressure bulge test), biaxial tensile test, shear test/combined tension–torsion test, and combined bending and in-plane test as listed in Figure 2.1. These tests are used to determine biaxial tensile strength, compression strength, flexural strength, fracture properties and fatigue life of material for different specimen types.

It is noticed that the deformation behavior of sheet material depends on various process parameters. Hence, it is necessary to have a detailed knowledge of flow stress behavior and material properties to analyze the formability. Few studies have been reported for material properties and deformation behavior studies of Ni-based alloys. Table 2.1 gives the literature review for deformation behavior and material properties determination of Ni-based alloys, especially Inconel 718 alloy. Thomas et al. 2006 investigated deformation behavior of Inconel 718 alloy till 650ºC. It observed that deformation at elevated temperatures involves large strains at low stresses, but at the same time, substantial modifications on the microstructure occur. The resulting grain size depends on softening mechanisms, namely, dynamic recovery and recrystallization.

Table 2.1 Literature review showing deformation behavior and material properties determination of Ni-based alloy

Authors	Alloy	Tests Availed	Test Temperature	Strain Rates	Microstructural Studies	Flow Stress Determination	Material Properties Determined								
							σ_y	σ_{ut}	σ_c	σ_b	% elong.	$\varepsilon_f/\overline{\varepsilon_f}$	*r*	*n*	*m*
Thomas et al. 2006	Inconel 718	Uniaxial Compression Tests	900-1080 ºC	0.0005, 0.001-0.1 s^{-1}	✓	✓	✓	✓	×	×	✓	✓	×	×	×
Iturbe et al. 2017	Inconel 718	Uniaxial Compression Tests	21-1050ºC	10^0 to 10^2 s^{-1}	×	✓	✓	✓	×	×	✓	✓	×	×	×
Caliari et al. 2011	Inconel 718	Uniaxial Tensile Test	650-700 ºC	0.5 mm/min	✓	✓	✓	✓	×	×	✓	✓	×	×	×
Lin et al. 2014	Ni-Cr-Fe alloy	Hot Compression Tests	920–1040 ºC	0.001–1s^{-1}	✓	✓	✓	✓	×	×	✓	✓	×	×	×
Li et al. 2011	Inconel 625	Hot Compressions Tests	900-1200 ºC	0.1 s^{-1}	✓	✓	✓	✓	×	×	✓	✓	×	×	×
Prasad et al. 2017	Inconel 718	Uniaxial Tensile Test	Room Temperature	0.001–1 s^{-1}	✓	✓	✓	✓	✓	✓	✓	✓	✓	✓	✓
Prasad et al. 2019	Inconel 718	Uniaxial Tensile Test	500-700 ºC	0.001–1 s^{-1}	×	✓	✓	✓	×	×	✓	✓	×	×	×

Yield strength (σ_y), ultimate tensile strength (σ_{ut}), compression strength (σ_c), biaxial tensile strength (σ_b), ductility (% elong.), fracture strain ($\varepsilon_f/\overline{\varepsilon_f}$), uniaxial and biaxial Lankford/anisotropy coefficient (*r*), strain rate coefficient (*n*), and strain rate sensitivity (*m*)

Iturbe et al. 2017 reported that the Inconel alloy mechanical properties decrease by an average of 25% at 700 ºC. Afterward, there is a substantial drop in the mechanical properties. Caliari et al. 2011 studied the mechanical behavior of Inconel 718 alloy by hot tensile tests at a temperature range of 650ºC -700ºC. They observed the presence of formed γ' phase during hot tensile of alloys significant increase in yield strength with a decrease in ultimate strength and (%) elongation. Lin et al. 2014 investigated elevated temperature deformation behaviors of the Ni-based superalloy over wide ranges of test temperature and strain rate using processing maps. Improvement in material workability is observed at a higher temperature and lower strain rate region. The influence of temperature on workability was more predominant than the strain rate. Li et al. 2011 investigated the effect of temperature and strain on dynamic recrystallization and nucleation mechanisms have been discussed in the temperature range 920-1040 ºC. Recently, Prasad et al. 2017, 2019, reported the high anisotropy and two-stage work hardening behavior of Inconel at room temperature conditions. In summary, no literature have been reported on anisotropic material determination and deformation behavior at different strain rate and temperature for Inconel 718 alloy.

2.3 Strain Hardening and DSA Behavior

Strain hardening behavior describes the increase of stress necessary to continue deformation at any stage of plastic strain. The nature of curves in the plastic deformation stage in stress-strain curve explains interfering with the dislocation movement, grain boundaries. For a material with a high *n*-value, the flow stress increases rapidly with a rise in strain. This tends to distribute further strain to regions of lower strain and flow stress. A high n-value leads to a significant difference between yield strength and ultimate tensile strength which indicates of good workability of material and strain hardening assistances for the high elongation under slow strain rate. Various mathematical flow relationships have been proposed to describe the hardening behavior such as Holloman, Swift, Ludwick, Ludwigson, and Voce (Butuc et al. 2011; Markandeya et al. 2006; Mishra et al. 1989) in the plastic deformation region.

In literature, Mishra et al. 1989 examined the flow behavior of HSS at room temperature by these flow relationships. Temperature-dependent work hardening parameters have been used to define the flow stress for respective flow relations. Even Satyanarayana, Malakondaiah, and Sarma 2007 analyzed flow behavior of Aluminum alloy by using empirical flow relationships. It was observed that these relations fitted well in the high strain region and exhibit deviation in the low strain region. Prasad et al. 2018b studied the work hardening capacity and reported two-stage work hardening behavior of Inconel alloy at room temperature. Two-stage of work

hardening is descried by Hollomon and Swift hardening law. Recently, Wen et al. 2014 studied the work hardening behavior of aged Ni-base, Inconel 718 super-alloy, during hot deformation. It was concluded that the work-hardening behaviors of the studied super-alloy are significantly affected by deformation temperature, strain rate, strain, and presence of δ phase. In summary, the researcher concentrated on work-hardening behaviors of anisotropic sheet materials, namely steel and Aluminum alloys. It is observed that very few literature have been available on work-hardening behaviors of Ni-based alloy at elevated temperatures.

It is observed that high strength alloys, namely steels, Inconel exhibit serration behavior at elevated temperature. Serrated yielding was first observed by the Portevin and Le Chatelier in 1909 while studying the properties of mild steel at elevated temperatures. Portevin and Le Chatelier investigated this behavior in an aluminum alloy. The serrated plastic flow was subsequently referred to as the Portevin Le Chatelier (PLC) effect or dynamic strain ageing (DSA). The temperature range within which the serrated yielding occurs is known as the DSA or PLC region. Further, Rodriguez discussed the phenomenon of serrated plastic flow or serrations, load drops, jerkiness or other discontinuities in the stress-strain curve for constant strain rates (Rodriguez 1984). According to Rodriguez, the serrated plastic flow is mainly caused by seven physical processes:

i. When there is an instantaneous increase in mobile dislocation density or average velocity of dislocations or both.
ii. Interaction of moving dislocations lead to sudden increases in mobile dislocation density and/or average velocity of dislocations
iii. Alloys undergoing order-disorder transformations, gradients, or modulations in the order encountered by moving dislocations
iv. Continual mechanical twinning. Twinning is characterized by a positive temperature dependence and a negative strain rate sensitivity for the flow stress
v. Sudden rise in the specimen temperature due to adiabatic heating (mainly in cryogenic conditions).
vi. Phase transformations induced by stress and strain.
vii. Yielding across fracture surfaces in brittle materials when tested under both hydrostatic pressure and triaxial non-hydrostatic stresses

Further, Rodriguez classified the plastic serration flow in A, B, C, D, and E type (Rodriguez 1984). Figure 2.6 distinguishes the serration flow observed in metal/alloy. These types can be characterized as:

i. **Type A**: An abrupt rise in flow stress followed by a drop in value below mean level in the stress-strain curve is characterized as type A serration, which usually occurs in low-temperature range (< 400ºC).

ii. **Type B**: The oscillation about mean level in the stress-strain curve is characterized as type B, which usually develops prolongation from type A with temperature range (< 750ºC). These are considered as locking serrations as the stress level fluctuates to the mean flow stress level. It can occur alone or with type A serrations during the propagation.

iii. **Type C**: As yield stress drops below the general level of mean flow stress level, the flow is characterized as type C. It is considered as an unlocking serration of dislocation by intermetallic present in the alloy. It occurs at lower strain rates and higher temperatures than in the case of types A and B serrations.

iv. **Type D**: Plateaus due to band propagation similar to Luders band with no work hardening or strain gradient ahead of the moving band front. It can occur alone or with type B serrations during the band propagation.

v. **Type E**: Type A serrations change over to type E serrations at high strains. The latter/end are similar to type A serrations but with little or no work hardening during band propagation.

Differently, confirming the serrated yielding phenomena is by the strain-rate sensitivity (m) parameter. The negative m value confirms the claim of the PLC or DSA effect in alloys. DSA also causes a little change in the strength, a peak in the Hall–Petch constant with minimum variation in ductility with temperature (Rodriguez 1984). Since DSA is a hardening phenomenon, it increases the strength of the material.

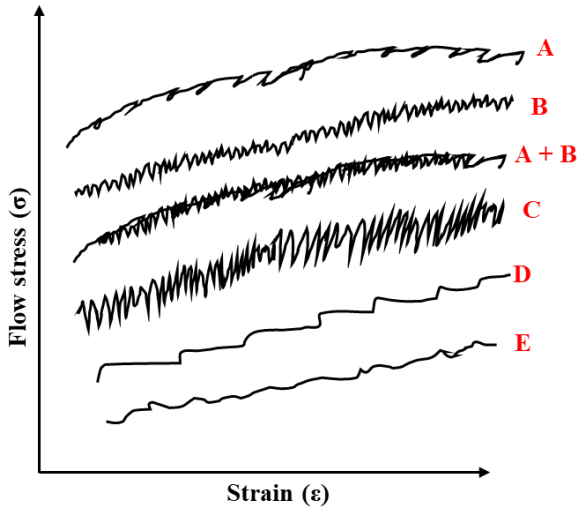

Figure 2.6 Schematic of different types of serration flows (Rodriguez 1984)

2.4 Material Models for Numerical Analysis

During hot forming processes, accurate determination of material model is crucial for precise measurement and description of the local and instantaneous response of the material (Shin and Kim 2010). This leads to trustworthy and accurate numerical simulations. In addition, anisotropy in SMF processes plays a significant role in material deformation behavior. The quality of the formed product is significantly influenced by anisotropy behavior (Barlat et al. 2003). Hence it is vital to understand anisotropy behavior and its modeling in FE analysis. The modeling of plastic anisotropy itself and its implementation in FE code is overly complex. Moreover, the complexity can be further increased at elevated temperature conditions. The material model requires for SMF processes is mainly categorized as constitutive models (for flow stress prediction) and yield criteria. Below section describe the detailed literature review pertaining to constitutive models and yield criteria.

2.4.1 Constitutive Models

The deformation behavior of material varies considerably, depending on the base metal, alloying elements present, processing, heat treatment (Schafrik et al. 2001). The response to plastic deformation manifests itself through different phenomena, such as hardening and softening, failure, and fracture. These phenomena are significantly influenced by many factors such as strain, strain-rate, and temperature. During the hot forming process, for a given combination of thermo-mechanical parameters, these microstructure of the alloy changes, which affect the mechanical characteristics such as the flow stress. Therefore, it may deeply affect the behavior of the sheet metal. During hot forming processes, accurate determination of constitutive equations (for flow stress prediction) is crucial for precise measurement and description of local and instantaneous response of the material (Panicker et al. 2015). This leads to trustworthy and accurate numerical simulations. In literature, considerable investigations have been attempted to develop constitutive equations of metals and alloys from experimentally measured data to describe the hot deformation behavior (Xu and Huang 2015). Broadly, constitutive models are divided into three categories i.e. (i) Phenomenological constitutive model, (ii) Physical-based constitutive model, and (iii) Artificial Neural Network (ANN) model (Lin and Chen 2011).

Phenomenological constitutive models provide a classical approach for modeling material behavior, which is focused on the visco-plastic theory. In this theory, several variables were designed to simulate processing parameters by strain rate softening, work hardening as well as thermal softening (Lin and Chen 2011). Phenomenological-based constitutive models

were developed by regression analysis of the experimental stress–strain data. Most popular phenomenological based constitutive models are Cowper-Symonds, Arrhenius equation, Johnson–Cook (JC) model, Khan–Huang (KH), Khan–Huang–Liang (KHL) model, modified Fields–Backofen (m-FB) model with some other phenomenological models, as shown in Figure 2.7. Cowper and Symonds developed the Cowper and Symonds model to describe the true stress in terms of uniaxial effective plastic strain and strain rate (Tari and Worswick 2015). Johnson and Cook derived the Johnson-Cook (JC) model to relate flow stress and strain, temperature and strain rate (Che et al. 2018). This model reflects only individual effect of processing parameters, but it fails to define the material properties at high strain rate and elevated temperatures (Cheng et al. 2008). The coupled effect of processing parameters has been considered by the researcher in modified the original JC model for IC10 and Al-Zn-Mg alloy (Cheng et al. 2008; Wen et al. 2014). Further, Lin, Chen, and Liu 2010 used m-JC model for tensile flow behavior of typical high-strength steel alloy for quasi- static strain rates at an elevated temperature range (850-1100ºC).

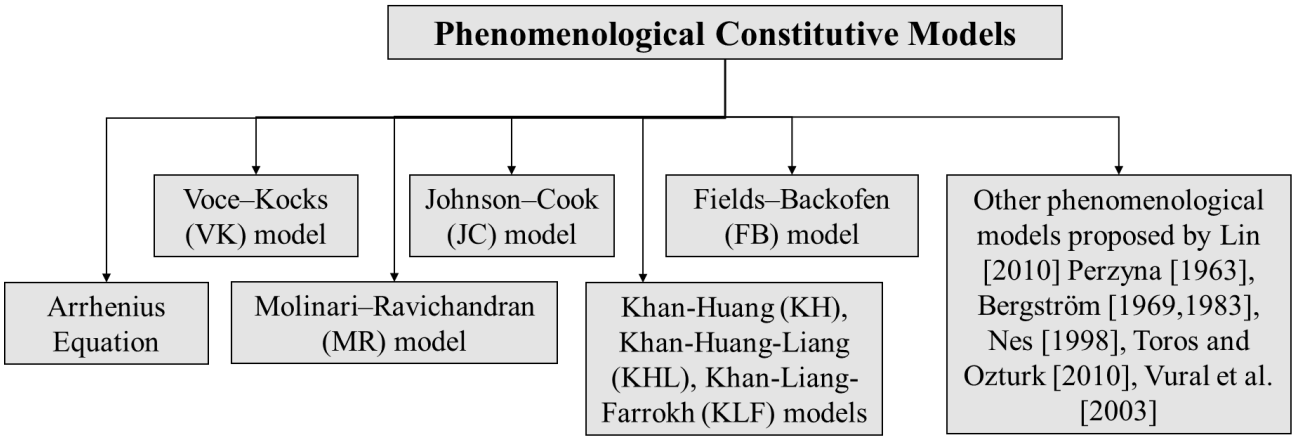

Figure 2.7 Classification of Phenomenological constitutive models (Lin and Chen 2011)

The physical-based constitutive model is based on the micro-mechanism of crystal plastic deformation. These are mostly centered on physical aspects, where thermodynamics theory, dislocation movement-activated thermally, and slips kinetics were involved (Lin and Chen 2011). The most popular physical-based constitutive models are Zerilli and Armstrong (ZA), Mechanical threshold stress (MTS), Rusinek – Klepaczko (RK), Preston Tonks Wallace (PTW), with some other physical-based models, as listed in Figure 2.8. Zerilli and Armstrong (ZA) model (Samantaray, Mandal, and Bhaduri 2009) is a more popular physical-based model because of the integral response of processing parameters, such as strain rate and temperature. However, the flow predicted using this model gives imprecise results at higher temperature (> 0.6 of melting temperature of the alloy) and lower strain rates (Mu et al. 2020). Samantaray,

Mandal, and Bhaduri 2009 formulated the modified ZA (m-ZA) model by integrating strain and temperature, strain rate, at elevated temperature. Further, researchers combined the JC and ZA model by including the average temperature rise to predicate the flow behavior of high-strength steel and Ti-6Al-4V alloy at elevated temperatures (Che et al. 2018; Lin and Chen 2010).

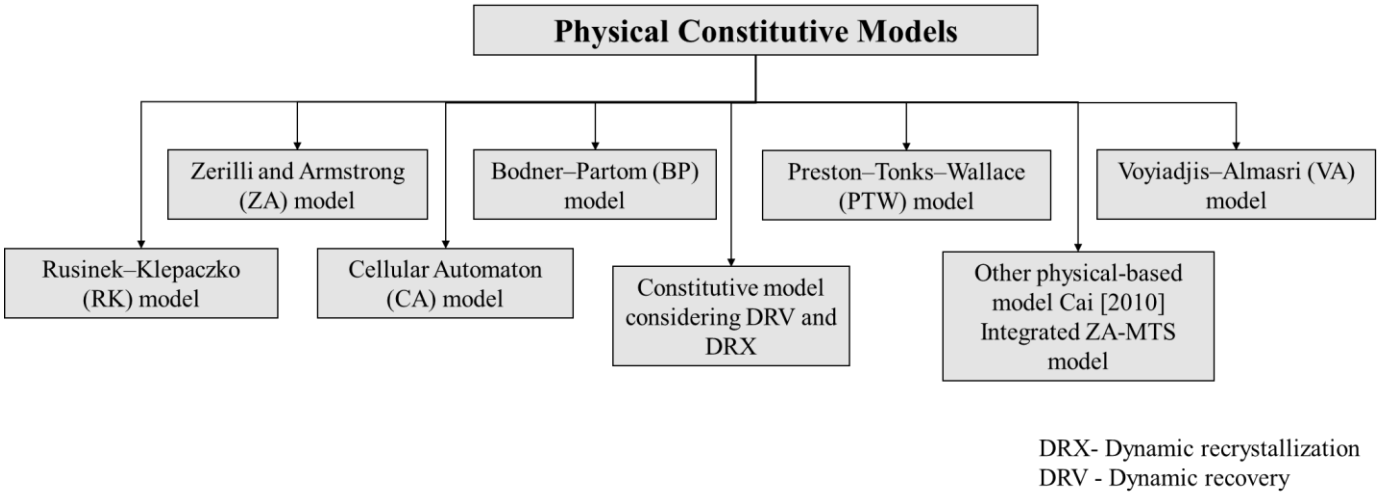

Figure 2.8 Classification of Physical-based constitutive model (Lin and Chen 2011)

Nowadays, artificial intelligent technology, neural networks based on genetic algorithms and back propagation algorithm, offers many promising outcomes in the materials science field, material processing, and forming (Lin et al. 2017; Lin, Zhang, and Zhong 2008). These are well-defined algorithm reduces the complex calculations and requirement of plenty of experiments to obtain material constants. While artificial neural network (ANN) flow stress models work by machine learning, artificial intelligence, parallel processing, statistics, and other to solve nonlinear flow behavior and factors affecting it, which is not accounted in the above constitutive models. Neural networks provide vitally different approaches to the materials modeling and control techniques for material processing than numerical methods.

The strain hardening exponent and strain rate sensitivity are essential variables to characterize the sheet metal plastic deformation as it reflects the microstructural evolution. Theses variables are sensitive to test conditions namely strain rate, test temperature, deformation degree and alloy composition. Ma et al. 2011 deliberated the hot plastic deformation behavior of Al-Li alloy for given strain rate. With rise in temperature, significant rise in the strain rate sensitivity was observed with decrease in strain hardening exponent. Influence of original microstructure on the strain hardening exponent and strain rate sensitivity and flow stress, has been studied by Luo et al. 2016. A few studies have been reported the relationships between flow stress and deformation parameters of Ni-based superalloy. Table 2.2 gives the literature review of different uniaxial constitutive models studied for Inconel 718 alloy.

Table 2.2 Literature review showing different uniaxial constitutive model studied for Inconel 718 alloy

Authors	Tests availed	Test temperature	Strain rates	Constitutive model studied														
				JC/m-JC	KH/KHL/KLF	Arr./m-Arr	CS/mCS	FB	ZA	RK	BP	PTW	MTS	VA	CA	JC-ZA	ANN/GA	Others
Zhang et al. 1999	Hot compression test	980-1040°C	0.005-5, 0.001-10 s^{-}	×	×	✓	×	×	×	×	×	×	×	×	×	×	×	✓
Na et al. 2003	Isothermal compression tests	925–1070 °C	5×10^{-4} - 10 s^{-1}	×	×	✓	×	×	×	×	×	×	×	×	×	×	×	×
Thomas et al. 2006	Uniaxial compression tests	900-1080°C	0.0005-0.1 s^{-1}	×	×	✓	×	×	×	×	×	×	×	×	×	×	×	×
Wang et al. 2009, 2013	Uniaxial tensile test	950-1050°C	5×10^{-4} - 10^{-2} s^{-1}	✓	×	✓	×	×	×	×	×	×	×	×	×	×	×	×
Wu et al. 2011	Hot compression test	950-1150°C	0.0003–1 s^{-1}	×	×	✓	×	×	×	×	×	×	×	×	×	×	×	×
Nowotnik A, Pędrak P, Sieniawski J 2012	Hot compression test	720-1150°C	10^{-4}- 4×10^{-4}	×	×	✓	×	×	×	×	×	×	×	×	×	×	×	×
Prasad et al. 2018a	Uniaxial tensile test	500-650 °C	0.001–1 s^{-1}	✓	×	×	×	×	×	×	×	×	×	×	×	×	×	×
Lin et al. 2015, 2017; Lin et al. 2014a; Lin et al. 2014b	Hot compression test	920-1040°C	0.001-1	×	×	✓	×	×	×	×	×	×	×	×	×	×	✓	✓
Chen et al. 2014	Hot compression test	920-1040°C	0.001-1	×	×	×	×	×	×	×	×	×	×	×	×	×	×	✓
Xu and Huang 2015	Hot compression test	950 - 1100°C	10^{-3} -1 s^{-1}.	×	×	×	×	×	×	×	×	×	×	×	×	×	×	✓
Azarbarmas et al. 2016	Hot compression test	950-1100°C	0.001-10 s^{-1}	×	×	✓	×	×	×	×	×	×	×	×	×	×	×	✓
Prasad et al. 2018a	Uniaxial tensile test	500-700 °C	0.001–1 s^{-1}	✓	×	✓	×	×	✓	✓	×	×	✓	×	×	×	✓	×

Recently, Lin et al. 2017 compared multi-gene genetic programming (MGGP), ANN, and Arrhenius type phenomenological models for flow stress prediction on Ni-based superalloy at elevated temperatures. It was concluded that MGGP model is more accurate and reliable in describing the hot deformation behaviors of the Ni-based superalloy. Specially, Lin et al. 2015 developed a new phenomenological constitutive model to define deformation behavior of aged Inconel 718 superalloy over a temperature range of 920- 1040ºC and strain rate range 0.001-1 s^{-1}. This new model considered the viscoplastic constitutive model for work hardening, softening, and dynamic recovery behavior and phenomenological constitutive models for dynamic softening stages. Li, Du, and Peng 2018 investigated the hot deformation characteristics of Ni-Cr-Fe-Ti alloy over a temperature range of 880-1030ºC with strain rates of 0.01-10 s^{-1} to establish the dynamic material model (DMM) and processing map. Xu and Huang 2015 studied the hot deformation behavior of Inconel 718 alloy by using hot compression tests at temperatures ranging from 950 to 1100°C with strain rates of 10^{-3} to 1 s^{-1}. The results show good agreement of flow stress prediction using hyperbolic-sine type constitutive equation. Limited efforts were made for the constitutive model development of Inconel 718 alloy. However, a detailed comparative study of various constitutive models for Inconel 718 is not reported yet.

2.4.2 Yield Criteria

Anisotropy of sheet metal during forming is a combination of the initial anisotropy due to its previous history of thermo-mechanical processing and the plastic deformation during the forming operation. Several efforts have been made for the development of anisotropic yield criteria, which consider plastic anisotropy. Figure 2.9 gives different yield criteria used to define the isotropic and anisotropic behavior of metal or alloy. Tresca and Von-Mises are the most popular yield criteria for isotropic material. Further, Hill (1948) proposed an extension of the Von-Mises isotropic criterion, which considers plastic anisotropy. The model considered orthotropic symmetry and four anisotropy coefficients in the plane stress condition (Hill 1952). Table 2.3 gives the summary of the number of parameters and mechanical tests required for various considered yield criteria. Barlat and Lian 1989 proposed another yield criterion, which need only four anisotropic parameters to define yielding behavior. Both the yield criteria are popularly used in the industries because of simplicity in determining the material constants by only using uniaxial tensile test and easy to implement in FE simulations. Therefore, till now, these yield criteria are extensively verified for varieties of metals and alloys.

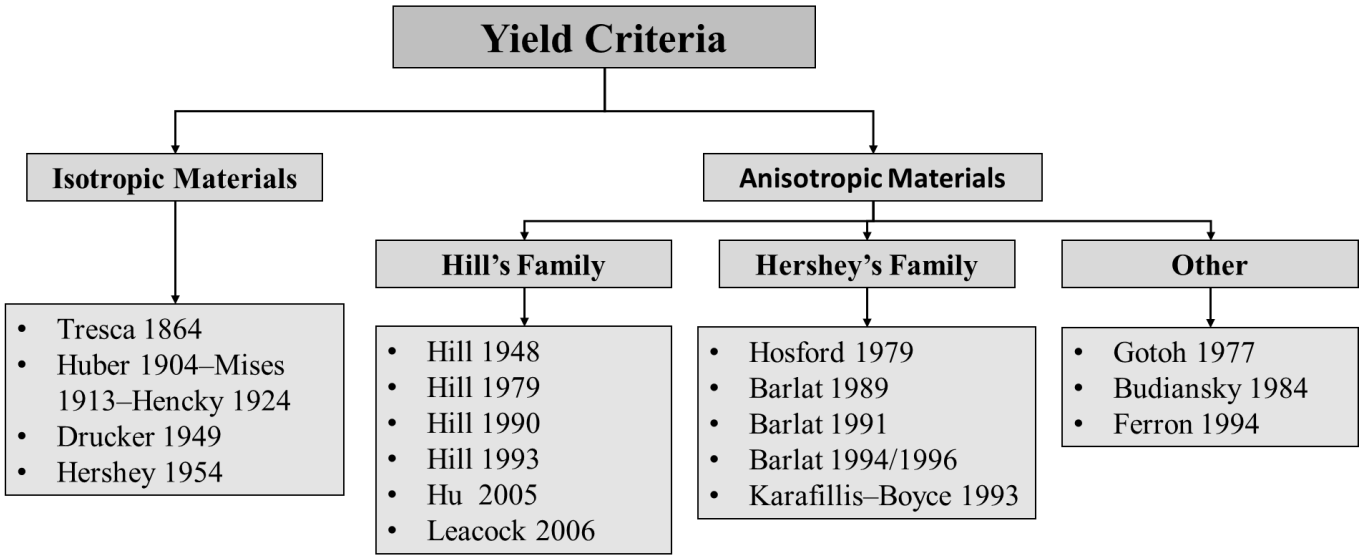

Figure 2.9 Different types of yield criteria (Banabic et al. 2010)

Table 2.3 Mechanical tests required for various recently used yield criteria in the literature

Yield Criteria	**Parameters**	**Tests Required**								
		σ_0	σ_{45}	σ_{90}	σ_b	r_0	r_{45}	r_{90}	r_b	σ_c
Hill'48	4	*		*		*		*		
Hosford'79	3	*				*		*		
Barlat'89	4	*				*	*	*		
Hill'93	5	*		*	#	*		*		
Barlat 2000	8	*	*	*	#	*	*	*	#	
Cazacu Barlat	9	*	*	*	#	*	*	*	#	$
* Uniaxial Tensile test, # Biaxial Tensile test, $ Compression test										
σ_0 , σ_{45} , σ_{90} , σ_b and σ_c -Yield strength at 0°, 45°, 90° to RD, balanced biaxial and compression condition. r_0, r_{45}, r_{90} & r_b - Lankford anisotropy coefficients at 0°, 45°, 90° to RD and balanced biaxial condition										

In literature, it is observed that Hill 1948 and Barlat 1989 are unable to predict accurately the biaxial deformation behavior, which is prominent in all forming processes. Moreover, the model cannot capture simultaneously the planar variation of the uniaxial yield stress and uniaxial coefficient of plastic anisotropy (Banabic 2000; Banabic et al. 2010). Therefore, many further efforts have been made to develop advanced anisotropic yield criteria which is able to predict accurate biaxial or multiaxial deformation behavior. Such as Hill (1993) enhanced plastic behavior criterion in textured sheet, particularly when complicated loads are applied along the planar orthotropic axes (Xu and Weinmann 1998). Plunkett, Cazacu, and Barlat 2008 proposed a more general expression of the yield function. Further refinement in general expression has been done in 1994 and 1996. The results were validated by cylindrical cups earing drawn by deep-drawing. The new criterion shows very good agreement in the predicted earing with the experimental data. Barlat proposed a new advanced anisotropic yield

criterion which considers the effect of stress asymmetry (Plunkett, Cazacu, and Barlat 2008; Tari and Worswick 2015). Recently, Cardoso and Adetoro 2017 suggested an extension of Hill's yield function with a non-uniform rational B-spline function. This new quadratic function predicts the r-values variation and directional flow stresses in the stress tensor simultaneously. It is able to describe the biaxial symmetric stress state accurately.

It is always been difficult to explain completely anisotropic plastic strain rates and yield behavior using a single function, as the associated flow rule requires. The metal forming industry commonly use isotropic or typically anisotropic material models, and accept the resultant inconsistencies as an approximation to the real behavior. Currently, a higher degree of accuracy is required of material models. Thus an approach was propose with more complex functions with addition of parameters. These parameter are defined by strain ratios and yield stresses measured at additional stress states. This satisfactory approach is used by the Barlat and Lian 1989, Barlat et al. 1991, 1997, and Yoon et al. 1999, 2000 to improve the characterization of the behavior of aluminum alloys. An approach which defines the plastic flow and plastic yielding behaviors as a same function were reported. A small pressure-sensitivity in the yield criterion was reported by Spitzig and Richmond 1983 for aluminum and steel. This parameter is not accompanied by an expected plastic di-latency which is necessary by associated flow rule. This confirmation that the associated flow rule is not strictly true.

Further, Lee 1988 describes a self-consistent non- associated flow rule material model considering the Spitzig and Richmond experiments. A pressure-sensitive mechanisms which can break the associated flow rule is proposed by the Richmond 1980. Lademo et al. 1999 analyzed the several proposed material model without considering the pressure-sensitive effects. Due to the inadequacy of the associated flow rule, failure may be observed. Further, Stoughton 2002 proposed an improved model that shows good agreement with experimental data for both yield and plastic strain ratios in uniaxial, equi-biaxial, and plane strain tension under proportional loading for steel, aluminum and other alloys. The proposed model is based on the non-associated flow rule where the plastic potential and yield surface functions are defined by quadratic functions of the stress tensor. The plastic potential model is similar to Hill's proposal for a quadratic anisotropic plastic function defined by observed r values.

Notably, Iyer and Lissenden 2000 proposed a generalized threshold function for viscoplastic materials, which can also serve as a yield function in rate-independent plasticity. Bulge tests with hydrostatic pressure and pure torsion test are used for material constant determination. It observed predominant stress asymmetric in Inconel 718 alloy at elevated temperature. However, limited literature has been reported to investigate the various advanced

anisotropic yield criteria for Inconel 718 alloy at elevated temperatures. Hence, it is vital to study the comprehensive behavior of constitutive models and anisotropic yield models of Inconel 718 alloy at elevated temperatures.

2.5 Forming, Fracture and Wrinkling Limit Diagram

2.5.1 Experimental Prediction Of Forming and Fracture Limit Diagrams

Generally, Formability is the ability of a given metal workpiece to undergo plastic deformation without being damaged. Formability tests can be basically divided into three main categories, namely intrinsic tests, simulative tests, and tests devoted to the determination of the Forming Limit Diagrams (FLDs), as listed in Figure 2.10. The intrinsic tests provide comprehensive information about the basic mechanical properties of the sheet metals, which are related to sheet metal formability characteristics independent of the sheet thickness and surface conditions. However, it reproduces strain states much simpler than that characteristic of the industrial processes, and completely rule out the effect of the processing variables. Some of the popular intrinsic tests are the uniaxial tensile test, plane-strain tensile test, Marciniak biaxial stretching test, and Hydraulic bulge test.

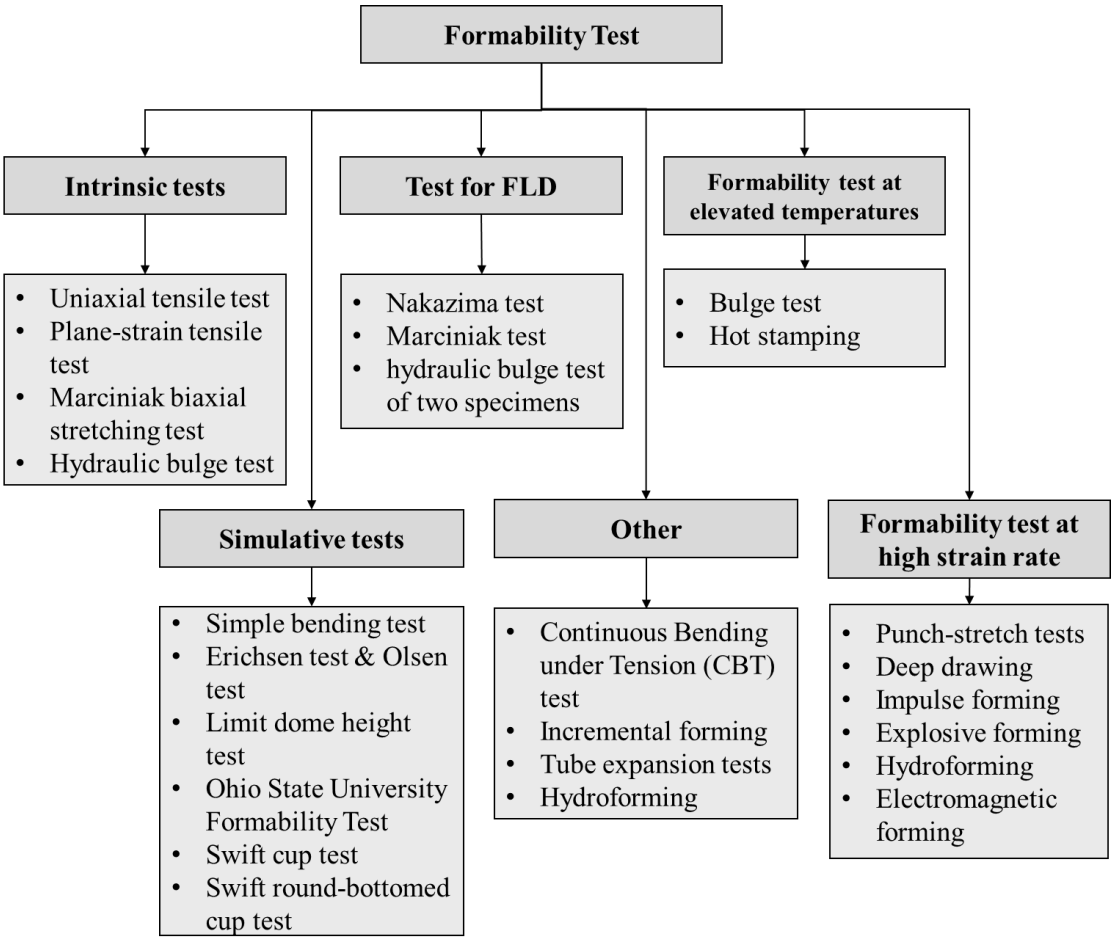

Figure 2.10: Experimental prediction of formability of sheet metal (Bruschi et al. 2014)

The most widely used intrinsic test is the uniaxial tensile test (Bruschi et al. 2014). This test applies a stress state typical of the drawing region under the blank-holder, where the minor strain is negative. The main advantages are easiness and rapidity in carrying out tests on universal testing machines and extracting data, the absence of friction effects, the low scatter presented in the experimental results, and the chance to use optical devices for the strain measurement. Plane-strain tensile test, Marciniak biaxial stretching test are less popular methods. The plane-strain tensile test evaluates the material response in the plane-strain state and ensures the minor strain component equal to zero. The modification of geometry is very simple by increasing its width and decreasing the gauge length. The Marciniak biaxial stretching test creates a uniform in-plane biaxial strain at the sample center by using a cylindrical punch with a central hole to overcome the friction effect (Huang and Shi 2018). The hydraulic bulge test allows biaxial stretching deformation of the sample into a dome by the action of a pressurized fluid, which involves out-of-plane stresses and strains in the blank (Prakash et al. 2020).

The simulative tests impose strain and stress states that closely reproduce the ones arising in a particular forming operation and include the effects of parameters. Some of the popular simulative tests are the simple bending test, Erichsen test and Olsen test, Limit dome height test, Ohio State University Formability Test, Swift cup test, and Swift round-bottomed cup test. The simulative tests are usually classified according to the forming operation they are aimed at reproducing, namely bending, stretching, drawing, and stretch-drawing. The simple bending test provides the minimum recommended inside curvature radius to form a 180° bend in a sheet of specified thickness without failure (Leu 1997). The Erichsen test and the Olsen test were the first to be developed for estimating the sheet metal stretchability, namely the sheet metal formability under stretching conditions. Both the tests stretch the sheet over a hardened steel ball, and the height of the produced cup at failure is the measure of the material stretchability (Takuda et al. 2000). The limit dome height test is another stretching test carried out with a large diameter hemispherical punch (dia. 100 mm) and draw beads in the die to prevent draw-in, specifically dedicated to the reproduction of plane stretching conditions (Venkateswarlu et al. 2013). The Ohio State University Formability Test (OSUFT) was introduced to overcome the limit dome height test limitations, using a punch whose geometry was optimized by numerical simulation to guarantee plane strain conditions (Bruschi et al. 2014). The Swift cup test involves drawing of circular samples of various diameters into cups by the action of a flat-bottomed cylindrical punch.

The Forming Limit Diagram (FLD) is extensively used in SMF analysis to define the limit of deformation of materials without necking or fracture. FLD provides a comprehensive picture of material deformation capability and limiting strains. Keeler (Keeler and Backofen 1961) and Goodwin (Goodwin G M 1970) introduced the FLD concept in the 1960s. Since then, it has been widely used for studying the formability of sheet metal. Keeler determined strains only on the right-hand side of the FLD, and Goodwin extended the FLD by determining the strain in the left-hand side (negative minor strains). The test proposed by Keeler and Goodwin requires to use different radii punches to vary the stress state. The main disadvantages of these tests are the large amount of experimental work, high tooling cost and position of FLC is influenced by punch radii. Furthermore, Hecker developed simplified techniques for evaluating FLD experimentally where sheet specimens are clamped at the periphery and stretched over hemispherical punch until failure (Hecker 1975). The test is performed by varying the lubrication or reducing the width of the original specimen to overcome this friction effect.

Over the years, experimental FLD has been determined using various proposed experimental techniques, of which stretching with a hemispherical punch is most common (Banabic et al. 2010). Basically, two different types of tests are currently used to draw FLDs, namely stretching tests producing out-of-plane deformation and tests producing only in-plane deformation. For both the test types, the sheet is marked with a grid pattern and then deformed. The deformation of the grid pattern is measured in those regions where either necking or fracture occurs, giving the major and minor strains values. The notable development have been suggested by Nakazima, Kikuma, and Hasuka 1989 for the development of experimental FLD. Simplicity, in used setup and specimen shapes, were key features of Nakazima test. Rectangular specimens of different width were stretched with a hemispherical punch in order to determine limiting strains. This test is capable to explore both biaxial tension (T-T) and tension–compression (T-C) regions of FLD (Hu, Li, and Chen 2019). Turetta, Bruschi, and Ghiotti 2006 first improved the Nakazima test by adding an induction heating system and an optical system (an infrared thermo-camera) to attain more accurate FLD in high-temperature operation.

Among the tests producing in-plane deformation, the Marciniak test is the most used (Bong et al. 2012). It uses punches of different cross-sections (circular, elliptical, rectangular) with a central hole and sheets of different widths. The Marciniak test provides better measurement accuracy. But it has negative aspects, such as the complex shape of the tools, the need for a carried blank, and the limitation in the thickness of the tested sheets. The comparison of results between the two types of tests shows a close agreement for negative minor strains,

whereas the stretching methods give slightly higher values of formability for plane strain and positive minor strains. A new method based on the hydraulic bulging of two specimens was proposed by Banabic et al. 2013. Main advantages include the capability of investigating the whole strain range specific to the SMF processes, the simplicity of the equipment, and the reduction of the parasitic effects induced by the friction, as well as the occurrence of the necking in the polar region.

Over the years, many non-conventional testing were proposed to evaluate the formability. Some of the formability tests are Continuous Bending under Tension (CBT) test, Incremental forming, Tube expansion tests, and Hydroforming. CBT test was developed to study the different failure mechanisms arising from the imposed stress state and generate cyclic stretch-bending. Further, the incremental sheet forming gives an interesting aspect related to the formability characterization. Since the deformation mechanisms in incremental forming differ from the ones of conventional deep drawing. In different incremental techniques were developed to achieve different strain paths and states. But, obtained FLDs are quite different from the conventionally obtained curves (Basak and Panda 2019a). Tube expansion tests are also applied to study the formability of sheet metals. This multi-axial tube expansion test was proposed: a multi-axial tube expansion testing machine was developed that can realize different principal stress or strain paths by controlling the axial force and internal pressure (Anderson et al. 2017). Some of the formability tests presented above were modified and adapted in terms of equipment and testing procedures to enable the sheet metal formability limits at elevated temperature and high strain rates.

2.5.2 Theoretical and Numerical Prediction Of Forming and Fracture Limit Diagrams

Over the years, many researchers had performed the experimental analysis of FLDs, which mostly showed that the maximum admissible limiting strains strongly depend on several physical factors. The most important physical factors are work-hardening rate, strain rate sensitivity, and plastic anisotropy induced by the cold rolling process. It was reported earlier that FLD is extremely sensitive towards sheet metal pre-formed conditions, particularly non-linear deformation paths followed by any of the forming processes (Dilmec et al. 2013). In many engineering applications, complex workpieces are manufactured by undergoing several processes (Hazra et al. 2011). Hence, the prediction of trustworthy experimental FLD at elevated temperatures is particularly challenging. Under such conditions, the FLD cannot be applied to predict whether the forming process will be successful or failed. Moreover, only safe region prediction in FLDs will not serve the purpose of a better quality of formed products.

Hence, the prediction of FLD by theoretical and semi-empirical models is gaining special attention. Extensive work has been done on the development of various theoretical models for FLD prediction (Basak and Panda 2019a; Kotkunde et al. 2017). Figure 2.11 gives theoretical and numerical models used for FLDs prediction in sheet metals. Theoretical models' prediction is basically characterized based on Bifurcation Theory, Geometrical Imperfection Theory, Continuum Damage Mechanics, and some other theories. Theoretical models based on Bifurcation Theory, namely Swift, Hora and Hill, have been developed by considering localize and diffuse necking theory, whereas Storen-Rice and Dudzinski-Molinari models have considered the bifurcation theory and linearized perturbations theory respectively (Banabic et al. 2010). Swift developed a diffuse necking theory by using a biaxially loaded element that depicts the right-hand side (RHS) deformation modes of the FLD. The Swift's model, also recognized as the maximum force criterion (MFC), usually underestimates limit strains compared with experimental data (Banabic et al. 2005). Further, Hill proposed the localized necking phenomena, which predicts the left-hand side of the FLD (Hill 1952). Therefore, diffuse and localized necking theories are used together in constructing the FLD for all straining modes, which vary from uniaxial to biaxial strain states. However, these models were developed based on the assumption of material homogeneity in multiaxial modes. It unable to predict failure when there is a negligible change in thickness of material. Thus, it is difficult to predict a full comprehensive picture of FLD using these models.

Marciniak–Kuczynski model (M–K) was proposed considering non-homogeneity (in geometrical & structural) sheet metals for FLD calculation (Banabic 2010a; Banabic et al. 2019). In the literature, it is observed that the M-K model is a realistic model for FLD prediction at the onset of necking. The M–K model is based on thickness variation and necking theory for FLD prediction. The failure strain depends on the growth of an initial inhomogeneity. The accuracy of the predicted FLD is significantly influenced by the shape of the employed yield surface, constitutive model, and strain rate sensitivity (Paul 2016). Many efforts had been made to predict strain-based FLDs by incorporating yield criteria and constitutive models in the M-K model predictions. Kotkunde et al. 2017 studied the yield criteria variation for theoretical FLDs prediction using the M-K model. It is observed that M-K model prediction capability is highly dependent on constitutive models and yield criteria selection. Kuroda and Tvergaard 2000 stated that predicted localization strains are quite sensitive to deviations from the usual assumptions in M-K model analyses, where the tension in directions inclined to the initial orthotropic axes of the anisotropy.

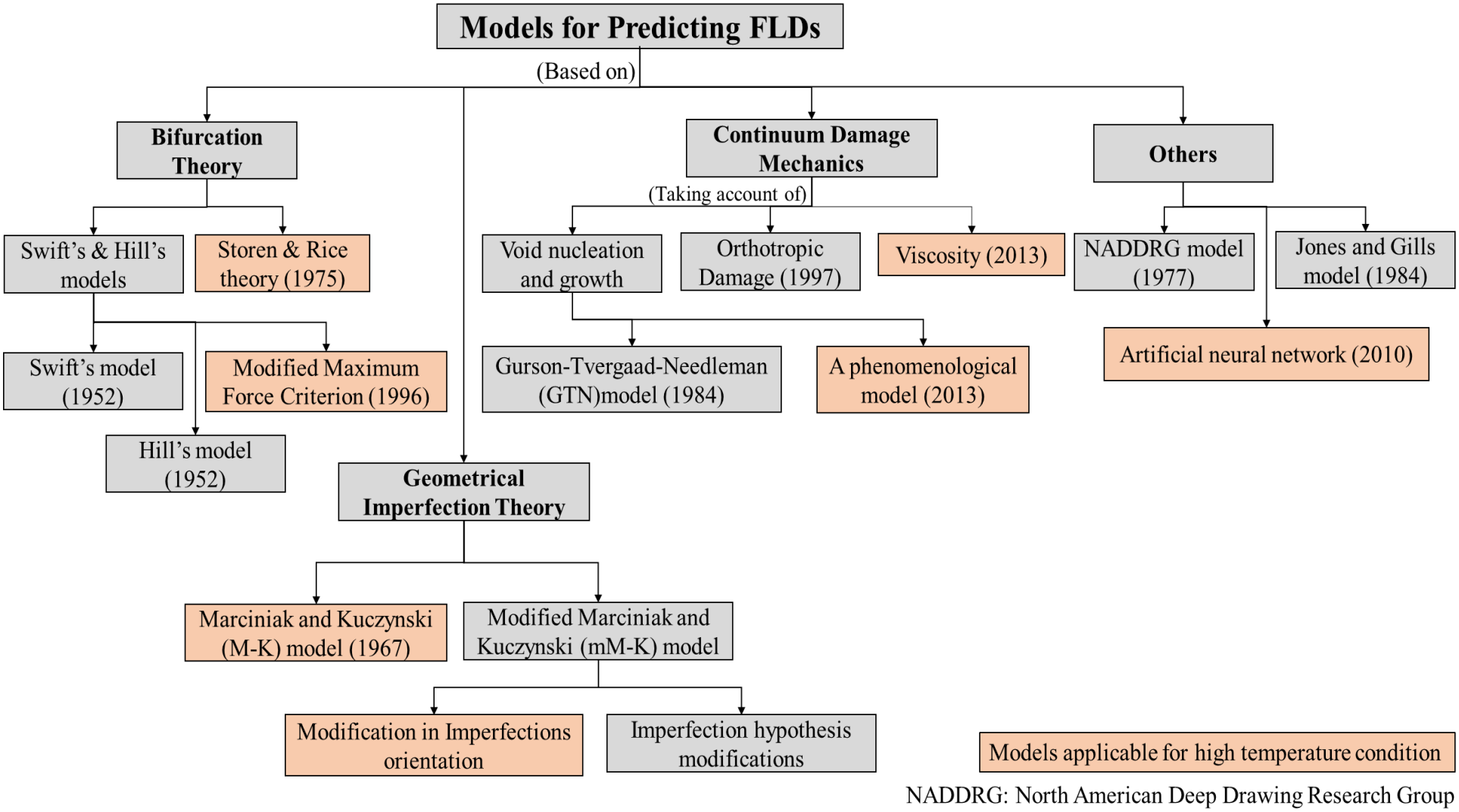

Figure 2.11: Theoretical and numerical models used for FLDs prediction in sheet metals (Zhang, Shao, and Lin 2018)

It was reported in the literature that this model is unable to predict failure when there is a negligible change in thickness of considered metal (Bruschi et al. 2014; Dilmec et al. 2013; Güler and Efe 2018). Also, the position of forming limit curve depends upon inhomogeneity factor (f_0), sheet thickness, anisotropy, strain hardening coefficient (n), strain rate sensitivity (m), and shape of yield function. Inhomogeneity factor (f_0) is highly dependent on the material properties, grain size, surface quality, and thickness of the sheet. Further, it is known as a negative or low-stress triaxiality region (Banabic 2010a; Marciniak and Kuczyński 1967). Also, it was reported that the M-K model is not suitable for different strain paths, wrinkling, and fracture-based FLDs (Banabic 2010a). Thus, an improved M-K model was proposed by considering modification in the imperfections orientation and imperfections hypothesis.

The deformation of sheet metals usually contains three stages, namely micro-void nucleation, growth, and coalescence (Banabic 2010b) . A Gursone-Tvergaarde-Needleman (GTN) model and a phenomenological model were proposed, based on the assumption of necking occurred at the incipient of void coalescence, to predict limit strains for sheet metals (Gurson 1977). Orthotropic damage was usually observed in extensive plastic deformations. An empirical model or North American Deep Drawing Research Group (NADDRG) model, proposed by Keeler and Brazier, is used to predict the major principal strain under the plane strain state. Further, Paul, Manikandan, and Verma 2013 developed a new model to prognosticate complete FLC using a nonlinear regression equation based on simple uniaxial tensile properties. Experimental results show that the uniaxial tensile properties were strongly interrelated to the plane strain forming limit (FLD_o). The capability of the proposed equation was verified with experimentally measured FLD_o of fifty-six steel grades with different thickness and strength. In semi-empirical models, Chow, Jie, and Hu 2003 developed an analytical expression to predict the FLC based on generalized plasticity deformation theory. Expression for the critical tangent modulus was estimated for the left and right sides of FLC separately by considering three different yield criteria. Theoretically predicted FLC by this theory for Al2028 and Al6111-T4 alloy shows an excellent agreement with experimental values. Jones and Gillis model was also used to predict limit strains at the onset of necking. Even a model based on an ANN proposed by Elangovan, Sathiya Narayanan, and Narayanasamy 2010 is used to predict FLDs for a perforated sheet with different geometrical features.

For high strength materials, it is difficult to determine forming limits at the onset of necking as fracture occurred without an obvious neck formation. FLD itself is not sufficient to give information that failure occurred with or without the hint of substantial localized necking

(Bruschi et al. 2014; Güler and Efe 2018). Thus, it is necessary to identify the optimal conditions within the deforming sheet at the onset of fracture. In recent times, few researchers evaluated strain-based fracture forming limit diagram (FFLD) to describe fracture strains (Basak and Panda 2019a; Basak et al. 2015). FFLD is used to predict the limits of fracture over a space of minor strain(ε_2) vs major strain(ε_1) from biaxial tension (T-T) to uniaxial compression (T-C) region. First, Atkins 1996 studied the fracture by bulge forming test by using anisotropic yield criterion. (Jain, Allin, and Lloyd 1999), used ductile fracture criteria for fracture limit prediction by assuming that sheet metal obeys the Hill's quadratic yield criterion. It was observed that the maximum shear stress criterion by Tresca provides good agreement with the experimental FFLD over a range of strain ratios. Narayanasamy and Narayanan 2006 discussed aspects on the fracture limit diagram, which is developed for different steel sheet thickness by considering the ratio of Mohr's circle shear strain to effective strain for average void sizes.

Analytical fracture forming limit diagram (FFLD) of SMF can be predicted using the continuum ductile damage models coupled with plane stress-based plasticity theory. Various ductile damage criteria had been proposed earlier, and it was found that the Bao and Wierzbicki (BW) damage model had been extensively calibrated with the experimental data for forming applications. It was also shown that the fracture forming limit diagram (FFLD) was attributed due to the appearance of tensile cracks into the sheet metal. Basak and Panda 2019a have reported failure strain of EDD and AA5052 thin sheets by FFLD at RT. FLD and FFLD based on experimental limiting strain data were developed and validated with the M-K and B-W models. It was concluded that the capability of these models was highly dependent on the incorporation of yield criteria. Especially, Prasad et al. 2018b, developed FFLD for Inconel 718 alloy (solution treated) at RT. It was reported that alloy is an extremely high strength material and thus, it is difficult to have any substantial necking after forming it at RT condition. Similar findings at RT were reported by Roamer et al. 1997 for 625LCF, 718, and 718SPF alloy.

2.5.3 Wrinkling Limit Diagram

Wrinkling and tearing are considered as critical defects in SMF processes. The occurrence of wrinkling in sheet metal-forming operations depends on the current state of the stress and local geometry developed in the critical region of the workpiece during the testing. Wrinkling is a kind of local buckling of sheet metal formed by inordinate compressive stresses. In other words, it results in instability under compressive stresses. Fundamentally, there are four main causes of local surface buckling in response to various types of loading, i.e. (i) compressive stress, (ii) shear stress, (iii) non-uniform tension, (iv) in-plane bending (Du et al.

2020), as listed in Figure 2.12. Occurrence/initiation and growth of the wrinkling instability in forming operations depends on current stress state, mechanical properties, process parameters, boundary conditions, workpiece geometry, especially local geometry developed in the critical region of a sheet metal workpiece during testing (Abbasi et al. 2012; Wang and Cao 2000). Further, complication increases due to boundary conditions with multi-dies constraints, disconcertion of clearances between dies and workpiece, changing contact conditions (space and time).

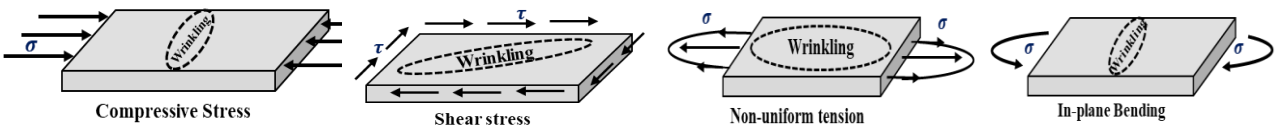

Figure 2.12 Basic causes of wrinkling instability /Surface buckling when subjected to different types of loads (Du et al. 2020)

In literature, few studies are reported for experimental determination of wrinkling behavior in SMF processes. It has been noticed that the Yoshida buckling test (YBT) is effectively used to define a relationship between deformation conditions and wrinkle defects (Du et al. 2020). Over the years, many modifications in the specimen's size and dimensions were proposed by different researchers to investigate geometry effect and stress ratios on the wrinkling initiation and growth (Han and Liewald 2014; Kim, Yoon, and Yang 2000; Riks 1979). Han and Liewald 2014 proposed a new approach to enhance the accuracy of the buckling test. Authors claimed that specimens with comparatively smaller size and an increasing curved radius lead to larger strain levels and more accurate buckling tendency prediction.

Recently, numerical techniques were reported for the prediction of wrinkling behavior. The popular numerical techniques are static equilibrium method, initial imperfection method, energy method, eigenvalue buckling analysis method, static-implicit and dynamic explicit FE method (Liu et al. 2016). The energy-based method was used to predict the wrinkling tendency in the circular deep drawing process (Johnson and Yu 1982). The study concluded that the most effective method to decrease the wrinkles is to monitor blank holder force on the circular flange. Also, a modified energy method coupled with the plastic bending theory was used to predict flange and side wall wrinkling in deep-drawn cup. This method was used to validate critical buckling stress and wavelength related to binding force and further validated experimentally by YBT and square cup forming test. (Cao and Boyce 1997; Wang and Cao 2000). Further, the effect of the geometric imperfections on wrinkling instability was predicted by the bifurcation method and the wrinkling limit curves (WLCs) by plastic buckling for short-wavelength

(Ameziane-Hassani and Neale 1991). Later, a Donnell-Mushtari-Vlasov (DMV) shell theory was proposed to predict wrinkling instability in compound shell curvatures of a sheet (elastic isotropic and plastic anisotropic) when subjected to the internal forming stresses (Wang, Kinzel, and Altan 1994). The combination of plastic bifurcation theory and DMV shell theory was reported to analyzed wrinkling behavior in thin sheets (Kim and Son 2000).

The effect of the Lankford coefficient and anisotropy in the Hosford yield criterion for flange wrinkling occurrence was investigated. The effect of various yield criteria for the wrinkling prediction for IF galvanized steel sheets were investigated by Shafaat 2011. The effect of the boundary condition in sheet metal and the viscous medium with blank holder pressure on wrinkling instability and fracture formation were investigated (Liu and Wang 2010). For constant compressive loading, the onset of flange wrinkling was characterized by ε-WLCs (Magrinho et al. 2018). Recently, a phenomenological wrinkling criterion was developed to find critical compressive strain and bending strain with specific triaxiality (Won et al. 2019). This criterion shows superior performance in the prediction of wrinkling instability. Sensitive prediction of the wrinkling instability by triple nonlinearity evolution was analyzed by Li et al. 2019. This triple nonlinearity evolution with multi-geometric micro-defects and anisotropy displayed in the numerical simulations. A buckling limit diagram, an improved YBT, with circular blanks with different radii, for IF steel was proposed by dynamic explicit FE method (Bayraktar, Isac, and Arnold 2005). Effect of variation of test specimen geometry on WLCs by using cone cup drawing test and improved YBT were achieved by Han and Liewald 2014.

Based on thorough literature survey, it is observed that very few studies on forming, fracture, and wrinkling prediction are reported for Ni-Cr-alloy. Thus, it is essential to understand the complete forming behavior of material in different deformation regions such as safe region, wrinkling, and fracture region. Also, it is necessary to focus on theoretical models to determine the forming, fracture, and wrinkling limiting strains to produce a defect free-formed product.

2.6 Finite Element Analysis for SMF

Nowadays, modeling and simulation can be used for many purposes, namely to predict material flow behavior, analyze stress-strain and temperature distribution, determine forming forces and predict potential sources of defects and failures of SMF processes. Rigorous experimental trials can also be reduced by performing a simulation of different material forming processes with the help of FEM. However, the trustworthiness of the numerical simulations

largely depends on the used input material models and the correctness of the input material data. Particularly, the selection of an appropriate yield criterion is essential because it provides an accurate prediction of the observed initial and subsequent yield behaviors of a material. Further, researchers suggest mesh convergence study for prediction of different failure modes in forming process such as fracture and wrinkling, thickness variation, etc. with high accuracy (Prasad et al. 2018b).

Recently, Evangelista, Lirani, and Al-Qureshi 2002 focused on the influence of tool geometry, material models (yield criterion and plastic constitutive equation), friction, and a strain localization or damage criterion in FLD prediction. (Situ, Jain, and Metzger 2011), proposed a new methodology to obtain the FLD by utilizing routing obtained experimental punch load vs. displacement traces from hemispherical punch stretching experiments and by analyzing strain history of test samples from FE simulations. The proposed method for FLD determination considers out-of-plane displacement, punch-sheet contact and friction, and avoids using experimental strain measurement in the vicinity of the neck on the dome specimens. The method suggested to use arbitrary inhomogeneity factor to trigger localization.

Kotkunde et al. 2016 investigated the influence of yield criteria on warm forming FE analysis of Ti-6Al-4V alloy at elevated temperature for circular deep drawing process. It was observed that the appropriate selection of a yield criterion plays a significant role in FE simulations. Soyarslan, Klusemann, and Bargmann 2016, performed the formability analyses using FE models of the stochastic Marciniak-Kuczynski and Nakazima tests. The role of reduction in the yield locus curvature on the shape of the forming limit diagrams was investigated. An explicit analysis of deep drawing to capture the in-plane quadrant hardening was investigated by Wallmeier et al. 2015. Recently, Prasad et al. 2018b, investigated the limiting dome height, strain distribution, and failure location of Inconel 718 alloy at room temperature using FE analysis.

As of now, FE simulation study is mainly focused on the prediction of necking tendency in sheet materials. However, other failures such as wrinkling and fracture need to be explored further. Moreover, no literature has been reported on FE analysis of formability prediction for Inconel 718 alloy at elevated temperature. Therefore, FE simulation study with the incorporation of suitable material models is vital for understanding the possible forming, fracture, and wrinkling behavior of Inconel alloy at elevated temperatures.

2.7 Research Gaps in Existing Literature

Based on the extensive literature survey, the following research gaps have been identified.

i. Understanding the deformation behavior and material properties determination are prerequisites to optimize the process parameter. Few studies were reported on deformation behavior at room temperature conditions. Thus, it is essential to thoroughly investigate the deformation behavior of Inconel 718 alloy over wide range of temperatures and strain rates. The detailed analysis with microstructural support helps to understand the material behavior during the hot working conditions.

ii. The extensive literature is available on constitutive model development and anisotropic yield criteria for structural steels and Aluminum alloys. However, very limited literature has been reported for material model development for high-strength alloy such as Inconel alloy. Thus a comprehensive and comparative study of material models for Inconel 718 alloy is essential.

iii. Generally, high-strength alloy exhibits limited necking tendency. So traditional FLD approach for the prediction of limiting strains based on necking limits may not suitable for Inconel 718 alloy. Very few studies are reported for fracture forming limiting diagram prediction of Inconel 718 alloy at room temperature conditions. There are many challenges to form Inconel 718 alloy at room temperature condition. Few studies shows promising improvement in forming behavior at elevated temperature. It is worthy to understand the effect of temperatures on fracture and forming limit predictions.

iv. High-strength alloys generally display severe wrinkling tendency. The wrinkling tendency unable to predict based on traditional forming and fracture limiting strains. A few recent studies demonstrate the wrinkling limiting strain predictions based on buckling theory. Thus, it is interesting to investigate the wrinkling limits of Inconel 718 alloy at different temperatures. The prediction of forming, fracture and wrinkling limits helps to analyze the complete forming limit diagrams Inconel 718 alloy at different test temperatures.

v. A systematic strategy for experimental and theoretical validation of forming behavior needs to be proposed. It is vital to avoid unnecessary experimental tryouts and material wastage.

2.8 Research Methodology Adopted

The methodology proposed for the research work is shown in Figure 2.13. The basic objective of the present research work is to investigate forming, fracture, and wrinkling limit diagram of Inconel 718 alloy at elevated temperature (RT-700ºC). To analysis, the forming

behavior of Inconel 718 alloy, the first material properties, and deformation behavior have been studied from room temperature to 700ºC at an interval of 100ºC with quasi-static strain rates (0.0001, 0.001, 0.01, and 0.1 /s) using uniaxial tensile tests. Microstructure Characteristics, namely microstructure, fractography, XRD, and EBSD studies, of post tensile test specimen have been investigated at elevated temperature (RT-700ºC).

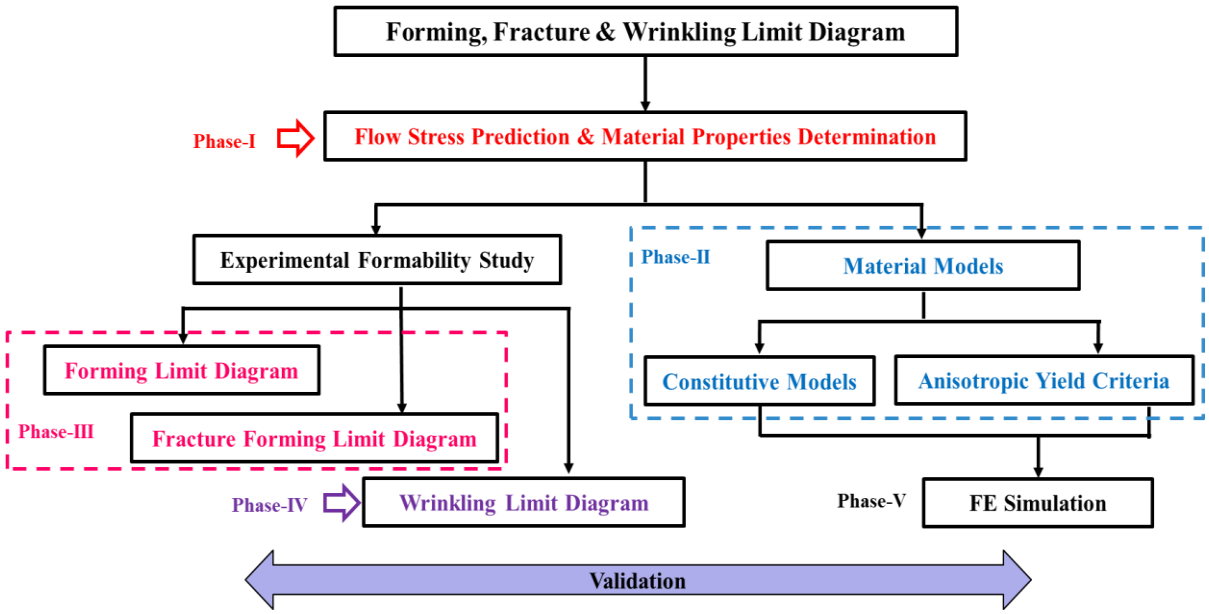

Figure 2.13 Methodology adopted for proposed research work

From evaluated anisotropic material properties, various constitutive modeling and anisotropic yield criteria have been developed for Inconel 718 alloy up to 700ºC. The developed models were compared and validated with experimental data. The best model from constitutive models for deformation behavior prediction and yield criteria have been identified and used for further numerical studies. The forming, fracture, and wrinkling limit diagram of Inconel 718 alloy at elevated temperature have been investigated. The experimental forming and fracture limit diagrams have been determined using the Nakazima test. Whereas the experimental wrinkling limit has been determined by the modified Yoshida buckling test. The safe, necking, fracture and wrinkling limiting strains have been identified to plot complete FLDs at elevated temperatures. Further, various qualitative aspects of stretch forming, namely strain distribution, thickness distribution, and limit dome height also studied.

Theoretical forming and fracture limit curves have been predicted by using M-K and B-W Model coupled with anisotropic yield criteria. Father FE analysis of stretch forming process and buckling instability have been performed using ABAQUS-Explicit-SIMULIA™. Experimental results are validated with FE simulation by incorporating material models, friction coefficients, and boundary condition as input. Formability by means of load

displacement, limit dome height, and thickness distribution of Inconel 718 alloy have been determined. Additionally, the load-displacement curves and effect of blank holding pressure on wrinkling progression have been compared with experimental results. The wrinkling tendency in deep drawn cups have been validated experimentally and numerically at different temperatures

2.9 Objectives of the Study

Following are the objectives for the present research on Inconel 718 alloy:

I. Study of deformation behavior & mechanical properties of Inconel 718 alloy at elevated temperatures (RT-700ºC).
II. Uniaxial constitutive modeling for Inconel 718 Alloy at elevated temperatures.
III. Study of various anisotropic yield criteria for Inconel 718 alloy at elevated temperatures.
IV. Experimental determination of forming, fracture and wrinkling limit diagrams at elevated temperatures.
V. Numerical analysis and validation of forming, fracture and wrinkling limit diagrams.

2.10 Research Map

The detail research map is as shown in the Figure 2.14.

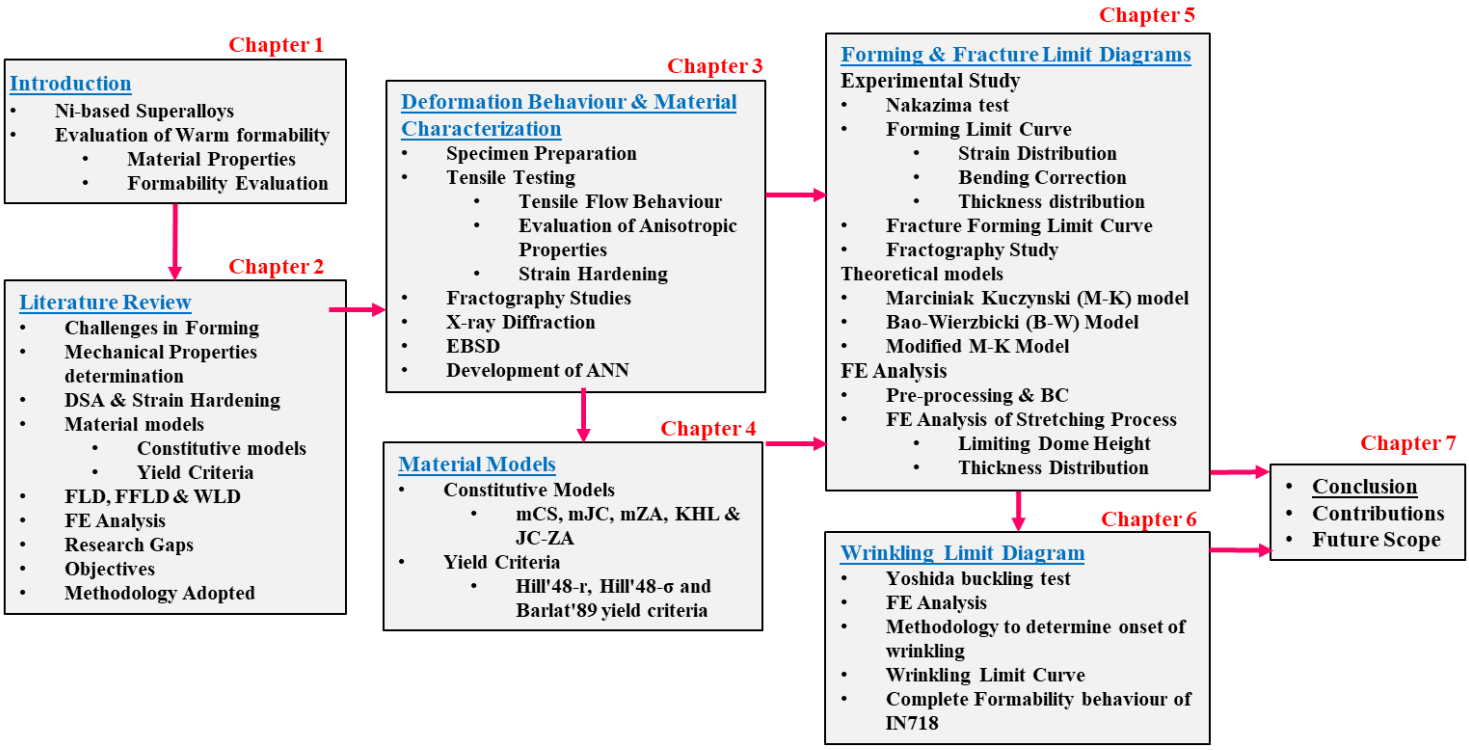

Figure 2.14 Research map of the dissertation with chapter and their respective contents

Summary

Through literature review has been carried out on deformation behavior, DSA, various formability aspects, material model development for FLD prediction and FE studies. Further, the effect of process parameters on the forming, fracture and wrinkling limits diagrams have been studied in detail. From extensive literature review, research gaps and objectives have been identified.

Next chapter discusses in detail about deformation behavior and mechanical properties of Inconel 718 Alloy at elevated temperatures evaluated using uniaxial tensile test.

3. Deformation Behavior & Microstructural Characteristics

It is essential to have a thorough understanding of the deformation behavior for optimizing the process parameters and ensuring safe performance during SMF processes. This chapter deals with material properties determination and deformation behavior of Inconel 718 alloy thin sheet at different temperatures. The findings are well supported with microstructural examinations.

3.1 Material and Specimen Preparation for Tensile Testing

The commercially available Inconel 718 alloy thin sheet (Grade: N07718) of thickness 1 mm is used for tensile testing. Inconel 718 alloy is Nickel-Chromium-Iron based precipitate-hardenable superalloy. The key feature of Inconel 718 alloy is exceptional high tensile strength and ductility at elevated temperature conditions (Thomas et al. 2006). It is also highly resistant towards corrosion (mostly pitting and crevice corrosion), and oxidation. Alloy is stable in extreme/high temperatures and pressure working conditions (Reed 2006). The addition of Chromium (~10-20 % wt.) in Nickel alloy provided both creep resistance and oxidation resistance (~ 982°C), usually forms oxide scale of Chromium over base alloy protect in elevated temperature environment and restricts diffusion rate of Sulphur and Oxygen internally (Reed 2006). The chemical composition of the Inconel 718 alloy sheets is found using the spark emission spectrometer. Standard ASTM E3047-16 test for emission vacuum spectrometric analysis has been used to determine the material composition of Inconel 718 alloy. (ASTM E3047-16 2018). The chemical composition of Inconel 718 alloy is listed in. Table 3.1.

Table 3.1. Chemical composition of Inconel 718 alloy

Element	**Ni**	**Fe**	**Cr**	**Nb**	**Mo**	**Ti**	**Al**	**Cu**
wt.%	51.463	20.441	18.279	5.0122	2.87	1.09	0.5611	0.0306
Element	**C**	**Mn**	**Si**	**Co**	**P**	**S**	**Zr**	**B**
wt.%	0.0271	0.0616	0.0505	0.0925	0.001	0.002	0.0091	0.0024

The as-received sample (10 mm ×10 mm) was cold mounted by using a commercially available cold setting compound (resin powder + liquid). Further, samples were wet ground on progressively finer grades of silicon carbide impregnated emery paper with ample amount of water (act as a lubricant and coolant). Subsequently, the ground samples were polished mechanically using five micron-diamond paste. A perfect mirror-like finish of the surface of

the polished sample was achieved using one-micron diamond paste with ample amount of water. The polished mirror surface of the sample was observed under an optical microscope.

Figure 3.1 shows the optical micrographs of Inconel 718 alloy at different orientations, i.e., rolling direction (RD), diagonal direction to rolling direction (ND) and transverse direction to rolling direction (TD). The average diameter is 15.9 μmm with difference in morphology in RD, ND, and TD of the Inconel sheet. Mostly elongated and compressed grain structures can be perceived in the RD and ND. This can be accredited to large-scale rolling to achieve the sheet material. Specimens confirm mostly fine grain size with considerable carbide stringers/ intermetallic phases in an austenitic matrix consisting of fine equiaxed grains. The presence of initial carbide/intermetallic phases is due to the solidification procedure and influence parameters like solidification time, Nb/C ratio of alloy and cooling rate.

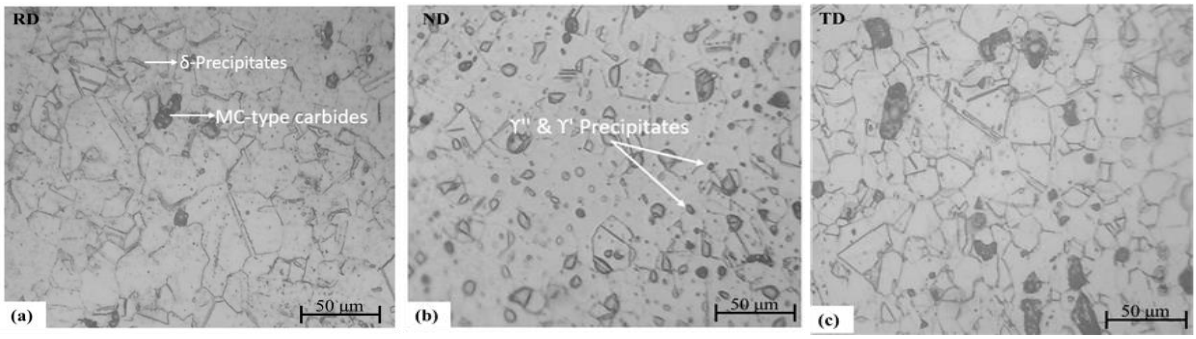

Figure 3.1: Microstructure of parent Inconel 718 alloy at different orientations (a) RD (b) ND (c) TD

The tensile test specimens were machined by using the wire-cut Electro-Discharge Machining (EDM) process for high dimensional accuracy and good surface finish. The dimensions of tensile test specimens were prepared as per sub-sized ASTM E08/E8M-11 standard as shown in Figure 3.2(a). In sheet metal, mechanical properties and deformation behavior is varying with respect to the direction due to the inherent anisotropic nature of sheet materials. Thus, tensile test samples were prepared at rolling direction (RD), Diagonal to rolling direction (ND), and transverse direction (TD), as shown in Figure 3.2(b).

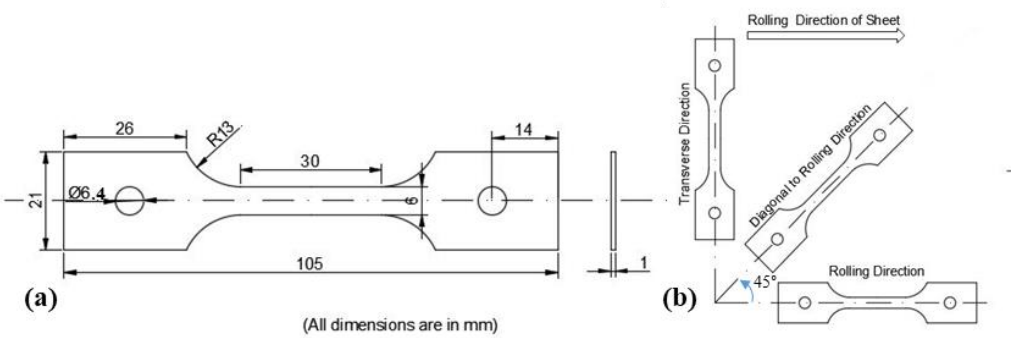

Figure 3.2 Schematic of tensile test specimen (a) sub sized ASTM E08/E8M-11 standard (b) with different orientation

3.2 Tensile Testing

Tensile tests have been conducted on a computer-controlled Universal Testing Machine (UTM), as shown in Figure 3.3. The maximum load capacity of the machine is 50 kN, and heating capacity from RT to 1000°C with ± 3°C accuracy. Two-zone split heating cylindrical furnace was used for the heating purpose as shown in Figure 3.3. The contact type of extensometer was used to capture the true load vs displacement data during the tensile testing. The machine is equipped with a closed-loop feedback control system to carry out an exponential increase of actuator speed for constant true strain rates. The constant strain rate is controlled based on Equation 3.1. For constant strain rate, cross-head speed is varied exponentially.

$$v = \dot{\varepsilon} L_0 exp(\dot{\varepsilon} t) \tag{3.1}$$

where, v, ε̇, L_0 and t are the cross-head speed, constant strain rate, gauge length of the specimen and time.

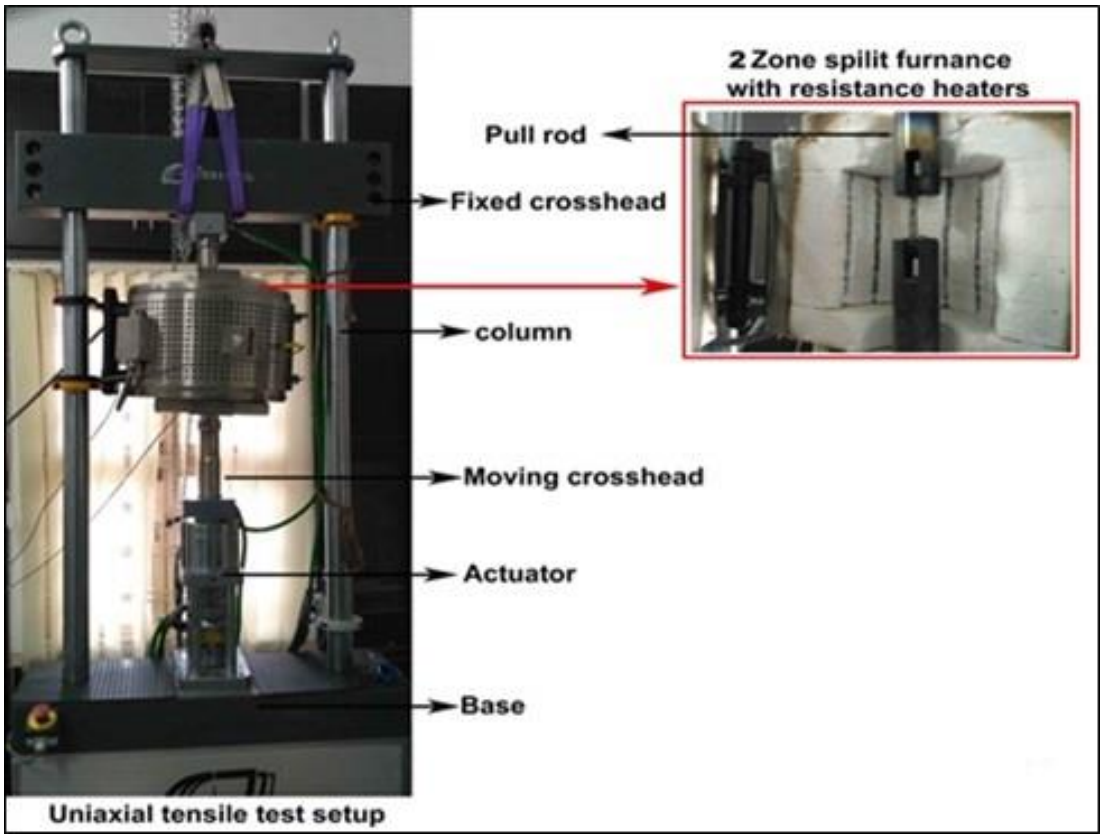

Figure 3.3 Experimental set up of UTM of 50 kN capacity with two-zone split heating furnace

The material and forming behavior are sensitive towards its process parameters, i.e. temperature, strain rate, and orientation of sheet. Previously published articles reported that mechanical properties of the material tested at quasi-static strain rates are more consistent than tested at higher strain rates (Bruschi et al. 2014; Field et al. 2004). Also, nickel alloys, intended for jet engines and power generation gas turbines, will be exposed to high temperatures while

in service. Thus, for assessing high-performance alloy, high temperature tensile tests are selected. Also, the elevated-temperature tension test gives a useful estimate of the static load-carrying capacity of metals under short-time, tensile loading. By considering all these facts, Experiments are performed at quasi-static strain rates range (10^{-4}-$10^{-1}s^{-1}$) from RT to 700°C at an interval of 100°C. Samples are first heated to the desired deformation temperature at 20 °C/min heating rate. The heat preservation time is 9-10 minutes to ensure a uniform temperature prior to loading, as shown in Figure 3.4. Then, a quasi-static hot tensile test is performed at a desired temperature and strain rate. After the test, tested specimens can air cool. Three samples were tested in each test set, and average values are reported.

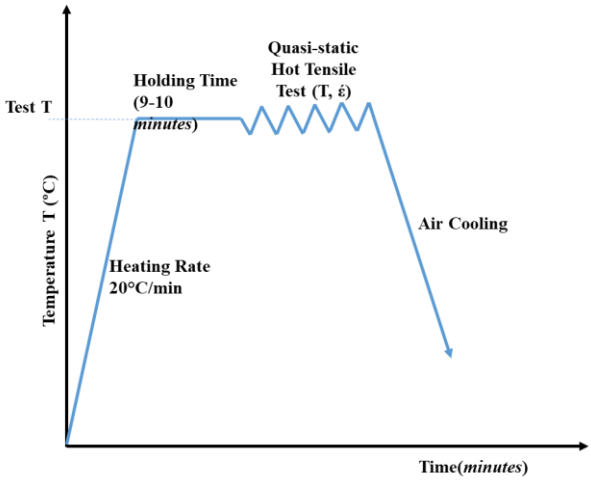

Figure 3.4: Experimental time-temperature-deformation sequence followed for quasi-static hot tensile test

3.2.1 Tensile Flow Behavior

The representative flow stress behavior along RD at different strain rates and temperatures is shown in Figure 3.5(a-d). As expected, the flow stress decreases with an increase in test temperatures. The variation of flow stress at different temperatures is significant. An increase in strain rate shows an increase in flow stress at RT but the considerable effect at 700°C. However, the general trend is that the flow stress decreases with a decrease in the strain rates. Inconel alloy shows appreciable strain hardening. The strain hardening of material at strain rate of 0.0001 s^{-1} is observed to be higher than other considered strain rates (0.001, 0.01 and 0.1 s^{-1}). This behavior might be because of adiabatic heating and consequent thermal softening during sheet manufacturing. Flow stresses are sharply increasing with small rise in strain (up to 0.05), followed by a slow increase in flow stress till ultimate tensile strength (σ_{uts}). A sharp increase in tensile strength is because of uniform macroscopic deformation.

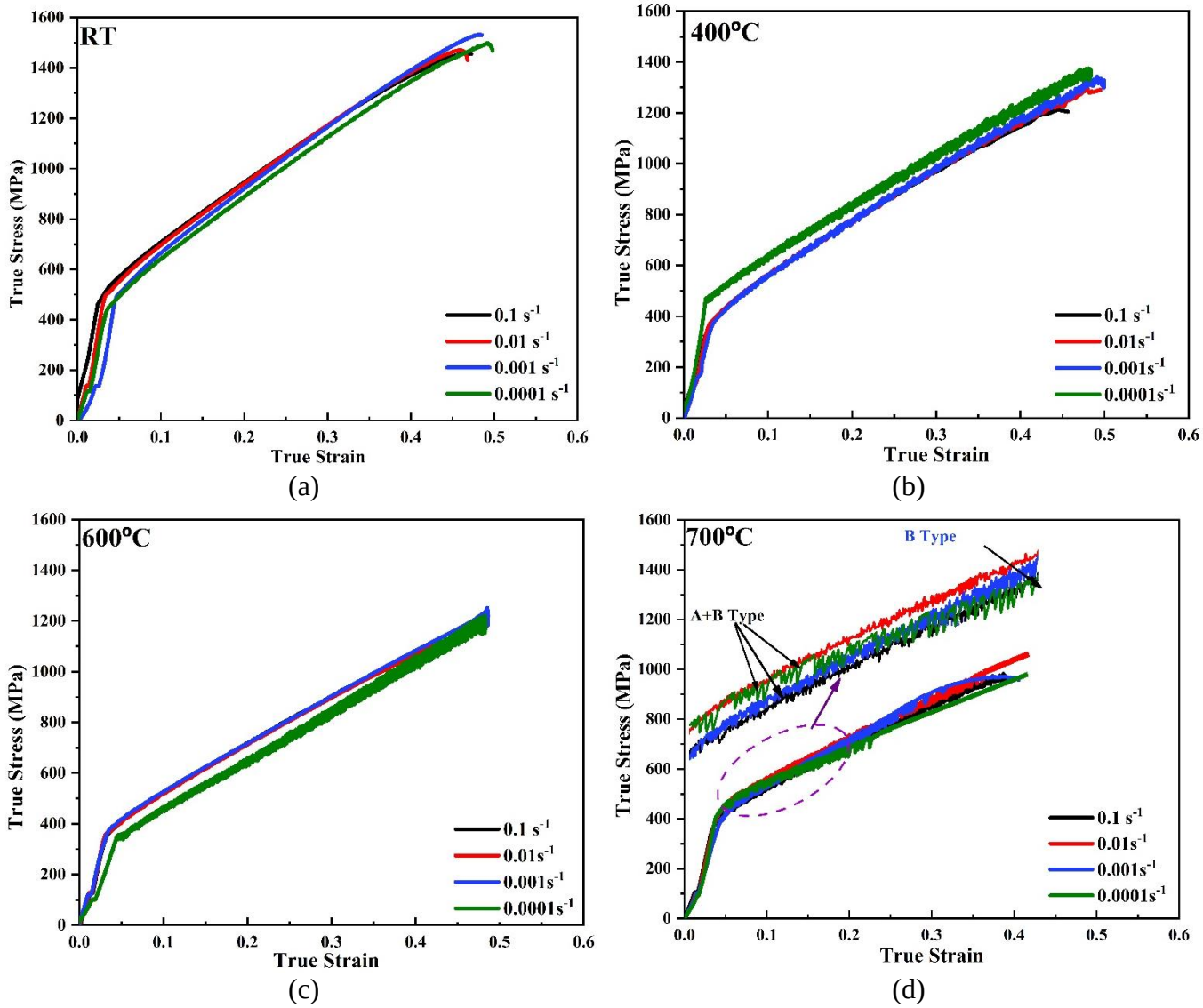

Figure 3.5: Representative true stress-strain curves along RD at different strain rates and temperatures (a) RT, (b) 400ºC, (c) 600ºC, and (d) 700ºC.

The representative flow stress behavior shows the variation of temperature at two different strain rates (0.01 s^{-1} and 0.0001 s^{-1}) as shown in Figure 3.6 (a-b). The material shows temperature dependency as ultimate tensile strength decreases from 1530 MPa (at RT) to 984 MPa (at 700°C) at the strain rate of 0.01 s^{-1}.

Figure 3.7 shows the effect of the direction of the sheet on flow stress behavior. However, the σ_{ys} values are maximum and minimum along RD and TD samples, respectively. This shows the peak stress value is very sensitive to the presence of crystallographic texture in materials (Dieter 2011).

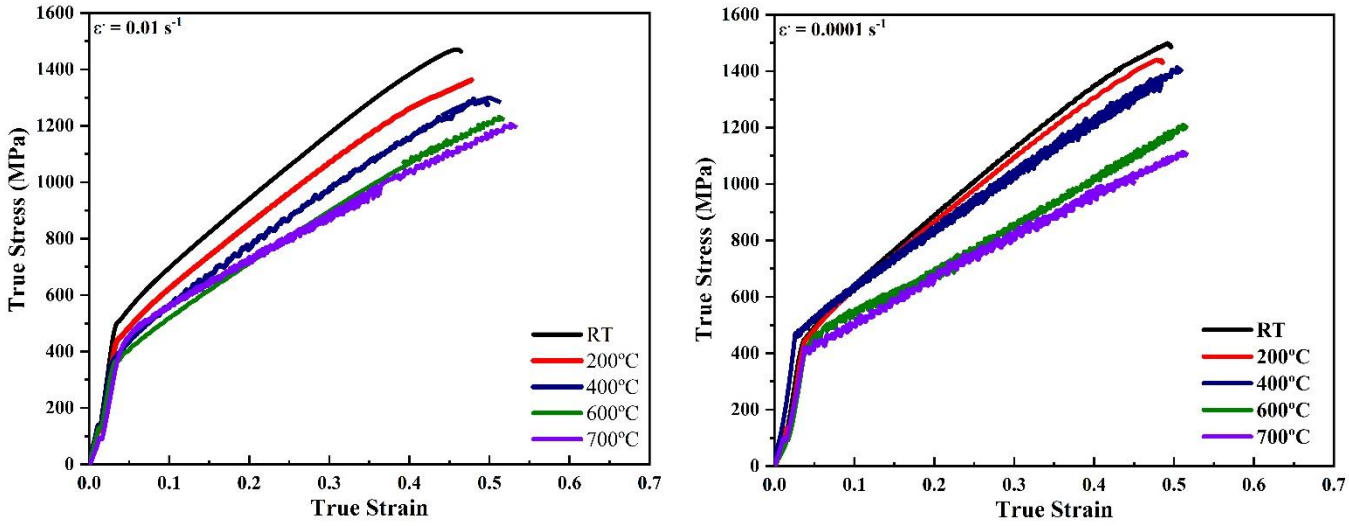

(a) (b)

Figure 3.6 Representative true stress–strain curves at different temperature and strain rates (a) 0.01 s^{-1} (b) 0.0001 s^{-1}.

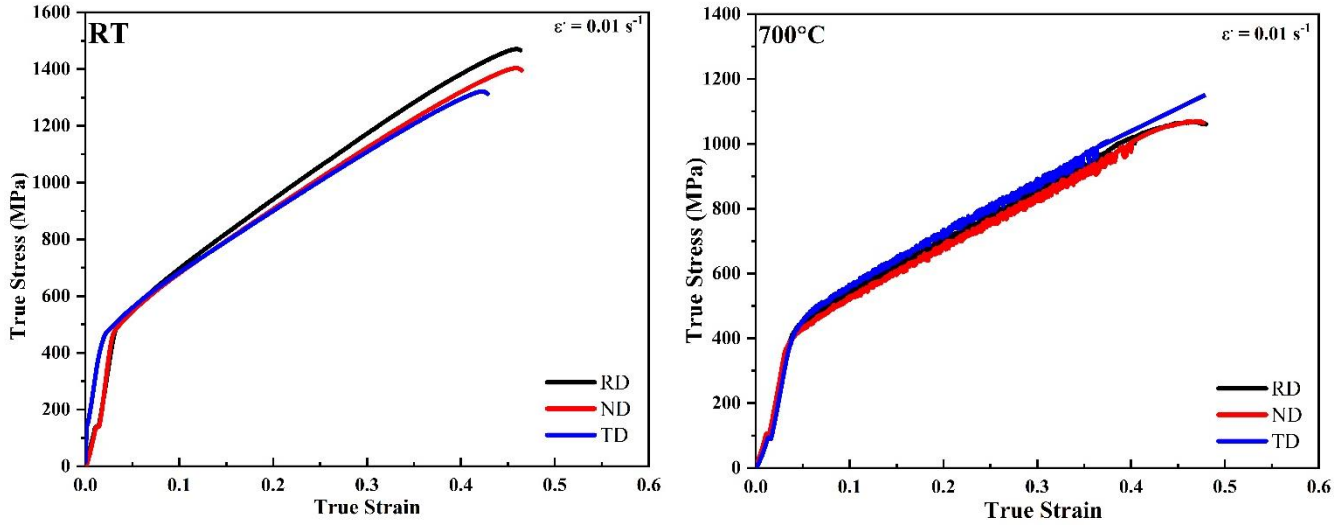

(a) (b)

Figure 3.7 Representative true stress–strain graphs at (a) RT, and (b) 700°C, with different sheet orientations

The material properties are evaluated at different temperatures and quasi-static strain rates conditions in RD, ND, and TD orientations. Firstly, the average 0.2% offset yield strength (σ_{ys}) is determined at different temperatures, as shown in Figure 3.8 and Table 3.2. It is seen in Figure 3.8(a) that (σ_{ys}) is the highest in case of the RD and least in the case of ND. The average yield strength found at RT is 505 MPa. As the temperature increases, yield strength decreases. It is observed from Table 3.2 that around 19% yield strength decreases at 700°C. Figure 3.8(b) shows the variation of ultimate tensile strength (σ_{uts}) with different orientations of sheet. The σ_{uts} is maximum at RT in RD. The variation of σ_{uts} value is similar to σ_{ys}, i.e., maximum in RD and least in TD. The average σ_{uts} reported at RT, and 700°C is 1530 and 984 MPa, respectively. Thus, around 35% reduction in σ_{uts} is noticed for Inconel 718 alloy at 700°C.

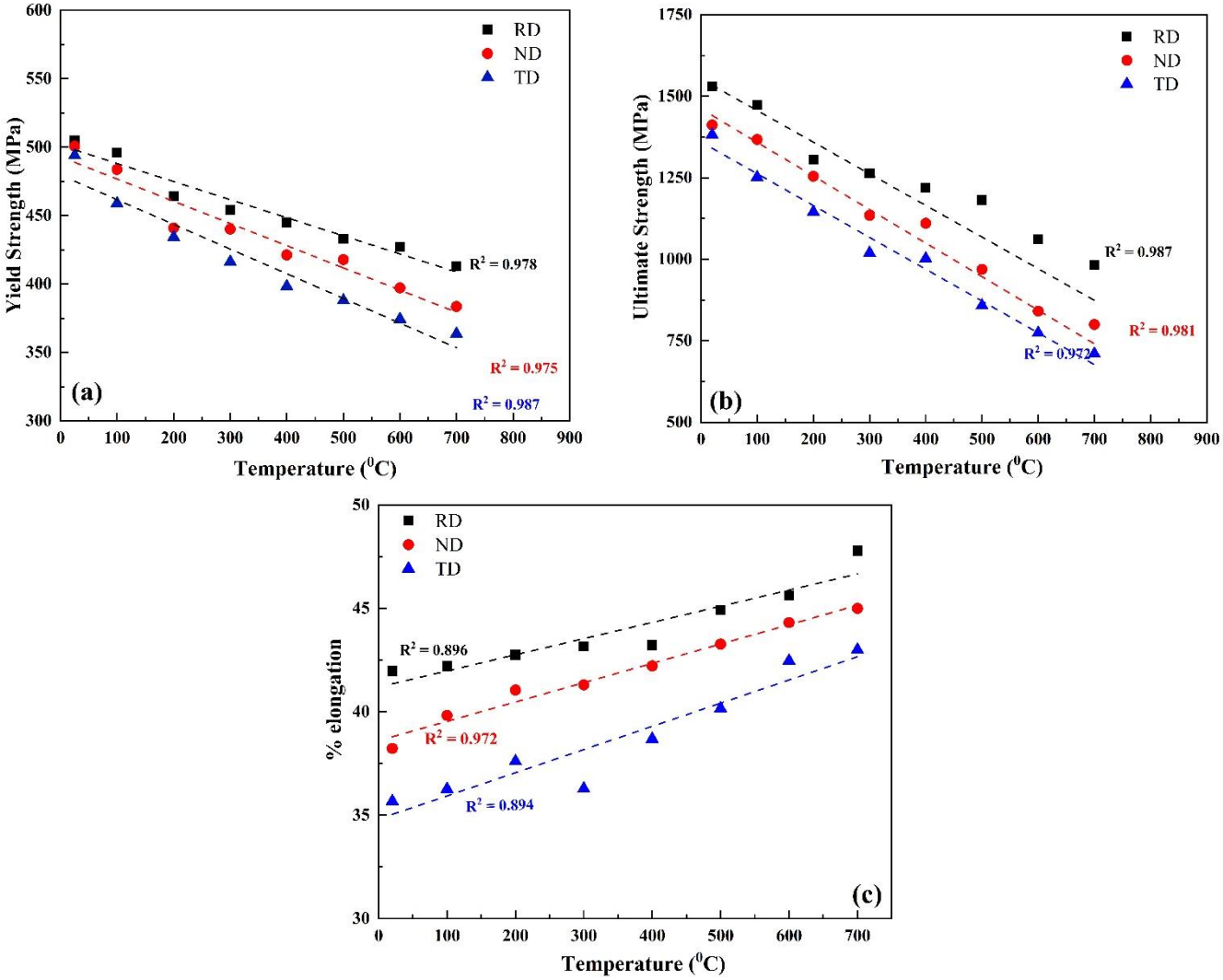

Figure 3.8: Effect of test temperature on (a) yield strength (b) ultimate strength and (c) % elongation, in three different orientations.

Table 3.2 Mechanical properties of Inconel 718 alloy at 0.001 s^{-1} in RD

Temperature (°C)	σ_{ys} (MPa)	σ_{uts} (MPa)	% Elongation (%)
RT	505± 6%	1530 ± 10%	41.97 ± 0.6
100°C	496± 5%	1474 ± 6%	42.20 ± 0.6
200°C	464 ± 3%	1306 ± 5%	42.75 ± 0.5
300°C	454± 5%	1264.40 ± 4%	43.16 ± 0.5
400°C	445 ± 4%	1219.73 ± 6%	43.22 ± 0.7
500°C	433 ± 6%	1181.33 ± 8%	44.91 ± 0.4
600°C	427 ± 4%	1062.14 ± 6%	45.62 ± 0.4
700°C	413± 5%	983.22 ± 6%	47.78 ± 0.7

Generally, the main reason for occurrences of plastic deformation is the motion of many dislocations. The dislocation motion based mechanism is composed of three processes generation, glide or climb, and annihilation (Kuhlmann-Wilsdorf 1989). Theoretically, the strength of a defect free crystal material is extremely high as plastic deformation would require simultaneous breaking of many bonds. Dislocation density (number of dislocations in a unit volume of a crystalline material) defines the tensile yield strength of an alloy. Since increase in dislocation density increases the shear stress essential to move the dislocations. At low temperature, activation energy is low and vibration of atoms is less with less thermal anxiety compared to elevated temperature, resulting in obstruction to the dislocation movement. This results in large strength to tear dislocation from respective atomic equilibriums. Hence, metal exhibits high tensile strength at low temperatures (Dieter 2011). Work hardening mechanism delays dislocation motion. But, the increase in temperature, climb, and annihilation process will be improved. Further, internal energy increases as atomic vibration increases resulting in less obstruction for atomic movement and increased or decreased dislocation in interatomic distance leads to expansion or compression of metal structure at elevated temperature. This affects the material strength directly, and there is the reduction in strength of alloy at elevated temperature compared to RT. Thus, deformation exhibits higher elongation because of easier grain boundary slides and grain rotation activities which results in a noticeable effect on texture (Dieter 2011; Lin et al. 2014). The % elongation at RT is found to be around 42% which is higher than other metallic alloys such as stainless steels. The rise in % elongation is around 48% at 700°C. It is also observed that % elongation is higher in case of RD and lower in TD.

It is noteworthy to mention that serrated flow stress behavior has been reported from 400° to 700°C temperature range for all strain rates as represented in Table 3.3. The serration behavior is popularly described by the Portevin–Le Chatelier effect or dynamic strain aging (DSA). According to the classification of Rodriguez, the serrations type A, B, and C are observed in metal (Rodriguez 1984). Oscillation type of flow stress behavior is found from 400-500°C, which indicates B-type of serrated flow behavior. Above 500 °C, a combination of A and B-type of serration is reported for Inconel 718 alloy. Table 3.3 indicates a summary of types of serrated flow behavior at different temperatures and strain rates. The serration type A and B is observed with raise in test temperature. The fluctuation of flow stress is because of rapid DRX, where the former process ends before the latter one starts (Mishra et al. 1989). Similar observations were reported by (Lin et al. 2014a; Lin et al. 2014b).

Table 3.3 Observed serration at different temperatures and strain rates

Temperature ⟹	**400°C**			**500°C**			**600°C**			**700°C**		
Orientation ⟹	RD	ND	TD	RD	ND	TD	RD	ND	TD	RD	ND	TD
Strain Rate (s^{-1}) ⇓												
0.1 s^{-1}	-	-	-	-	-	-	A	A	-	A+B	-	-
0.01 s^{-1}	B	A	-	B	B	A	A	A	A	A+B	A	A
0.001 s^{-1}	B	A	B	B	B	B	A+B	A+B	B	B	A+B	A+B
0.0001 s^{-1}	A+B	A+B	A+B	A+B	A+B	B	A+B	A+B	A+B	A+B	A+B	A+B

Another way to confirm the DSA phenomena is negative strain rate sensitivity (m). The negative value of m confirms the claim of PLC or DSA effect in a metal (Jobba, Mishra, and Niewczas 2015; Singh, Mahesh, and Gupta 2010). The dependence of flow stress on strain rate is measured by strain rate sensitivity (m) and experimentally determined by comparing the stress levels at the same strain of two tensile tests at different strain rates at a particular temperature (Mishra et al. 1989; Prasad, Rao, and Sasidhara 2015). It is calculated as,

$$m = \frac{\dot{\varepsilon}\, d\sigma}{\sigma\, d\dot{\varepsilon}} = \frac{\partial(\ln \sigma)}{\partial(\ln \dot{\varepsilon})} \qquad (3.2)$$

The measured strain rate sensitivity (m) along the rolling directions (RD) is 0.0053 at RT (Table 3.4). This indicates that the alloy is sensitive to strain rate at RT. The strain rate sensitivity (m) is observed to have a non-negative value up to 300 °C (Table 3.4). Afterward, as the serration yielding is started, strain rate sensitivity (m) along RD is observed to have a negative value till 700°C. This is observed due to energy conversion while plastic deformation at various strain rates and at high temperatures due to enhanced dislocation motion (Rodriguez 1984). It is observed that the strain rates have a clear influence on both the strength and ductility of the alloys. The m value decreases as temperature increases indicating variation in flow. The m value first drops & then rises as deformation temperature increases. It is because of microstructure evolution which needs more heat dissipation for a particular test temperature.

Table 3.4 Strain rate sensitivity exponent (m) at various temperatures in the DSA regime Temperature

Temperature (°C)	**RT**	**100**	**200**	**300**	**400**	**500**	**600**	**700**
Strain rate sensitivity (m)	0.0053	0.0049	0.0019	0.0011	-0.121	-0.179	-0.281	-0.12

3.2.2 Evaluation of Anisotropy Properties

The directionality of material properties is defined as an anisotropy parameter (r), and it is related to the variance of atomic spacing within crystallographic orientations. Plastic

anisotropy of a rolled sheet metal is typically characterized in terms of strain ratio by the Lankford coefficient. Lankford coefficients are determined as per the ASTM 517-00:2010 standard (ASTM 517-00:2010 2010). Generally, the test will be conducted beyond the yield point and before the ultimate tensile strength point using a uniaxial tensile test machine. The test is interrupted after yielding (around 15% elongation), much before UTS. Zwick/Rolle computerized controlled Universal Testing Machine (UTM) is used for testing purposes.

The strip of size (175 mm × 20 mm) is wire cut in three directions i.e., RD, TD and ND as shown in Figure 3.9(a). The metal strip is marked at five different places in gage length (l_o = 20 *mm*) before uniaxial test as shown in Figure 3.9(b). A uniaxial tensile test is conducted at a quasi-static strain rate of 10^{-2} s^{-1} and stopped at 15% elongation after yielding. Change in width ($w_{1\text{-}5}$) and thickness ($t_{1\text{-}5}$) at five different places is measured after uniaxial loading.

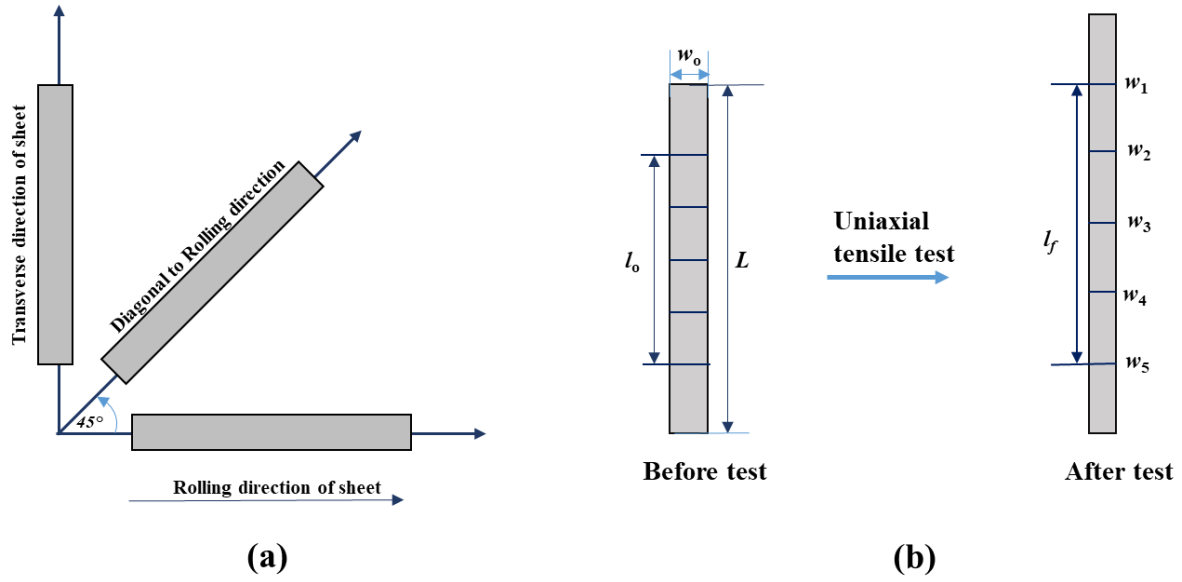

Figure 3.9 Schematic diagram shows representative test specimen for r-test (a) with different orientations of a sheet (b) marked five different places in gage length

Mathematically the Lankford coefficients is defined as,

$$r = \frac{\varepsilon_w}{\varepsilon_t} \qquad 3.3$$

Where ε_w and ε_t strains in the width and thickness directions, respectively.

$$\varepsilon_w = \ln(\frac{w_f}{w_0}) \text{ and } \varepsilon_t = \ln(\frac{t_f}{t_0})$$

Where, w_f and t_f are the final width and thickness after the test. w_o and t_o are the original width and thickness before the test. Since the thickness of the specimen is much smaller compared to its other two dimensions, thickness strains are not measured directly while calculating *r*. The following Equation 3.4 resulting from volume constancy is used.

$$\varepsilon_t = \ln\left(l_0 w_0 / l_f w_f\right)$$

$$\text{Now, } r = \frac{\ln\left(\frac{w_f}{w_0}\right)}{\ln\left(l_0 w_0 / l_f w_f\right)} \qquad 3.4$$

For accurate measurement, an optical microscope is used. To assure consistency of the results, each test is repeated for the three times and average values are reported. The calculated Lankford coefficient (r) are mentioned in Table 3.5. It is noticed that there is not noticeable change at different temperatures.

The Normal anisotropy ($\bar{R}$) parameter represented the drawability of a material. During a deep drawing, metal with high R_N experiences less thinning than metal with small ($\bar{R}$) with the same metal flow characteristics (Banabic 2010b). The normal anisotropy ($\bar{R}$) value is given by Equation 3.5.

$$\bar{R} = \frac{r_0 + 2r_{45} + r_{90}}{4} \qquad 3.5$$

where r_0, r_{45} and r_{90} are plastic strain ratios along 0°,45°and 90° orientations to RD. The normal anisotropy is reported in Table 3.5. It is interesting to notice that change in $\bar{R}$ value is very insignificant at higher temperatures. The possible reason may be the occurrence of DSA at higher temperatures.

Table 3.5 Anisotropic properties of Inconel 718 alloy at different test temperatures

Temperature (°C)	**Lankford coefficient (r)**			**Normal anisotropy ($\bar{R}$)**	**Planar anisotropy (ΔR)**	**In-plane Anisotropy (A_{IP})**	**Anisotropy index (δ)**
	(r_0)	(r_{45})	(r_{90})				
RT	0.7813	0.9471	1.0432	1.0665	0.0979	0.0332	0.0482
100°C	0.7737	0.7798	0.9169	1.0877	-0.0297	0.0287	0.0461
200°C	0.9694	0.8765	0.9655	1.0121	-0.1194	0.0240	0.0441
300°C	0.997	1.0952	0.9694	0.9580	-0.1062	0.0207	0.0405
400°C	0.8808	0.8972	0.9177	0.9231	-0.0209	0.0225	0.0382
500°C	0.9971	1.0953	0.9694	0.7196	-0.4283	0.0216	0.0379
600°C	1.1423	0.9694	0.9174	0.7086	-0.2603	0.0228	0.0361
700°C	1.1231	1.3361	1.1321	1.231	-0.2082	0.0198	0.0356

The planar anisotropy (ΔR) is expressed by the difference of strain ratio in three orientations of the sheet. It is signifying the ears formation in drawn cups and uneven thinning. It is expressed as,

$$\Delta R = \frac{r_0 - 2r_{45} + r_{90}}{2} \qquad (3.6)$$

The measured value of planar anisotropy is mentioned in Table 3.5. Smaller value of ΔR indicates lesser possibility of formation of earing. This also reduces the defect of wrinkling and tearing in deep drawing. It is observed that ΔR is very insignificant with rise in temperatures.

It has been mentioned in the literature that the normal and planer anisotropy parameters are sensitive in nature. There are some other robust stress-based parameters such as in-plane anisotropy (A_{IP}) and anisotropic index (δ). Jata et al. 1996 proposed an anisotropic parameter in terms of yield stress variation. This behavior of metal properties is called in-plane anisotropy (A_{IP}). It is mathematically represented based on yield strength (σ_{ys}) in different rolling directions as

$$A_{IP} = \frac{2 \times \sigma_{ys}^{0} - \sigma_{ys}^{90} - \sigma_{ys}^{45}}{2 \times \sigma_{ys}^{0}} \qquad (3.7)$$

where, σ_{ys}^{0} is tensile yield strength at 0° orientation to RD,σ_{ys}^{45} is tensile yield strength at ND, and σ_{ys}^{90} is tensile yield strength at TD. For isotropic metal, A_{IP} = 0, as $\sigma_{ys}^{0} = \sigma_{ys}^{45} = \sigma_{ys}^{90}$. An increase in the values of A_{IP}, indicates an increase in the extent of anisotropic nature. Values of A_{IP} for Inconel 718 alloy are calculated and listed in Table 3.5. A_{IP} value is decreasing with an increase in temperature, shown in Figure 3.10(a).

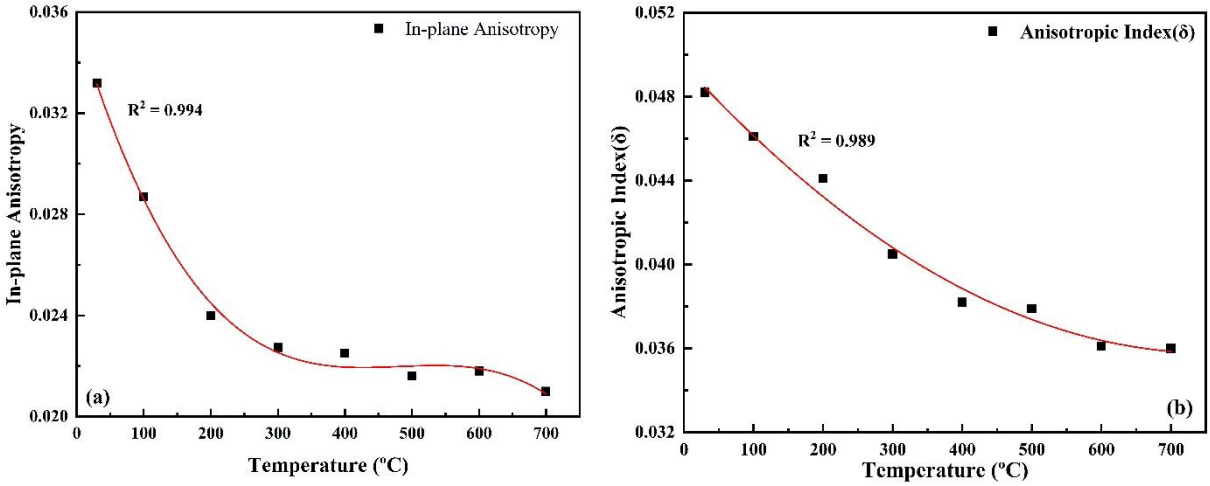

Figure 3.10 Effect of deformation temperature on (a) in-plane anisotropy (A_{IP}) (b) anisotropic index δ at 0.001 s^{-1} strain rate

Wu and Koo 1997 proposed anisotropy behavior of a material in terms of % elongation; it is called anisotropic index δ. It is mathematically calculated as,

$$\delta = \frac{(\%El)^{0} - (\%El)^{90}}{(\%El)^{0} + (\%El)^{90}}, \qquad 0 \leq \delta < 1 \qquad (3.8)$$

where, (%El)° is % elongation at 0° orientation to the rolling direction, and $(\%El)^{90}$ is % elongation at 90° orientation to the rolling direction. A decrease in anisotropic index δ is observed with an increase in deformation temperature for Inconel 718 alloys (Table 3.5). The

presence of low values of anisotropic index δ indicates very less elongation anisotropy with rise in deformation temperature.

Figure 3.10 shows the plots of in-plane anisotropy (A_{IP}) and anisotropic index δ of Inconel 718 alloys varying with test temperatures at various strain rates. The in-plane anisotropy (A_{IP}) value is the highest at RT and replicates large variations of tensile yield strengths in three directions. As yield strength is also influenced by crystallographic texture, i.e., grain size and precipitates in material (Kuhlmann-Wilsdorf 1989; Wu and Koo 1997), decrease in-plane anisotropy and anisotropic index will be observed with rise in temperature. During hot deformation, sliding of grain boundary and rotation of grains progressed. Due to the rotation of grains, the favored orientation of a texture will be modified to random distribution. Hence, the effect of texture on plastic deformation reduces as deformation progresses. As grain boundary sliding is easier at elevated temperature, alloy deformed at elevated temperature is expected to show higher elongation. In the earlier stage of deformation at elevated temperature, the texture change is less due to low magnitude sliding of grain boundary and grains rotation. As deformation progresses, texture will be reformed by sliding of grain boundary and grain rotation (Dieter 2011). This is the main reason for the reduction in in-plane anisotropy (A_{IP}) and anisotropic index δ at a high deformation temperature.

3.2.3 Strain Hardening Behavior

The strain hardening behavior of alloy describes the increase in stress necessary to continue deformation at any stage of plastic strain. The nature of curves in the plastic deformation stage in the stress-strain curve explains interfering with the dislocation movement, grain boundaries. Strain hardening coefficient (*n*) defines the dependence of flow (yield) stress on the level of strain. In materials with a high n value, the flow stress increases rapidly with strain. A high *n* value leads to a major difference between yield strength σ_{ys} and ultimate tensile strength σ_{uts}, which are an indication of good workability of material and strain hardening assistant for high elongation under slow strain rate (Dieter 2011). In the literature, strain hardening capacity (H_C) parameters are used to define the workability or deformation capacity of the material. It signifies the capacity to which the material can be strain-hardened. Afrin et al. 2007 proposed a normalized H_C to calculate the strain hardening capacity.

$$H_C = \frac{\sigma_{uts} - \sigma_{ys}}{\sigma_{ys}} \tag{3.9}$$

Figure 3.11 represents average H_C values at various temperatures with respect to different orientations of a sheet. H_C value is significantly improved at higher temperature, which signifies better workability at a higher temperature region. As expected, trends like σ_{ys} and σ_{uts},

H_C value is higher in RD and least in TD. A decrease in the difference of tensile strength and subsequent reduction in yield strengths leads to an increase in strain hardening capacity. As strain hardening capacity of Inconel 718 is improved remarkably, result in excellent combination of strength & ductility (as example σ_{uts} = 951.92 MPa & (%) elongation = 41.97 % at RT and σ_{uts} = 343.58 MPa & (%) elongation = 54.78 % at 700°C). It might be due to high dislocation interaction in the metal originated by slip system activation within grains.

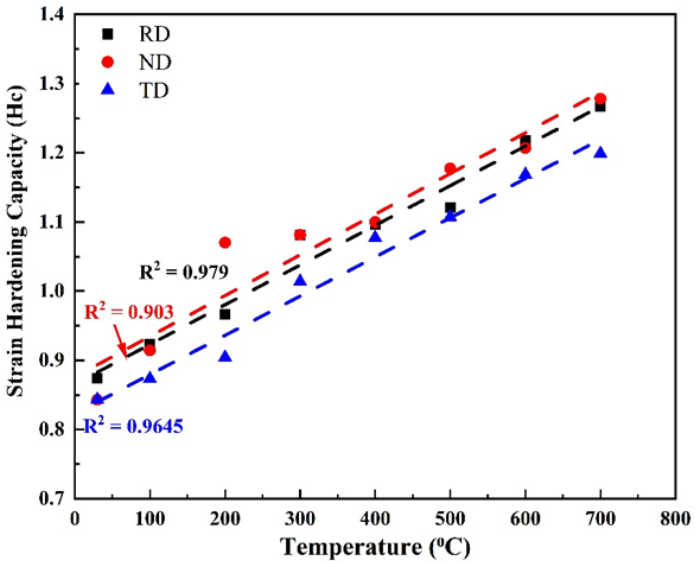

Figure 3.11 Effect of deformation temperature on strain hardening capacity, in three different orientations

Various mathematical flow relationships proposed to describe the stress-strain relationship such as Holloman (Equation 3.10), Swift (Equation 3.11), Ludwick (Equation 3.12) and Voce (Equation 3.13) in plastic deformation region and strain hardening behavior of metal are listed below,

Hollomon Equation $$\sigma = k_H \varepsilon^{n_H} \quad (3.10)$$

Ludwik Equation $$\sigma = \sigma_y + k_L \varepsilon^{n_L} \quad (3.11)$$

Swift Equation $$\sigma = k_s(\varepsilon + \varepsilon_0)^{n_s} \quad (3.12)$$

Voce Equation $$\sigma = \sigma_s - (\sigma_s - \sigma_I)[1 - \exp\left(-\frac{\varepsilon}{\varepsilon_c}\right)]$$

$$\text{or, } \sigma = \sigma_s - (\sigma_s - \sigma_I)\exp(n_V \varepsilon) \quad (3.13)$$

where, σ is true stress, ε is true plastic strain, K_H, K_L, K_S are strength coefficient, and n_H, n_L, n_S are strain-hardening exponent, σ_s is saturation stress (saturation stress at high strains where instantaneous work hardening is negligible), σ_I is initial true stress onset of plastic deformation, ε_c is a constant & $n_V = -1/\varepsilon_c$, rate at which flow stress reaches steady value usually occurs in high strains.

The most popular relationship that defines flow behavior by the stress-strain curve is the Hollomon empirical equation represented at constant strain rate and temperature by Equation 3.10. At different test temperatures and strain rates, the log-log plot of true plastic stress–true strain is plotted, as shown in Figure 3.12 (a-b). From the plot, two stages of strain hardening were identified, with two different *n* values. It can be concluded that the log-log plots of true stress-true plastic strain at various temperatures are linear at high strains, signifying applicability of the Hollomon equation only at high strains. A similar observation of two-stage work hardening of Inconel 718 alloy at RT is reported by Prasad et al. 2017.

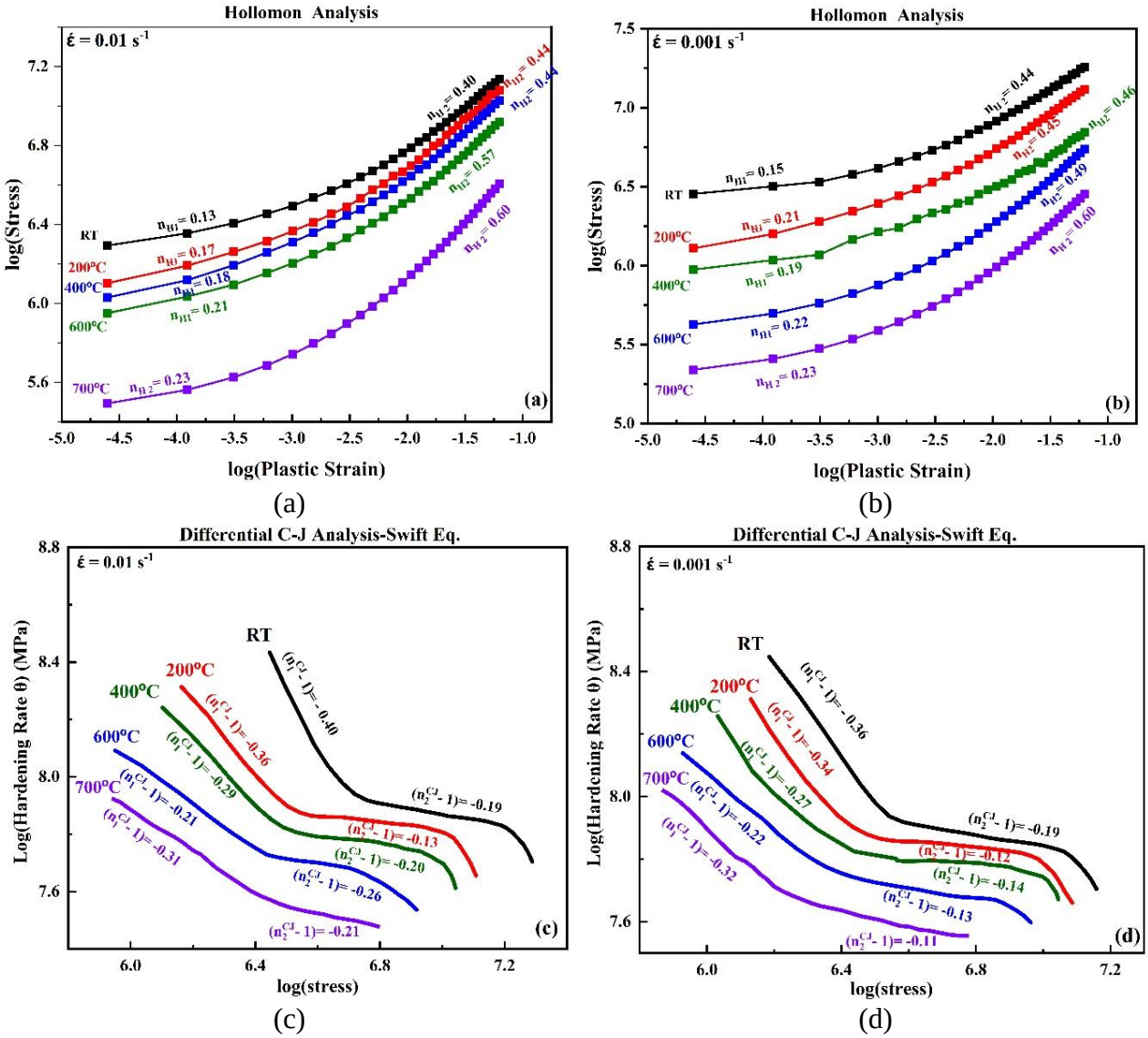

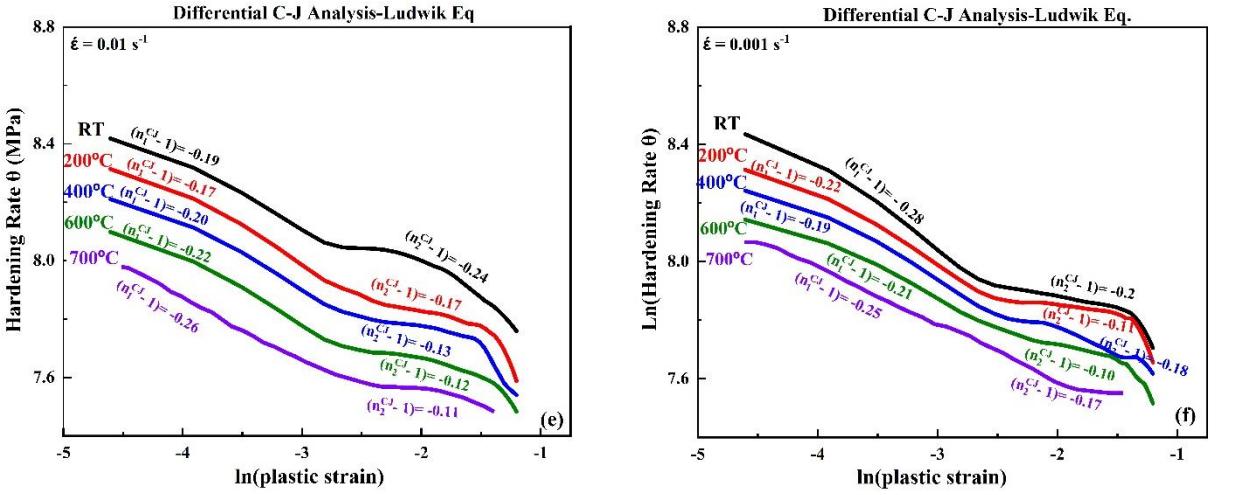

(e) (f)

Figure 3.12 Logarithmic true stress-plastic strain plots for (a-b) Hollomon Equation (c-d) Swift Equation and (e-f) Ludwik Equation in rolling direction

An optimum set of parameters for the Swift & Ludwik Equation are derived for the plastic deformation range of stress-strain data using an optimization method. Crussard–Jaoul (C-J) analysis is used to study the strain hardening behavior by Swift & Ludwik Equation (Equation 3.11-12). After differentiation with respect to ε, a log–log plot (dσ/dε) - σ for Swift equation and log-log plot (dσ/dε) -ε for Ludwik Equation. Figure 3.12 (c-d) reveals a sigmoidal plot with slope and gives value of '($n^{CJ} - 1$)' and intercept is given by $k_s n_s$ & $k_L n_L$ for Equation 3.11-12 respectively. It also shows two different strain hardening stages. It is seen that the slope (n_2^{CJ}-1) in the second stage is higher than (n_1^{CJ}-1) in the first stage. The Swift Equation (Equation 3.11) considered the pre-strain present in the metal. Whereas the Ludwik relation (Equation 3.12) is frequently used to represent the flow stress behaviour of FCC alloy with low stack fault energy (SFE).

From Figure 3.12 (a-b), it is observed that the value of strain hardening exponent in the higher strain region is significantly higher compared to the value in the lower strain region. An increase in the value of strain hardening exponent in higher strain region, retains the even elongation during plastic deformation. The Hollomon hardening law shows more accurate values compared to the Swift and Ludwik hardening laws because of more closeness to the experimental observation. It is observed that the work-hardening rate increases with a decrease in deformation temperature. It can also be stated as an increase in strain rate observed with decrease in critical strain at the incidence of dynamic recrystallization.

The physical significance for the Voce relationship was given by Kocks–Mecking (K–M) phenomenological model (Jobba et al. 2015; Prasad et al. 2015). In the K-M approach, evaluation of dislocation movement with increase in strain at constant strain rate is assumed to

be a single parameter of structure which is responsible for the plastic deformation. During plastic deformation, the work hardening rate is usually controlled by dislocation movement or rearrangement of dislocations in the structure. The free mean path of sliding dislocation is assumed to be determined by localized obstacles causing dislocation. Even other obstacles like grain boundaries and second phase particles to dislocation slide are considered. K-M approach is used to understand the tensile work hardening behavior of metals by plotting strain-hardening rate (θ) as a function of net flow stress (σ- σ_y). The representative K-M plot at different test temperatures and strain rates is shown in Figure 3.13. The slope of θ-(σ- σ_y) linear plot is the measure of rate at which work hardening lowers with the rise in net flow stress.

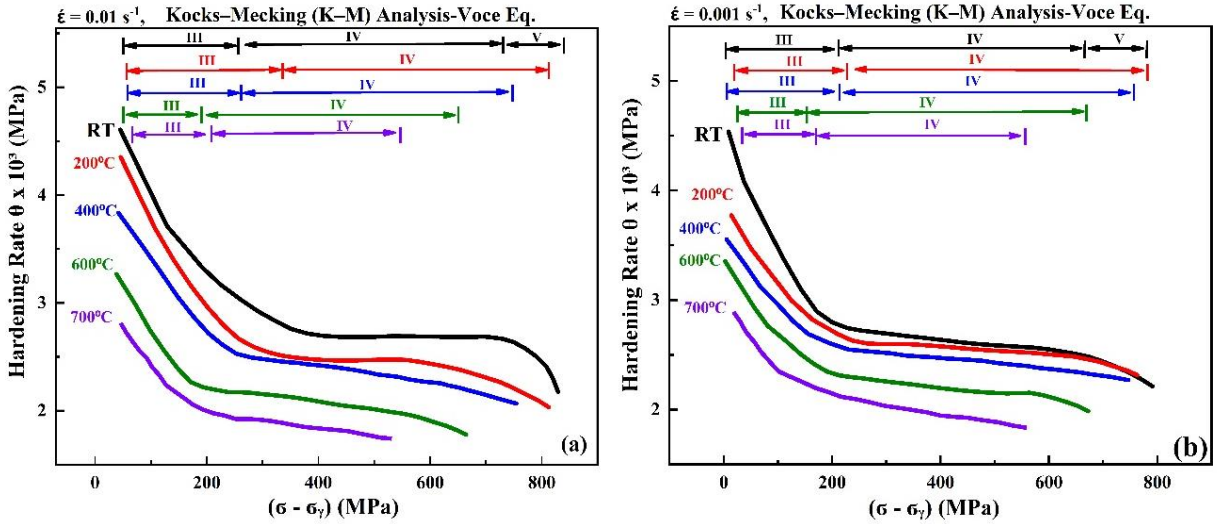

Figure 3.13 K–M plot of instantaneous strain hardening rate (θ) vs. net flow stress (σ - σ_y).

From the literature, the work hardening stages in crystalline structure are distinguished in five stages with an increase in plastic strain (Liu et al. 2017; Quan, Pan, and Wang 2016). Stage I corresponds to zero work hardening, i.e. single slip stage in a crystal and, is observed only in the single crystal. Stage II corresponds to the sudden linear hardening after stage I, i.e., double slip started in crystal. Strain hardening begins in polycrystalline structure from stage II and is observed for a very short period. Stage III corresponds to multiple slip patterns in individual crystals, i.e., parabolic strain hardening, followed by linear hardening – stage IV, and finally stationary stage, the stage V strain hardening stops. Softening observed after stage IV, is ascribed to dynamic recrystallization that occasionally leads to deformation localization if the temperature is sufficiently high. In stage III, dislocation grouping starts in microstructure which is responsible for deformation progress resulting in a drop of total energy.

Strain hardening stages observed in the Inconel 718 alloy are stage III with parabolic hardening, followed by linear strain hardening stages IV and V. It is observed that Stage III ends at net flow stress below ~200 MPa for all test temperatures. The curve is shifted to lower

stresses, i.e., towards the origin with the increase in temperature. Stage IV is observed for large net flow stress i.e., at large plastic strain. With the increase in test temperature, the strain hardening rate has decreased. Further, a steady reduction in length of region IV has been observed with an increase in test temperatures. Finally, the strain hardening stops at stage V. A transition stage occurs parabolic in nature for test temperature for Inconel alloy. This transition stage observed might be because of a grouping of slip dislocations bands, dislocation tangling, and splitting of dislocations into partial dislocation due to interaction of ϒ" precipitates in alloy (Mitchell 2005).

The two-stage work hardening behavior during hot deformation is represented by Hollomon, Swift, Ludwik and Voce in the present study (Figure 3.14). For which study of Hollomon and Voce relationships are best fitted by the correlation coefficient of determination (> 0.99) in both strain regions. Ludwick shows poor prediction capacity in both lower and higher strain regions for all temperatures and strain rates. Swift shows poor prediction only in the lower strain region. The strain hardening exponent (*n*) is high in the higher strain regions, and represents the large uniform deformation. This confirms the change in behavior of Inconel 718 alloy during hot tensile deformation. These changes might be the effect of dislocation bands, tangling, and splitting into incomplete dislocation interaction with precipitates (γ″ particles) (Mitchell 2005). The higher plastic strain with a gradual decrease in strain hardening rate shows the suitability of Inconel 718 alloy for formability at elevated temperature. The same trends of work hardening rate are observed in the other two orientations.

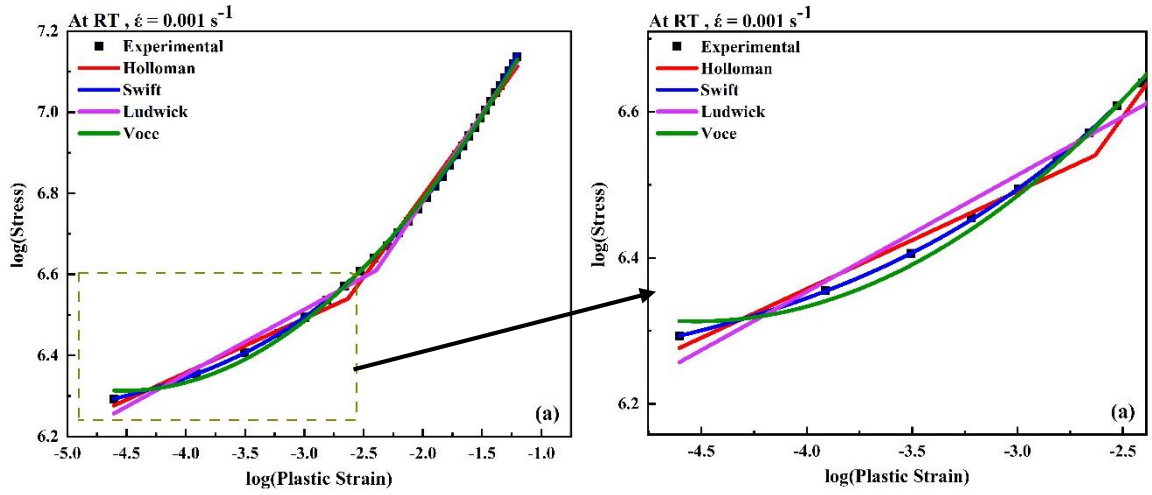

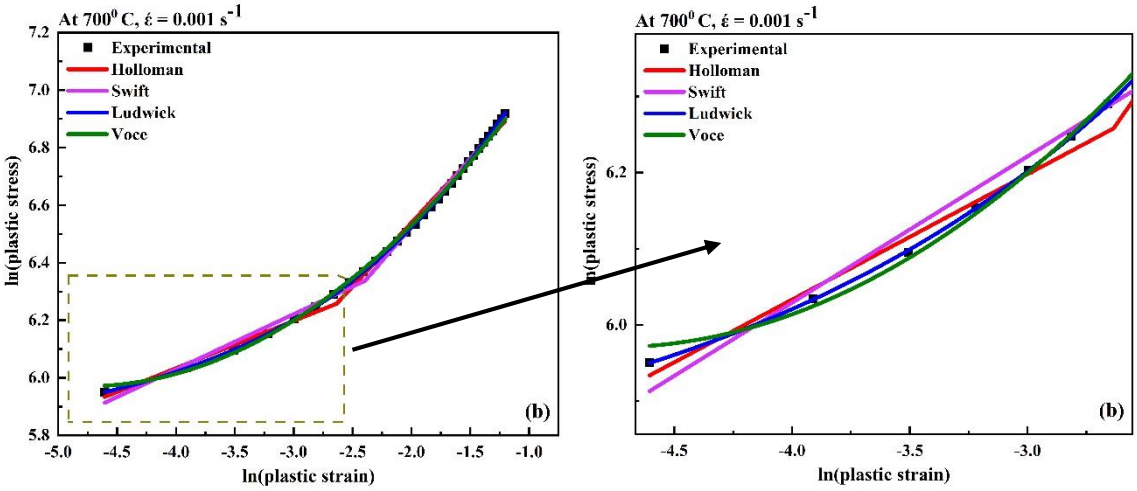

Figure 3.14 Comparison of various flow relations on log-log stress-strain plot at (a) RT (b) 700°C

3.3 Development of ANN for Material Properties Determination

ANN is an interpretation of the biological neuron system, is a highly interconnected system of parallel distribution, neural calculating elements that have the capability to grasp and learn to procure knowledge and make it available to use. The architecture of a neural network consists of a specific number of layers, number of neurons in each layer, sort of activation function accomplished by each neuron, and accessible connections between neurons. There are three basic steps for neural network architecture, namely the data collection, ANN modeling, and application. Data collection is the basic step that can be done through experimentation. Network architecture is created and configured by weights and biases with training and validating the network. After creating the neural network, it is possible to predict the results by giving concerned input to the proposed model.

In literature, it has been mentioned that controlled learning is designed to train networks for performance improvement. Used layered feed-forward ANN's is accomplished by the back-propagation algorithm, where the artificial neurons are arranged in layers and sending their signals ''forward'' and then errors are supposed to be promulgated backward. The back-propagation algorithm practices controlled learning to calculate error, i.e. difference between experiment and predicted results. The purpose of the back-propagation algorithm is to minimize the error, till the network acquires through training data. The training starts with random variables, and the objective is to arrange such that errors must be minimized (Singh et al. 2010; Wen et al. 2015). The data for testing and training the neural network is normalized from 0 and 1 using the transfer function (Desu et al. 2016). For the finest combination of layers, experimental data are divided randomly, first 70% training data for training ANN and the

remaining 30% as test data. The proficient ANN model is executed in MATLAB 2018a and trained by Levenberg–Marquardt algorithm.

In this study, the material properties considered are namely $\sigma_{ys}, \sigma_{uts}$, % elongation & n. The input parameters considered to determine the material properties are shown in the schematic drawing of the neural network structure (Figure 3.15a). The selection of the optimum hidden layer for the neural network is by a novel technique as mentioned by Desu et al. 2016. Based on the trial-and-error method, different numbers of hidden layers are varied to get the least mean square error. Figure 3.15b shows a representative plot of mean square error and number of hidden layers for Inconel 718 alloy material properties determination. It has been seen that the least mean square error was achieved for 22 hidden layers. Thus, chosen ANN model has a single layer with 2 inputs (strain & temperature) and 4 outputs ($\sigma_{ys}, \sigma_{uts}$, % elongation and n) as shown in Figure 3.15a. The ANN architecture of Inconel 718 has [2-22-4] layers, indicates 22 neurons in the middle-hidden layers with (2) inputs and (4) outputs.

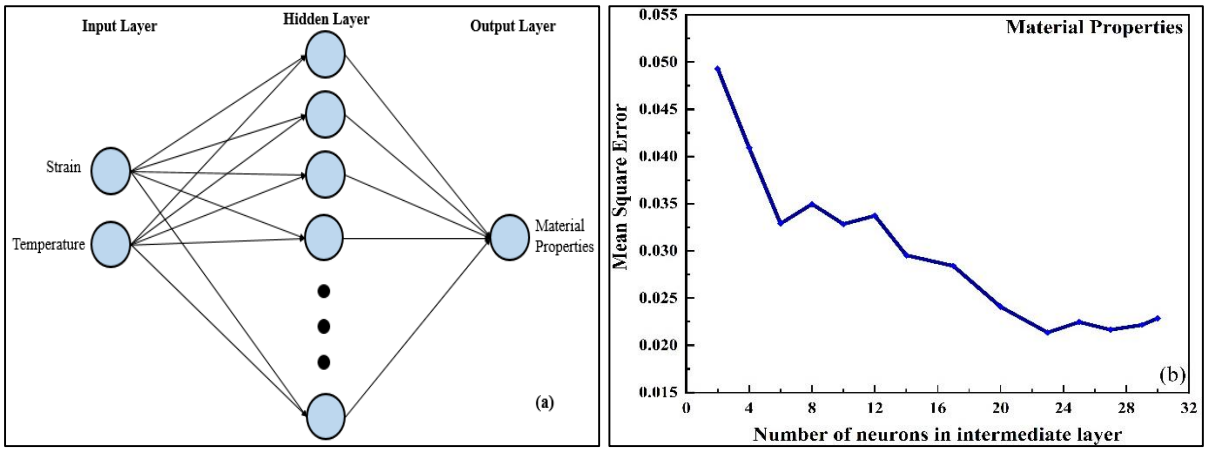

Figure 3.15: (a) ANN architecture used for material properties determination (b) Plot of mean square error vs. number of hidden layers for material properties

The input parameters considered to determine the anisotropic properties are similar to neural network structure (Figure 3.15a) with input (Thickness, orientation, temperature, and yield strength) and 5 outputs. The minimum mean square error (MSE) is observed when the number of hidden layers is 19. Selected ANN architecture of Inconel 718 has [4-19-5] layers. The input parameters considered to determine the Work hardening behavior is similar to neural network structure (Figure 3.15a) with input (strain, strain rate, true strength, and Temperature) and 4 outputs. As shown in Figure 3.16, minimum Mean Square Error (MSE) observed at 11,9,13 & 10 number of hidden layers for Hollomon, Ludwik, Swift & Voce relations, respectively.

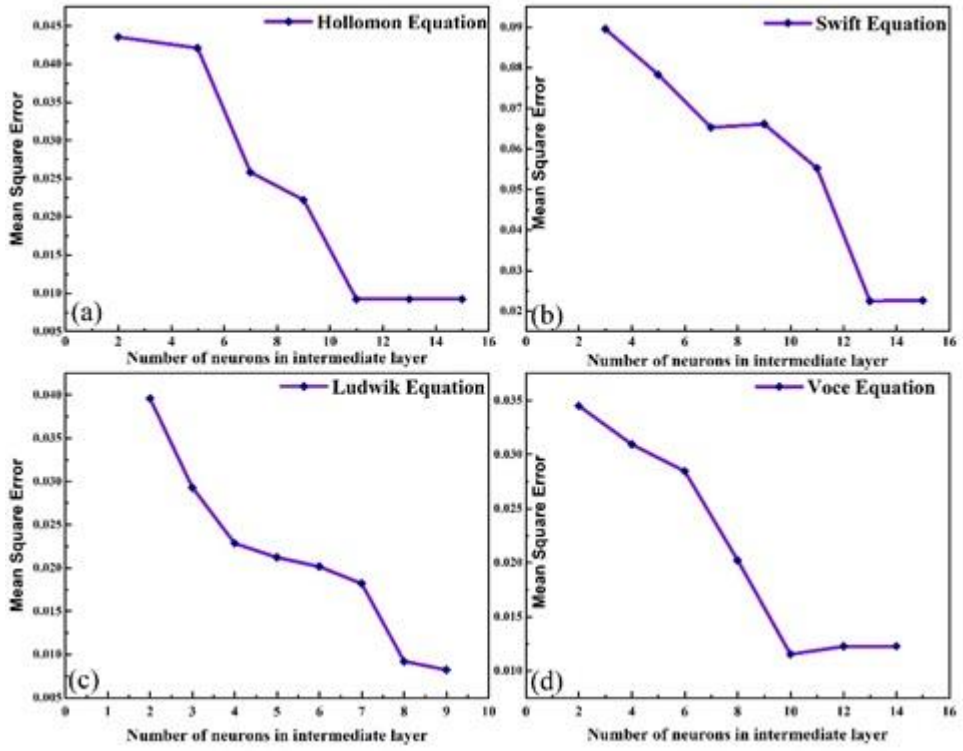

Figure 3.16: Plot of mean square error vs. number of hidden layers for hardening models

Validation of neural networks is compared through standard deviation, correlation coefficient, and average absolute error. The correlation coefficient is a statistical tool that provides the relation between predicted and experimental variables. The closeness of predicted value with experimental value is calculated with average absolute error. Equations used to calculate the correlation coefficient and average absolute error are,

$$R = \frac{\sum_{i=1}^{i=N}(y_{exp}^{i} - \bar{y}_{exp})(y_{p}^{i} - \bar{y}_{p})}{\sqrt{\sum_{i=1}^{i=N}(y_{exp}^{i} - \bar{y}_{exp})^2 \sum_{i=1}^{i=N}(y_{p}^{i} - \bar{y}_{p})^2}} \tag{3.2}$$

$$\Delta = \frac{1}{N}\sum_{i=1}^{i=N}\left|\frac{y_{exp}^{i} - \bar{y}_{p}}{y_{exp}^{i}}\right| \times 100 \tag{3.3}$$

Where, y_{exp} & y_p are experimental and predicted values, $\bar{y}_{exp}$ & $\bar{y}_p$ are average values of y_{exp} & y_p respectively, and N is the complete number of data points considered (Desu et al. 2016).

Table 3.6 represents the correlation coefficient, standard deviation, and average absolute error for the Inconel 718 alloy. The training data for Inconel 718 alloy shows excellent correlation as R-value for all properties is greater than 0.97 and the average percentage error less than 2.5%, indicates the true prediction of the ANN model. Higher R values of σ_{ys} and σ_{uts}, indicate that the Inconel 718 alloy follows the power-law or Hollomon equation. It is observed

that even through the R value of σ_{ys} & $\bar{R}$ is high with high average percentage error compared to other material properties. Hence, standard deviation with error values has to be taken into account duringvalidation of modal. The plots for the correlation coefficient for testing data of material properties determined are shown in Figure 3.17.

Table 3.6: Statistical parameters for training data for Inconel 718 alloy

Testing	**70% of the data**			**30% of the data**		
	R	**Δavg (%)**	**Std. Deviation (%)**	**R**	**Δavg (%)**	**Std. Deviation (%)**
			Material Properties			
$\boldsymbol{\sigma_{ys}}$	0.99994	2.49346	2.45358	0.98499	1.44939	1.07456
$\boldsymbol{\sigma_{uts}}$	0.99994	1.72241	1.60329	0.96499	1.09294	1.07701
% elongation	0.99686	1.06172	1.04835	0.94082	0.44311	0.34305
n	0.99344	1.22887	1.03383	0.96099	0.20036	0.17432
			Anisotropic Properties			
$\boldsymbol{\bar{R}}$	0.99941	2.00247	1.81957	0.96689	1.98682	1.79732
$\boldsymbol{\Delta R}$	0.97435	1.09865	0.99014	0.99691	1.91406	0.99872
A_{IP}	0.99948	1.89824	0.98391	0.98599	1.05912	0.92233
$\boldsymbol{\delta}$	0.99978	1.77483	1.44968	0.96098	1.29332	0.98399
			Work Hardening Behavior			
Hollomon Eq.	0.99799	0.62322	0.56516	0.99991	0.91336	0.75985
Ludwik Eq.	0.99888	0.87502	0.63215	0.99799	1.46816	1.02499
Swift Eq.	0.99699	0.74652	0.59135	0.97069	1.03641	0.93254
Voce Eq.	0.99869	0.50217	0.45389	0.99699	1.03641	0.93254

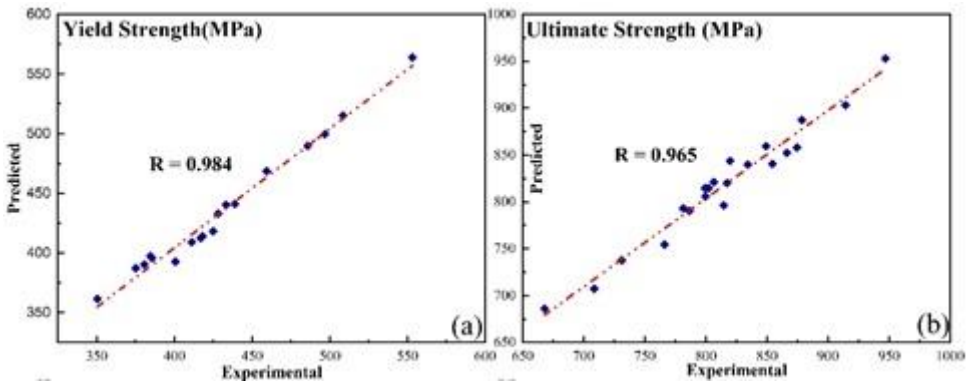

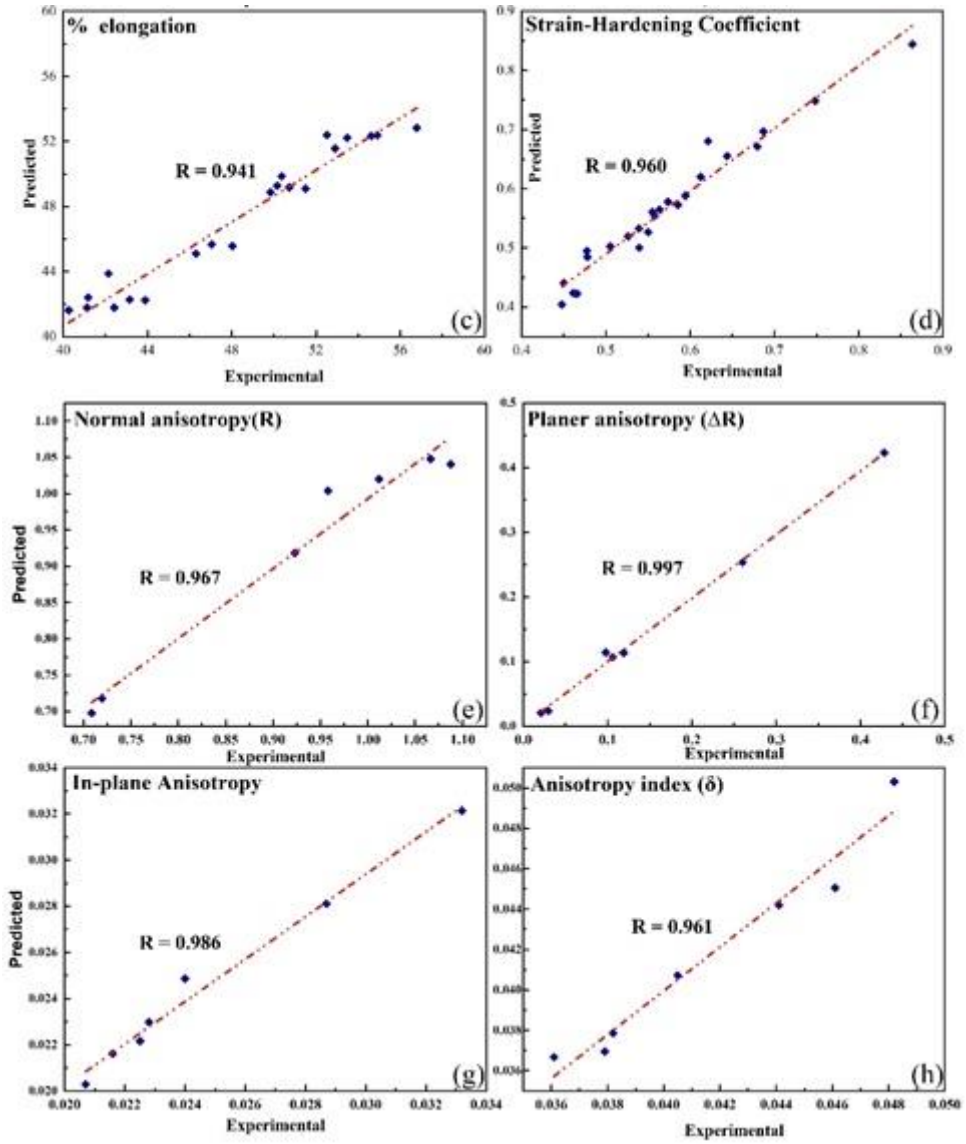

Figure 3.17: Correlation coefficient between the experimental & predicted values for testing data of (a)yield Strength (b) ultimate Strength (c)% elongation (d) strain hardening Coefficient (e) Normal Anisotropy (f) planer Anisotropy (g) In-plane Anisotropy (h) Anisotropy index.

Hardening models (namely Hollomon, Ludwik, Swift & Voce) are developed with the application of ANN with regression methods (namely multiple regression and logistic regression methods). Significant variables were constituted to predict the strain hardening behavior of Inconel alloy. Figure 3.18 gives the correlation coefficient for testing data of hardening models and results shows good correlation (> 97%).

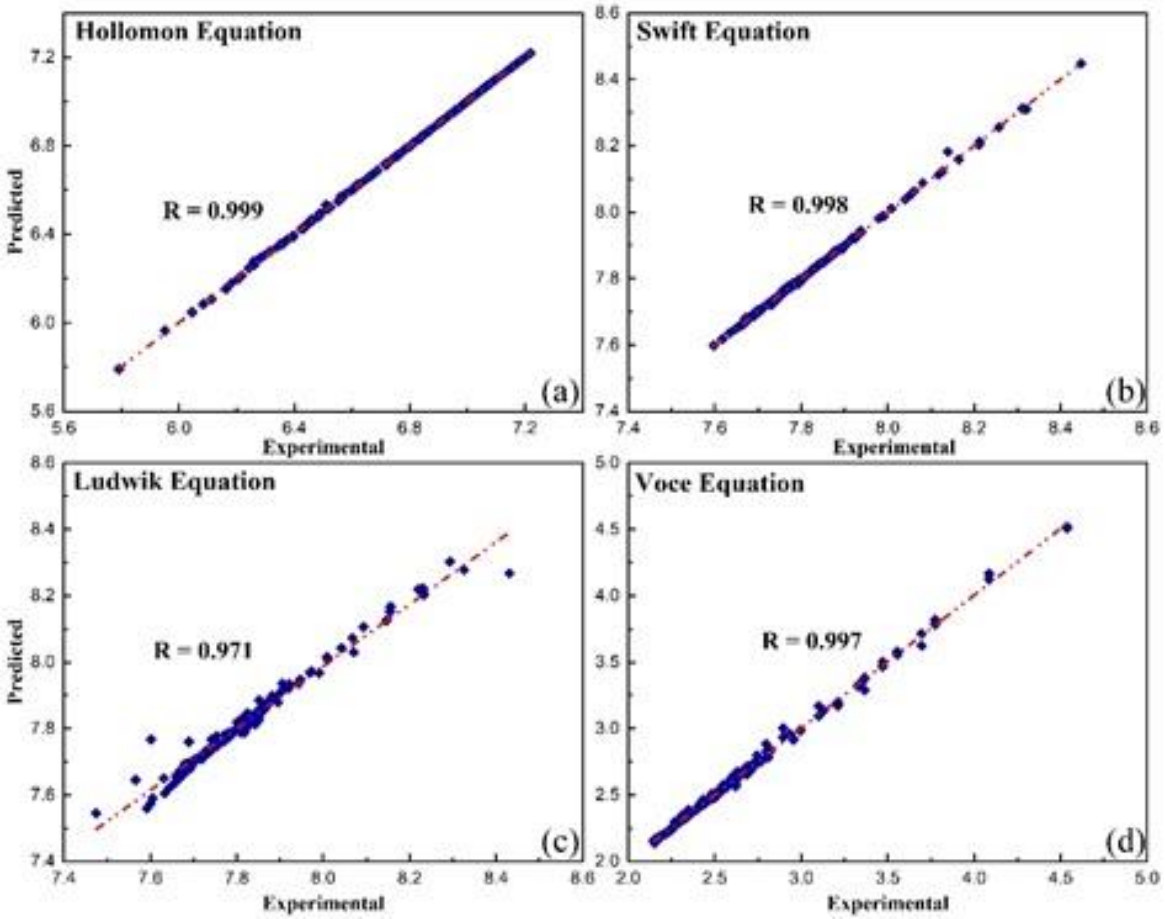

Figure 3.18: Correlation coefficient between the experimental & predicted values for testing data of hardening models

For comparing the exactness in a fit of the ANN model, some hypothesis tests, namely *t*-test (for test the means) and f-test (for variance), are done for the model construction process. Two sample t-test compare location parameters of two independent sample populations, i.e. paring of the samples from one to another. Two sample f-test is related to the test statistic (ratio of two sample variances) (Snedecor and Cochran 1989). In paired t-test, two-sample populations (observations in one sample & observations in the other sample) can be paired. F-test can be used only for equal variances of two populations (Snedecor and Cochran 1989). The p-values are obtained after performing the test. Rejection of null hypothesis will not be done if p-value lies above 0.05. These statistical tests are performed using MATLAB 2018a. The paired t-test piloted between experimental data and predicted data. Table 3.7 shows *p*-values for mean paired *t*-test and *F*-Test directed between two data (experimental and predicted) are above 0.05. For all material properties and hardening models, the p-values are observed greater than 0.05. Therefore, statistically ANN prediction has satisfied goodness of fit for modeling.

Table 3.7: Hypothesis testing to validate the ANN training

	***p*-values**	
	t-Test	*F*-Test
Material Properties		
σ_{ys}	0.8356	0.8388
σ_{uts}	0.9934	0.6235
% elongation	0.6541	0.6285
n	0.7498	0.6879
Anisotropic Properties		
$\bar{R}$	0.9591	0.9594
ΔR	0.9864	0.9707
A_{IP}	0.9354	0.8562
δ	0.9727	0.8126
Work Hardening Behavior		
Hollomon Eq.	0.9943	0.9839
Ludwik Eq.	0.9509	0.5637
Swift Eq.	0.9854	0.9945
Voce Eq.	0.9472	0.9825

3.4 Fractography Study of Post Tensile Test Samples

The fractured morphologies of fully deformed tensile test samples are examined using a scanning electron microscope (SEM) of Hitachi, S-3400N accelerating voltage 15 kV. The observed samples are sectioned parallel to the fracture surface, as shown in Figure 3.19. The fracture surfaces are observed with different magnifications to conclude macroscopic fracture mode and to concurrently characterize the intrinsic features on the tensile fracture surface during uniaxial tensile deformation. Factrography studies have been carried at Central Analytical Laboratory, Department of Chemistry, BITS Pilani, Hyderabad Campus, Hyderabad, India.

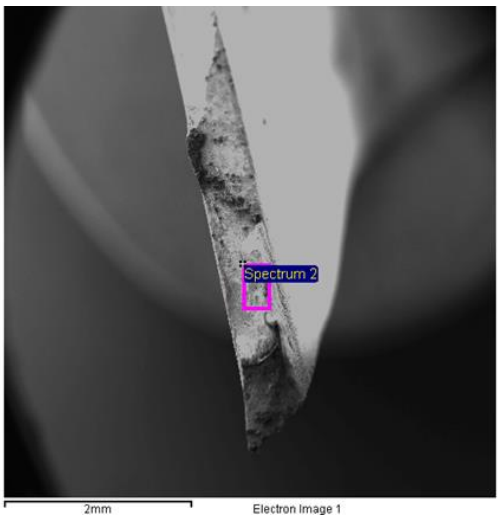

Figure 3.19 Fractography sample location of deformed test specimen

Figure 3.20 (a-j) shows the sectional fracture surface of the post-tensile specimen of Inconel 718 at different temperatures. The sectional fracture surface is covered with plenty of dimples-serpentine sliding characteristics appearing on dimple walls, flat regions, and tearing edges in Figure 3.20 (a-f). Formed carbides in Inconel 718 with dimples and tearing edges are observed in Figure 3.20 (g-j). These observations clearly indicate that the fracture mode of Inconel 718 alloy at various temperatures is a mixture of ductile and brittle trans-granular fracture with dimples seen on the main fracture feature. The size of the cell-like structure and dimple is fine in nature from RT to 400°C, while the dimple size appears to increase drastically at 700°C. Similarly, fracture surfaces show large numbers of voids at RT, which tends to decrease with increase in temperature. Nucleation and micro- voids growth are the main fracture phenomena observed in Inconel 718 alloy. At 600°C and 700°C, the number of micro-voids observed was minimal with the presence of NbC-carbides and oxides in large-sized dimples (Figure 3.20 g-j). The presence of carbide at 600°C and 700°C indicates that the precipitating phase of Inconel 718 alloy has started. Prasad et al. 2017, 2018b reported that the precipitation phase mainly includes body-centered tetragonal and FCC coherent precipitates of γ" (Ni_3Al) and γ' (Ni3Al), respectively. These distinct types of formed carbides also improve the creep strength of alloy at respective working temperatures. It is observed that grains in the center of specimen are heavily deformed and evidence of slip bands is found inside the grains, up to the temperature of 700°C (Figure 3.20 i-j). Slip bands are usually related to strain hardening phenomena, which are the main deformation mechanisms observed in the stress–strain curves at less temperature of 700°C (Figure 3.20 a-g). The observed serration flow phenomenon promotes the flow localization and reduces ductility, raising the deformation temperature (Lin et al. 2018).

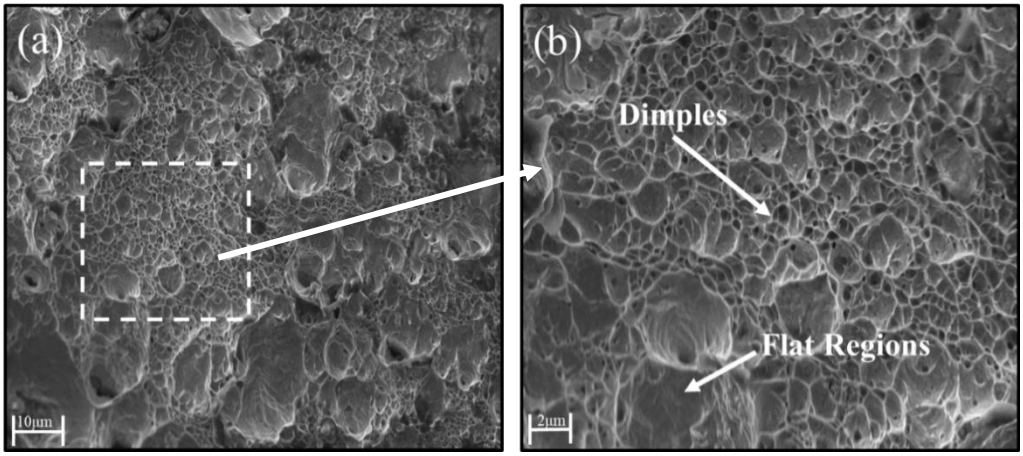

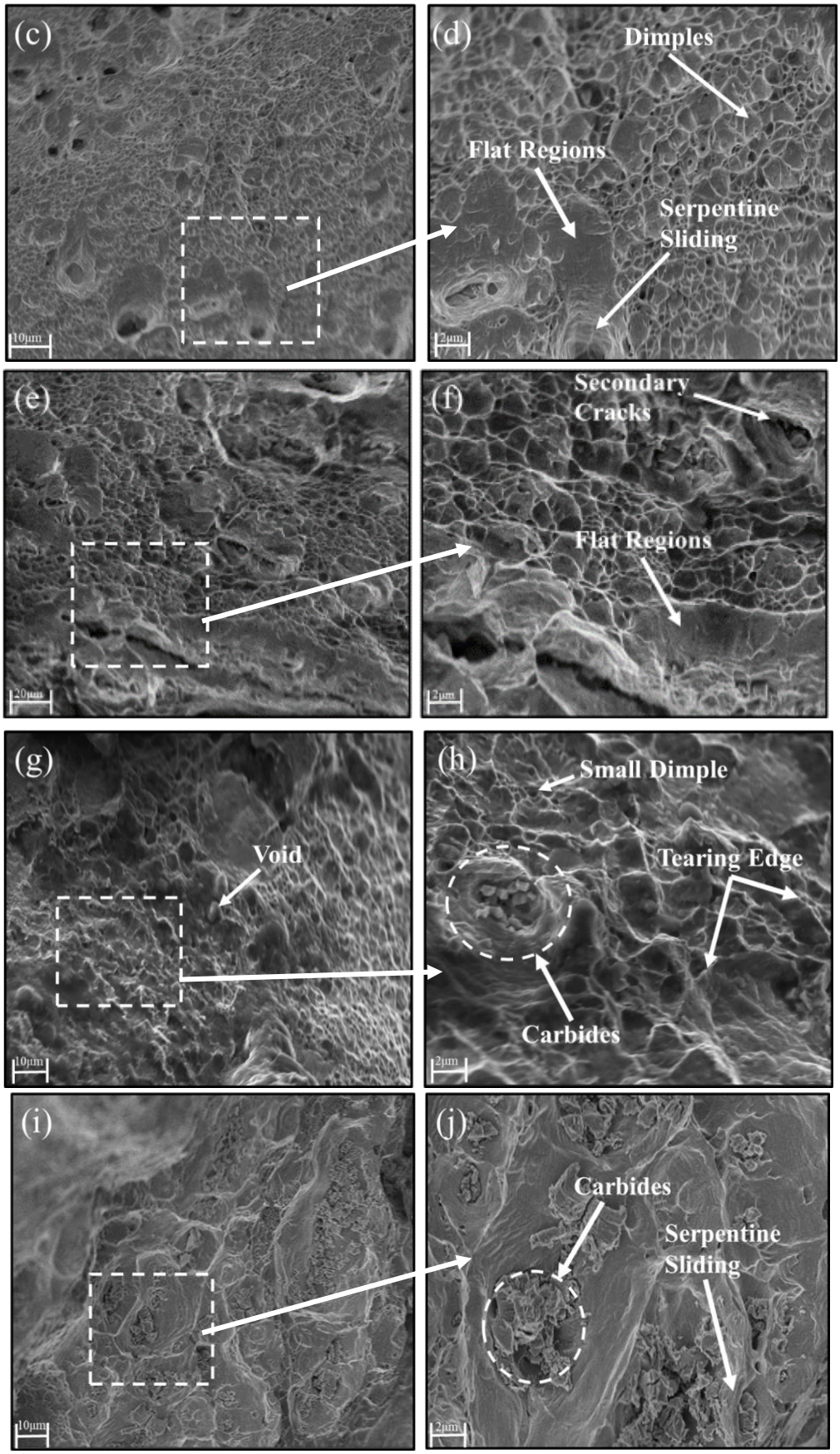

Figure 3.20 Fracture surface of Inconel 718 alloy at (a-b) RT, (c-d) 200°C, (e-f) 400°C, (g-h) 600°C, and (i-j) 700°C.

3.5 X-Ray diffraction Study of Post Tensile Test Samples

The XRD plots of Inconel 718 alloy at various temperatures are shown in Figure 3.21 at various temperatures. In Inconel 718 alloy, the peaks corresponding to (111), (200), (220), and (311) planes are observed. There exist overlapping peaks in a single peak observed in the 2θ range of 41°-45°, i.e., (111) peak of γ, (111) peak of Ni_3(Al,Ti)and (311) peak of γ". Similarly, overlapping occurs at (200) and (220), i.e., (200) of γ overlaps with (121) peak of Ni_3(Nb) phase, while (220) peak of γ overlaps with (132) peak of Ni_3Nb phase and (400) of γ" phase. It is observed that the presence of Ni-based γ phase corresponds to face-centered cubic (FCC) structure and the intermetallic phases such as NiCr, Ni_3Al and Ni_3Nb (γ" phase) (Christopher et al. 2011; Prasad et al. 2018b). A similar observation is reported by Prasad et al. 2017 that the precipitation phase mainly includes body-centered tetragonal and FCC coherent precipitates of γ" (Ni_3Al) and γ' (Ni_3Al), respectively. These different types of formed carbides also improve the creep strength of alloy at respective working temperatures.

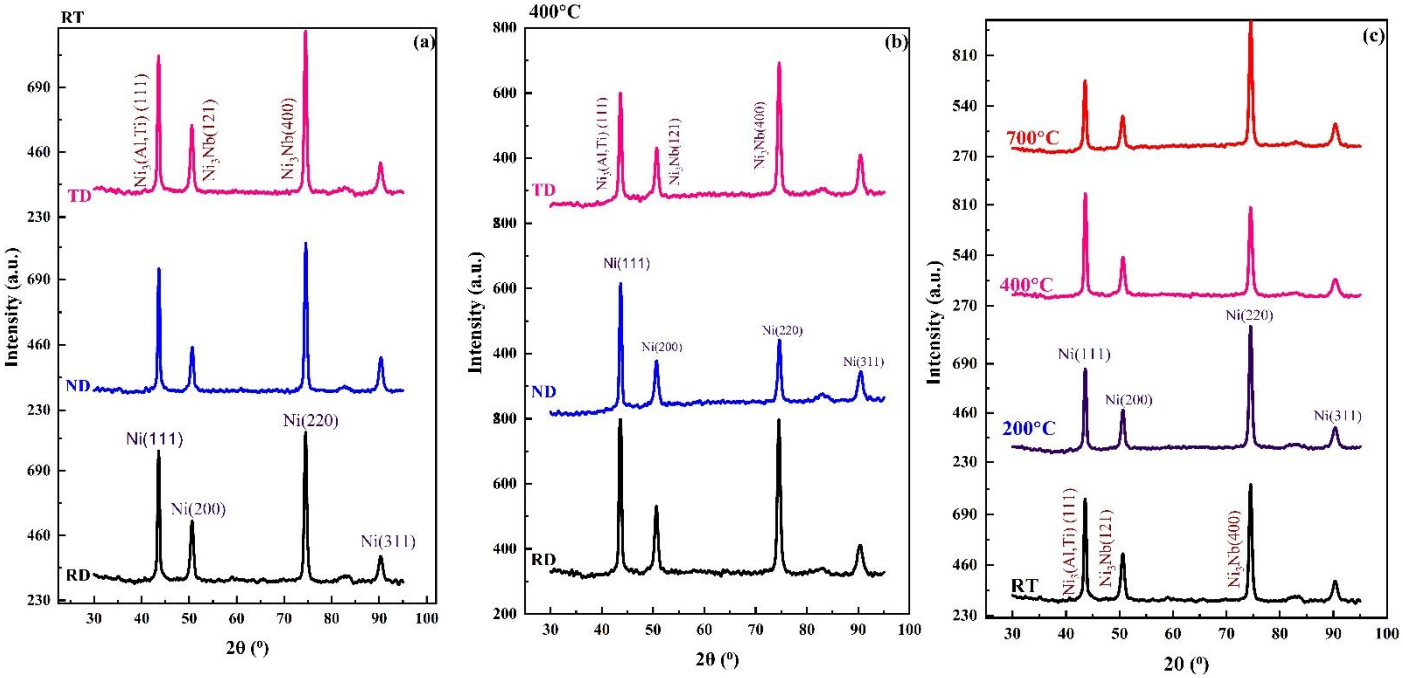

Figure 3.21 X-ray diffraction pattern for Inconel 718 alloy at (a) RT (b) 400°C, and (c) various temperature in rolling direction.

3.6 EBSD Study of Post Tensile Test Samples

Electron backscattered diffraction (EBSD) analysis has been studied using an orientation imaging microscopy (OIM) attachment to a field-emission scanning electron microscope (FE-SEM) operated at 20 kV. The specimen location is chosen near to the deformation zone, as shown in Figure 3.22. OIM facility for EBSD studies was availed at the

Department of Metallurgical Engineering and Material Science, Indian Institute of Technology Bombay, India.

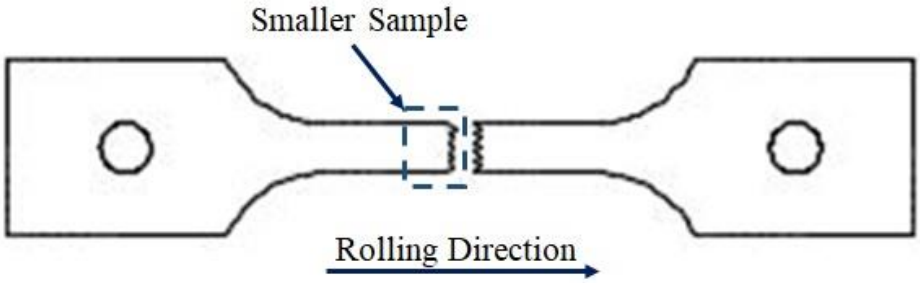

Figure 3.22 EBSD sample location of deformed test specimen

EBSD studies were carried out to understand the influence of temperature on microstructural evolution during dynamic recrystallization. The OIM and corresponding misorientation angle distribution of Inconel 718 alloy subjected to tensile testing at RT, 400°C, 600°C, and 700°C are shown in Figure 3.23(a-h). The grain size of tensile-tested samples at RT, 400°C, 600°C and 700°C samples are ~ 12.12, 12.08, 12.09 and 10.87 µm, respectively. It is interesting to observe that grain coarsening has not occurred in Inconel 718 alloy, mainly due to the pinning effect by the presence of intermetallic phases at the grain boundaries. This infers that in case of Inconel 718 alloy, the dynamic recrystallization mechanism seems to start at relatively lower testing temperature, and the effect is more pronounced at a higher testing temperature. Generation of substructures during DRX is a thermally activated process and is enhanced at higher testing temperatures (Nayan et al. 2015). This contributes to an increase in the frequency of DRX grains, leading to a significant increase in the average misorientation angle from ~ 14 to 28°. However, DRX seems to dominate at all the testing temperatures, and the formation of these grains leads to dynamic softening and a substantial decrease in the tensile strength.

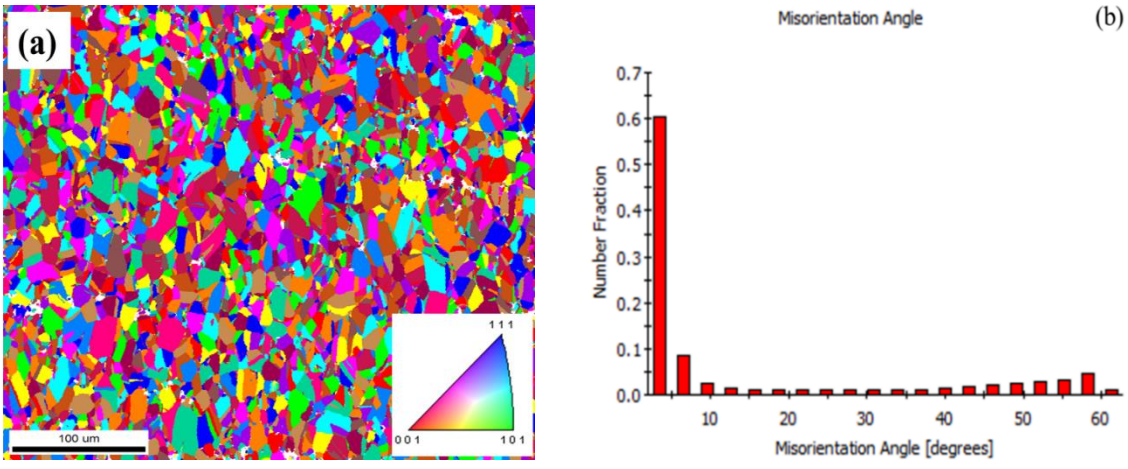

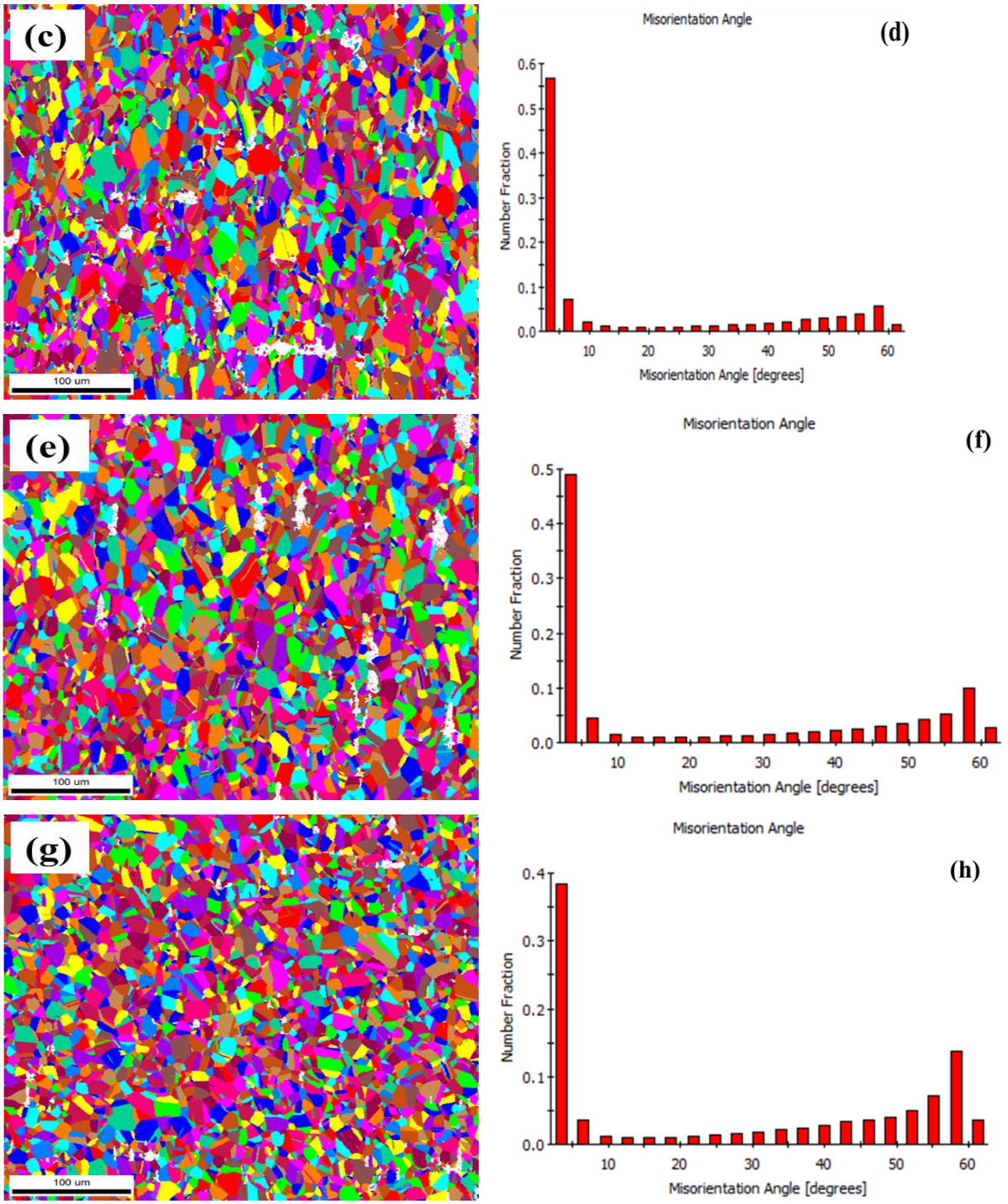

Figure 3.23 Orientation imaging micrograph and misorientation angle distribution at different temperatures (a-b) RT (c-d) 400°C (e-f) 600°C (g-h) 700°C.

Summary

This chapter discussed the experimental investigations about uniaxial tensile flow behavior at different temperatures and strain rates. The flow stress and strain hardening behaviors are affected by strain rates and test temperatures in Inconel alloy. The DSA phenomena is reported from 400°C-700°C at all the strain rate conditions. Mainly, *B* and

combination of *A* + *B* type of serrations are observed at different temperatures and strain rates. The two-stage hardening behavior has been noticed and predicted well with Hollomon and Voce empirical equations. Further, the factographs revealed a ductile-brittle kind of fracture. From EBSD study, dynamic recrystallization mechanism seems to start at lower testing temperatures, i.e., 300°C and the effect is more pronounced at higher temperatures. Furthermore, ANN model is used to predict the mechanical properties, anisotropic parameters and work hardening behavior of Inconel 718 alloy.

These outcomes will help to build uniaxial constitutive models and anisotropic yield criteria. These findings can also be useful during finite element simulations of the stretch forming process.

4. Formulation of Material Models for Numerical Analysis

An accurate and trustworthy numerical analysis is essential to predict the deformation and forming behavior of a material. It helps to reduce the tedious experimental work, unnecessary tryouts, and wastage of materials. The reliability of advanced numerical analysis, including FE analysis, depends on an appropriate selection of material models and material properties. Material models comprise various constitutive models and anisotropic yield functions. The present chapter deals with the formation of different constitutive and anisotropic yield models for Inconel 78 alloy at different temperature and strain rates.

4.1 Uniaxial Constitutive Models

Material deformation mechanism under thermal processing is characterized by a constitutive model, which relates the effective flow stress to strain, strain rate, and temperature. These mathematical governing equations are calculated by a set of experimental outcomes in the plastic deformation domain.

In the present study, phenomenological based constitutive models, namely; modified Cowper–Symonds (m-CS), modified Johnson-Cook (mJC), Khan–Huang–Liang (KHL), physical-based constitutive model namely modified Zerilli and Armstrong (m-ZA), and integrated JC-ZA model have been developed to predicate the flow behavior of Inconel 718 alloy at elevated temperatures and mentioned in Figure 4.1.

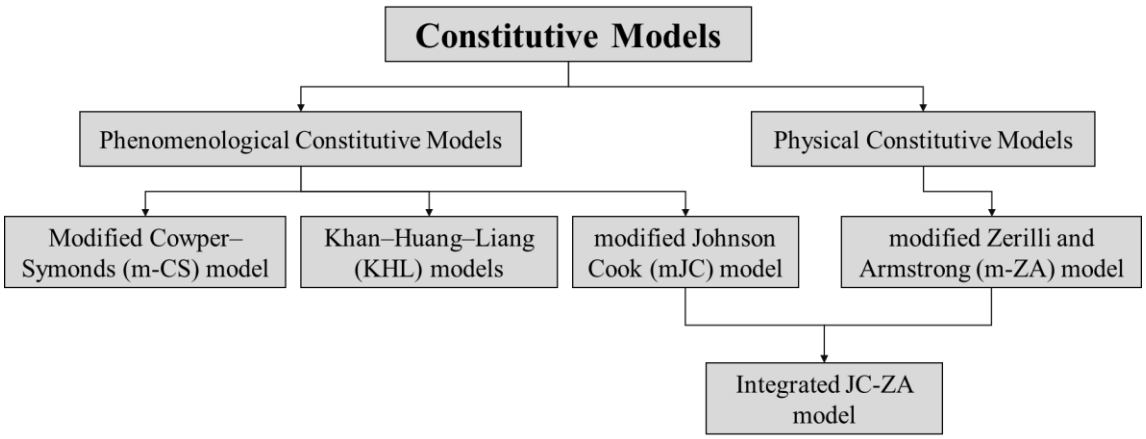

Figure 4.1: Considered constitutive model for flow stress prediction

4.1.1 Modified Cowper Symonds (m-CS) model

Cowper and Symonds (CS) developed a model to describe true stress in terms of uniaxial effective plastic strain (ε) and strain rate ($\dot{\varepsilon}$) (Alves 2000). Thus, this model describes

the influence of strain rate sensitivity and strain hardening. The flow stress for the isothermal condition in the CS model is formulated as

$$\sigma_y(\varepsilon,\dot{\varepsilon}) = K\left[\varepsilon + \left(\frac{E}{K}\right)^{\frac{1}{(n-1)}}\right]^n\left[1+\left(\frac{\dot{\varepsilon}}{C}\right)^{\frac{1}{p}}\right] \quad (4.1)$$

Where, σ is flow stress in high-velocity testing condition, strain sensitive parameters (C & p) and hardening parameters (K & n) are evaluated by fitting stress-strain data (between yield strength and ultimate strength) at different strain rates (Panicker et al. 2015; Tian et al. 2014). The CS model initially defines a direct correlation between quasi-static deformation and high-velocity deformation. However, the effect of strain rate is simply considered as a strain rate function, which is not appropriate to reflect the constitutive correlation of Inconel 718 alloy. Therefore, the effect of strain and strain rate are combined in modified CS (m-CS) (Tian et al. 2014) as,

$$\sigma_y(\varepsilon,\dot{\varepsilon}) = \sigma_y^s(\varepsilon)\left[1+\left(\frac{\dot{\varepsilon}}{C}\right)^{\frac{1}{p}}\right]\times f(\varepsilon) \quad (4.2)$$

Where, $f(\varepsilon)$ reflects the effect on strain rate sensitivity by strain and $\frac{\sigma_y(\varepsilon,\dot{\varepsilon})}{\sigma_y^s(\varepsilon)}$ defines coefficient of strain rate. The following steps are followed to calculate the material constants:

Step I:

A relationship between ε and σ_y/σ_y^s is obtained, where a linear relationship, between the coefficient of strain rate $\frac{\sigma_y(\varepsilon,\dot{\varepsilon})}{\sigma_y^s(\varepsilon)}$ and strain rate, is observed. As, at early stage of deformation, the strain rate coefficient gives a positive linear relationship with strain (Figure 3.5). After the strain value of 0.15, it decreases with the strain.

Step II:

The function $f(\varepsilon)$ defines the influence of strain on strain rate coefficient, which can be further expressed as $f(\varepsilon) = a.\exp(b.\varepsilon) + c.\exp(d.\varepsilon)$. Here a, b, c and d are constant to define an exact description of linear relationship. The calculated material constants are listed in Table 4.1. The equation for m-CS model for Inconel 718 alloy is,

$$\sigma = (430.06 + 3.2325\times10^3.\varepsilon^{0.9936})(1+0.0078\ln\frac{\dot{\varepsilon}}{0.01})[1-\frac{T-25}{1302}]^{1.6221} \quad (4.3)$$

Table 4.1 Material constants for *m-CS* constitutive model

Temperature (°C)	K(MPa)	*n*	*C*	P	R-square
RT	438.69	0.435	6.21	7.02	0.991
100°C	402.58	0.379	7.52	9.653	0.983
200°C	395.29	0.375	9.39	14.20	0.969
300°C	365.96	0. 367	9.66	15.65	0.948
400°C	325.18	0.264	10.93	16.14	0.940
500°C	321.54	0.152	13.52	11.55	0.926
600°C	308.06	0.157	15.56	8.097	0.923
700°C	292.63	0.255	16.35	9.577	0.945

4.1.2 Modified Johnson Cook (m-JC) Model

Original Johnson-Cook model reflects only the individual effect of processing parameters, but it fails to define the material properties at high strain rates and elevated temperatures (Lin and Chen 2010; Samantaray, Mandal, and Bhaduri 2009). A modification has been proposed in the original model to resolve this problem, in which strain, temperature, and strain rate couple effects are considered. Mathematical expression for the m-JC model is,

$$\sigma = (A_1 + B_1\varepsilon + B_2\varepsilon^2)\left(1 + C_1 \ln\frac{\dot{\varepsilon}}{\dot{\varepsilon}_{ref}}\right)\exp[(\lambda_1 + \lambda_2 \ln\frac{\dot{\varepsilon}}{\dot{\varepsilon}_{ref}})(T - T_{ref})] \quad (4.4)$$

where A_1, B_1, B_2, C_1, λ_1, λ_2 are material constants. The m-JC model captures the coupled effect of strain rate & temperature, and strain & temperature, which is not captured by the original JC model. The following steps are followed to calculate the material constants:

Step I:

At reference temperature (25ºC) and reference strain rate ($0.001s^{-1}$), Equation 4.4 is reduced to:

$$\sigma = (A_1 + B_1\varepsilon + B_2\varepsilon^2)$$

The values of A_1, B_1 and B_2 are calculated from σ vs ε plot and summarized in Table 4.2

Step II:

At reference temperature (25ºC), Equation 4.4 is reduced to:

$$\frac{\sigma}{(A_1 + B_1\varepsilon + B_2\varepsilon^2)} = \left(1 + C_1 \ln \frac{\dot{\varepsilon}}{\dot{\varepsilon}_{ref}}\right)$$

The value of C_1 is obtained by $\frac{\sigma}{(A_1+B_1\varepsilon+B_2\varepsilon^2)}$ vs $\ln\frac{\dot{\varepsilon}}{\dot{\varepsilon}_{ref}}$ plot.

Step III:

After rearranging the terms and considering the natural logarithm on both sides of Equation 4.4, the equation reduce to

$$\ln\left\{\frac{\sigma}{(A_1 + B_1\varepsilon + B_2\varepsilon^2)\left(1 + C_1 \ln \frac{\dot{\varepsilon}}{\dot{\varepsilon}_{ref}}\right)}\right\} = \left(\lambda_1 + \lambda_2 \ln \frac{\dot{\varepsilon}}{\dot{\varepsilon}_{ref}}\right)(T - T_{ref})$$

In complete strain range, linear fitting gives three different values λ corresponds to specific strain rate. The values of λ_1 and λ_2 are estimated from $\left(\lambda_1 + \lambda_2 \ln \frac{\dot{\varepsilon}}{\dot{\varepsilon}_{ref}}\right)$ vs $\ln\left(\frac{\dot{\varepsilon}}{\dot{\varepsilon}_{ref}}\right)$ plot. Thus, all of the material constants of the m-JC model were calculated and listed Table 4.2. The equation for m-JC model for Inconel 718 alloy is,

$$\sigma = (444.95 + 3180.3\varepsilon - 187.29_2\varepsilon^2)\left(1 + 0.0036 \ln \frac{\dot{\varepsilon}}{0.01}\right)\exp[(-0.0002 + 0.0013 \times \ln \frac{\dot{\varepsilon}}{(0.01)})(T - 25)] \quad (4.5)$$

Table 4.2 Material constants for m-JC constitutive model

A_1(MPa)	B_1(MPa)	B_2 (MPa)	C_1	λ_1	λ_2
444.95	3180.3	-187.29	0.0036	-0.0002	0.0013

4.1.3 Modified Zerilli–Armstrong (m-ZA) model

Zerilli and Armstrong (Tari and Worswick 2015; Tian et al. 2014) suggested a constitutive equation based on thermal activation by dislocation. The modified Zerilli–Armstrong (m-ZA) (Samantaray et al. 2009) proposed as,

$$\sigma = (C_1 + C_2\varepsilon^n)\exp\{(-C_3 + C_4\varepsilon)(T - T_{ref}) + [C_5 + C_6(T - T_{ref}) \ln\left(\frac{\dot{\varepsilon}}{\dot{\varepsilon}_{ref}}\right)]\} \quad (4.6)$$

where, C_1 is the yield strength of Inconel 718 alloy at reference strain rate ($\dot{\varepsilon}_{ref}$ = 0.01 s^{-1}) and room temperature, C_2 is the strain hardening coefficient, *n*, C_3, C_4, C_5, C_6 are material constants that incorporates the influence of temperature, coupled effect of temperature and strain, the effect of strain rate & coupled effect of strain rate and temperature respectively. The following steps are followed to calculate the material constants:

Step I:

At reference strain rate ($\dot{\varepsilon}_{ref}$ = 0.01 s^{-1}), considering the natural logarithm on both sides on Equation 4.6, the equation reduce to:

$$\ln\sigma = \ln[(C_1 + C_2\varepsilon^n)(-C_3 + C_4\varepsilon)]\left(T - T_{ref}\right)$$

From σ vs $\left(T - T_{ref}\right)$ plot, intercept ($I = C_1 + C_2\varepsilon^n$) and slope ($-C_3 + C_4\varepsilon$) gives the values of $C_{1\text{-}4}$. At each plastic strain, a particular value of slope and intercept was obtained. For $C_{1\text{-}2}$, taking the exponential and then logarithm on intercept, the equation was transformed to

$$\ln(\exp(I) - C_1) = \ln(C_2) + nln(\varepsilon)$$

Similarly, from ($-C_3 + C_4\varepsilon$) vs ε plot, $C_{3\text{-}4}$ are obtained and mentioned in Table 4.3. A smaller value of C_3 and C_4 indicates lesser effect of temperature on flow behavior and strain rate sensitivity on Inconel 718 alloy

Step II:

For coupled effect, taking the natural logarithm on Equation 4.6, the equation was transformed to:

$$\ln\sigma = \ln(C_1 + C_2\varepsilon^n) + (-C_3 + C_4\varepsilon)(T - T_{ref}) + \left[C_5 + C_6(T - T_{ref})\ln\left(\frac{\dot{\varepsilon}}{\dot{\varepsilon}_{ref}}\right)\right]$$

From the plot of ln σ vs. ln $\left(\frac{\dot{\varepsilon}}{\dot{\varepsilon}_{ref}}\right)$, slope $C_5 + C_6(T - T_{ref})$ for a particular strain gives the value of $C_{5\text{-}6}$. The material constants (Table 4.3) are calculated using above procedure. Equation 4.12 for m-ZA is given as,

$$\sigma = (260 + 1452.5\varepsilon^{0.884})\exp\left(-(7.7465 * 10^{-4} - 7.533 * 10^{-4}\varepsilon)\ (T - 298)\right.$$
$$\left. + (0.0173 - 6.8605 * 10^{-5}(T - 298)\ln\left(\frac{\dot{\varepsilon}}{0.01}\right)\right) \quad (4.7)$$

Table 4.3 Material constants for m-ZA constitutive model

C_1(MPa)	C_2(MPa)	C_3	C_4	C_5	C_6	n
260	1452.5	7.7465e(-4)	-7.533e(-4)	0.0173	-6.8605e(-5)	0.884

4.1.4 Khan–Huang–Liang (KHL) model

For KHL model, equivalent flow stress is given as (Khan, Yu, and Liu 2012),

$$\sigma = \left[A + B\left(1 - \frac{\ln\dot{\varepsilon}}{D_p{}^0}\right)^{n1}\varepsilon_p^{n_o}\right]\left(\frac{\dot{\varepsilon}}{\dot{\varepsilon}^*}\right)^C\left(\frac{T_m - T}{T_m - T_{ref}}\right)^m \quad (4.8)$$

where, σ & ε_p true (Cauchy) stress and true plastic strain. T , T_{ref} & Tm are current, reference (25ºC) and melting (1330 ºC) temperature of Inconel 718 respectively. D_P^o=10^{-6} s^{-1}, is called as deformation rate (subjectively chosen upper bound strain rate) and $\dot{\varepsilon}$* =0.01 s^{-1} (reference strain rate, at a reference temperature of T_{ref} (RT), at which material constants A, B and n_0 are calculated). n_0, n_1, C and m are additional material constants. The following steps are followed to calculate the material constants:

Step I:

At reference temperature (25ºC) and reference strain rate $\dot{\varepsilon}$* =0.01 s^{-1}, the flow stress

Equation 4.8, after applying logarithm on both sides, can be written as

$$\ln(\sigma - A) = n_o \ln\varepsilon + \ln(B)$$

Using true stress-strain data at reference temperature and reference strain rate, A, B and n_o are obtained.

Step II:

The strain at the yield point is small. At reference temperature, Equation 4.8, after applying logarithm on both sides, can be written as

$$\ln \sigma_y = \ln A + C \ln(\dot{\varepsilon})$$

Slope of vs $\dot{\varepsilon}$, gives the value of C.

Step III:

At reference temperature material constant n_1 and m are expressed as

$$n_1 = \frac{ln\left(\frac{e^{\left(\frac{\sigma}{Cln\dot{\varepsilon}}\right)}-A}{Be^{n_o}}\right)}{ln\left(1-\frac{ln\dot{\varepsilon}}{lnD_P^o}\right)} \text{ and } m = \frac{\ln\left(1-\frac{\sigma}{K}\right)}{\ln\left(\frac{T-T_{ref}}{T_m-T_{ref}}\right)}$$

where, $K = \left[A + B\left(1 - \frac{\ln\dot{\varepsilon}}{D_p{}^0}\right)^{n_1} \varepsilon_p^{n_0}\right]\left(\frac{\dot{\varepsilon}}{\dot{\varepsilon}^*}\right)^C$

The values of n_1 and m are calculated for different strain rates and temperatures and average values of n_1 and m obtained. The material constant calculated for Inconel 718 alloy and mentioned in Table 4.4.

Table 4.4 Material constants for KHL model

A (MPa)	B (MPa)	n_0	C	n_1	m
828.9	580.06	0.62	1.3417	0.0135	1.385

The Equation for KHL is given by

$$\sigma = \left[828.9 \times 10^6 + 580.06 \times 10^6 \left(1 - \frac{ln\,\dot{\varepsilon}}{lnD_p^0}\right)^{0.0135} \varepsilon_p^{0.62}\right] \left(\frac{\dot{\varepsilon}}{\dot{\varepsilon}^*}\right)^{1.3417} \left(\frac{T_m - T}{T_m - T_{ref}}\right)^{1.385} \quad (4.9)$$

4.1.5 Integrated Johnson Cook and Zerilli–Armstrong (JC-ZA) model

Nadai (Che et al. 2018) first proposed an integrated JC-ZA model combining strain hardening term from JC model and strain rate & temperature coupled term from ZA model to take advantage of both models. The integrated JC-ZA model is mathematically expressed as

$$\sigma = (A + B\varepsilon^n)\left(-C_3 T + C_4 T \ln\frac{\dot{\varepsilon}}{\dot{\varepsilon}_{ref}}\right) \quad (4.10)$$

where, A, B, C_3, C_4 and *n*, are material constants, $\dot{\varepsilon}_{ref}$=0.01 s^{-1} considered. Considering the effect of plastic deformation energy, Equation 4.10 can be modified as (Lin and Chen 2010),

$$\sigma = (A + B\varepsilon^n)\left[C_3(T + \Delta T) + C_4(T + \Delta T)\ln\left(\frac{\dot{\varepsilon}}{\dot{\varepsilon}_{ref}}\right)\right] \quad (4.11)$$

where, ΔT is measured as an averaged rise in temperature due to deformation heat to overcome the substantial plastic work (Lin and Chen 2010). Further, a new integrated model is proposed by Che et al. 2018, considering first term consist of Hall–Petch relation (effect of grain size on σ_y and combined effect of strain rate & strain) and second term of m-ZA (combined effect of strain & temperature and of temperature & strain rate), mathematically expressed as

$$\sigma = \left(\left(a + \frac{k}{\sqrt{d}}\right) + B\left(1 - \frac{\ln\dot{\varepsilon}}{\ln D_0}\right)^{n_2} \varepsilon^{n_1}\right) \exp\{-(C_3 + C_4\,\varepsilon)(T - T_{ref}) + C_5 + C_6(T - T_{ref}) \ln\left(\frac{\dot{\varepsilon}}{\dot{\varepsilon}_{ref}}\right)\} \quad (4.12)$$

where, $\left(a + \frac{k}{\sqrt{d}}\right)$ is Hall–Petch relation, Where d is the grain size and a is the corresponding stress for large single crystals or very large grained material (we refer to it here as the yield stress), and k is material constant. D_0 is a deformation rate (arbitrarily selected as 10^6 upper bound strain rate), n_2, n_1, C_3, C_4, C_5 and C_6 have the same definition as the original m-JC and m-ZA model. This new integrated model increases the accuracy, as it considers the effect of grain size, strain rate, strain hardening, thermal softening and combined effects of strain, strain rate & temperature. The material constants are calculated by a similar procedure of m-JC and ZA and listed in (Table 4.5). The equation for JC-ZA is given as

$$\sigma = (260 + 1452.5\varepsilon^{0.884})\ \exp\ (-(7.7465 \times 10^{-4} - 7.533 \times 10^{-4}\varepsilon)(T - 25) + \left(0.0173 - 6.8605 \times 10^{-5}(T - 25)\ln\left(\frac{\dot{\varepsilon}}{0.01}\right)\right) \quad (4.13)$$

Table 4.5 Material constants for integrated JC-ZA constitutive model

a(MPa)	k(MPa)	B	n_1	n_2
536.06	901	1980	-1.1764	0.0884
C_3	C_4	C_5	C_6	
7.7465×10^{-4}	7.533×10^{-4}	0.0173	6.8605×10^{-5}	

4.1.6 Comparison of constitutive models

The capability of m-CS, m-JC, m-ZA, KHL and JC-ZA models has been evaluated by comparing the predicted flow stress with experimental data. Figure 4.2(a-e) represents comparative flow stress behavior at different temperatures and strain rates for the m-CS, m-JC, m-ZA, KHL and JC-ZA model, respectively. Figure 4.2 (a) indicates a linear relationship between the coefficient of strain rate ($\frac{\sigma_y(\varepsilon,\dot{\varepsilon})}{\sigma_y^s(\varepsilon)}$) with strain at test temperature. But it is observed that, there are some nonconformities between experimentally measured and predicted values of flow stress at lowest strain rate of 0.0001 s^{-1} for m-CS model. In the case of the m-JC model (Figure 4.2(b)), the prediction is better than the m-CS model except at RT condition. Whereas the KHL model shows an extremely poor relationship with predicted results Figure 4.2(c). Subsequently, m-ZA and JC-ZA models show a good correlation between predicted and experimentally measured flow stresses Figure 4.2(d-e).

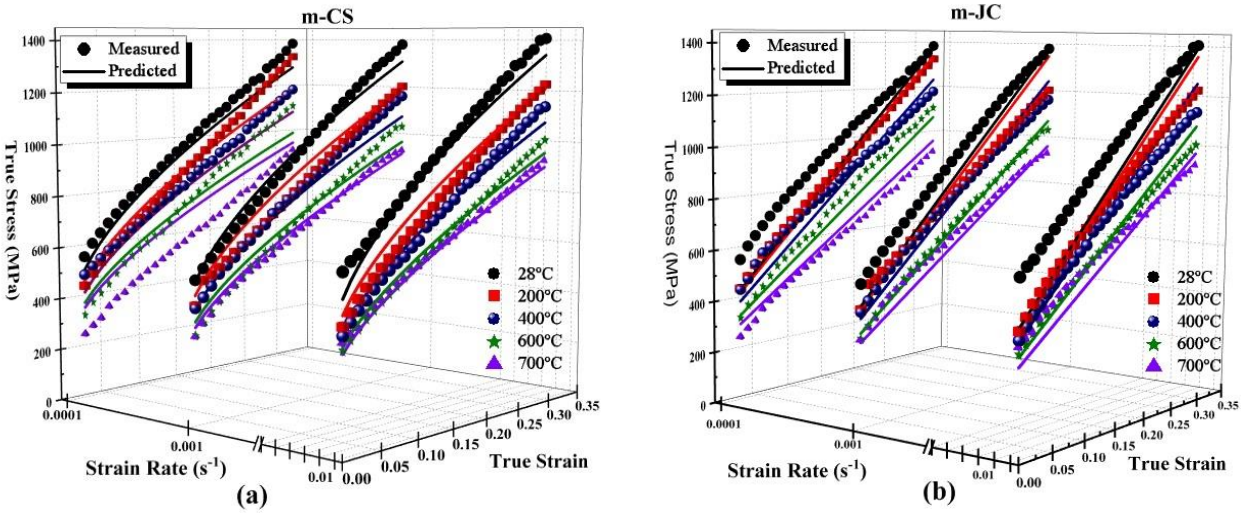

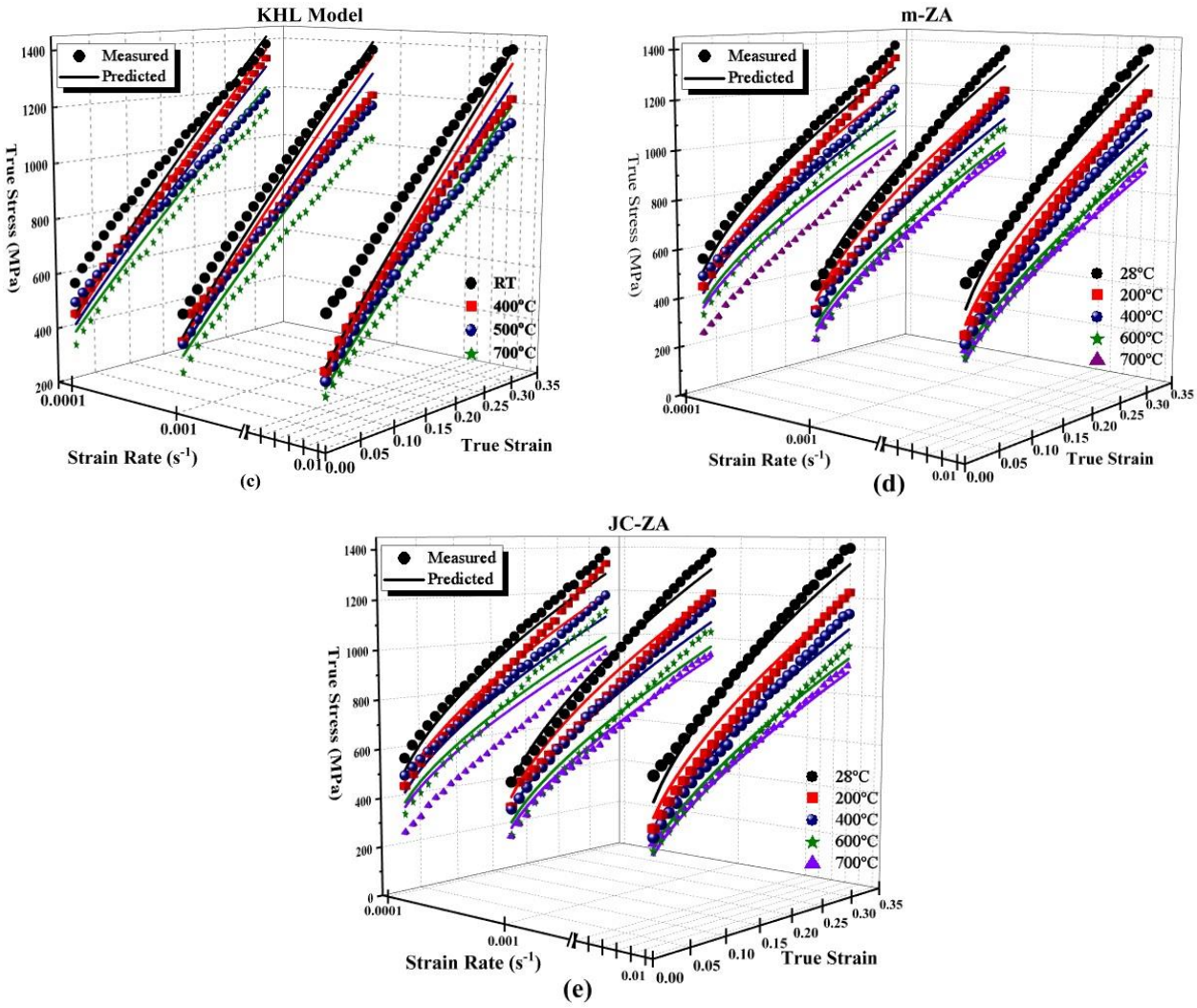

Figure 4.2 Plot showing comparison between experimentally measured and predicted flow stress for strain rates: 0.01 s^{-1}, 0.001 s^{-1} and 0.0001 s^{-1} by (a) m-CS model (b) m-JC model (c) KHL model (d) m-ZA model and (e) JC-ZA model.

The suitability of constitutive models has been compared by various statistical parameters like correlation coefficient (R). Table 4.6 provides a comparison of statistical parameters for all considered models. It is found from Table 4.6 and Figure 4.3 that m-CS model and KHL model show poor correlation coefficient (R = 0.9324 and R = 0.9182) among all other models. All other models show a better and comparable correlation coefficient, as R value is above 0.96. Since the correlation coefficient is a biased parameter and value may be biased towards higher or lower values (Chen et al. 2015; Lin and Chen 2010; Samantaray, Mandal, and Bhaduri 2009), other statistical parameters such as average absolute error (Δ) and its standard deviation (s) are considered for comparison. Table 4.6 gives average values of average absolute error (Δ) and its standard deviation (s) for all the models. It can be observed that absolute error value and its standard deviation for the integrated JC-ZA model are less,

compared to other models. The highest error value is found for the KHL model of 13.47%. Based on all the statistical parameters comparison, the JC-ZA model shows the highest correlation with the least average absolute error and standard deviation than other models.

Table 4.6 Comparison between m-CS, m-JC, KHL, m-ZA and integrated JC-ZA model

Comparative Parameters	***m-CS***	***m-JC***	***m-ZA***	***KHL***	***JC-ZA***
R	0.9324	0.9637	0.9641	0.9182	0.9873
***Δ* (%)**	7.53	8.46	11.19	13.47	2.44
***s* (%)**	13.32	5.49	5.48	10.64	4.08

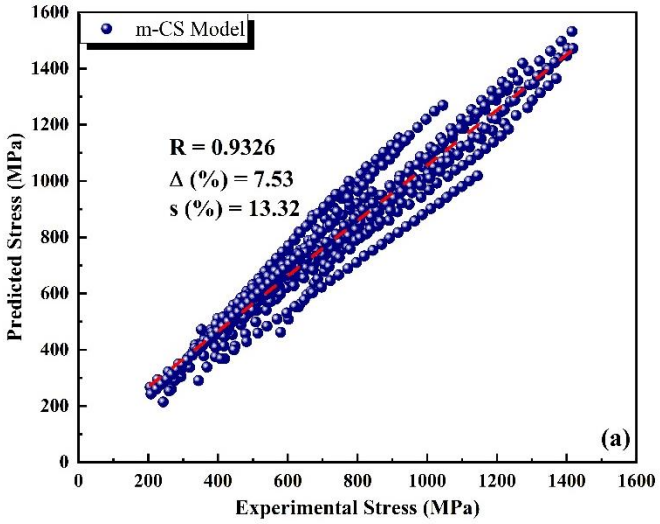

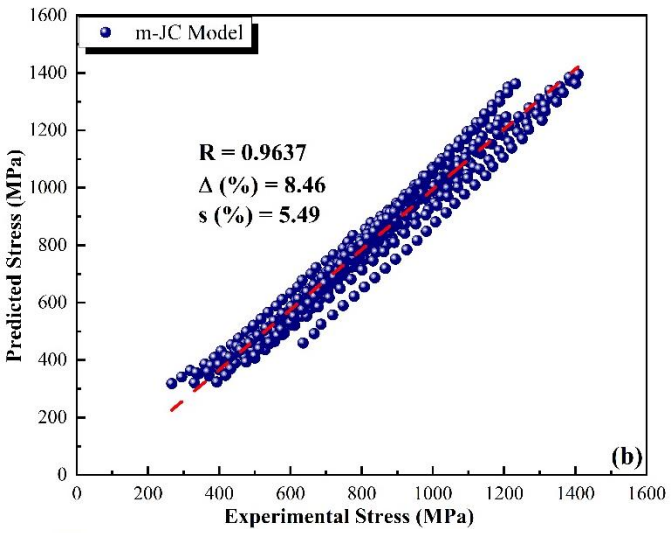

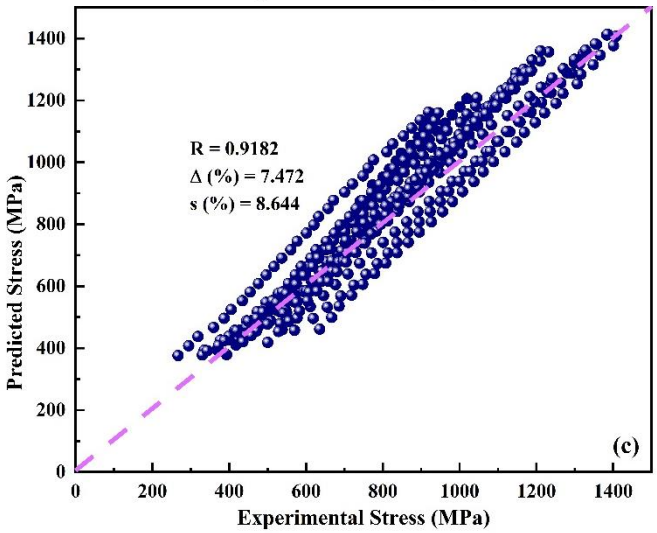

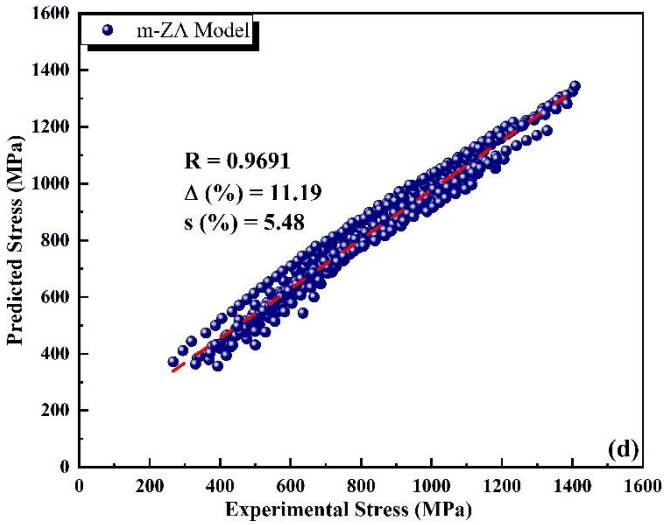

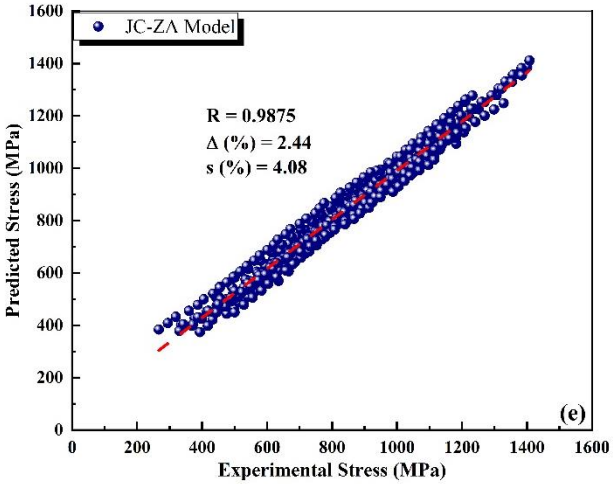

Figure 4.3 Correlation coefficient between the experimental and predicted stress values for (a) m-CS, (b) mJC, (c) KHL (d) mZA and (e) JC-ZA

The above comparative discussion is based on average absolute error (Δ) and its standard deviation (s). Since, m-JC is a phenomenological based model, i.e., the model does not consider the physical aspects of materials like dislocation movement, kinetics of slips and various thermodynamic aspects while predicting the flow stress. Whereas m-ZA is a physical based model. Thus, the m-ZA model is considered over m-JC model for flow stress prediction. Furthermore, the integrated JC-ZA model shows the least error values. The integrated JC-ZA model considers the strain hardening with Hall–Petch relation to describe the flow stresses at equivalent strain value. Moreover, the concept of thermal softening along with the effect of grain size, is accountable for the thermal activation energy along with mobile dislocation interactions mechanisms at higher strain. Therefore, the integrated JC-ZA model is best suitable for flow stress prediction of Inconel 718 alloy over the wide range of temperatures, strain, and strain rates.

4.2 Anisotropic Yield Criteria

Yield criterion is a hypothesis defining the elasticity limit in a material and onset of plastic deformation for any stress combination. The yield strength is often used to determine the maximum allowable load in a mechanical component, since it represents the upper limit to forces that can be applied without producing permanent deformation. In the SMF experiment, plane stress condition ($\sigma_3 = 0$) is assumed. It is well-known that traditional von Mises or Tresca yield criteria are inadequate to describe the plastic behavior of sheet metal due to significant anisotropy tendency. In the past, several efforts have been made for the development of anisotropic yield criteria which consider plastic anisotropy (Barlat and Lian 1989). In the present study, the yielding behavior of Inconel 718 alloy has been predicted based on various

anisotropic yield criteria namely; Hill'48-r, Hill'48-σ, and Barlat'89 yield criteria at all test temperatures.

4.2.1 Hill 1948 Yield Criterion

Hill (Hill 1990) proposed an extension of von-Mises yield criterion by addition of planar anisotropy in the original von-Mises yield function. Mathematically, the extended yield function is expressed as

$$f(\sigma) = \bar{\sigma}_H^2 = F\sigma_2^2 + G\,\sigma_1^2 + H\,(\sigma_1 - \sigma_2)^2 + 2N\sigma_{12}^2 \qquad (4.14)$$

The material constants (G, H, F and N) can be evaluated by two methods, namely, σ-value and r-value based method (Basak and Panda 2019a). Constants are evaluated using formulas shown in Table 4.7. In the r-value method, coefficients are calculated by r-values (r_0, r_{45}, r_{90}), while in σ-value methods, normalized yield stresses ($\tilde{\sigma}_0 = \sigma_0/\sigma_0$, $\tilde{\sigma}_{45} = \sigma_{45}/\sigma_0$, $\tilde{\sigma}_{90} = \sigma_{90}/\sigma_0$ & $\tilde{\sigma}_b = \sigma_b/\sigma_0$) are used. The biaxial yield stress and biaxial anisotropic coefficient are taken from the literature (Xiao et al. 2016). A systematic procedure to evaluate material constants is described by (Basak and Panda 2019a). The material constants calculated for Inconel 718 alloy are listed in Table 4.8.

Table 4.7 Different methods to calculate anisotropic material constants for Hill'48 criterion

r-value based	**σ-value based**
$G(r) = \left(\frac{1}{1+r_0}\right)$	$G(\sigma) + H(\sigma) = 1$
$H(r) = \left(\frac{r_0}{1+r_0}\right)$	$H(\sigma) + F(\sigma) = \frac{1}{\tilde{\sigma}_{90}^2}$
$F(r) = \left(\frac{r_0}{r_{90}(1+r_0)}\right)$	$F(\sigma) + G(\sigma) + 2N(\sigma) = \frac{4}{\tilde{\sigma}_{45}^2}$
$N(r) = \left(\frac{(r_0+r_{90})(1+2r_{45})}{2r_{90}(1+r_0)}\right)$	$F(\sigma) + G(\sigma) = \frac{1}{\tilde{\sigma}_b^2}$

Table 4.8 Material constants for Hill'48 yield criterion by two different methods

Temp.	**H**		**G**		**F**		**N**	
	Hill'48-r	Hill'48-σ	Hill'48-r	Hill'48-σ	Hill'48-r	Hill'48-σ	Hill'48-r	Hill'48-σ
RT	0.4386	0.6651	0.5615	0.3349	0.4204	0.5039	1.4149	1.7816
100 ºC	0.4362	0.6672	0.5638	0.3328	0.4757	0.4932	1.4091	1.6814
200 ºC	0.4922	0.6598	0.5078	0.3402	0.5098	0.4876	0.9362	1.6242
300 ºC	0.4993	0.6691	0.5007	0.3309	0.5155	0.4784	1.6209	1.5793
400 ºC	0.4683	0.7584	0.5317	0.2413	0.5103	0.4598	0.9374	1.3654

500 °C	0.4992	0.8167	0.5007	0.1833	0.5753	0.4615	1.5303	1.6729
600 °C	0.5332	0.6584	0.4668	0.3416	0.5812	0.5614	1.0134	1.6694
700 °C	0.5290	0.6469	0.4710	0.3531	0.4675	0.5519	1.7227	1.6671

4.2.2 Barlat 1989 Yield Criterion

Barlat and Lian stated an anisotropic yield function for the plane stress condition (Barlat and Lian 1989) and given as

$$f(\sigma) = 2\bar{\sigma}_B^p = a|k_1 + k_2|^p + a|k_1 - k_2|^p + c|2k_2|^p \quad (4.15)$$

where, k_1 and k_2 are calculated as

$$k_1 = \frac{\sigma_1 - h\sigma_2}{2} \qquad k_2 = \sqrt{\left(\frac{\sigma_1 - h\sigma_2}{2}\right)^2 - q^2\tau_{12}^2} \quad (4.16)$$

In Eq. (4.15) and (4.16), anisotropy ratio functions a, c and h can be shown in terms of Lankford coefficient as,

$$h = \sqrt{\frac{r_0}{1 + r_0} \times \frac{1 + r_{90}}{r_{90}}}$$

$$c = 2 \times \sqrt{\frac{r_0}{1 + r_0} \times \frac{r_{90}}{1 + r_{90}}}$$

$$a = 2 - c$$

To find *q*-value in Equation 4.16, Lankford parameter variation w. r. t. θ (loading angle) from RD is calculated as

$$r_\theta = \frac{2q\sigma_0^p}{\sigma_\theta\left(\frac{\partial\phi}{\partial\sigma_{11}} + \frac{\partial\phi}{\partial\sigma_{22}}\right)} - 1 \quad (4.17)$$

θ-Value is considered to be 45° in order to initially find q-value. In all the above equations, *p*-value is considered as 8 (Barlat et al. 2003). Material constants (a, h, c, and q) were calculated by the detailed procedure described by Barlat et al. 2003 and listed in Table 4.9.

Table 4.9 Material constants for Barlat'89 yield criterion at different temperatures

Temp.	**a**	**c**	**h**	**q**	**p**
RT	1.0537	0.9463	0.9269	1.4121	8
100 °C	1.0432	0.9568	0.9549	1.4121	8
200 °C	1.0083	0.9917	1.0010	1.4102	8
300 °C	1.0087	0.9913	1.0074	1.4040	8
400 °C	1.0470	0.9734	0.9893	1.4040	8
500 °C	1.0987	0.9871	1.0528	1.4040	8
500 °C	1.0543	0.9802	1.0557	1.4040	8

700 ºC	1.0492	0. 9805	0.9982	1.4040	8

4.2.3 Comparison of Yield Criteria

Yield criteria performance is evaluated by comparing experimental and predicted data. This comparison includes analysis of the yield loci, planar distribution of uniaxial yield stress and plastic anisotropy coefficient. Also, the global accuracy index is used in the selection of yield criteria (Banabic 2000, 2010b). Figure 4.4 shows yield loci according to Hill'48-r, Hill'48-σ, and Barlat'89 criteria at test temperatures. It was perceived that the yield locus according to Hill'48-σ yield function is not able to capture biaxial stress state. However, in Barlat'89 loci pass through biaxial and uniaxial states in RD and TD very well. This further confirms the suitability of Barlat'89 for representation of yield loci in the case of Inconel 718 alloy.

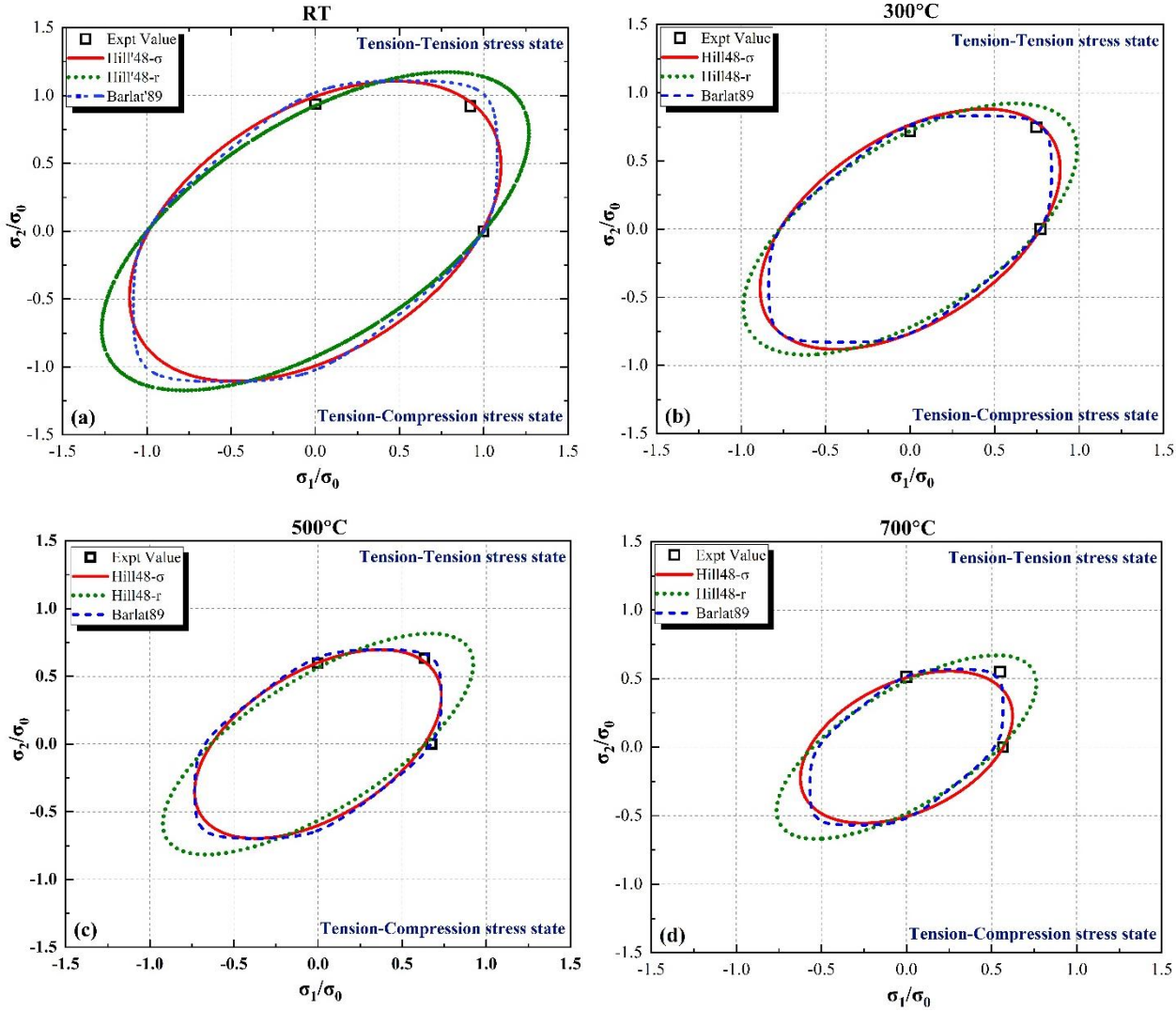

Figure 4.4 Experimental validation of normalized yield loci for Inconel 718 using different yield models RT, 300ºC, 500ºC and 700ºC

The capability of any yield criteria can also be evaluated by comparing predicted r and σ values with experimental results. Figure 4.5 shows normalized σ and r-values deviation with loading angle from RD. In the case of Hill'48-*σ* yield criteria, a good agreement can be seen in σ and significant discrepancy observed for *r*-variation. Thus, it is very much required to numerically evaluate the performance of studied yield criteria before concluding their suitability for the prediction of yielding behavior of Inconel 718 alloy.

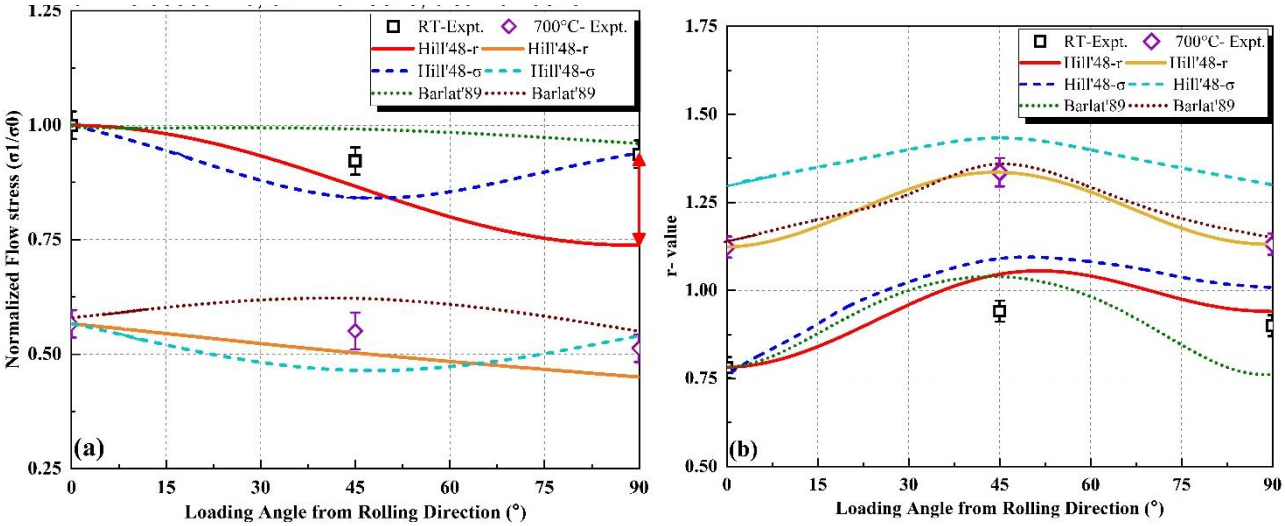

Figure 4.5 Deviation of (a) normalized flow stresses and (b) *r*-value directionality for Hill'48-*σ*, Hill'48- r and Barlat'89 yield criteria

In order to evaluate different yield criteria performance, global accuracy index (ω) was used for the analysis of yield locus shape and to visualize planer uniaxial stress distribution and anisotropic coefficients (Banabic et al. 2010). It can be mathematically expressed as,

$$\omega = \varphi + \delta + \gamma \ [\%] \tag{4.18}$$

$$\text{where, } \varphi = \frac{\sqrt{\sum_{i=1}^{n} d^2(P_i, Q_i)}}{Y} \times 100\ \%$$

$$\delta = \sqrt{\sum_{i=1}^{n} \left(\frac{\sigma_{\theta_i}^{exp} - \sigma_{\theta_i}^{pre}}{\sigma_{\theta_i}^{exp}} \right)} \times\ 100\ \%$$

$$\gamma = \sqrt{\sum_{i=1}^{n} \left(\frac{r_{\theta_i}^{exp} - r_{\theta_i}^{pre}}{r_{\theta_i}^{exp}} \right)} \times\ 100\ \%$$

Where, φ is an accuracy index for predictability of the yield locus shape in the principal stresses plane, γ and δ is an accuracy index for predictability of planar anisotropic coefficients and distribution of uniaxial stresses. $d^2(P_i, Q_i)$ is square of distance from P_i (experimental value) to

Q_i (its projection) in predicted yield locus in mm. j is total number of experimental points and q_i is an angle measured from RD in °(deg.).

Barlat'89 yield criterion shows minimum error function compared to Hill'48-σ, Hill'48-r yield criteria as for predicting the yielding behavior of Inconel 718 at all considered temperatures as shown in Figure 4.6. This indicates the suitability of Barlat'89 yield criterion for Inconel 718 alloy at all test temperatures.

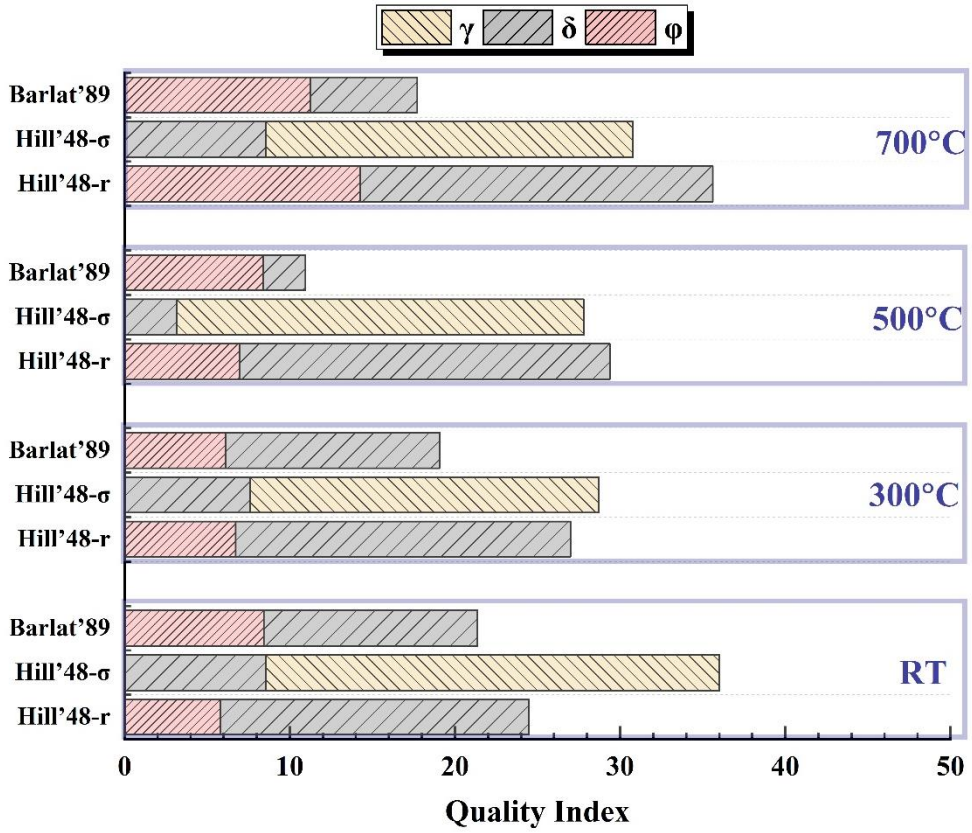

Figure 4.6 Quality index (ω) for yield criteria evaluation at different temperatures

Summary

This chapter discussed the formulation of different uniaxial constitutive models and anisotropic yield criteria for Inconel 718 alloy. The suitability of the models have been analyzed. The JC-ZA model shows best prediction capability of flow stress behavior with highest correlation coefficient and least error percentage. Barlat'89 yield criterion exhibited better yielding prediction at different temperatures and strain rates.

The findings of these studies will be helpful in the numerical analysis of stretch forming processes. The next chapter discusses in detail experimental and theoretical studies of forming and fracture limit diagrams using studied material models.

5. Experimental & Numerical Investigation of Forming and Fracture Limit Diagrams

This chapter is focused on experimental and numerical investigation of forming and fracture limit diagrams of Inconel 718 alloy. The experimental forming and fracture limit diagram are determined using the Nakazima test. The detailed fracture morphology of stretch-formed specimens have been examined using a scanning electron microscope (SEM). FE model has been developed using commercially available Abaqus-Explicit-SIMULIA^{TM}. The qualitative aspects of stretch forming processes have been investigated and validated with experimental and theoretical outcomes.

5.1 Experimental Set-up for Nakazima Test

The stretch forming tests were performed on a 40-Ton hydraulic press shown in Figure 5.1(a). The Laboratory-scale, stretch-forming tooling setup (hemispherical punch, blank holder, and die) is shown in Figure 5.1(b). Induction heating setup with a temperature controller having a K-type thermocouples system was used for heating of the die and specimens at a desired temperature. The K-type thermocouples were placed at appropriate locations of punch and die to measure the temperature. The water-cooling arrangement was made to maintain the desired temperature. This helps to avoid overheating of dies by water circulation from the cooling tower. All the stretch forming experiments were performed using molybdenum-based lubricant (MOLYKOTE). In literature, many researchers used molybdenum-based lubricant for high temperature applications. The different geometry and dimension blanks as per the ASTM E2218-15 standard were used for plotting FLDs and FFLDs (ASTM E2218-15 2015). The detailed dimensions of the blanks are shown in Figure 5.2. In stretching test, Hasek specimens (ISO12004-2 standard) were considered to prevent draw bead failure caused by lower width rectangular specimens (Basak and Panda 2019a). The groove bead was present in the blank holder for holding the blank tightly without any slipping action. It also stops the easy flow of the flat flange part into the die cavity. Few trials were conducted initially in order to set optimized process parameters for stretch forming experiments. Stretching tests were performed at different test temperatures (RT, 300ºC, 500ºC & 700ºC) with fixed blank holding pressure (BHP) of 2.5 MPa and punch speed as 2 mm/min.

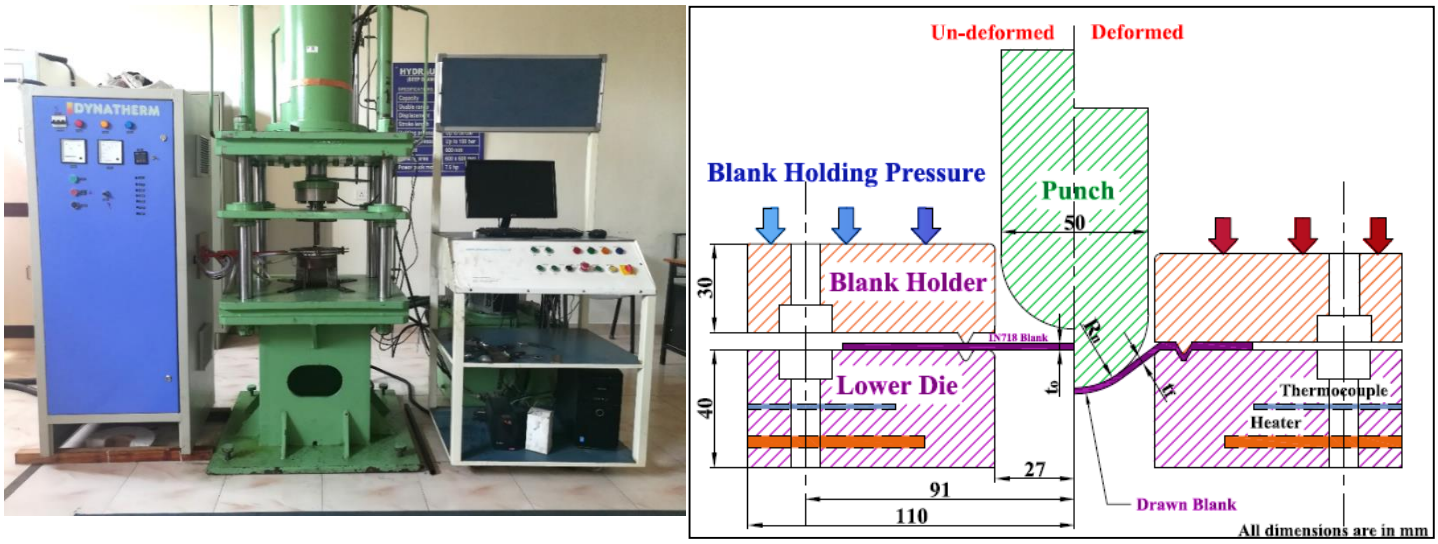

Figure 5.1(a) Hydraulic press of 40-Ton capacity used for stretch forming (b) Schematic diagram of stretch forming setup for FLD and FFLD

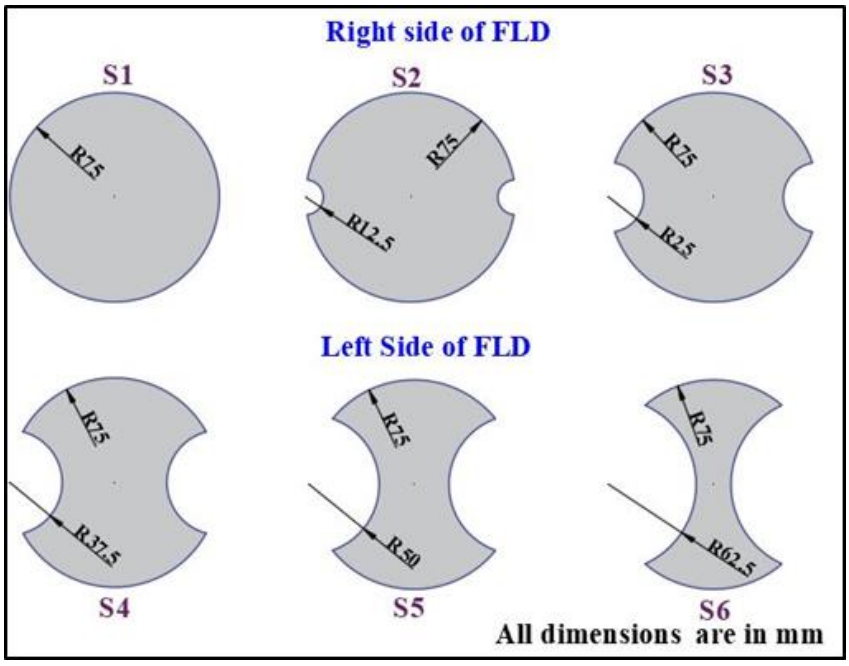

Figure 5.2 Schematic of specimen geometry considered for plotting FLDs and FFLDs

All the stretch-formed specimens were laser-etched using 2.5 mm diameter circular grid for measuring the minor and major strains. The stretched specimens were differentiated by safe, necking, and fracture states. Representative stretch formed specimens at 300°C test temperature are displayed in Figure 5.3. The precise and accurate measurement of the deformed grid is one of the critical issues to get accurate limiting strains in the FLD. Major and minor diameters of deformed grid (ellipses) in drawn/stretched blanks were measured using an optical microscope to estimate the engineering minor (e_2) and major (e_1) strains using Equation 5.1. Then transferred into corresponding true strains (ε_1 & ε_2) as in Equation 5.2,

$$e_1 = \frac{\text{major axis of deformed ellipse} - \text{grid diameter}}{\text{major axis of deformed ellipse}}, \quad e_2 = \frac{\text{minor axis of deformed ellipse} - \text{grid diameter}}{\text{minor axis of deformed ellipse}} \tag{5.1}$$

$$\varepsilon_{1,2} = \ln (1 + e_{1,2}) \tag{5.2}$$

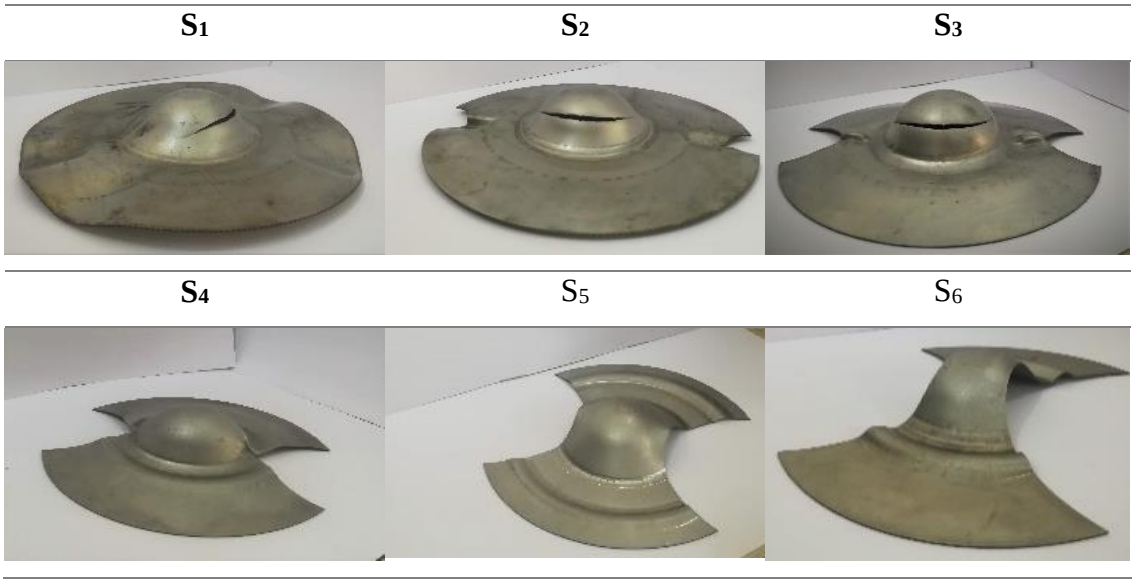

Figure 5.3 Representative stretched specimens at 300°C for FLD prediction

5.2 Experimental Forming Limit Curve

True minor and major strains were calculated and plotted as shown in Figure 5.4. Distinct symbols and distinct colors were assigned in order to differentiate between safe, necking, and failed ellipses with six different width specimens (S_1-S_6). Inconel 718 alloy specimens failed without a substantial prior hint of the necking. It has been observed that very few necked ellipses are present in the deformation region. Particularly, in the tension-tension region, no necking tendency has been seen. Similar observations are stated by Roamer et al. 1997 and Prasad et al. 2018b. The necking strains are measured at all conditions. A line has been drawn to separate limits between these maximum safe and failed strains. The possible reason for such failure behavior is the high strength of Inconel 718 alloy and the presence of a large amount of second-phase (i.e., γ' or γ'' phase) particles as stated by Prasad et al. 2017, 2018b. In FLD, at RT, the highest major limiting strains in T-C and T-T region (equi-biaxial tension) are 0.4555 and 0.4402 respectively. For a particular strain path, an average value of strain ratio ($\alpha = \frac{\varepsilon_2}{\varepsilon_1}$) from experimental points on forming limit curve is considered. The limiting strain value at plane strain state (i.e., $\alpha = 0$) is 0.374 (Limiting true strain value at the intersection of FLD to y axis). This is also called as plane strain forming limit (FLD_o). These

limiting strain values are comparable with previous reports by Roamer et al. 1997 and Prasad et al. 2017.

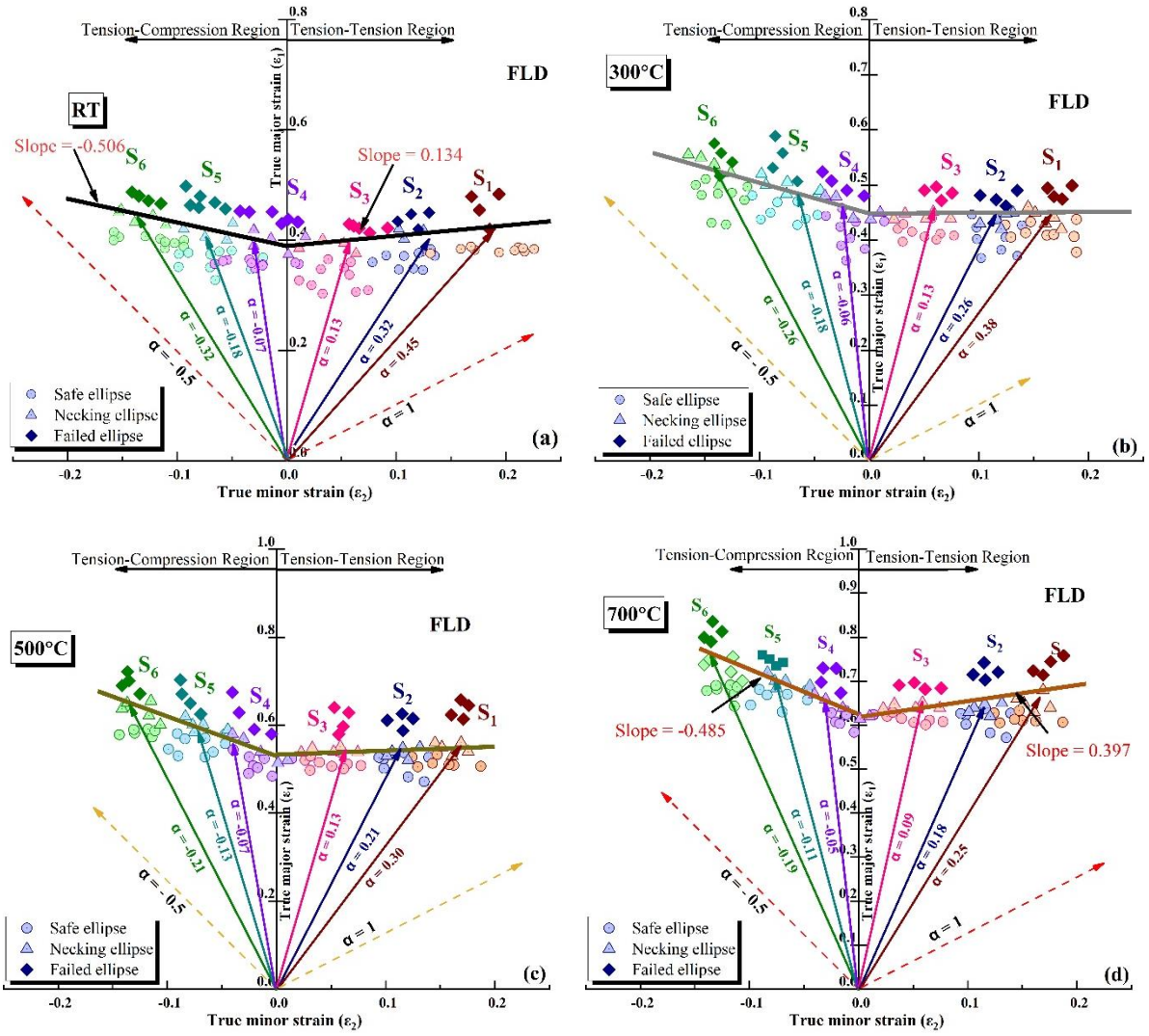

Figure 5.4 FLD of Inconel 718 alloy at (a) RT (b) 300ºC (c) 500ºC and (d) 700ºC

As expected, limiting true strains are apparently increasing with an increase in test temperature in all deformation regions (T-T, plane strain and T-C) as shown in Figure 5.4 (b-d) and Figure 5.5(a-b). The substantial necking tendency has been identified at higher temperatures due to the material becoming more ductile in nature. Improvement in maximum major safe strain for T-C and T-T region were found to be 21% and 4 % at 300ºC, respectively with respect to RT. Thus, number of necking points increased in both the regions of FLD at 500°C and 700°C as presented in Figure 5.4 (c-d). At 500ºC, improvement in maximum major safe strain for T-C and T-T region were found to be 42 % and 28% , respectively with respect to RT. Whereas, limiting true strain observed at 700ºC are much higher than that at RT.

Improvement in maximum major safe strain for T-C and T-T region (equi-biaxial tension) were found to be 66.16% and 54.35 % at 700ºC respectively, with respect to RT. Figure 5.5(c) gives the improvement in a safe strain of material with respect to RT. FLD_o also shows similar behavior with increase in temperature. Thus, FLD_o has high dependency over temperature. FLD_o value for all test temperatures is lower than limiting strains obtained in the T-T and T-C region Figure 5.5(b). It was also observed that the absolute value of FLD slope at 700ºC increases significantly in both regions (Figure 5.5 a).

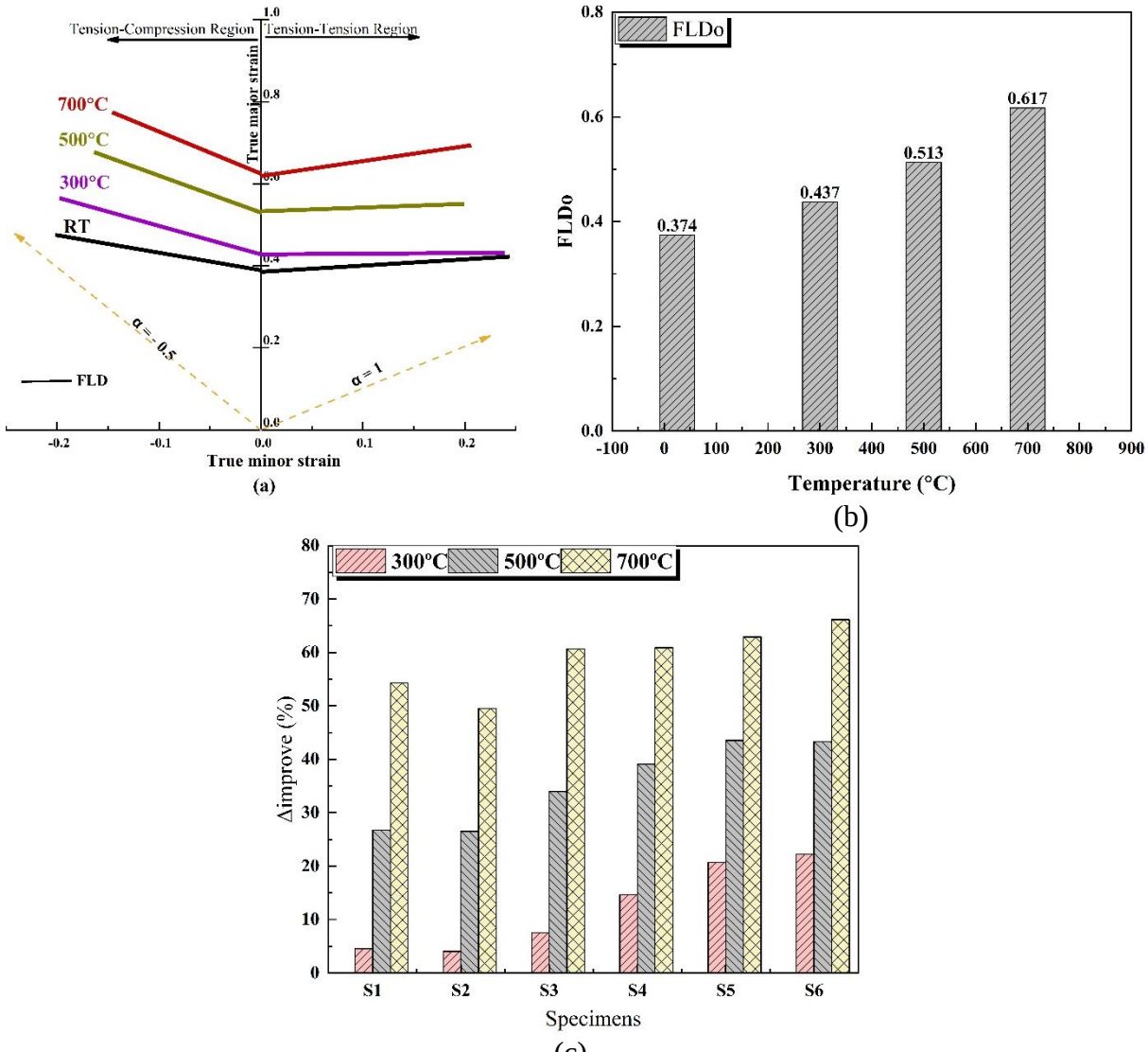

Figure 5.5 (a) Effect of temperature on FLDs (b) FLD_o and (c) Improvement (%) in maximum major safe strain measured for different specimens (RT values referred as datum)

5.2.1 Strain Distribution

It is noteworthy to mention that failure location in S_1, S_2, and S_3 specimens (Biaxial region) is slightly away from the apex of the dome. One of the possible reasons is the high coefficient of friction while warm stretch forming. As friction between a tool and the workpiece

has a significant effect on the material deformation, forming load, component surface finish, and die wear. The coefficient of friction, if controlled properly, could generate the required shear stresses to deform the metal workpiece to the desired shape. It could also lead to instability occurrence, flow localization or fracture of the sheet specimen if not controlled properly (Hecker 1975; Zhang and Lu 2019). In the present study, we used the molybdenum-based lubricant (MOLYKOTE) to reduce the friction between a tool and the workpiece. During hot working, lubrication is more problematic as it may evaporate. Hence the friction coefficient at high test temperature will often be much higher than room temperature. It may well become meaningless as the interface shear stress exceeds the flow shear stress (Bruschi et al. 2014; Güler and Efe 2018). Frictionless contact between punch and sheet specimen surface causes the sheet in the contact area is under more tension than other sheet's areas. Therefore, fracture happens at slightly away from the apex of the dome of samples. Secondly, it might be due to the influence of strain hardening and strain-rate sensitivity of workpiece. Jackson 2000 reported that the variation in both strain rate sensitivity and interface friction factor lead to significant variations in the predicted strain distribution as, Inconel 718 alloy has high value strain hardening exponent and strain-rate sensitivity (Prasad et al. 2017). A similar failure nature is reported by Prasad et al. 2017, 2018b for Inconel 718 alloy at RT.

The surface strain distribution (strain signature) is plotted for maximum stretched ellipse along the longitudinal direction. The representative true (major and minor) strain distribution contours of three different specimens have been plotted in Figure 5.6 (a-c). True strains plotted as a function of pole (highest distance) in stretched specimens. S_6 experienced lateral drawing with negative (compressive) values of minor strain and positive (tensile) values of major strain. In Figure 5.6 (c), the high value of peak major strain (around 0.46) at RT, is due to higher strain hardening of Inconel 718 alloy (Khan et al. 2017). Peak major strain has been observed approximately at a distance of 7 mm, the similar location where stretched specimen fails. In Figure 5.6 (a-b), both minor and major true strains are positive values representing biaxial tension induced in S_4 and S_1. However, minor strain values in S_4 are comparatively lower in magnitude signifies the plane strain deformation. Whereas closer positive values of the minor and major strains in S_1 signifies biaxial tensile deformation (equi-biaxail tension). Effect of temperature on strain profile for all three specimens is also shown in Figure 5.6(a-c). It clearly indicates that the strain distribution curve has been raised with rise in temperature from RT to 700°C. This rise in the surface strain values is due to the thermal softening material become more flowable and ductile.

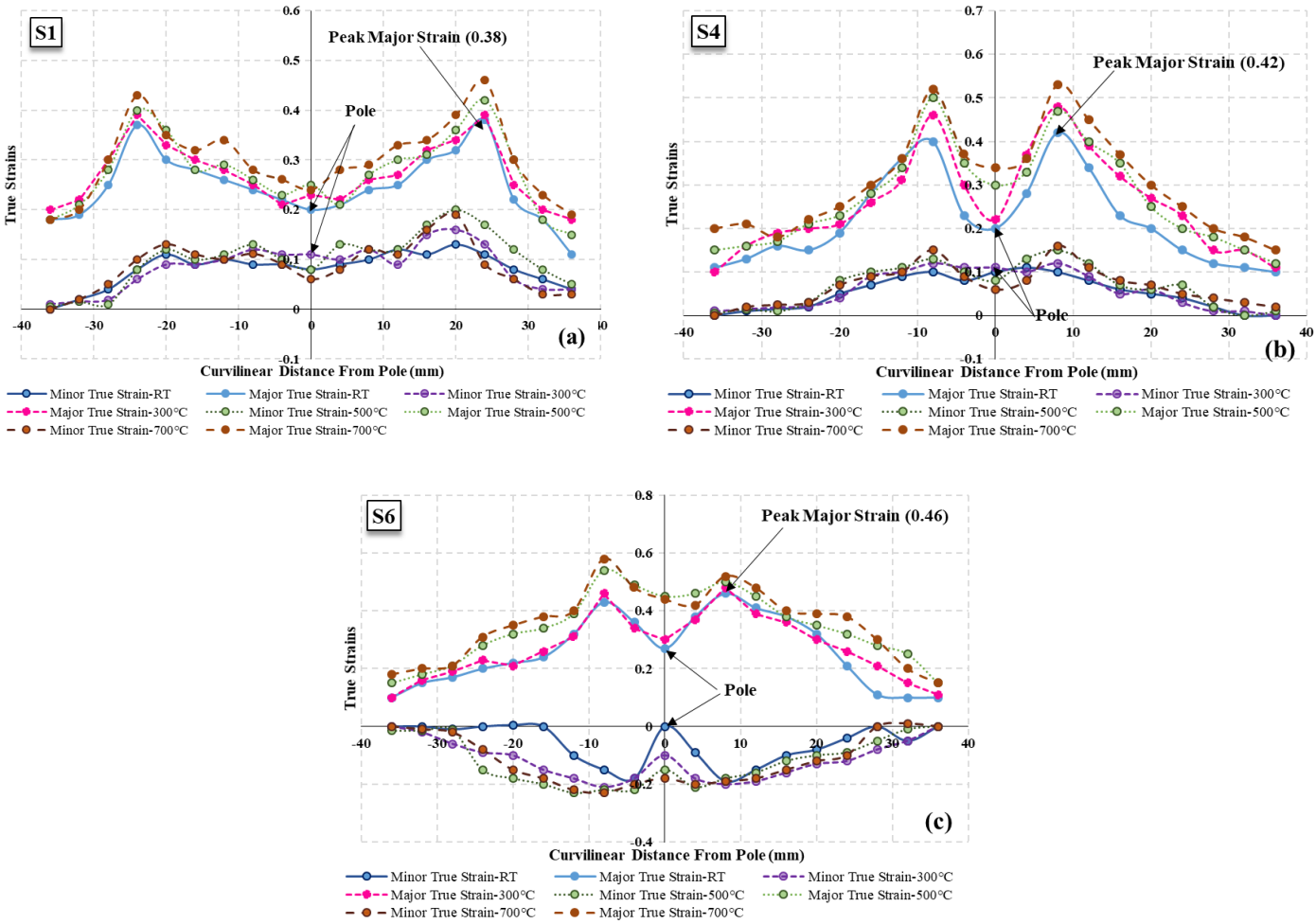

Figure 5.6 Strain distribution profile along rolling direction (a) S_1 (b) S_4 (c) S_6

5.2.2 Bending Correction

A sub-sized hemispherical punch (diameter = 50 mm) is used in this study rather than a standard punch (diameter = 101.4 mm) as suggested by Hecker (Charpentier 1975; Hecker 1975). It is downsized to optimize usage and reduce wastage of the material. Thus, the effect of bending strain was also detected over the blank outer surface in a region where enfolding around sub-sized punch takes place during stretching (Figure 5.7 a). Hence, it is essential to consider the punch curvature effect on stretching limits as specimens were stretched into a convex shape. This effect of strain gradient along the thickness of a sheet on strain measurement has also been reported in previous literature (Charpentier 1975). It was reported that the position of FLD is highly dependent upon geometrical factors. Specifically, at a constant sheet thickness, punch curvature (1/R) was found to be directly proportional to limiting strains (Charpentier 1975). Bending strain is mathematically represented as Equation 5.3.

$$\varepsilon_{bending} = \ln\left(1+\frac{t_f}{2R_n}\right), \text{ where } t_f = t_o - \exp\left(-\varepsilon_1 - \varepsilon_2\right) \quad (5.3)$$

Measured surface strains are a combination of bending and stretching strains. Induced bending strains were subtracted from the measured true strains, so as to measure correct limiting surface strains ($\acute{\varepsilon}_{1n,2n}$) using Equation 5.4

$$\acute{\varepsilon}_{1n,2n} = \varepsilon_{1,2} - \varepsilon_{bending} \quad (5.4)$$

Limiting strains in FLDs were corrected by using Equation 5.3 and Equation 5.4. Figure 5.7 (b) shows the effect of bending strain on measured and corrected FLD. It was noticed that the corrected FLDs shifted downwards by 4-5% approximately in all strain deformation regions at test temperatures.

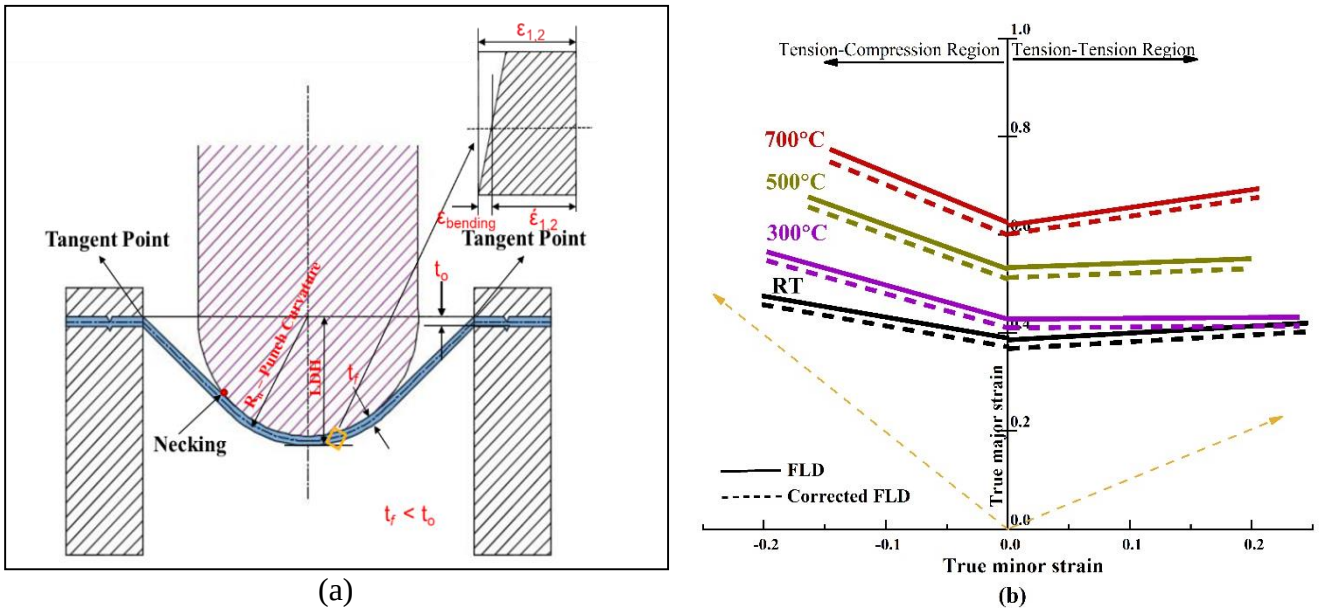

Figure 5.7 Schematic diagram of warm stretching setup showing punch curvature effect and influence of bending strains

5.2.3 Thickness distribution

Normalized thickness distribution for S_1 and S_6 specimens with curvilinear distance from the pole is shown in Figure 5.8 (a, c). It is observed that the thickness remains constant initially, and then it starts declining. Minimum thickness is observed at a location where generally necking and fracture occur. Then, thickness is raised gradually till the flange part of the specimen. The thickness on the flat flange part of the specimen is nearly equal to the original sheet thickness. The comparable nature of the curve is observed at tested temperatures for different samples. Thickness decreases with increase in test temperature because of thermal softening and hence improved ductility at high temperature. Even a rise in the temperature leads to a decrease of strain hardening exponent, thus localized thinning tendency is higher. The quality of stretched samples is analyzed by some qualitative parameters such as Thickness Deviation (TD), Equation 5.5 and Maximum Thinning Rate (MTR), Equation 5.6. Thickness

variation is an important phenomenon in metal forming applications. Minimum thickness variation is expected for the desired formed product. MTR and TD are calculated as

$$TD = \frac{1}{n-1} \sum_{i=1}^{n} (t_i - \bar{t})^2 \quad (5.5)$$

$$MTR = ((t_{initial} - t_{min}) / t_{initial}) \times 100 \quad (5.6)$$

Here, $t_{initial}$ - initial thickness of specimen, t_{min} - minimum thickness of deformed specimen, t_i - thickness at any instant deformed specimen, $\bar{t}$ – average thickness and n is the total number of tested specimens.

Figure 5.8 (b, d) shows the representative MTR and TD plots for specimens. As expected, the thickness variation of the drawn hemispherical cup is affected by the test temperature. A rise in TD and MTR is observed with increases with temperature. It is noticed that the MTR and TD decrease with an increase in sample width as there is a restricted flow of material. Hence the fracture occurred much before the necking started, which resulted in less deviation of thickness.

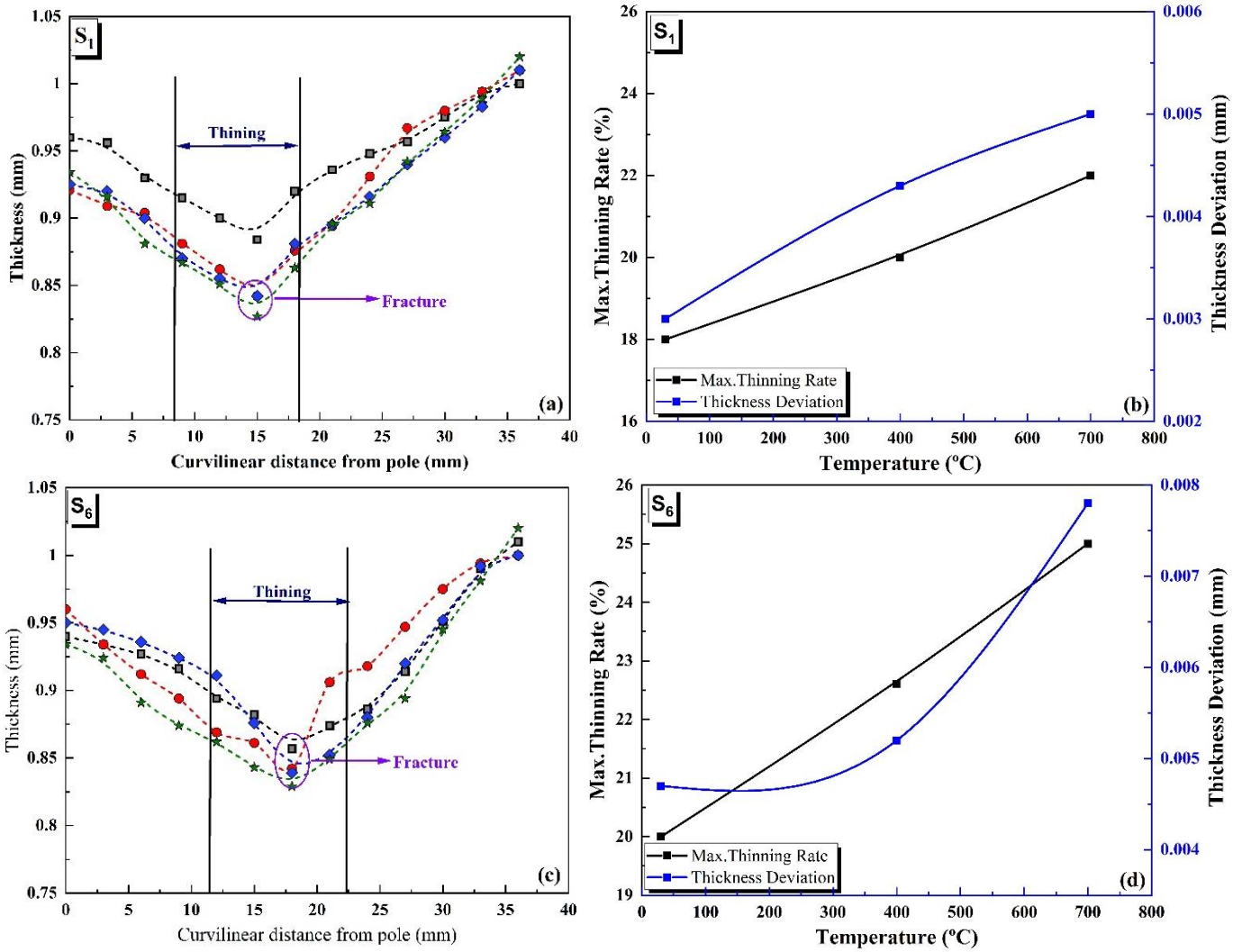

Figure 5.8 Thickness distribution, Maximum thinning rate (MTR) and thickness deviation (TD) for (a-b) S_1 (c-d) S_6

5.2.4 Limit dome height

Limiting Dome Height (LDH) is an important parameter that helps to understand the drawability of different width sheet specimens at different test temperatures. LDH is measured as the drawn height of formed cup just before occurring of fracture. The variation of LDH with temperature is shown in Figure 5.9. It is observed that LDH is directly proportional to testing temperature and width of specimen. High limit dome height at RT is might be because of high strain hardening exponent at RT. High strain hardening exponent at RT results in a low tendency of localized necking at the critical area of deformed specimen. As a result high LDH is observed. An increase in dome height is might be due to decrease in strain hardening with rise in temperature. Therefore, LDH or total elongation is highly sensitive to temperature.

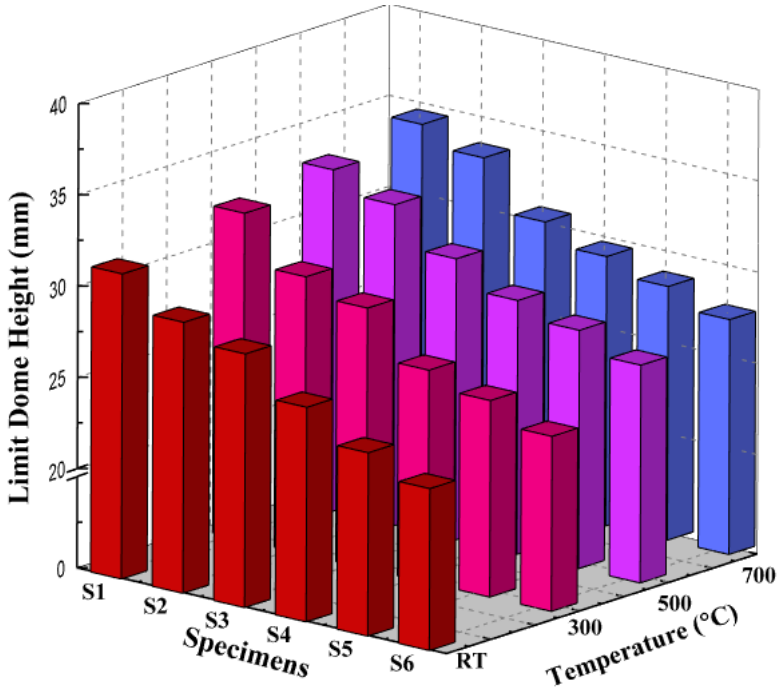

Figure 5.9 Variation of LDH at different processing temperatures

5.3 Fracture Forming Limit Curve

The solid-color diamond symbol shown in Figure 5.4 (a-d) denotes an already failed ellipse on the deformed surface of specimens. But these fracture strains did not characterize the onset of fracture in sheet specimens. In order to accurately measure strain at onset of fracture, the volume constancy relation is used, as suggested (Basak et al. 2015; Prasad et al. 2018b). It is expressed as Equation 5.7,

$$\varepsilon_{1f} + \varepsilon_{2f} + \varepsilon_{3f} = 0 \qquad (5.7)$$

Considerable lateral stretching of the blank has not been observed after the appearance of necking in the blank. Thinning of specimens takes place along the thickness direction because

of excessive strain localization. Hence, numerical values of minor fracture strain (ε_{2f}) and necking strain (ε_{2n}) were assumed to be the same. Furthermore, each fractured specimen was wire cut perpendicular to the line of fracture (Figure 5.10). Perpendicular distances (t_{1f} & t_{2f}) from the beginning of the fracture edge of the maximum thinned cross-section were measured under an optical microscope. The smallest fracture thickness value between t_{1f} and t_{2f} was considered for evaluation of true thickness fractured strain (ε_{3f}). From Equation 5.7, fractured major strain (ε_{1f}) was calculated, and fracture strain state was also inserted in FLD. For an individual strain path, multiple fracture points (ε_{1f}, ε_{2f}) were evaluated. The solid-colored square symbols in Figure 5.11 (a) represented the onset of fractured points on the deformed surface of specimens at RT. A straight line, named as FFLD, was drawn just below scattered fracture points. Figure 5.11 (b) shows experimental FFLD drawn for Inconel 718 alloy along various strain paths for all test temperatures. Fracture strains in the FFLD were increased with an increase in test temperatures in all deformation regions similar to limiting strains in FLDs. Fractured strains at 700ºC temperature were found much higher than that at RT due to the thermal softening. Improvement in onset of fracture true strain values for FFLD in T-C and T-T region were found to be 65.19% and 68.91% at 700ºC with respect to RT.

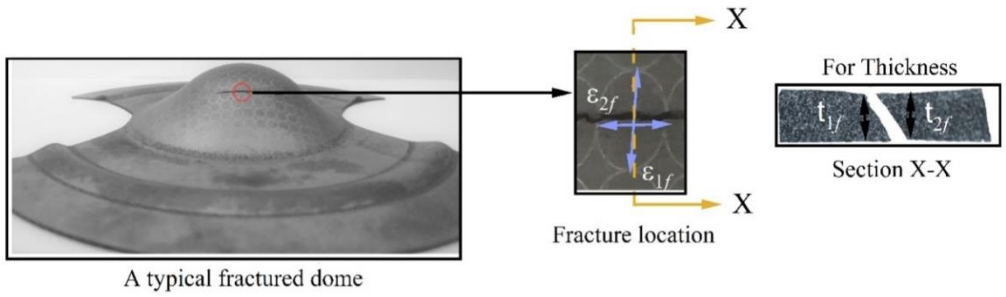

Figure 5.10 Measurement technique for fracture along the thickness direction of a fractured specimen

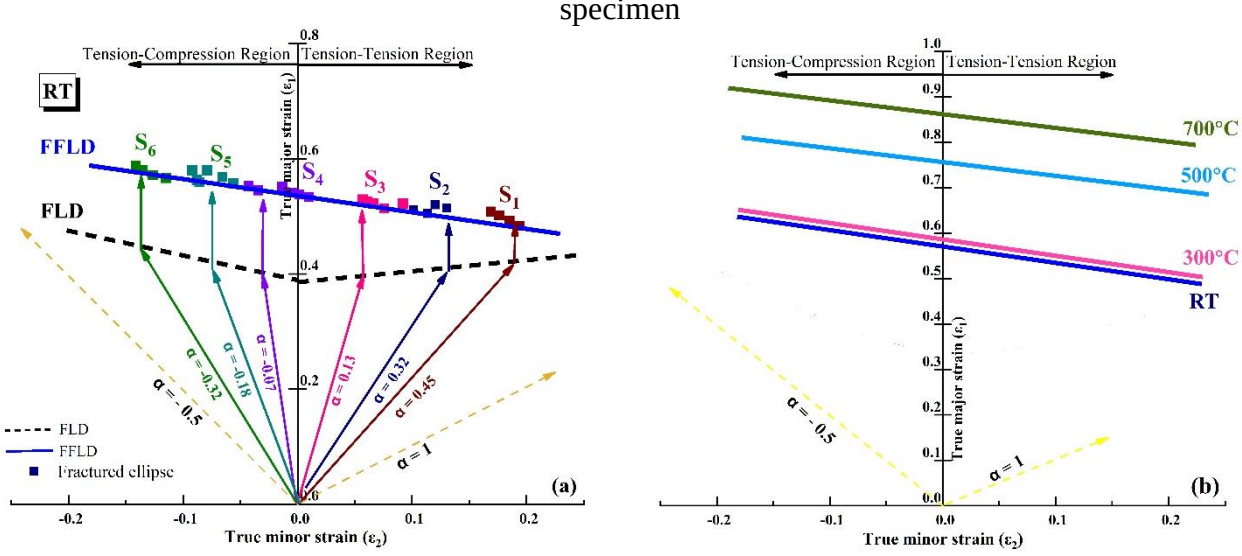

Figure 5.11 FFLD diagram for Inconel 718 at (a) RT (b) Effect of temperature on FFLDs

5.4 Fractography Study of Post-stretched Samples

Fractured surfaces of fully deformed stretched samples were comprehensively examined using a scanning electron microscope (SEM) of Hitachi, S-3400N. A sample has been taken from fractured specimens and observed parallel to the fracture surface. Figure 5.12 gives the sectional fracture surface of stretched specimens (S_1, S_4 and S_6) in T-T, plane strain, and T-C regions, respectively, examined using the SEM. The fractured surface was found to be fully enclosed with plenty of equiaxed dimples, flat regions, tearing edges and serpentine sliding characteristics. Figure 5.12(a) shows the factograph of S_1 in Tension-Compression (T-C) regions. It shows plenty of equiaxed dimples, indicates that specimens have gone through a large extent of plastic deformation before onset of fracture due to metal matrix ductile rupture. This confirms high ductility of Inconel 718 alloy with higher limiting strain values on the left side of FLD compared to right side (Figure 5.4 a). From RT to 300°C, size of cell-like structure and dimples are fine in nature while the dimple size seems to increase significantly at 500 and 700°C. As material shows high plasticity due to softening and diffusion healing of micro-pores. This evidence of an increase in limiting strain values at high temperatures. A mixed-mode fracture was observed in plane strain condition due to a considerable localized straining before crack propagation as shown in specimen S_4 in Figure 5.12. This is the main reason for higher fracture strains at plane strain condition ($\alpha = 0$) for FFLD compared to others. At 500ºC, it has been observed that factographs contain of shallow elongated dimples due to shear-prompted failure. At 700ºC, the presence of visible carbide indicates the early precipitating phase of Inconel 718 alloy. Previous reports by Prasad et al. 2018b also indicate that these were inclusions or precipitates of Ni-Al/Ti/Nb. These observed phases were mainly responsible for the improvement in fracture strains at 700ºC.

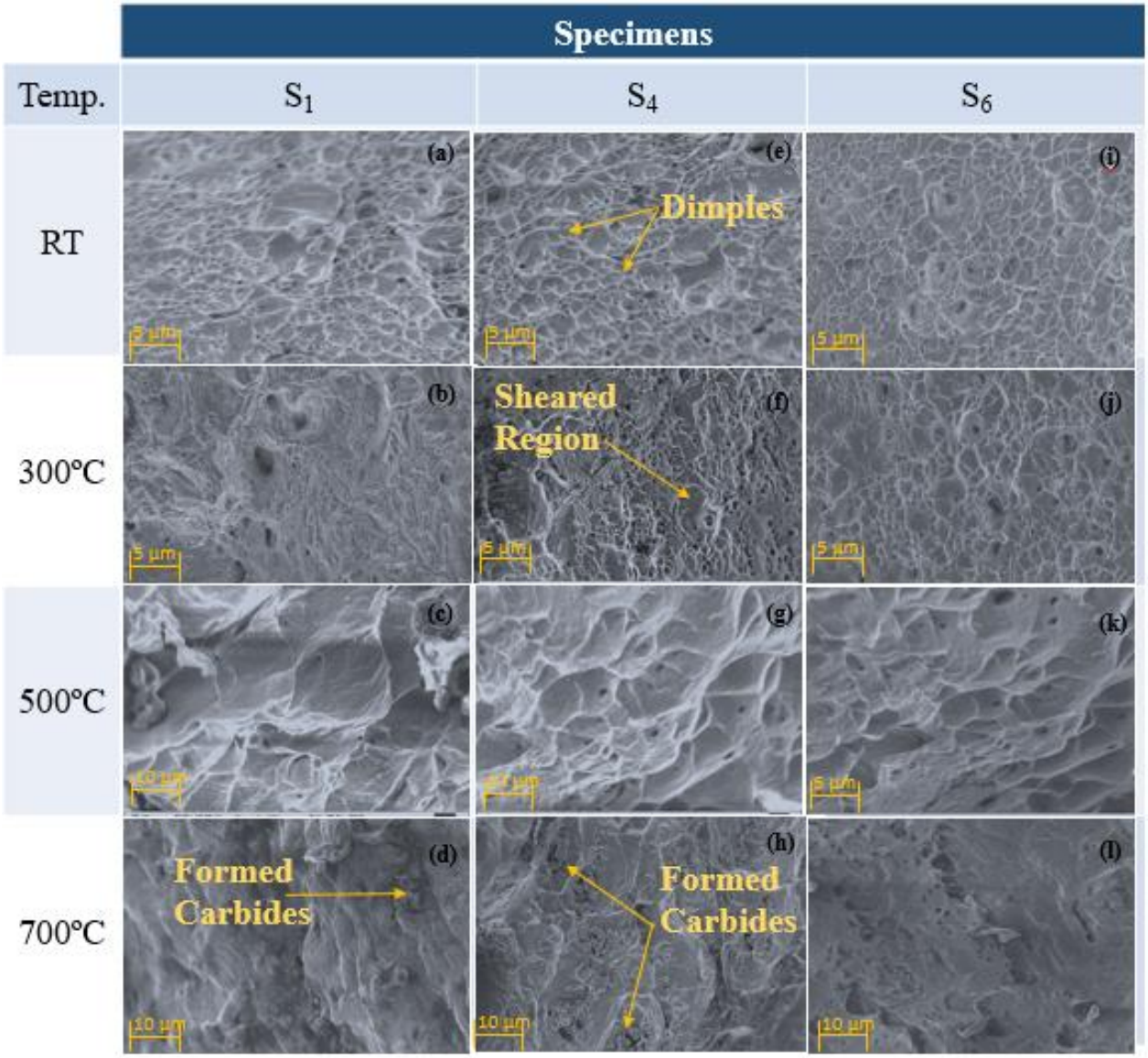

Figure 5.12 Fractographs of stretched specimens in T-T (S_1), plane strain (S_4) and T-C (S_6) regions at all test temperatures

5.5 Theoretical models for Forming and Fracture limit curve prediction

Marciniak–Kuczynski model (M–K) was proposed considering non-homogeneity (in geometrical & structural) sheet metals for FLD calculation (Banabic 2010a). The M–K model is mainly based on thickness variation and necking theory for FLD prediction. But, the M-K model is unable to predict failure when there is a negligible change in thickness of considered metal. Thus, analytical FFLD was predicted by continuum ductile damage models with plane stress-based plasticity theory. Among various ductile damage criteria, it is observed that Bao and Wierzbicki (BW) damage model has been widely calibrated with experimental data in the forming applications.

5.5.1 Marciniak Kuczynski (M-K) model

Marciniak Kuczynski (M-K) model is widely used for the prophecy of localized necking strain in metal forming processes (Bao and Wierzbicki 2004). Initial inhomogeneity, due to physical and geometric factors, is considered to be one of the fundamental assumptions while using M-K model (Marciniak and Kuczyński 1967). Model proposed that the specimen had two regions, namely, region A (thickness t_A) and region B (thickness of t_B) as shown in Figure 5.13.

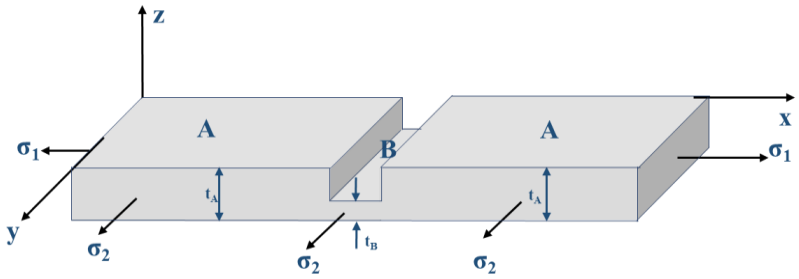

Figure 5.13 Geometric imperfection considered in M-K model

Inhomogeneity factor (f_0) and principal stress were always considered perpendicular to each other. Rolling, transverse and thickness directions were considered along 1 (x-axis), 2 (y-axis) and 3 (z-axis) respectively. The ratio of t_A and t_B gives initial imperfection or inhomogeneity factor (f_0) and is expressed as,

$$f_0 = \frac{t_A}{t_B} < 1 \tag{5.8}$$

In these regions, stress and strain states were analyzed with respect to ε_1^A and ε_1^B. It is considered that deformation is localized in region B of specimen when $\varepsilon_1^B/\varepsilon_1^A$ ratio tends to ∞ (too high). However, ε_1^A in region A will be referred as non-significant straining compared to region B where it represents limiting strain ε_1^{A*} (Banabic 2010a). Limiting/ principal strains ε_1^{A*} and ε_2^{A*} in region A, describes a point in FLD. By varying this strain ratio ($0 < \alpha^A < 1$), different points in FLD can be obtained in a biaxial region. Variation of f_0 helps in knowing the relation between experimental and theoretical FLD under plane strain condition ($\alpha = 0$). Necking initialization was marked when deformation in region B is more than region A. Failure of a material is defined as,

$$\frac{d\overline{\varepsilon_A}}{d\overline{\varepsilon_B}} < W \tag{5.9}$$

Integer W should be small enough so as to have confirmation that sufficient deformation (necking) took place in region B as compared to that of A. Generally, W-value is taken as 0.15 based on previous literature (Banabic et al. 2019). An explicit algorithm is followed to solve

the M-K model and executed in MATLAB 2018a (Figure 5.14). Following were steps followed to execute the algorithms.

Step I:

First ratios α and f_0 were assumed randomly for initiation of calculation. Equation 5.10 defines the effective strain and stress ratio as,

$$\rho = \frac{\sigma_2}{\sigma_1} \;\&\; \alpha = \frac{\varepsilon_2}{\varepsilon_1} = \frac{d\varepsilon_2}{d\varepsilon_1} \tag{5.10}$$

Step II:

A small increase in strains ($d\varepsilon_1^B$) was given in groove region B as

$$\overline{\sigma\varepsilon} = (\sigma\varepsilon)_1 + (\sigma\varepsilon)_2 = (\sigma\varepsilon)_1 (1+ \alpha\rho) \tag{5.11}$$

Associative flow relation is given as,

$$d\varepsilon_{ij} = d\lambda \frac{\partial\bar{\sigma}}{\partial\sigma_{ij}} \tag{5.12}$$

By using Equation 5.12 and volume constancy relation, Values of $d\varepsilon^B$, $d\varepsilon^A$, $d\varepsilon_1^B$ and $d\varepsilon_1^A$ were calculated by iterative computation,

$$d\varepsilon_1 + d\varepsilon_2 + d\varepsilon_3 = 0$$

A compatibility condition is incorporated in MK-model as

$$d\varepsilon_2^A = d\varepsilon_2^B \tag{5.13}$$

Further, the balancing of forces has been used by considering the deformation in the sheet metal in order to achieve equilibrium and is represented as,

$$\varphi_A C\left(\varepsilon = \overline{\varepsilon^A} + \overline{d\varepsilon^A}, \dot{\varepsilon} = d\varepsilon^A\right) = f\varphi_B C\left(\varepsilon = \overline{\varepsilon^B} + \overline{d\varepsilon^B}, \dot{\varepsilon} = d\varepsilon^B\right) \tag{5.14}$$

where, f = $\frac{t_A}{t_B}$, $\varphi = \frac{\sigma_1}{\bar{\sigma}}$ and C represented a hardening law or constitutive model function. f – value has been further resolved and written as,

$$f = f_0 \exp(\varepsilon_3^A - \varepsilon_3^B) \tag{5.15}$$

Step III:

If equality in Equation 5.14, is satisfied, $\frac{d\varepsilon^A}{d\varepsilon^B}$ value is calculated. If this value is smaller than 0.15, a necking condition will occur. This strain ratio gives a fixed point in FLD. But, if equality in Equation 5.15 does not satisfy then that point is marked below FLD in the safe zone.

Step IV:

To impose necking condition, the value of $d\varepsilon_1^B$ is increased by iteration and the above-mentioned steps were repeated. This process was repeated until necking occurred for selected α-value. Thus, a full FLD was obtained by repeating above mention steps with different α value.

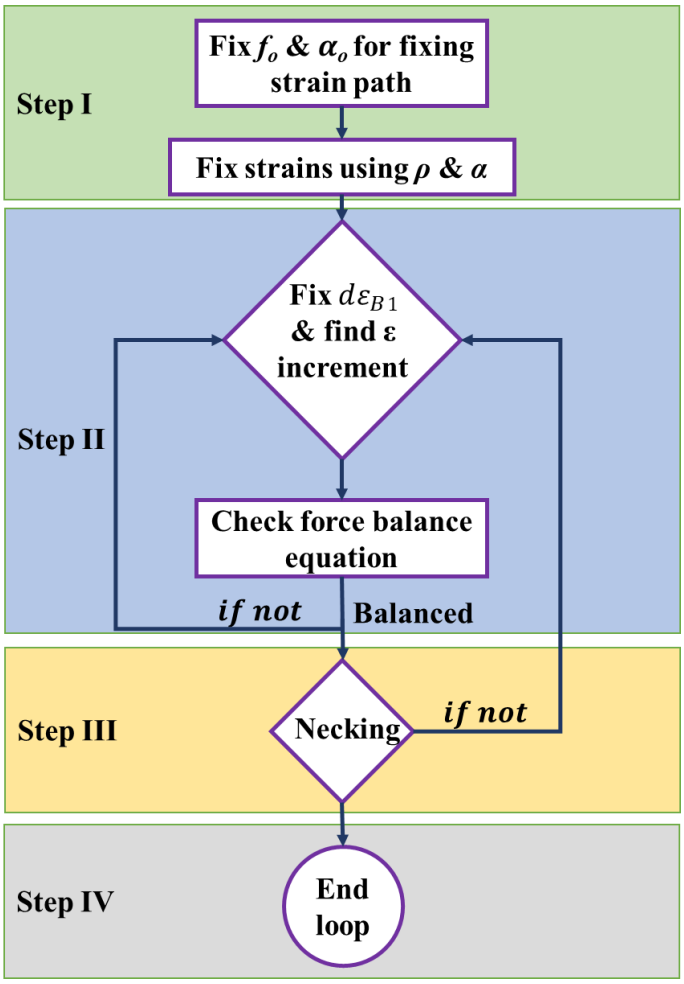

Figure 5.14 Flow chart to execute algorithm for M-K model of FLD prediction

For various combinations of inhomogeneity factor (f_0) and strain ratio (α), the procedure was repeated. It has been mentioned in literature that predicted FLD based on the M-K model is majorly affected by inhomogeneity factor (f_0) (Basak and Panda 2019a; Kotkunde et al. 2016). Inhomogeneity factor (f_0) is highly dependent on material properties, grain size, surface quality, and sheet thickness (Kuroda and Tvergaard 2000; Xu and Weinmann 1998). In order to achieve better accuracy in FLD prediction, f_0 value was varied for all possible combinations of hardening laws and yield criterion. Figure 5.15 gives the representative variation of f_0- value in FLD prediction by Hill'48 yield criterion at RT. Table 5.1 gives an inhomogeneity factor (f_0) and strain ratio (α) selected for the best predicted theoretical M-K model based FLD for Inconel 718 alloy at all test temperatures.

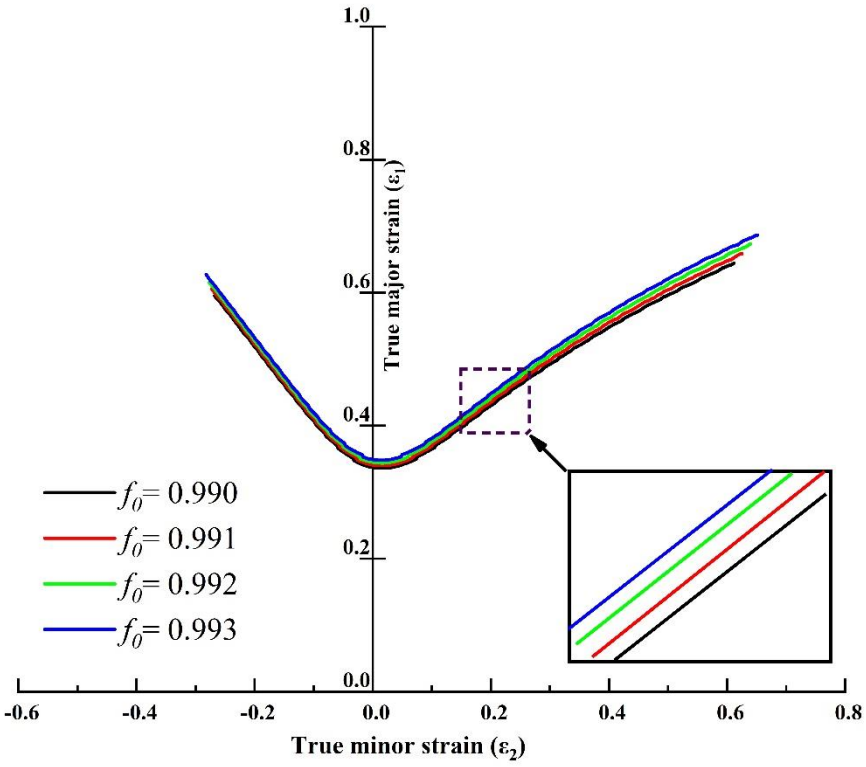

Figure 5.15 Representative variation of f_0- value for FLD prediction by Hill'48 yield criterion at RT.

Table 5.1: Strain ratio (α) corresponding to the initial inhomogeneity factor (f_0) at different test temperature

Temperature							
RT		300ºC		500ºC		700ºC	
f_0	α_0	f_0	α_0	f_0	α_0	f_0	α_0
0.990	0.055	0.992	0.065	0.991	0.060	0.992	0.068

Figure 5.16 shows a comparison of experimentally calculated FLD and predicted MK-FLD using Hill'48-r, Hill'48-σ and Barlat'89 criteria at respective temperatures. It was observed that necking strains by the M-K model with Barlat'89 criteria displayed better predictability in the T-T region as compared to T-C region. M-K model with Hill'48-σ criteria predicts lower necking strains compared to Barlat'89 yield criteria due to smaller yield locus. Figure 5.17 gives FLDo comparison for predicted value by MK-FLD coupled with different yield criteria and experimentally recorded FLDo value for Inconel 718 alloy. It has been observed that FLDo value predicted by MK-FLD combined with Barlat'89 yield criteria displayed a good match with experimentally reported values.

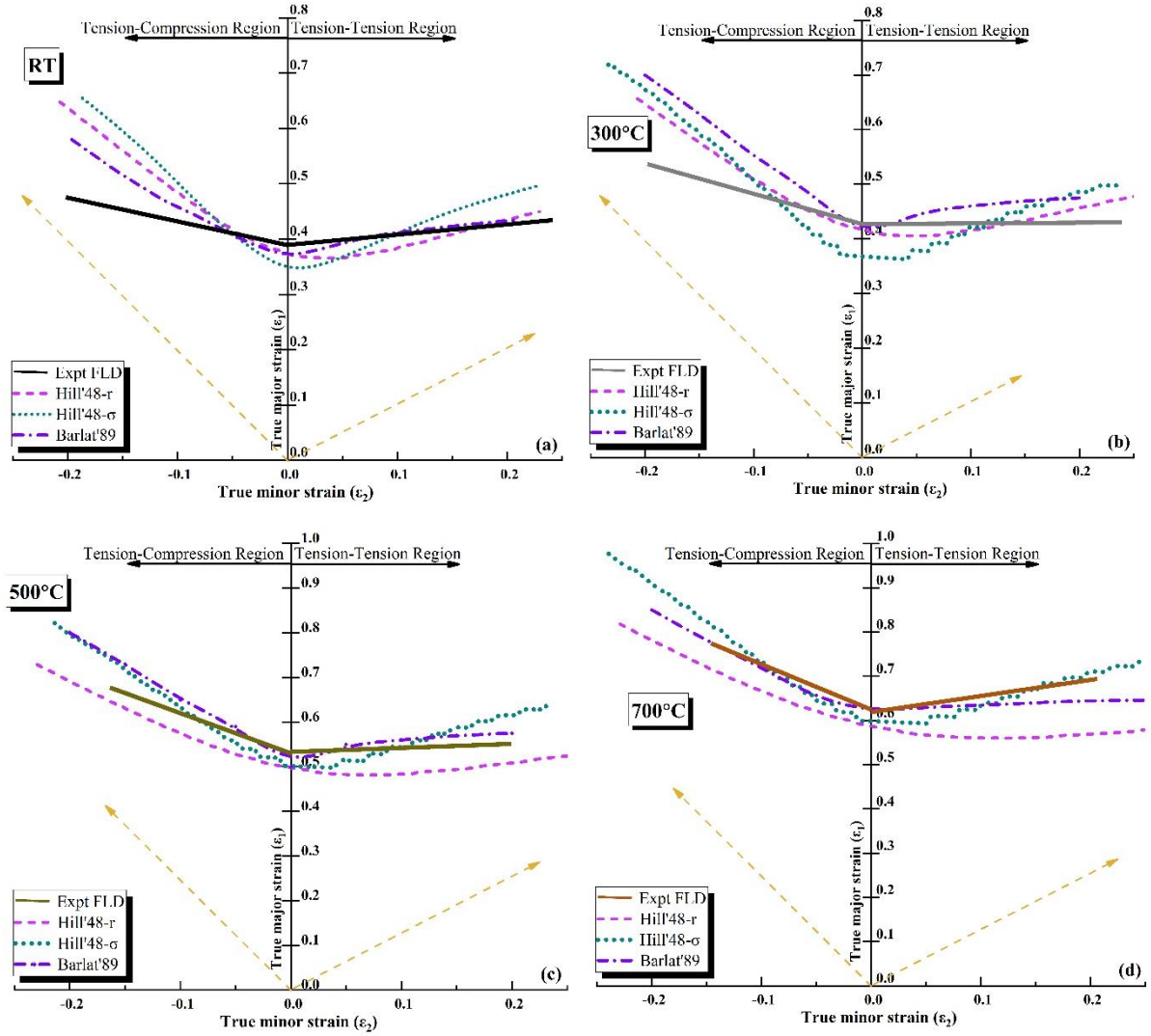

Figure 5.16 Comparison of experimental and theoretically predicted MK-FLD at (a) RT, (b) 300°C, (c) 500°C and (d) 700°C

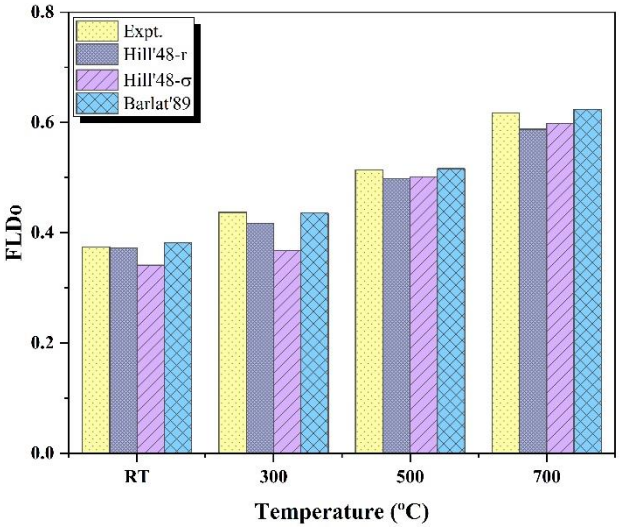

Figure 5.17 Comparison of predicted FLD_o by MK-FLD coupled with different yield criteria

In order to compare the predictive efficiency of limiting strains, deviation of predicted and experimental limiting strains is calculated along different strain paths. Respective maximum limiting strains obtained from different stretched specimens (S_1-S_6) in Nakazima test were compared with predicted strains. Statistical parameter, namely, correlation coefficient (R^2), average absolute error AAE (Δavg), root mean square error (RMSE) is used to quantify prediction error as,

$$R^2 = \frac{\sum_{i=1}^{M}(\varepsilon_{1exp}-\bar{\varepsilon}_{1exp})(\varepsilon_{1pre}-\bar{\varepsilon}_{1pre})}{\sqrt{\Sigma_i^M(\varepsilon_{1exp}-\bar{\varepsilon}_{exp})^2(\varepsilon_{1pre}-\bar{\varepsilon}_{1pre})}} \quad (5.16)$$

$$\text{AAE } (\Delta avg) = \frac{1}{M}\sum_{i=1}^{M}\left|\frac{\varepsilon_{1exp}-\varepsilon_{1pre}}{\varepsilon_{exp}}\right| \quad (5.17)$$

$$\text{RMSE, (s)} = \sqrt{\frac{\Sigma_i^M(\varepsilon_{1exp}-\varepsilon_{1pre})^2}{M}} \quad (5.18)$$

Figure 5.18 (a-c) gives a comparison of various statistical parameters for the M-K model coupled with different yield functions. The M-K model with Barlat'89 yield criteria showed good prediction compared to other criteria with least AAE and RMS, respectively. This might be because of the M-K model coupled with Barlat'89 yield criteria given good estimation of strength ratio (ρ) and strain ratio (α) compared to other yield criteria as discussed in Chapter 4.

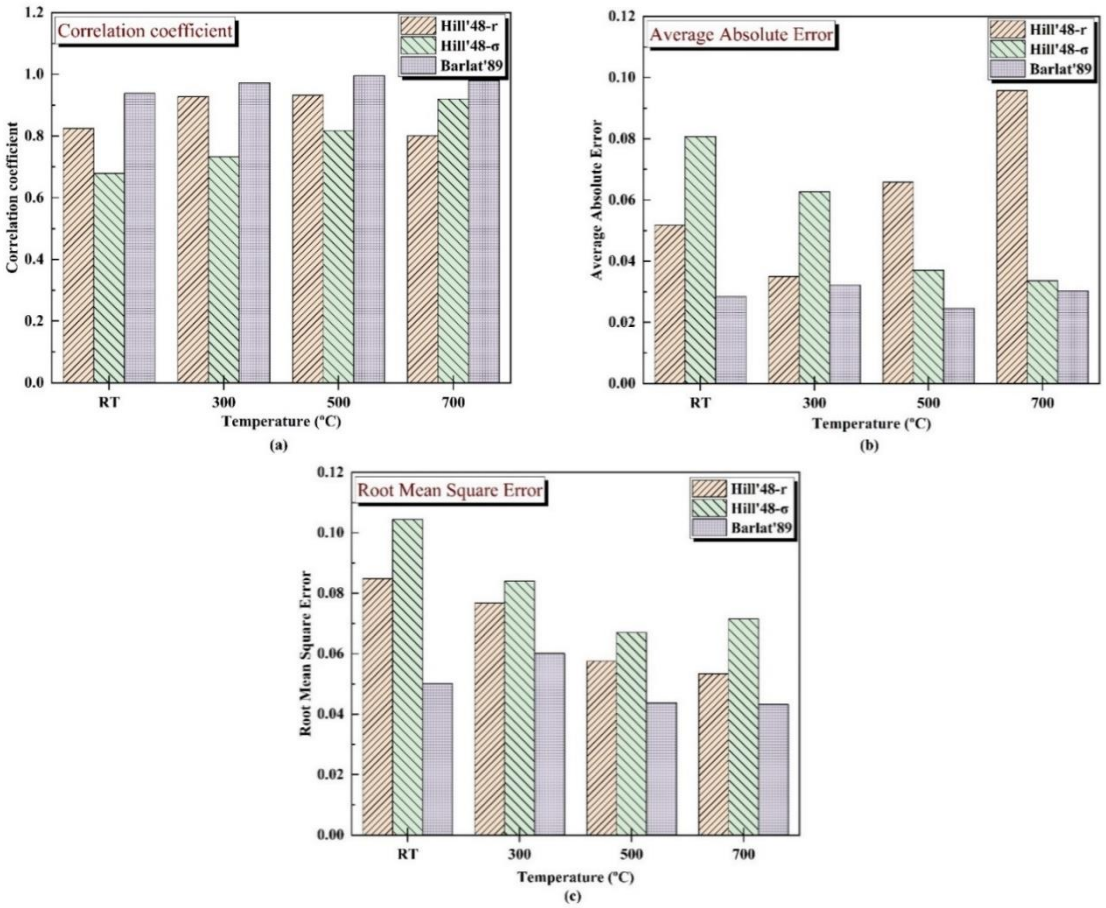

Figure 5.18 Calculated statistical parameters between experimental and predicted MK-FLDs by different yield criteria

5.5.2 Bao-Wierzbicki (B-W) Model

Most popular ductile fracture criterion is Bao-Wierzbicki (B-W) Model. This model gives a general methodology to construct fracture locus of material. Effective fracture strain or fracture ductility of material highly depends upon stress triaxiality (Bao and Wierzbicki 2004; Basak et al. 2015). In SMF operation, stress triaxiality (η) and effective plastic strain ($\bar{\varepsilon}_f$) are correlated as (Basak and Panda 2019b),

$$\bar{\varepsilon}_f = \frac{b}{3\eta} \tag{5.19}$$

where, b is an unknown parameter. Effective stress functions according to Hill'48 and Barlat'89 stress function have been calculated by using Eq. 5.20-23 and Eq. 5.24-27 respectively.

For Hill'48 yield criteria

$$\bar{\sigma} = \sqrt{\frac{r_0 r_{90}(1-\rho)^2 + r_{90} + r_0\rho^2}{r_{90}(1+r_0)}} \times \sigma_1 \tag{5.20}$$

$$\alpha = \frac{r_0}{r_{90}}\left(\frac{\rho - r_{90}(1-\rho)}{1 + r_0(1-\rho)}\right) \tag{5.21}$$

$$\xi = \frac{(1+\alpha\rho)\sqrt{r_{90}(1+r_0)}}{\sqrt{r_0 r_{90}(1-\rho)^2 + r_{90} + r_0\rho^2}} \tag{5.22}$$

$$\eta = \frac{1}{3} \times \frac{(1+\rho)}{\sqrt{\frac{r_{90} + r_0\rho^2 + r_0 r_{90}(1-\rho)^2}{r_{90}(1+r_0)}}} \tag{5.23}$$

For Barlat'89 yield criteria

$$\bar{\sigma} = \left[\frac{1}{2}\{a + a|h\rho|^p + c|1-h\rho|^p\}\right]^{\frac{1}{p}} \times \sigma_1 \tag{5.24}$$

$$\alpha = \frac{a|h\rho|^{p-1} - ch|1-h\rho|^{p-1}}{a + c|1-h\rho|^{p-1}} \tag{5.25}$$

$$\xi = \frac{(1+\alpha\rho)}{\left[\frac{1}{2}\{a + a|h\rho|^p + c|1-h\rho|^p\}\right]^{\frac{1}{p}}} \tag{5.26}$$

$$\eta = \frac{1}{3} \times \frac{(1+\rho)}{\left[\frac{1}{2}\{a + a|h\rho|^p + c|1-h\rho|^p\}\right]^{\frac{1}{p}}} \tag{5.27}$$

Further, the stress state of a material can be characterized using Lode parameter (L_p) and stress triaxiality (η). Lode parameter Lp is defined as,

$$L_p = \frac{2\sigma_2 - \sigma_1 - \sigma_3}{\sigma_1 - \sigma_3}$$

Where, $\sigma_1 \geq \sigma_2 \geq \sigma_3$. In the present stretching experiments, plane stress condition ($\sigma_3 = 0$) is assumed. Additionally, in stretching process, forming region lies between uniaxial tensions ($\sigma_1 \geq 0$, $\sigma_2 = \sigma_3 = 0$) to biaxial tension ($\sigma_1 \geq \sigma_2 > 0$, $\sigma_3 = 0$). Hence, simplified Lode parameter is expressed as,

$$L_p = \frac{2\sigma_2 - \sigma_1}{\sigma_1} \tag{5.28}$$

Critical damage term ($C_{B\text{-}W}$) is calculated as,

$$C_{B-W} = \int_0^{\varepsilon_f} \eta \, d\bar{\varepsilon} \tag{5.29}$$

Several researchers have proposed that the whole strain path till fracture should be divided into 3 segments which should be linear, piecewise fitted in case of uniaxial tensile testing (Basak and Panda 2019a). Figure 5.19 represents general strain paths followed till fracture for the uniaxial tensile test specimen.

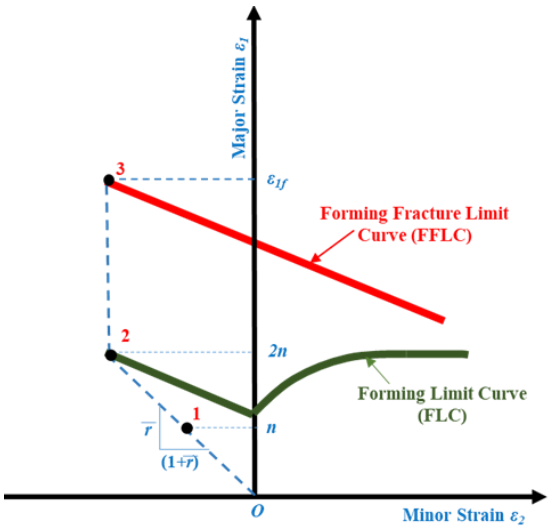

Figure 5.19 Strain path till fracture for uniaxial tensile testing

In Figure 5.19, points 1 represents the start of diffused necking, points 2 marked as onset of localized necking, and points 3 as fracture respectively. On detailed analysis, fracture strain till diffused (ε_{1d}) and localized (ε_{1l}) necking has been found as n and 2n respectively (where n is strain hardening exponent) (Basak and Panda 2019a; Lee 2005). As already discussed in Section 5.8.1, plane strain condition (α=0) is applicable up to the fracture after localized necking (Basak and Panda 2019a; Basak et al. 2015). By implying this boundary condition with two different

anisotropic yield criteria at different temperatures, values of η, ρ and ξ have been calculated by using the above Equation 3.20-27.

By using above mention yield criteria, these uniaxial strain paths can be expressed as

$$\text{Up to 0-1: } \alpha = -\frac{\bar{r}}{1-\bar{r}} = \alpha_M, \rho = f(\alpha_M) = \rho_M \text{ and } \xi = f(\rho_M) = \xi_M \tag{5.30}$$

$$\text{Up to 1-2: } \alpha = -\frac{\bar{r}}{1-\bar{r}} = \alpha_M, \rho = f(\alpha_M) = \rho_M \text{ and } \xi = f(\rho_M) = \xi_M \tag{5.31}$$

$$\text{Up to 2-3: } \alpha = 0, \rho = f(\alpha) = \rho_N \text{ and } \xi = f(\rho_N) = \xi_N \tag{5.32}$$

By utilizing above Equation 5.30-32, $C_{B\text{-}W}$ can be derived as,

$$C_{B-W} = \int_0^{\varepsilon_{1f}} \frac{\sigma_m}{\sigma_1}.\frac{\sigma_1}{\bar{\sigma}}.\frac{d\bar{\varepsilon}}{d\varepsilon_1} d\varepsilon_1 = \int_0^{\varepsilon_{1d}} \frac{(1+\rho)(1+\rho\alpha)}{3\xi^2} d\varepsilon_1 + \int_{\varepsilon_{1d}}^{\varepsilon_{1l}} \frac{(1+\rho)(1+\rho\alpha)}{3\xi^2} d\varepsilon_1 + \int_{\varepsilon_{1l}}^{\varepsilon_{1f}} \frac{(1+\rho)(1+\rho\alpha)}{3\xi^2} d\varepsilon_1 \tag{5.33}$$

$$= Q'\varepsilon_{1f} + 2n(P' - Q')$$

where, $P' = \frac{(1+\rho_M)(1+\rho_M\alpha_M)}{3\xi^2}$ and $Q' = \frac{(1+\rho_N)}{3\xi_N{}^2}$

From analysis of circular grid, it is difficult to calculate experimental major fracture strain (ε_{1f}). Therefore, ε_{1f} is considered as a function of $\bar{\varepsilon}_f$ by dividing the domain of integration into 3 linear paths piecewise. It can be calculated as,

$$\bar{\varepsilon}_f = \int_0^{\bar{\varepsilon}_f} d\bar{\varepsilon} = \int_0^{\varepsilon_{1d}} \frac{(1+\rho\alpha)}{\xi} d\varepsilon_1 + \int_{\varepsilon_{1d}}^{\varepsilon_{1l}} \frac{(1+\rho\alpha)}{\xi} d\varepsilon_1 + \int_{\varepsilon_{1l}}^{\varepsilon_{1f}} \frac{(1+\rho\alpha)}{\xi} d\varepsilon_1 \tag{5.34}$$

$$= S'\varepsilon_{1f} + 2n(R' - S')$$

where, $R' = \frac{(1+\rho_M\alpha_M)}{\xi_M}$ and $S' = \frac{1}{\xi_N}$. The $C_{B\text{-}W}$ can be determined by the relation containing both final (t_f) and initial thickness (t_0) as Basak et al. 2015.

$$C_{B-W} = \frac{2}{3}\ln\left(\frac{t_0}{t_f}\right) \tag{5.35}$$

On equating Equation 5.34 and 5.35, parameter b which is unknown can be easily evaluated as

$$b = \bar{\varepsilon}_f = \frac{2}{3}\frac{S}{Q}\ln\left(\frac{t_0}{t_f}\right) + 2n\left(R' - \frac{P'S'}{Q'}\right) \tag{5.36}$$

S´, R´, P´, and Q´are calculated using corresponding yield criterion. For Hill'48 and Barlat'89 yield criteria, these constants are calculated as per Table 5.2,

Table 5.2 Calculated Constants in Equation 5.34 & 5.36

	P´	**Q´**	**R´**	**S´**
Hill'48 yield criteria	$\frac{(1+\rho_{H1})(1+\rho_{H1}\alpha_{H1})}{3\xi_{H1}^2}$	$\frac{(1+\rho_{H2})}{3\xi_{H2}^2}$	$\frac{(1+\rho_M\alpha_{H1})}{\xi_{H1}}$	$\frac{1}{\xi_{H2}}$

Barlat'89 yield criteria	$\frac{(1+\rho_{B1})(1+\rho_{B1}\alpha_{B1})}{3\xi_{B1}^2}$	$\frac{(1+\rho_{B2})}{3\xi_{B2}^2}$	$\frac{(1+\rho_M\alpha_{B1})}{\xi_{B1}}$	$\frac{1}{\xi_{B2}}$

For Hill'48 yield criteria, $\rho_M = \rho_{H1} = \frac{H-\bar{r}G}{H+F(1+\bar{r})}$, $\xi_{H1} = f(\rho_{H1})$, $\rho_N = \rho_{H2} = \frac{H}{F+H}$ and $\xi_{H2} = f(\rho_{H2})$

For Barlat'89 yield criteria $\rho_M = \rho_{B1}$, $\xi_{B1} = f(\rho_{B1})$, $\rho_N = \rho_{B2}$ and $\xi_{B2} = f(\rho_{B2})$.

By considering anisotropic behavior, FFLD of Inconel 718 has been predicted with the help of BW model. Tensile test data (Table 3.2) have been used to evaluate parameter b. Effective fracture strains ($\bar{\varepsilon_f}$) have been evaluated using different parameter b-values within triaxiality stress range ($0.33 < \eta < 0.67$) (Basak et al. 2015; Jackson 2000). Calculated effective fracture strains have been decoupled into two components of principal fracture strains (ε_{1f} ,ε_{2f}) by two different yield criteria. Figure 5.20 gives the comparison of all calculated FFLDs with experimental data at different test temperatures.

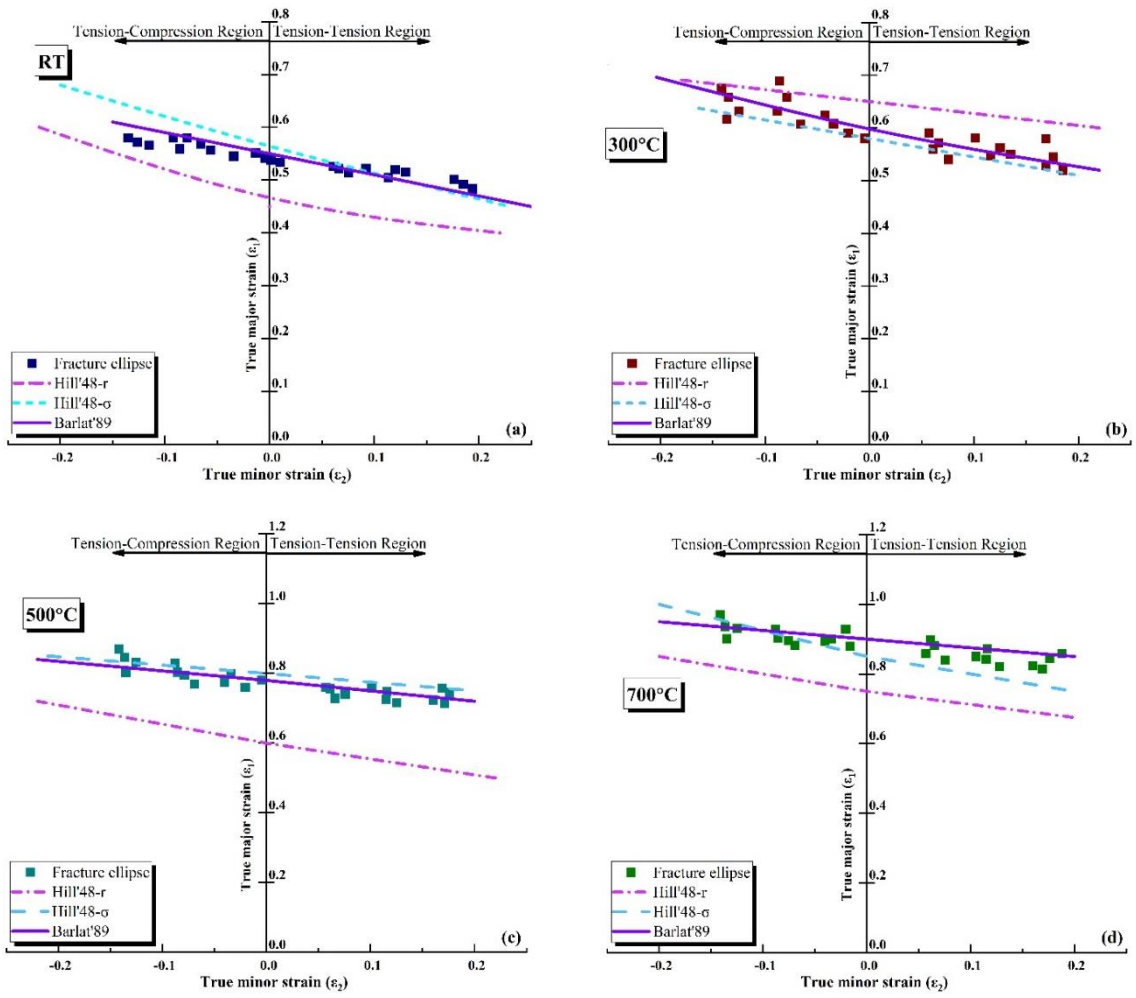

Figure 5.20 Comparison for experimental and theoretically predicted BW-FFLD at (a) RT (b) 300°C (c) 500°C and (d) 700°C

The predictive efficiency of the B-W model with different yield criteria for Inconel 718 has been evaluated by using Equation 5.16-5.18 for each tested temperature. From different strain paths of FLD, experimental minor necking strains (ε_{1n})exp. have been recorded. At this specific minor strain for each strain path, major strain (predicted,ε_{1pred}) has been calculated from respective FFLD. Figure 5.21 gives a predictive efficiency of alloy for limiting strain at fracture by B-W model. It was observed that BW model coupled with Hill'48-σ and Barlat'89 criteria shows a good prediction over Hill'48-r yield criteria. However, the B-W model with Barlat'89 yield criteria gives the best prediction of experimental fracture strains with least RMSE and AAE. From the above discussion, it can be concluded that Barlat'89 yield criteria best predict theoretical necking and failure limits of Inconel 718 alloy at test temperatures.

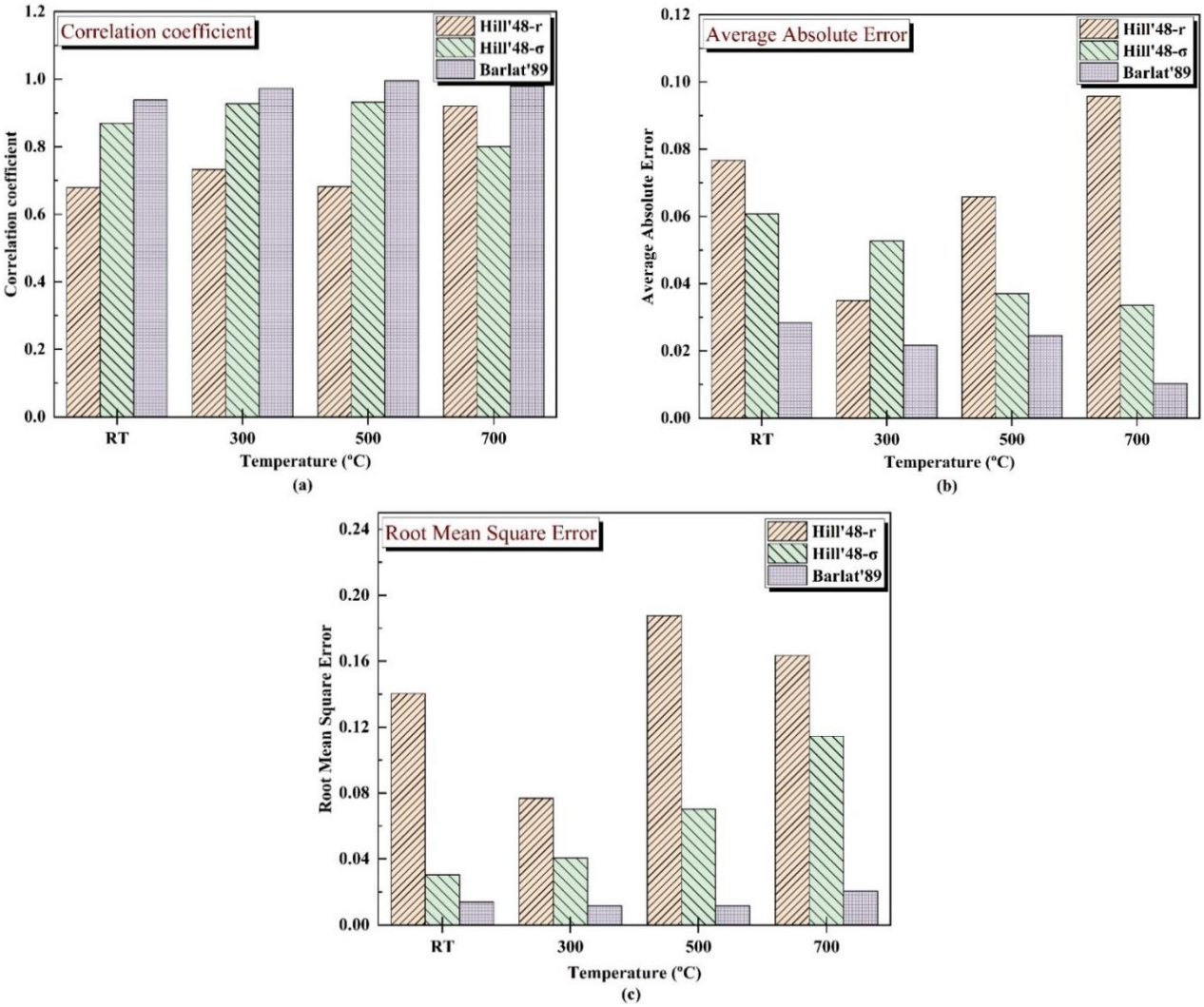

Figure 5.21 Calculated statistical parameters between experimental and predicted BW-FFLDs by different yield criteria

5.5.3 Modified Marciniak Kuczynski (M-K') Model

The traditional M-K model is commonly used to predict the localized necking in SMF (Bao and Wierzbicki 2004). An explicit algorithm is followed to solve an improved Marciniak–Kuczynski (M-K′) model with ductile fracture criteria. An integrated model is executed in MATLAB 2018a by using the Newton–Raphson method. The flow chart to execute the program is shown in Figure 5.22.

The following steps were followed for the execution of the algorithms.

Step I:

As represented in Figure 5.13, there were two regions (A and B) with a thickness t_A & t_B. Initial inhomogeneity factor (f_0), because of geometric and physical elements, is an essential assumption in the M-K model. Inhomogeneity factor or initial imperfection (f_0), it is mathematically expressed as

$$f_0 = \frac{t_A}{t_B} < 1,\ 0 < f_0 < 1 \tag{5.37}$$

Strain and stress states, in these regions (A & B), were considered with respect to ε_1^A and ε_1^B. When the ratio $\varepsilon_1^B/\varepsilon_1^A$ tends to infinity, deformation in region B was considered as localized. Yet, strain in the region A (ε_1^A) referred to as a non-significant strain compared to strains in the region B (Banabic 2010a).

Step II:

When a small increment of the principal strain ($\Delta\varepsilon_1^A$) is applied. The equivalent stress for any load state with ($\sigma_1 > 0$) is given as,

$$\bar{\sigma} = \sigma_1 . F(\rho_2),\ \rho_2 = \sigma_2/\sigma_1 \tag{5.38}$$

$F(\rho_2)$ defined by the yield criteria. To verify effectiveness of yield criteria in an integrated model, first improved M-K model estimation according to von- Mises, Hill'48 and Barlat'89 yield functions. These yield criteria are mathematically expressed as,

$$f(\sigma) = \bar{\sigma}_v^2 = \frac{1}{2}(\sigma_1 - \sigma_2)^2 + (\sigma_2 - \sigma_3)^2 + (\sigma_3 - \sigma_1)^2 \tag{5.39}$$

$$f(\sigma) = \bar{\sigma}_H^2 = F\sigma_2^2 + G\,\sigma_1^2 + H\,(\sigma_1 - \sigma_2)^2 + 2N\sigma_{12}^2 \tag{5.40}$$

$$\bar{\sigma} = \left[\frac{1}{2}\{a + a|h\rho|^m + c|1 - h\rho|^m\}\right]^{\frac{1}{m}} \times \sigma_1 \tag{5.41}$$

$$\text{Or } f(\sigma) = \frac{\bar{\sigma}}{\sigma_1} = \left[\frac{1}{2}\{a + a|h\rho|^m + c|1 - h\rho|^m\}\right]^{\frac{1}{m}}$$

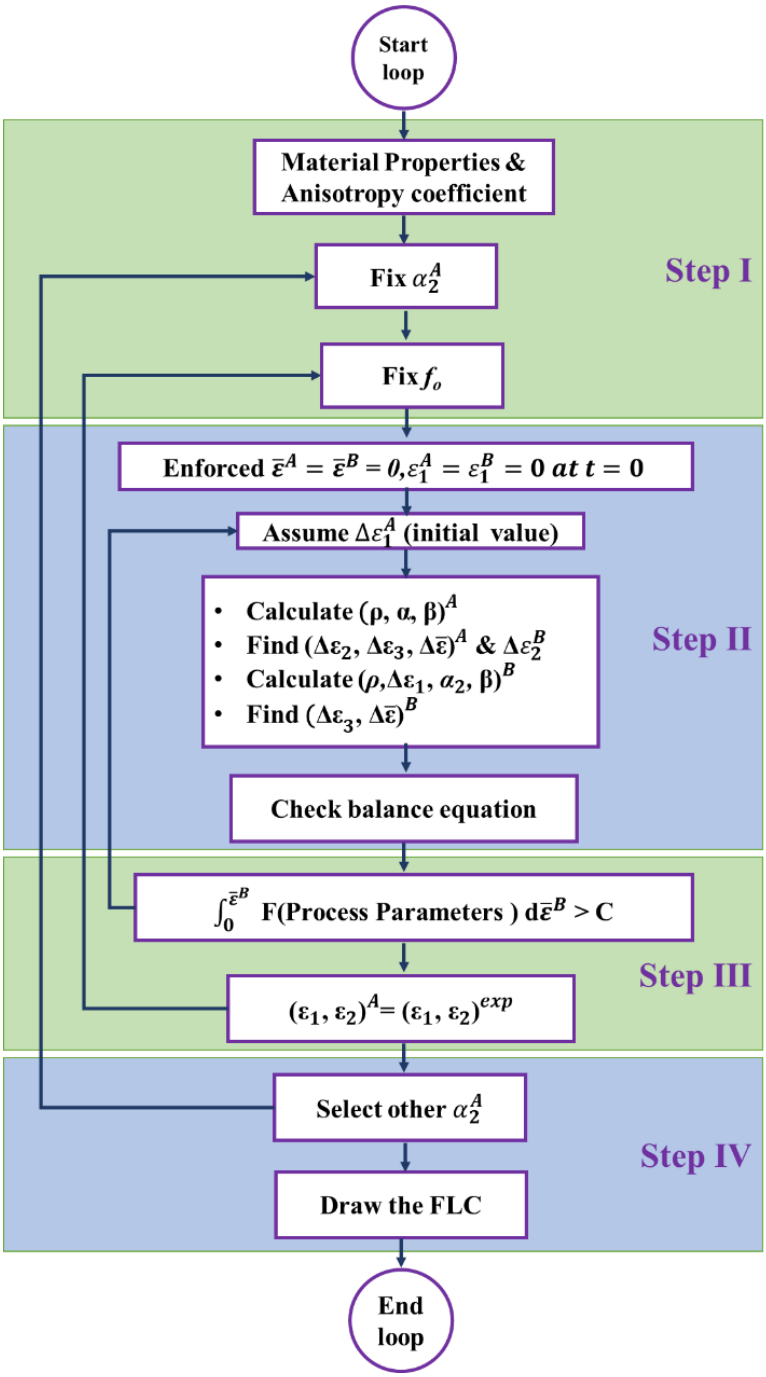

Figure 5.22 Flow chart to execute algorithm for the integrated M-K model coupled with ductile fracture criteria

The r-value based method in Hill′48 yield function was used to calculate anisotropic material constants F, G, H, and N (Basak et al. 2015). Table 4.7 gives the expression used to calculate these constants. In Barlat'89 yield criteria, m is a positive integer/exponent (for BCC materials m = 6 & FCC materials m = 8) (Banabic 2000). Anisotropy functions (h, c and a) are expressed by Lankford coefficient as,

$$h = \sqrt{\frac{r_0}{1+r_0} \times \frac{1+r_{90}}{r_{90}}} \tag{5.42}$$

$$c = 2 \times \sqrt{\frac{r_0}{1+r_0} \times \frac{r_{90}}{1+r_{90}}} \tag{5.43}$$

$$a = 2 - c \tag{5.44}$$

These anisotropy constants are shown in Table 4.9. It is observed from Figure 5.23 that von-Mises (Eq. 5.39), Hill'48 (Eq.5.40) yield criteria are not able to capture the experimental fracture data. An improved model with the Barlat'89 yield function shows the closeness to experimental data. It is reported in the literature that Barlat'89 yield function well predicts anisotropic yielding behavior of Inconel 718 (Mahalle et al. 2019a; Mahalle et al. 2020).

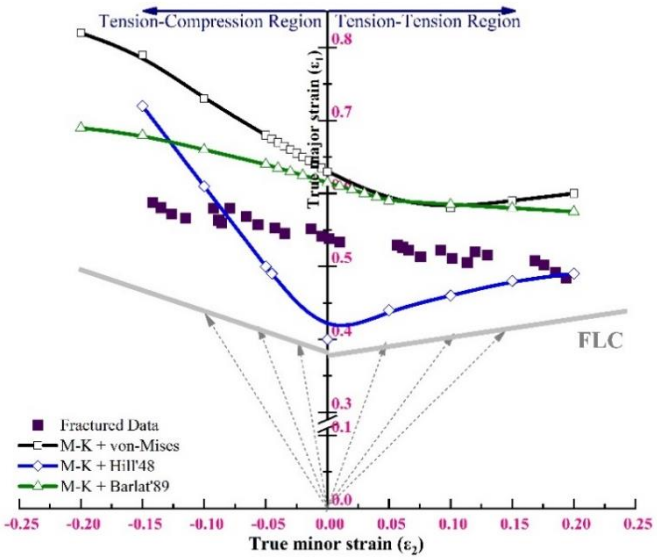

Figure 5.23 Comparison of predicted fracture curve by improved M-K model with different yield functions

Thus, Barlat'89 yield criteria is considered in the present study to define yielding behavior. Associative flow rule, Eq. 5.45, is used in Eq. 5.41 to determine the relationship between strain ($\alpha = \varepsilon_2/\varepsilon_1$) and stress ($\rho = \sigma_2/\sigma_1$) ratio as presented in Eq. 5.46.

$$d\bar{e}_{ij} = d\bar{\varepsilon}\frac{\partial\bar{\sigma}}{\partial\sigma_{ij}} \tag{5.45}$$

$$\alpha = \frac{d\varepsilon_2}{d\varepsilon_1} = \frac{a|h\rho|^{m-1} - ch|1-h\rho|^{m-1}}{a + c|1-h\rho|^{m-1}} \tag{5.46}$$

By considering the incompressibility constraint as

$$d\varepsilon_3 = -d\varepsilon_1 - d\varepsilon_2 \tag{5.47}$$

Ratio of the equivalent strain to major principal strain, by combining Eq. 5.41 and Eq. 5.47, can be expressed as,

$$\beta = \frac{d\bar{\varepsilon}}{d\varepsilon_1} = \frac{\left[\frac{1}{2}\{a + a|h\rho|^m + c|1 - h\rho|^m\}\right]^{1-\frac{1}{m}}}{a + c|1 - h\rho|^{m-1}} \quad (5.48)$$

Above equations can also be written specifically for A & B regions with principal strain ratio (α_A=$\Delta\varepsilon_2^A/\Delta\varepsilon_1^A$) and corresponding equivalent strain increment ratio (β_A = $\Delta\bar{\varepsilon}_2^A/\Delta\bar{\varepsilon}_1^A$). When plastic deformation in the region B is more than the region A, the necking initialization was noticed. Considering (i) continuity of έ in groove direction, i.e. $\Delta\varepsilon_2^A = \Delta\varepsilon_2^B$ and (ii) Normal loads equilibrium $\sigma_1^A t_A = \sigma_1^B t_B$, along interface. Thus, the principal strain ratio in region B is expressed as

$$\alpha_B = \Delta\varepsilon_2^B/\Delta\varepsilon_1^B = \alpha_A\Delta\varepsilon_1^A/\Delta\varepsilon_1^B \quad (5.49)$$

$$\frac{\partial\bar{\sigma}_B}{\partial\sigma_1^B}(\Delta\varepsilon_2^B) = \frac{\partial\bar{\sigma}_B}{\partial\sigma_2^B}(\Delta\varepsilon_1^B) \quad (5.50)$$

From Eq 5.46, principal stress ratio in the region B can be calculated as

$$a\,\alpha_2^B + c\alpha_2^B|1 - h\rho|^{m-1} = a|h\rho|^{m-1} - ch|1 - h\rho|^{m-1}$$

$$a\alpha_1^B - a|h\rho|^{m-1} + c\,(\alpha_2^B + h)\,|1 - h\rho|^{m-1} = 0 \quad (5.51)$$

From Eq. 5.49-5.51, values of α_B, $\Delta\varepsilon_1^B$ and α_2^B are calculated. As isotropic hardening behavior is assumed, a modified Swift law with temperature and έ components are given as

$$\bar{\sigma} = k_s(\varepsilon_o + \bar{\varepsilon})^n\dot{\varepsilon}^M \exp(p\bar{\varepsilon}^q + Tc_o) \quad (5.52)$$

Force-compatibility can be expressed as

$$f^B(\bar{\varepsilon}^A)^n(\bar{\varepsilon}^A)^M \exp(p(\bar{\varepsilon}^A)^q + Tc_o) = f^A(\bar{\varepsilon}^B)^n(\bar{\varepsilon}^B)^M \exp(p(\bar{\varepsilon}^B)^q + Tc_o)f_0 \quad (5.53)$$

Step III**:**

Once the parameters related to region B fulfills fracture condition, strain path inspection must be stopped. A limit point in FLD, as principal strains in region A is given as

$$\int_0^{\bar{\varepsilon}^B} \text{F(process Parameters)}\, d\bar{\varepsilon}^B > C \quad (5.54)$$

Table 5.3 gives most used ductile fracture criteria, which defines the influence of strain histories and stress. It was considered that fracture condition is satisfied in the region B of the specimen when integral tends to unity. The generalized integrals for ductile fracture criteria can be expressed as,

$$J = \int_0^{\bar{\varepsilon}_f} \text{F}(\textit{process parameters})\, d\bar{\varepsilon} = \int_0^{\varepsilon_{f1}} \text{F}(\textit{process parameters})\, \beta\, d\varepsilon_1 \quad (5.55)$$

Table 5.3 Different ductile fracture Criteria and considered Integrals

Criterion	Expression	Integral
Brozzo (Brozzo, De Luca, and Redina 1972)	$\int_0^{\bar{\varepsilon}_f} \frac{2\sigma_1}{3(\sigma_1-\sigma_m)}\, d\bar{\varepsilon} = \int_0^{\varepsilon_f} \frac{2}{3}\cdot\frac{1}{\left(1-\frac{\sigma_m}{\sigma_1}\right)}\cdot d\bar{\varepsilon} = C_1$	$J_1 = \frac{1}{C_1}\int_0^{\varepsilon_f} \frac{2}{3}\cdot\frac{1}{\left(1-\frac{\sigma_m}{\sigma_1}\right)}\, d\bar{\varepsilon}$
Cockcroft and Lathan 1968	$\int_0^{\bar{\varepsilon}_f} \sigma_{max}\, d\bar{\varepsilon} = C_2$	$J_2 = \frac{1}{C_2}\int_0^{\bar{\varepsilon}_f} \sigma_{max}\, d\bar{\varepsilon}$
Clift et al. 1990	$\int_0^{\bar{\varepsilon}_f} \bar{\sigma}\, d\bar{\varepsilon} = C_3$	$J_3 = \frac{1}{C_3}\int_0^{\bar{\varepsilon}_f} \bar{\sigma}\, d\bar{\varepsilon}$
Oyane et al. 1980	$\int_0^{\bar{\varepsilon}_f} \left(\frac{\sigma_m}{\bar{\sigma}}+C_4\right) d\bar{\varepsilon} = C_5$	$J_4 = \frac{1}{C_5}\int_0^{\bar{\varepsilon}_f} \left(\frac{\sigma_m}{\bar{\sigma}}+C_4\right) d\bar{\varepsilon}$

Table 5.3 defines the integrals for considered ductile fracture criteria. Experimentally determined principal strains, related to fracture along various strain paths, were translated in effective plastic strain effective stress $\bar{\sigma}$ by Eq. 18. The minor and major true stresses were calculated by evaluating $\bar{\sigma}$ by Equation 5.52 and stress ratio (ρ). The material constants $C_{1\text{-}5}$ are evaluated by Table 5 with uniaxial ($\bar{\sigma} = \sigma_1$ & $\sigma_2 = \sigma_3 = 0, \frac{\sigma_h}{\bar{\sigma}} = \frac{1}{3}$) and equi-biaxial tensile stress states $\left(\sigma_1 = \sigma_2, \sigma_3 = 0, \frac{\sigma_h}{\bar{\sigma}} = \frac{2}{3f}\right)$. With the principal stress ratio ρ_2 = 0, α = β = 1 (for uniaxial stress states) and $\phi = [\frac{1}{2}\{a + a|h|^m\}]^{\frac{1}{m}}$, $\beta = \frac{2f^{m-1}}{a}$ (for equi-biaxial tensile stress states) respectively. Table 5.4 gives the damage parameters for four considered fracture models. The above models were considered for fracture locus prediction and also validated with the experimental data.

Table 5.4: Calibrated fracture model parameters for Inconel 718 alloy

Calibrated Fracture Models	Damage Parameters	Values
Brozzo	C_1	23.67
Cockcroft & Latham	C_2	384.71
Clift	C_3	681.26
Oyane	C_4	0.55
	C_5	1.12

Step IV**:**

Limiting/ principal strains $\Delta\varepsilon_1^A$ and $\Delta\varepsilon_2^A$ in the region A, defines a point in the FLD. Variation of f_0 helps to understand relation between theoretical and experimental FLD under the plane strain condition (α = 0). With a variation of strain ratio ($0 < \alpha^A < 1$), different strain points in FLD can be attained.

The position of the forming limit curve highly depends upon inhomogeneity factor (f_0), sheet thickness, strain hardening coefficient (n), anisotropy, strain rate sensitivity (m), and shape of yield function (Basak and Panda 2019a; Kotkunde et al. 2017). Further, the inhomogeneity factor (f_0) is highly dependent on the sheet thickness, material properties, surface quality, and grain size (Banabic 2010a). Previous studies reported that sheet metals in stretching might have different yield surfaces due to intrinsic physical characteristics (Kuroda and Tvergaard 2000). For accurate FLD prediction, f_0- value was varied for all probable combinations of yield function and hardening laws. Figure 5.24 shows the effect of f_0 variation on improved M-K model (M-K′) with Barlat'89 yield function. The best predicted integral M-K FLD for Inconel 718, was given at a strain ratio ($\alpha = 0.055$) and inhomogeneity factor (f_0 = 0.99). Material failure is defined as

$$\frac{d\overline{\varepsilon_A}}{d\overline{\varepsilon_B}} < W \tag{5.56}$$

To ensure the adequate deformation (necking) in the region B compared to those of A, Integer W must be small. From previous literature, W=0.15 is taken for the analysis (Mahalle et al. 2020). It can be seen from Figure 5.24 that variation of f_0 for particular combination hardening law and yield criteria, follows a general trend. Since the f_0 –value is increasing, whole curve is shifted in a positive y-direction. f_0 –value denotes the maximum extent of thinning in groove region. This actually makes region B more liable to necking and results in an increasing deformation rate in comparison to region A. For f_0 = 0.99, the predicted fracture curve shows good agreement in uniaxial tension region, but it overestimates. These results signify a non-negligible effect of the strain path on predicted fracture strains. Hence, it is essential to introduce a criterion relating process parameters, meanly represent deformation history effect, for example ductile fracture criteria, which mainly depends on plastic deformation of a metal.

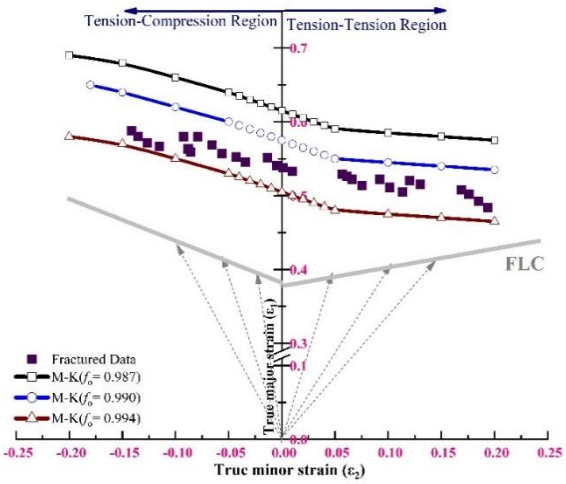

Figure 5.24 Effect of f_0 - variation on improved M-K model with Barlat'89 yield function

Figure 5.25 gives a comparison of the predicted fracture curve by improved M-K models coupled with different ductile criteria and experimental data (For f_0 = 0.99). It is observed that the integrated model with different ductile criteria was unable to represent complete experimental data. An integrated model with Oyane's ductile criteria shows a better prediction compared to other criteria. Especially, it shows better agreement with experimental data in biaxial tension region. Other improved models with three ductile criteria show nearly catastrophic predictions, which generally inadequate for most strain paths. Namely, improved M-K models with Clift and Cockcroft and Latham ductile criteria considerably underestimate the fracture strain values in all the deformation region. Whereas improved M-K models with the Brozzo's ductile criterion show sharp decrease as strain path changes from uniaxial tension to biaxial tension region, i.e. degree of biaxiality increases. Overall, the integrated model by combining Oyane's criterion in improved M-K model shows considerable performance with experimental values in all deformation regions, mainly effective in biaxial tensile region.

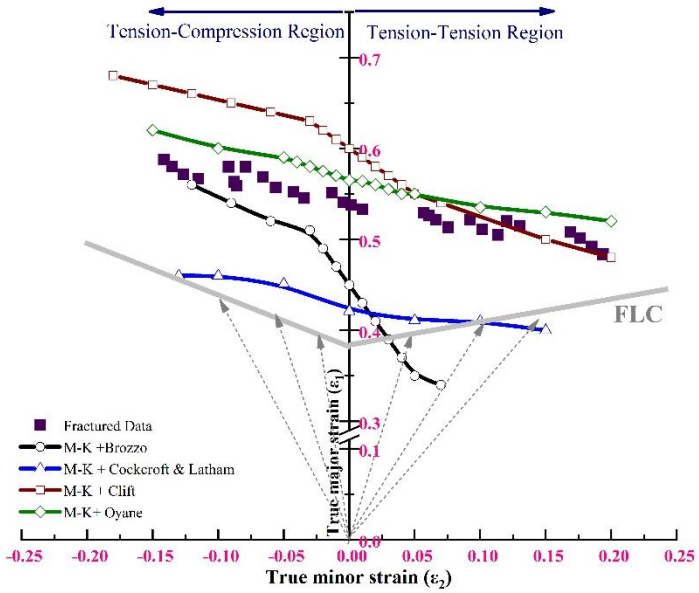

Figure 5.25 Comparison of predicted curve by improved M-K model with different fracture criteria

As initial thickness imperfection affects significant levels of the FFLD, this value must be selected properly. Figure 5.26 shows the effect of inhomogeneity factor on fracture strain values. This results in raising the fracture limits and as a result, FFLD shifts upwards. The best fit between the theoretical model and experiments for biaxial tensile region was found at an inhomogeneity factor (f_0) of 0.987 value.

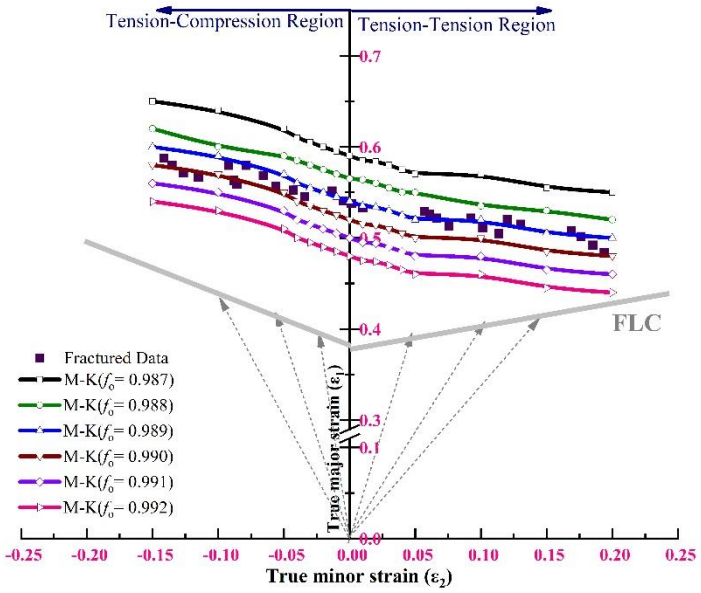

Figure 5.26 Effect of f_0 - variation on predicted curve by improved M-K model with Oyane's fracture criteria

In order to check the prediction accuracy of the considered fracture model for Inconel 718, experimental fracture limits were considered as a reference. Figure 5.27 represented the evaluated statistical parameters (R, RMSD & Δ_{avg}) for Inconel 718 alloy. First, R^2 was evaluated for all models and shown in Figure 5.27 a. Among all, improved M-K model coupled with Clift's and Oyane's fracture criteria shows better and comparable R-value. The minimum of R^2-value (R^2< 0.76) was observed for an improved M-K model with Brozzo's fracture criteria. Since R-value is a biased parameter and its values may be biased towards higher or lower data, other parameters (Δavg & RMSD) are required for comparison (Mahalle et al. 2019b). An improved M-K model coupled with Oyane's fracture criteria, shows least Δ_{avg}(0.075) and RMSD (0.105) with respect to the experimental values. Worst predictability (Δavg = 0.304) was displayed by improved M-K model coupled with Brozzo's criteria. By considering statistical parameter variation, the improved M-K model coupled with Oyane's fracture criteria is best suitable for fracture locus prediction of Inconel 718 alloy with higher accuracy. Generally, the position of FLD depends upon inhomogeneity factor (f_0), sheet thickness, anisotropy, strain hardening coefficient, strain rate sensitive, and shape of yield function (Banabic 2010a; Kuroda and Tvergaard 2000). At f_0 = 0.987, improved M-K model coupled with Oyane's fracture criteria shows a good agreement with the experimental data.

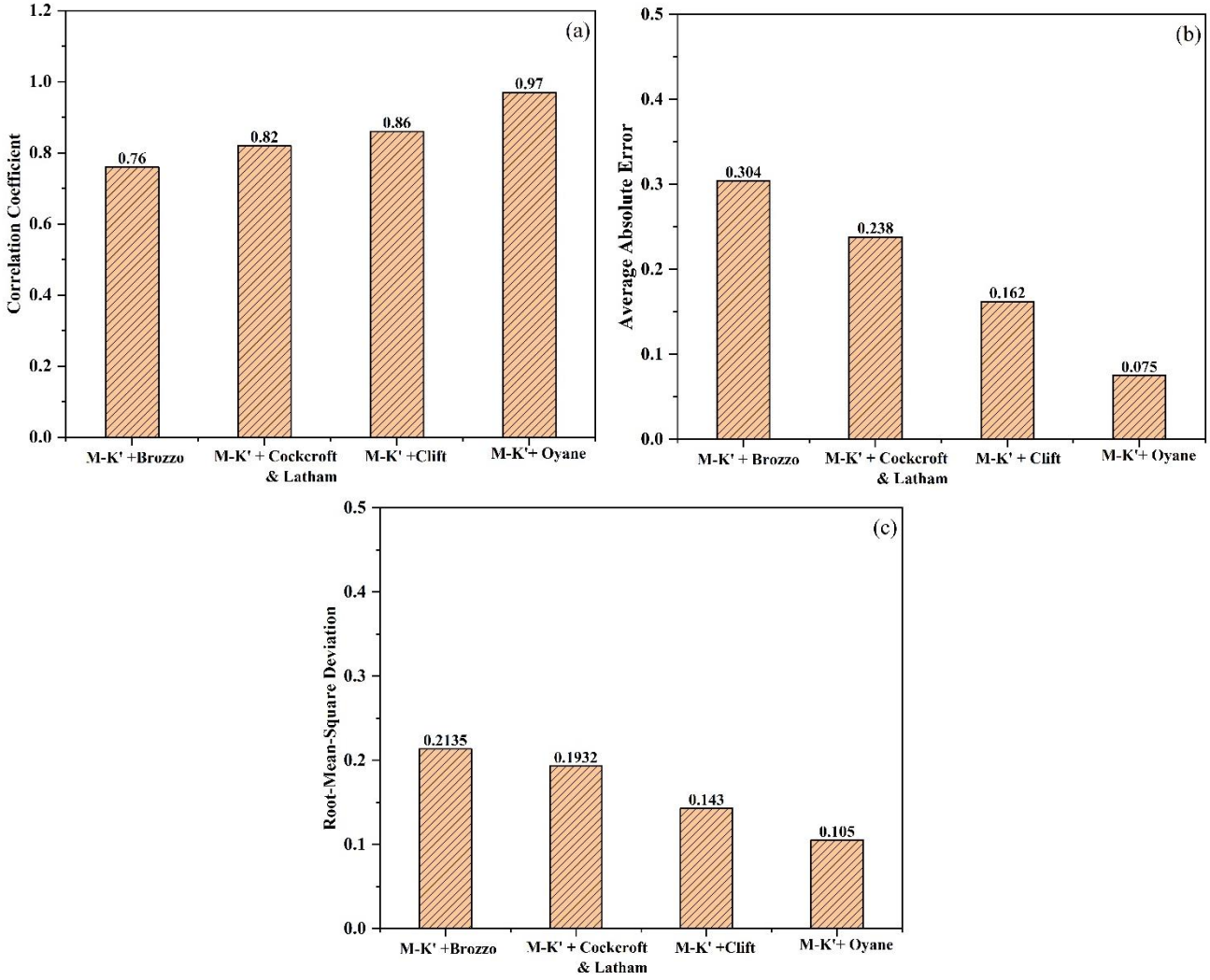

Figure 5.27 Deviation of improved models in terms of statistical parameters w.r.t. experimental data

5.6 Finite Element Analysis of SMF Process

In preliminary designing, FE simulation helps to understand the actual forming process with applied constraints and predict the possible defects/errors which helps for refinement of product at early stage of design before actual forming of product. This saves the experimental try-outs and enhances productivity while manufacturing. The ABAQUS-Explicit-SIMULIA™ is used for simulation among several available FE analysis codes for SMF at different test temperatures. Explicit analysis mode is used extensively due to nonlinearity in geometry with complex contact between stationary parts and moving. Various process parameter effects on formed products are studied along with material behavior in different test conditions. Figure 5.28 outlines the basic steps for conducting a representative FE simulation of a stretch forming process.

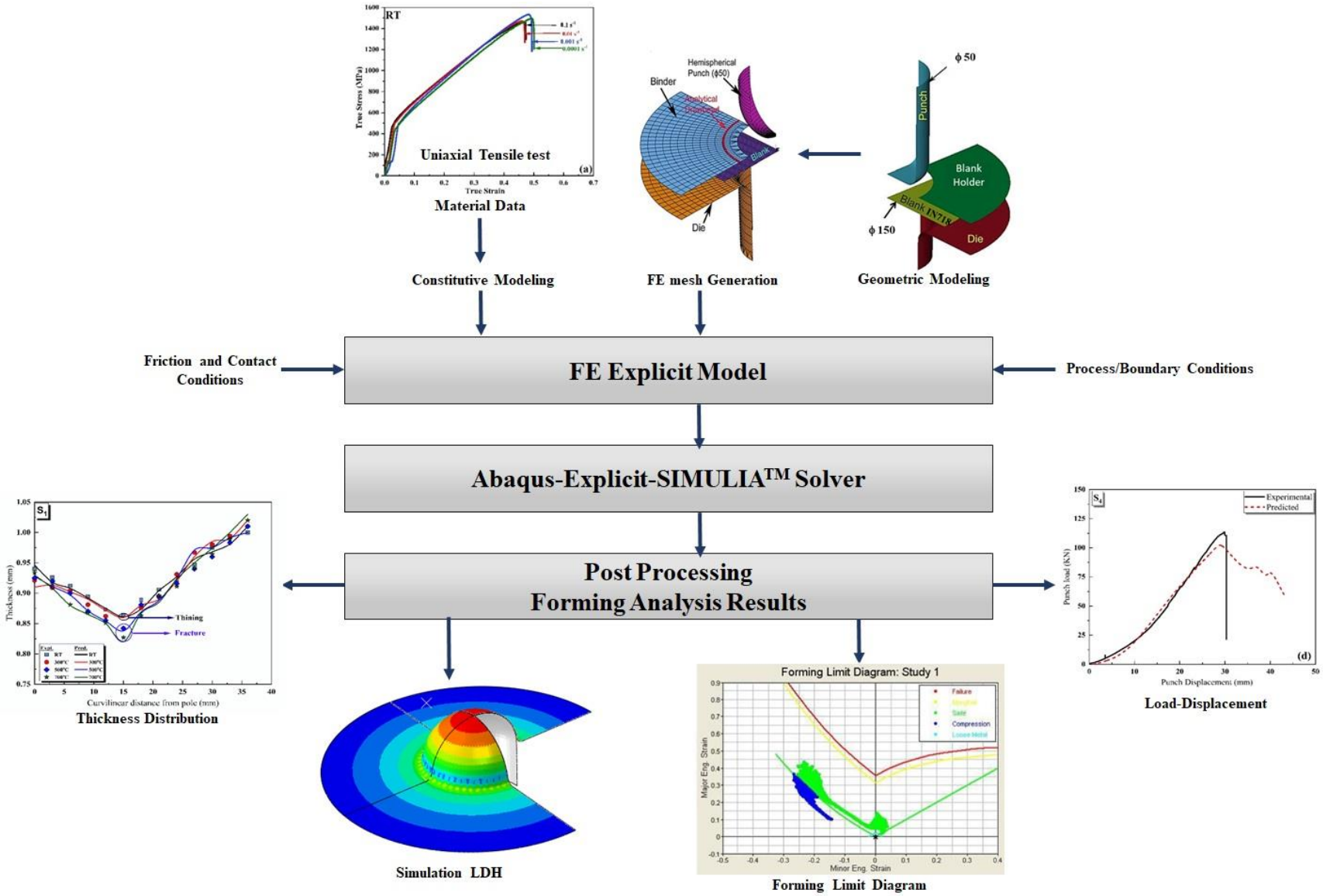

Figure 5.28 Schematic representation for FE simulation of sheet metal stretch forming process

5.6.1 Pre-processing for Stretching and Boundary Conditions

A quarter input FE model was developed in ABAQUS-Explicit-SIMULIA™ version 6.14 due to symmetric geometry and to reduce total computational time. ABAQUS-Explicit-SIMULIA™ contains numerous programmed functions to aid even for the complex tool geometry. Figure 5.29 gives FE simulation model of stretch forming set up with a blank, die, blank holder and hemispherical bottom punch respectively. Table 5.5 gives the tool dimensions for FE studies of stretch forming process (similar dimension followed as experimental tool set up). The circular draw bead is considered at 72 mm diameter in dies to restrict the material flow from flange region. It also prompts the tensile stretching of Inconel 718 blank (t =1 mm). Die, blank holder and hemispherical bottom punch are consigned as the rigid bodies. Inconel 718 blank is considered as a deformable body, including Hill-48 anisotropic quadratic (MAT-122) yield function. It was meshed by the C3D8R shell elements. Material properties of Inconel 718 alloy have been considered as input to FE simulation. These properties are already evaluated at different test conditions and presented in Chapter 3. Table 5.6 and Table 5.7 give the material properties for Inconel 718 sheet at test temperatures. Die is consigned as a fixed body and hemispherical bottom punch is progressed downward in the Z-direction with the trapezoidal velocity-profile. Blank holding pressure (in 0-20 MPa range) is also applied as per geometry of blank in the downward direction. Surface to surface contact forming is adopted with friction coefficient between blank and tool. The friction coefficient is taken from the literature (Table 5.7). Hill'48 anisotropic plastic potential has been selected as a material model in the numerical simulation at various test temperatures.

Stretch forming results were validated by means of thickness distribution limiting dome height (LDH) and forming limit curve (FLC). Experimentally considered different blank diameters and BHF were implemented in numerical simulation for validation reasons.

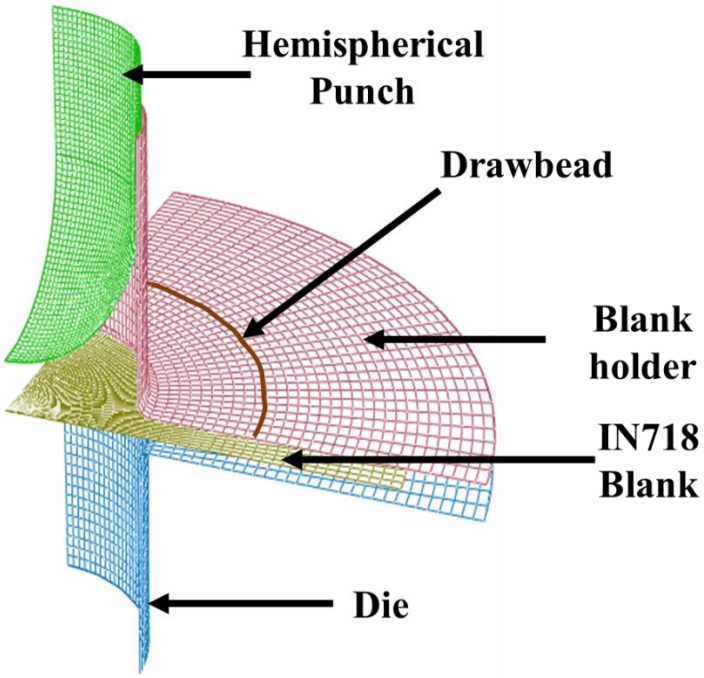

Figure 5.29 Quarter symmetric FE model for stretching process

Table 5.5 Tool dimensions for stretch forming

Parameters	Values (mm)
Punch Diameter	50
Outside die diameter	220
Inside die diameter	54
Die nose radius	4
Blank specimen	S1-6
Sheet thickness	1

Table 5.6 Physical Properties for Inconel 718 sheet at room temperature

Parameters	Values
Density (g/cm^3)	8.192
Poisson's ratio	0.294
Thermal conductivity (W/m×K)	11.4
Specific heat capacity J/g×°C	0.435
Thermal coefficient of linear expansion (α) (×10^{-6} K^{-1})	13

Table 5.7 Material properties as an input for FE analysis

Temperature (°C)	**Yield tensile stress (MPa)**	**Ultimate tensile stress (MPa)**	**Anisotropy coefficients**				**Total elongation**	**Strain-hardening exponent**	**Hardening coefficient (MPa)**	**Modulus of Elasticity (GPa)**	**Coefficient of friction**
	s_{yavg}	s_{utavg}	r_0	r_{45}	r_{90}	$(r)_{avg}$	$(\%)_{avg}$	$(n)_{avg}$	k_{avg}	E_{avg}	μ
RT	505.64	951.92	0.7813	0.9471	1.0432	1.0665	41.97	0.3912	2028	0.205	0.175
100 °C	486.30	873.52	0.7737	0.7798	0.9169	1.0877	44.20	0.4158	1986	0.196	0.17
200 °C	443.91	863.58	0.9694	0.8765	0.9655	1.0121	47.75	0.4169	1903	0.191	0.16
300°C	424.20	844.40	0.997	1.0952	0.9694	0.9580	48.16	0.4215	1801	0.184	0.15
400°C	394.66	819.73	0.8808	0.8972	0.9177	0.9231	49.22	0.46	1756	0.180	0.1
500°C	370.83	781.33	0.9971	1.0953	0.9694	0.7196	51.91	0.4631	1656	0.162	0.1
600°C	358.57	762.14	1.1423	0.9694	0.9174	0.7086	53.62	0.49	1485	0.158	0.1
700°C	343.58	753.22	1.1231	1.3361	1.1321	1.231	54.78	0.5983	1385	0.154	0.1

Average = $(X_0 + 2X_{45} + X_{90})/4$ where X is n or k-value or r-values

Mesh convergence study on all six blanks of Inconel 718 alloy at room temperature condition has been performed in order to get desired results in less computational time. A five-level refinement scheme has been adopted with the assumption of five thickness integration points. Table 5.8 gives final computational time with number of elements and final mesh size. The error of LDH (difference between experimental and FE study) and computational time are measured to finalize mesh size. This is further used to perform FE studies for all test temperatures.

Table 5.8 Mesh sensitivity analysis for Stretch forming

Specimen	**Element Size** (mm)	**Total elements on Blank**	**Computational Time** (s)
S_1	1.5x1.5	1215	3962
S_2	1x1	1492	4695
S_3	1x1	1306	4391
S_4	1x1	1288	4211
S_5	1x1	1251	3985
S_6	1x1	1196	3465

5.6.2 Finite Element Analysis of Stretching Process

The qualitative aspects of stretch forming process, namely load-punch displacement, limit dome height, thickness distribution and forming limit diagram, have been investigated and validated with experimental and theoretical outcomes.

Load−displacement curves

In ABAQUS software, punch speed for FE simulation was selected based on experimental quasi-static condition of stretch forming. Figure 5.30 gives the simulated punch displacement vs punch load profiles and compared with experimental values for different specimens at room temperature condition. It is observed that there is a good agreement between experimental tests results and numerical investigations. It is noted that initially, experimental and numerical punch load–displacement curves increase consistently, then reach a maximum value when fracture takes place, finally followed by a sudden decrease in punch drawing force. However, force reduction intensity in the experimental load–displacement curve is more evident than numerically investigated.

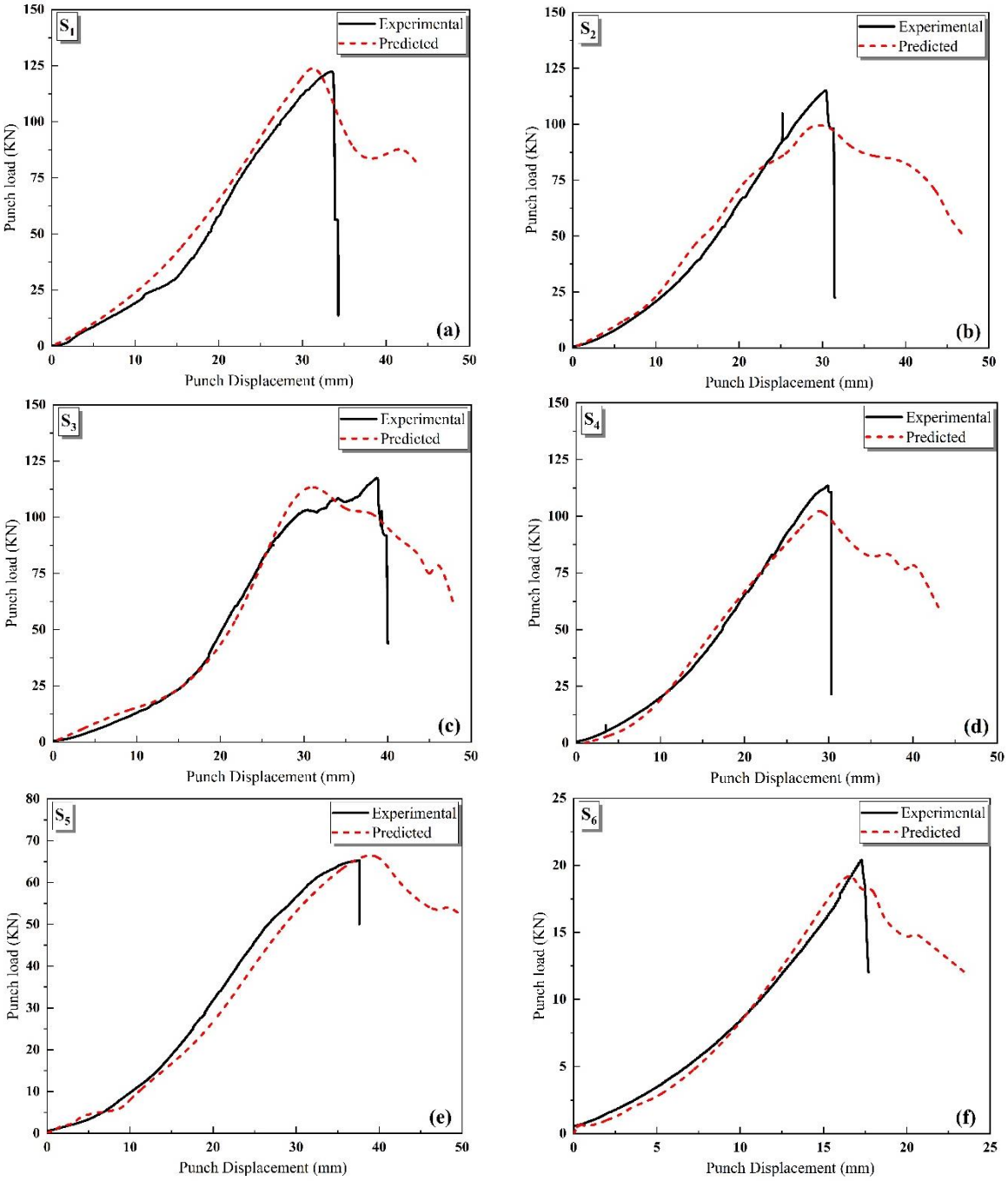

Figure 5.30 Punch load−displacement comparison of experiments and FE Analysis for samples (a) S_1; (b) S_2; (c) S_3; (d) S_4; (e) S_5 and (f) S_6 at RT conditions.

Limiting Dome Height

For better understanding, the difference of experiment results with numerical prediction of punch displacement till sheet necking, comparison of experimental and numerical results for punch displacement in terms of limit dome height at room temperature is shown in Figure 5.31 LDH is an important parameter that helps to understand the drawability of different width sheet specimens at different test temperatures (*Brammar & Harris, 1975*). LDH is measured as the drawn height of a formed cup just before occurring of fracture (until sheet necking). It is noticed

that the error values for specimens less than 5% except for specimen S_2. It indicates that numerically predicted punch displacement is close to the experiment values for these specimens. Therefore, blank holding pressure (BHP) is an important parameter that can affect LDH i.e., punch displacement till sheet necking. For specimen S_5 may be the selected BHP is not appropriate, which causes a difference of limit dome heights.

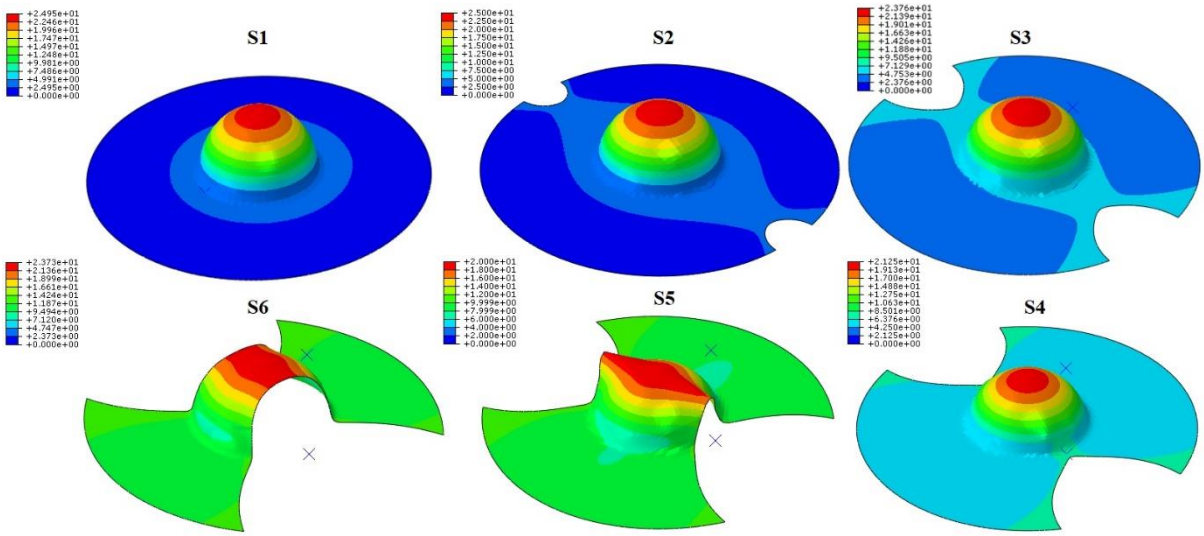

Figure 5.31 Limit Dome height for different specimen geometry at RT

The variation experimental and predicted LDH with temperature in Inconel 718 alloy is shown in Figure 5.32(a-b). The predicted LDHs is observed within 0.5-3% error range. It is observed that LDH is directly proportional to testing temperature and width of the specimen. High limit dome height at RT due to high strain hardening exponent at room temperature. High strain hardening exponent at RT results in low tendency of localized necking at critical areas of the deformed specimen as a result high LDH is observed (Dieter 2011). Dome height increases with a rise in temperature. This might be due to a decrease in strain hardening coefficient. Therefore, LDH or total elongation is highly sensitive to temperature.

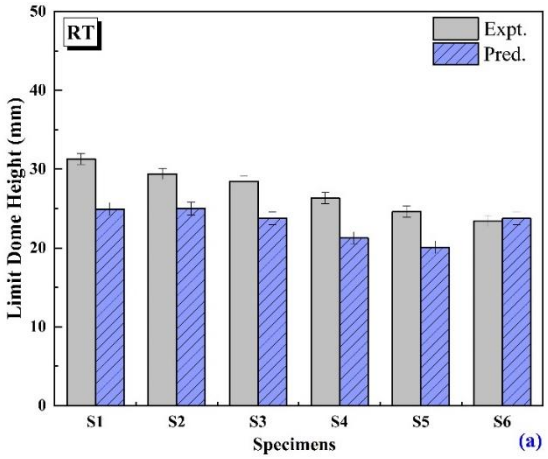

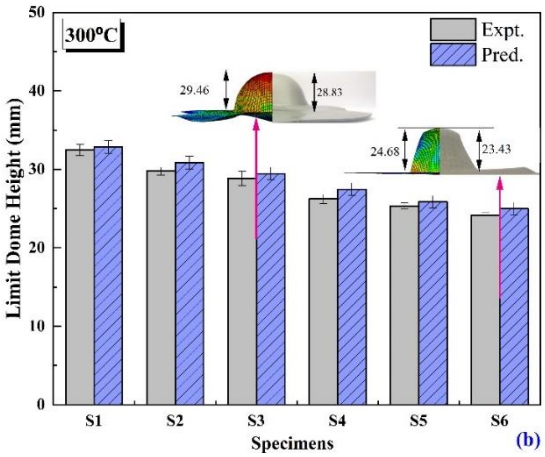

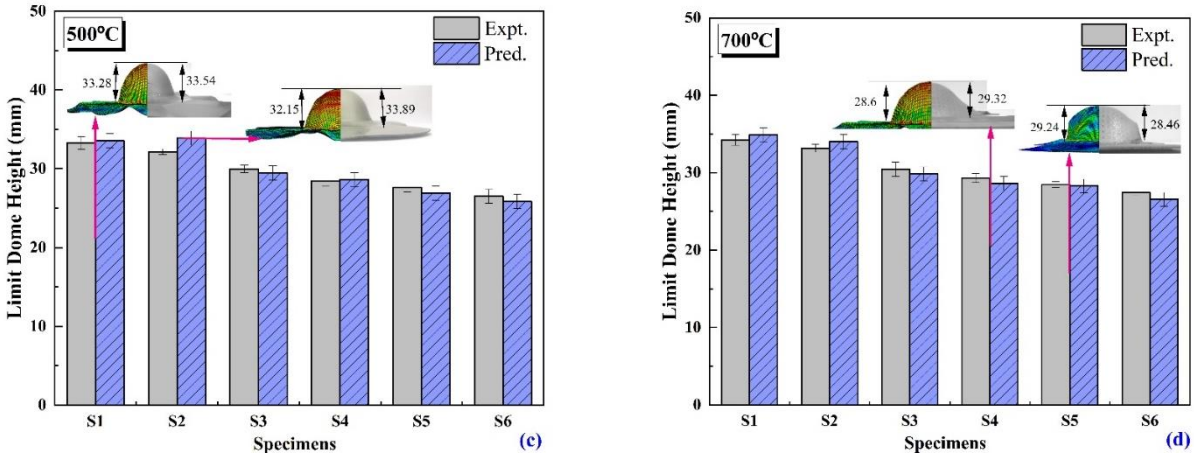

Figure 5.32 Comparison of predicted and experimental LDHs of Inconel 718 specimens at (a) RT (b)300ºC (c)500ºC and (d) 700ºC.

Thickness Distribution

Thickness distribution is another important qualitative aspect of stretch formed specimens. Numerical analysis has been carried out for specimens with variation of temperature from RT to 700ºC. Normalized experimental and predicted thickness distribution of S_1 and S_6 specimens with curvilinear distance from pole is given in Figure 5.33. It is observed that the thickness of stretched specimens remains constant initially and then it starts declining. Minimum thickness is observed at a location wherever necking and fracture occur. Thickness then is raised gradually till the flange part of the specimen. Thickness on the flat flange part of the specimen is nearly equal to the original sheet thickness. Comparable nature of the curve is observed at tested temperatures for different samples. Thickness is decreasing with increase in test temperature because of thermal softening and hence improved in ductility at high temperature. Even rise in the temperature leads to decrease of strain hardening exponent and hence localized thinning tendency is higher (Dieter 2011).

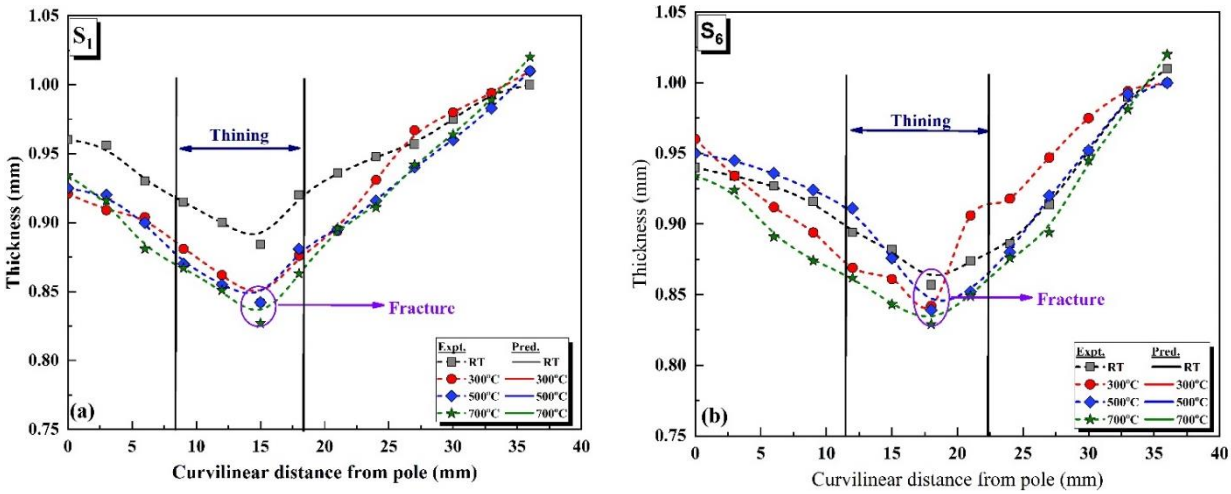

Figure 5.33 Experimental and predicted thickness distribution for (a) S_1 (b) S_6 with all test temperatures

Summary

This chapter deals with the experimental, theoretical and numerical investigations about Forming and Fracture Limit Diagrams of Inconel 718 alloy at elevated temperatures. Nakazima test has been used to determine the forming and fracture limits of alloy. Further, theoretical forming and fracture limits are determined by Marciniak-Kuczynski (M-K), Modified Marciniak Kuczynski (M-K) Model, and Bao-Wierzbicki (B-W) Models respectively. These experimental and theoretical findings are validated with numerical analysis of Inconel 718 alloy. Formability behavior by means of limit dome height (LDH) and thickness distribution were determined.

Thus, the next chapter mainly covers the experimental and numerical studies of Yoshida Buckling test which provides a reference for wrinkling instability of Inconel 718 alloy.

6. Experimental & Numerical Studies of Wrinkling Limit Diagram

Wrinkling is generally considered an undesirable defect during the SMF process. The wrinkling in the final sheet metal component seriously affects the functional requirements and aesthetic appeal of the final product. Particularly, it is highly unacceptable in outer skin panels of components where final component appearance is vital. Wrinkling instability on contact surfaces can negatively influence part assembly and its function. Also, other post-processing operations such as welding, machining affect drastically due to wrinkle defects in the sheet components. Testing/processing may damage tooling along with critical wrinkles. Therefore, prevention and prediction of wrinkling instability during the SMF process is very crucial.

This chapter is focused on a systematic investigation of experimental testing, i.e., modified Yoshida buckling test (YBT) to define the occurrence of wrinkling instability for in-plane compression in the SMF process. Further experimental and FE studies have been coupled to understand the crucial behavior of wrinkling at elevated temperatures. Finally, forming, fracture, and wrinkling limit curves of Inconel 718 have been successfully estimated to understand the complete formability behavior at elevated temperatures.

6.1 Experimental Yoshida buckling test

Yoshida buckling test (YBT) is used to investigate wrinkling tendencies of Inconel 718 alloy at different temperatures. The main aim is to replicate the physics behind the wrinkling occurrence by in-plane compression in diagonal direction. In YBT, a square metal sheet is subjected to in-plane tension in one diagonal direction as given in Figure 6.1. Stress-strain analogy between YBT specimen and edge of the flange of the deep drawn cup is schematically illustrated in Figure 6.2. The outer flange section (shown in the dark gray) is mainly subjected to the circumferential compressive stress and also considered as clamped along the radial direction because of drawing constraints along a circumferential direction.

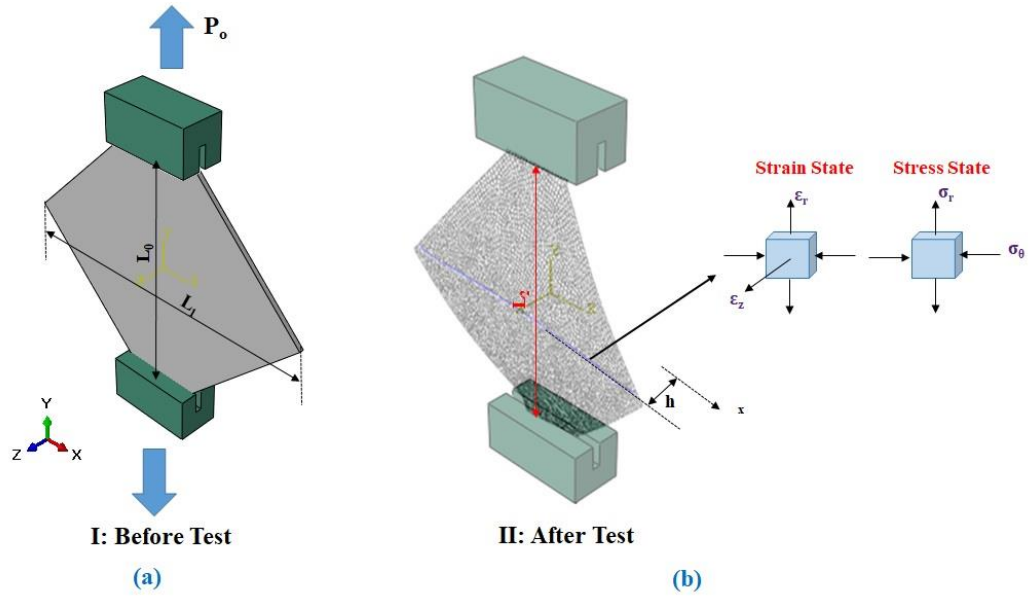

Figure 6.1: Schematic illustration of (a-b) before and after in-plane compression of YBT specimen with strain-stress states

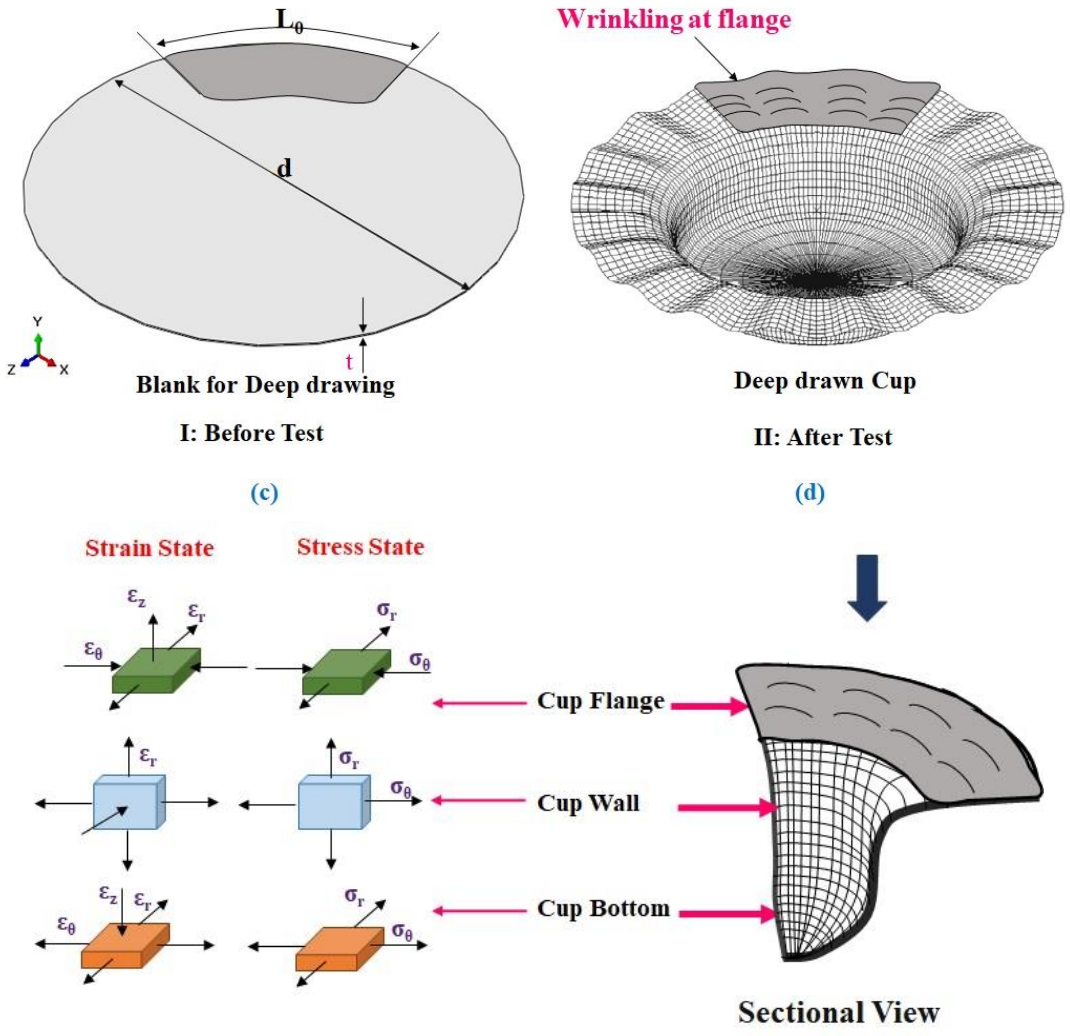

Figure 6.2: Schematic illustration of (a-b) analogy with strain-stress states at the edge of flange of deep drawn cup

In literature, modified YBT specimens, as shown in Figure 6.3, are used for testing a variety of deformation cases and at a wide range of stress ratios (Du et al. 2020). The stress ratio at the central region is varied by changing either the width (L_1) or gauge length (L_0).

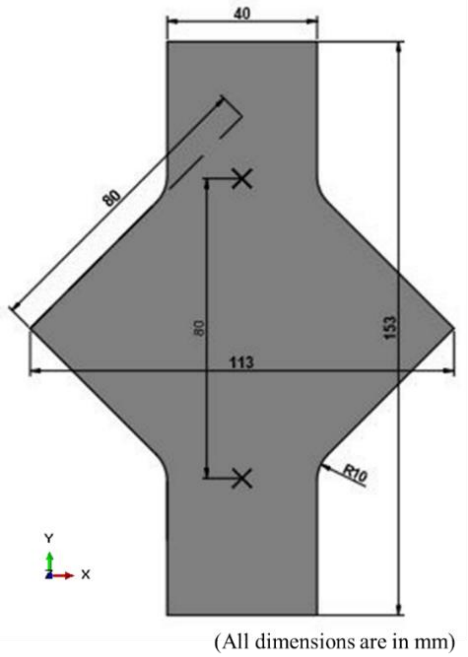

Figure 6.3: Schematic of YBT specimens used for wrinkling characterization

In the present study, dimensions of test specimens were prepared as per sub-sized specimens proposed by Kim et al. 2000 as listed in Table 6.1. The YBT was performed on a computer-controlled Zwick/Rolle Universal Testing Machine (UTM), with a maximum load capacity of 100 kN and heating capacity from RT to 1000°C with ± 3°C accuracy. The experiments were performed from RT to 600°C at an interval of 100°C with a quasi-static strain rate of $0.001s^{-1}$ with incremental tensile displacements of 5 mm, 6 mm, 7 mm and 9 mm respectively. Tensile deformation in an upward y-direction, once reached to a certain value, causes compressive stress in transverse direction (x) in the central region of the test specimen because of geometric constraints. This induced compressive stress in specimens initiates wrinkle formation. The real-time load vs. displacement data is captured. In order to extract the surface strains subsequently from the specimen after buckling, circular grids (d = 2.5 mm) were printed on the surface using an electro-corrosion process.

Table 6.1 YBT specimens used for onset of wrinkling characterization by varying width (L_1)

Gauge Length (L_0)	Width (L_1)	Ratio Width/Gauge length
80	113	1.41
80	100	1.25
80	90	1.13
80	80	1

Figure 6.3 gives buckled YBT specimens at a different test temperature for 5 mm, 6 mm, 7 mm, and 9 mm incremental tensile displacements. The evolution of in-plane strains was measured by measuring the deformed grid (ellipses) in buckled specimen along width with the help of an optical microscope. The lengths of major and minor axes (a & b) of deformed ellipses were measured to analyze the evolution of in-plane strains for different incremental distances. Each experiment was repeated 3 times, and average values were reported. The in-plane strains were measured by conventional methods as,

$$\varepsilon_1 = \ln\left(\frac{a}{d}\right) \text{ and } \varepsilon_2 = \ln\left(\frac{b}{d}\right) \tag{6.1}$$

here, the initial diameter of grid (d) is 2.5 mm. Also, deformed length (L_2 and $L_2 > L_0$) and plastic buckled wave amplitude (h) were measured for further calculation and instability plots.

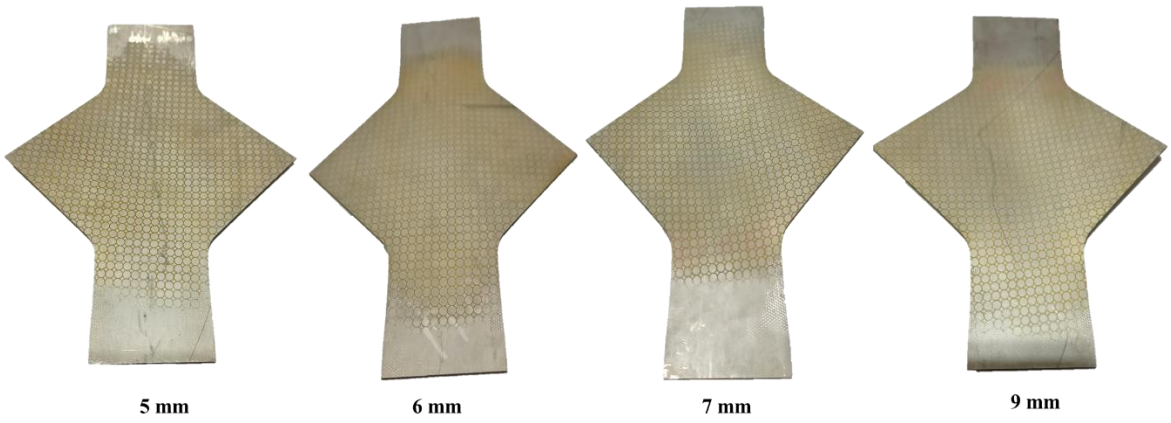

Figure 6.4 Representative buckled specimens for WLCs prediction

6.2 Numerical Analysis

A complete FE model of the YBT specimen was developed in the ABAQUS-Explicit-SIMULIA™ version 6.14. The specimen was considered as a deformable body and meshed by the 4 node S4R shell element. The main reason to select the 4 node S4R shell element for mesh is that these elements are more suitable for thick and thin shell structure modeling. This element is highly suitable for simulating large deformations and strains i.e., nonlinear behaviors. The trustworthiness of FE prediction for wrinkling mainly depends on wrinkling instability experimental test data with an appropriate selection of material models. Table 6.2 and Table 6.3 give the material and for Inconel 718 alloy considered as input to FE simulation. The physical properties of alloy were taken from the literature (Prasad et al. 2018b; Reed 2006). The true stress-strain response of Inconel 718 alloy was estimated by Hollomon's Equation. Hill'48 anisotropic

plastic potential has been selected as a material model in the numerical simulation. The anisotropic input parameters were calculated using below equations,

$$R_{22} = \sqrt{\frac{r_{90}(r_0 + 1)}{r_0\,(r_{90} + 1)}} \tag{6.2}$$

$$R_{33} = \sqrt{\frac{r_{90}(r_0 + 1)}{(r_{90} + r_0)}} \tag{6.3}$$

$$R_{12} = \sqrt{\frac{3 \times r_{90}(r_0 + 1)}{(2r_{45} + 1)\,(r_{90} + r_0)}} \tag{6.4}$$

As the SMF process is performed with assumption with the plane stress conditions. Thus, $R_{11} = 1$, is used. By substituting r_0, r_{45} and r_{90} values from Table 6.2 in above equations R_{22}, R_{33} and R_{12} are evaluated and listed in Table 6.3. Based on isotropic conditions, $R_{13} = R_{23} = 1$ is considered.

Table 6.2: Material properties as an input for FE analysis

Temperature (°C)	**Yield tensile stress (MPa)**	**Ultimate tensile stress (MPa)**	**Total elongation**	**Strain-hardening exponent**	**Hardening coefficient (MPa)**	**Anisotropy coefficients**		
	σ_{yavg}	σ_{utavg}	$(\%\,EL)_{avg}$	$(n)_{avg}$	K_{avg}	r_0	r_{45}	r_{90}
RT	505.64	951.92	41.97	0.3912	2028	0.7813	0.9471	1.0432
200 °C	443.91	863.58	47.75	0.4169	1903	0.9694	0.8765	0.9655
400°C	394.66	819.73	49.22	0.46	1756	0.8808	0.8972	0.9177
600°C	358.57	762.14	53.62	0.49	1485	1.1423	0.9694	0.9174

Table 6.3 Anisotropic properties as an input for FE analysis

Temperature (°C)	**Anisotropic input parameters**		
	R_{22}	R_{33}	R_{12}
RT	1.0789	1.0185	1.0275
200 °C	0.9990	0.9827	1.0348
400°C	1.0109	0.9597	1.0150
600°C	0.9473	0.9542	0.9869

All degrees of freedom of lower clamping edges of the specimen were restricted. The upper clamping surface was fully constrained except in the y-direction. The downward surface load was applied at the upper edges of the specimen. Mesh convergence study on the specimen at RT condition has been performed in order to get desired results in less computational time. Error in plastic buckled amplitude (difference between experimental and FE study) and computational time

are measured to finalize mesh size. Five different integrated points in the test model were specified along the thickness direction of shell element. Strain values (corresponds to these five integration points) are collected at the compressive surface of specimen. Thin plate wrinkling instability was modeled by using Explicit algorithms with a bifurcation path (Ameziane-Hassani and Neale 1991; Kim et al. 2017). It is possible to provide a variety of the initial pre-implanted defects namely, initial geometrical/physical defects and initial buckling type defects in explicit algorithm. Buckling mode study of YBT specimen was achieved by the Eigen value principle (Cao and Boyce 1997). Figure 6.5 summarized the steps followed while performing nonlinear buckling analysis.

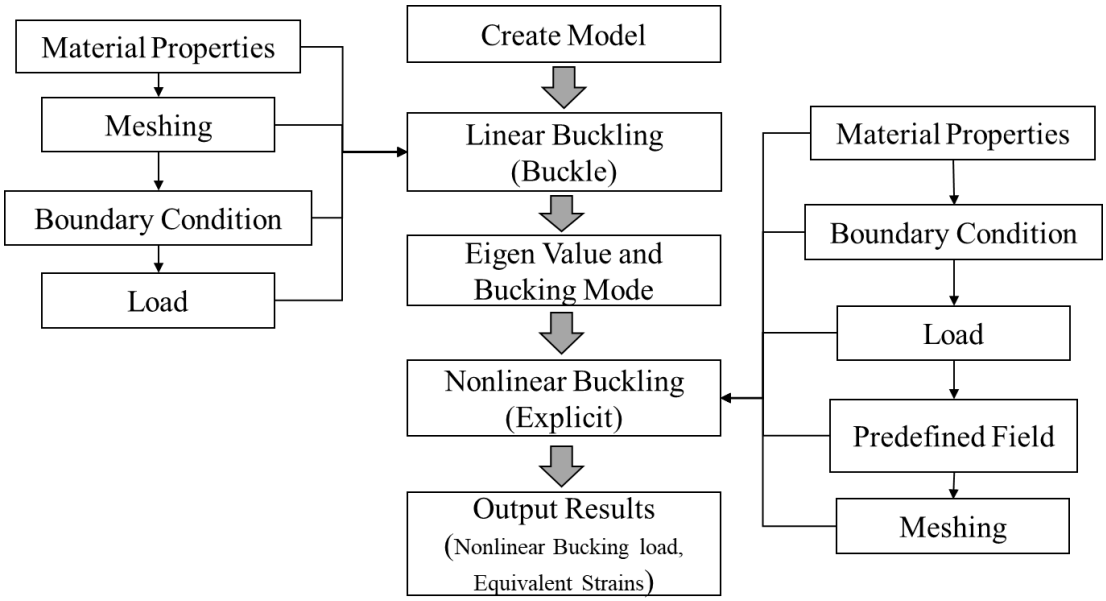

Figure 6.5 Steps followed for nonlinear buckling analysis

In linear eigenvalue analysis, for a certain external applied load P_o at elastic state, a small increment in load is given as,

$$\Delta P = [K + \lambda K(\sigma_o)]\Delta u \quad (6.5)$$

Where, ΔP is increased in external load for the incremental displacement of Δu, K and $K(\sigma_o)$ are the stiffness matrix of the structure and under the stress state (σ), λ is a buckling factor of eigenvalue. It can be evaluated by Eq 5 when ΔP = 0 and structure undergoes linear buckling with an incremental displacement, Δu ≠ 0, thus

$$[K + \lambda K(\sigma_o)]\Delta u = 0 \quad (6.6)$$

From the above Equation, the value of λ is determined and further critical buckling load (P_{cr}) is also calculated by multiplying buckling factor (λ) to the applied load P_o. While in nonlinear analysis material properties, unstable post-buckling response in terms of load and predefined field are considered. In order to have an ideal condition in the Explicit algorithm, the Eigen value

buckling analysis with the buckling mode is considered as a disturbance source. Thus, nonlinear buckling analysis is considered to examine the reliability of results.

6.3 Methodology to determine the onset of wrinkling

In order to determine the onset of wrinkling, integrated experimental and FE analysis was considered to find the critical strains. The coupled methodology adopted to calculate the critical strains at the onset of wrinkling is mentioned in Figure 6.6.

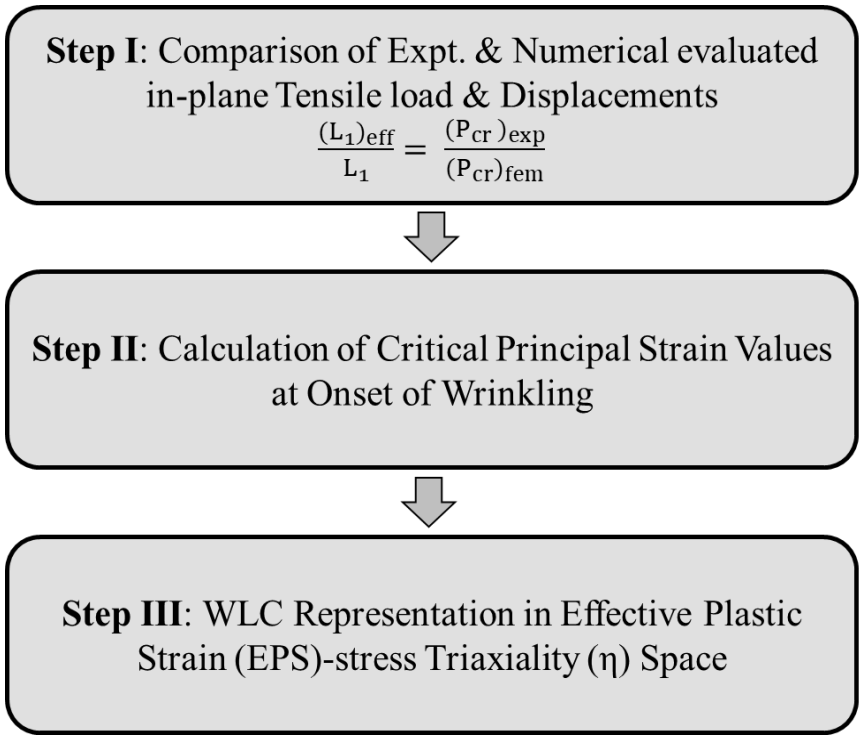

Figure 6.6: Steps followed to calculate critical strains at onset of wrinkling

Step I - Comparison of experimental and numerical (FE) evaluated in-plane compressive loads and displacements:

First, experimental and numerically evaluated in-plane compressive loads were compared. It is necessary to compare the in-plane loads and displacement, as practically the onset of wrinkling will not always occur simultaneously along the entire specimen width. This action even limits the localized deformation at the beginning of the YBT. This is nothing but the prompting onset of wrinkling for the smaller forces and displacement values than the numerical results. Thus, it is necessary to consider the effective width $(L_1)_{ef}$ to consider the experimental constraints. The experimental and numerically evaluated values were compared as,

$$\frac{(L_1)_{ef}}{L_1} = \frac{(P_{cr})_{exp}}{(P_{cr})_{FEA}} \tag{6.7}$$

Here, $(P_{cr})_{exp}$ and $(P_{cr})_{FEA}$ were experimental and numerical (FE) predicted loads at onset of the plastic instability.

Step II- Calculation of critical principal strain values at onset of wrinkling**:**

Experimental principal strain values after onset of wrinkling were evaluated by the circle grid analysis at selected incremental tensile displacements i.e., 6 mm, 7 mm and 8 mm. Additionally, major and minor principal strains values by FE analysis were utilized to determine the critical strain values $(\varepsilon_{1-2})_{cr}$ at onset of wrinkling, when h = L_1 (plastic buckled wave amplitude = deformed length) and the critical load Pcr were attained. These critical strain values for YBT specimens with different widths (L_1) were used to plot the ε-WLC in principal strains space. These FE results were checked and compared with experimental values to ensure the overall superiority of the predicted ε-WLCs.

Step III- WLC representation in effective plastic strain (EPS)-Stress triaxiality (η) space**:**

In order to study the wrinkling instability of Inconel 718 alloy in effective plastic strain ($\bar{\varepsilon}_f$) and stress triaxiality ($\eta = \frac{\sigma_m}{\bar{\sigma}}$ where $\sigma_m = \frac{\sigma_1+\sigma_2+\sigma_3}{3}$) space, effective stress functions ($\bar{\sigma}$) according to Hill'48 stress function and plane stress condition ($\sigma_3 = 0$) , is calculated as,

$$\bar{\sigma} = \sqrt{{\sigma_1}^2 + {\sigma_2}^2 - \frac{2R}{1+R}\sigma_1\sigma_2} \tag{6.8}$$

Where, R-average normal anisotropy (R = $\frac{r_0+2r_{45}+r_{90}}{4}$).

In SMF operation, effective fracture strain of the material highly depends upon the stress triaxiality (Bao and Wierzbicki 2004; Basak et al. 2015) and are correlated as (Basak and Panda 2019a),

$$\bar{\varepsilon_f} = \frac{b}{3\eta} \tag{6.9}$$

Where, b is an unknown parameter. The minor and major in-plane incremental strains $(d\varepsilon_2, d\varepsilon_1)$ according to Hill'48 stress function with applied stress are written as,

$$d\varepsilon_1 = \frac{d\bar{\varepsilon}}{\bar{\sigma}}\left[\frac{1}{1+R}\right](\sigma_1 + R(\sigma_1 - \sigma_2)) \tag{6.10}$$

$$d\varepsilon_2 = \frac{d\bar{\varepsilon}}{\bar{\sigma}}\left[\frac{1}{1+R}\right](\sigma_2 + R(\sigma_2 - \sigma_1)) \tag{6.11}$$

where $d\bar{\varepsilon}$ is the effective increment strain calculated as:

$$d\bar{\varepsilon} = \frac{1+R}{\sqrt{1+2R}}\sqrt{d\varepsilon_1{}^2 + d\varepsilon_2{}^2 + \frac{2R}{1+R}\,d\varepsilon_1 d\varepsilon_2} \tag{6.12}$$

The stress triaxiality (η) and strain ratio ($\alpha = \frac{\varepsilon_2}{\varepsilon_1} = \frac{d\varepsilon_2}{d\varepsilon_1}$) are correlated for any proportional strain loading paths of WLCs (any arbitrary maximum critical strain values at WLCs) as,

$$\eta = \frac{\sigma_m}{\bar{\sigma}} = \frac{\sqrt{1+2R}}{3} \times \frac{(1+\alpha)}{\sqrt{1+\frac{2R}{1+R}\alpha+\alpha^2}} \tag{6.13}$$

Equation 6.13 is used to transfer WLC from the principal strain space into the effective plastic strain vs. stress triaxiality space.

6.4 Wrinkling Limit Diagram

6.4.1 Load−displacement curves

Figure 6.7 gives the evolution of load with displacement applied over different width specimen during YBT at test temperatures. The critical buckling load and displacement correspond to onset of wrinkling/plastic instability for specimen with width (L1= 113 mm) are found higher to other widths for 6 mm incremental displacement. A similar observation was reported for 7 mm and 8 mm incremental displacements. It is observed that load increases sharply up to peak value (represents critical buckling load Pcr), after which there was steady increase in load at a slower rate with rise in displacement. This increase in force with displacement for YBT specimens corresponds to the thinning without occurrence of the plastic instability. This deformation mode is close to deformation mode usually observed in sheet metal forming (Sieczkarek et al. 2014).

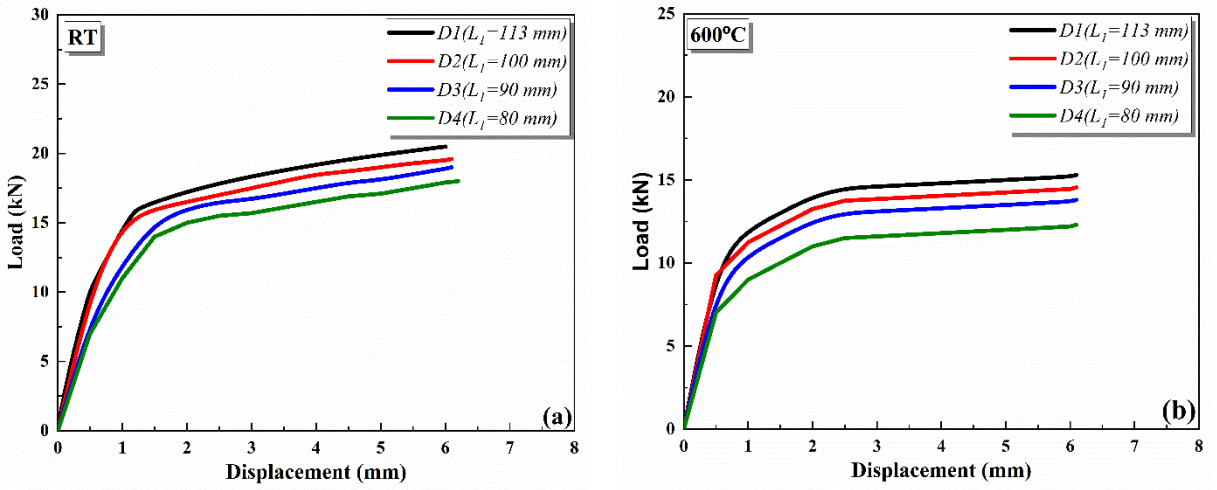

Figure 6.7: Buckling load vs displacement by YBT specimen for different widths at (a) RT and (b) 600°C

The effective width $(L_1)_{ef}$ plays an important role in confirming the compatibility between experimental and FE predicted load and displacement. Thus, initial width (L1) is corrected by

effective width $(L_1)ef$ by Equation 6.7. Figure 6.8 gives the comparison of experimental and simulated buckling load vs displacement for different width of specimen for given test temperatures. It is observed that there is a discrepancy for overall experimental and FE predicted buckling load and displacement at the critical load. This might be due to localized deformation at an early stage of YBT (from section 3) which prompts the amount of wrinkling instability.

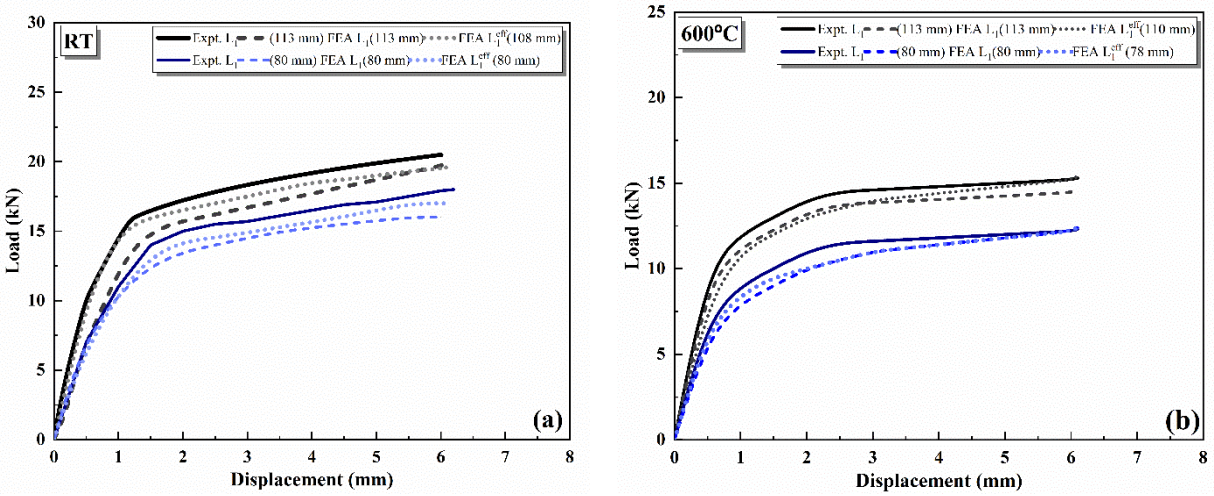

Figure 6.8 Comparison of the experimental and FE predicted buckling load vs displacement at (a) RT (b) 600°C for L1= 113mm and L1= 80 mm width YBT specimens

6.4.2 Establishment of onset of wrinkling (ε -WLCs)

The in-plane principal strains are obtained at critical buckling load Pcr. Minor and major critical wrinkling surface strains are measured from buckled YBT specimens and compared with FE results. It is observed that there is a discrepancy in principal strain values between experimental and FE results. This might be due to elastic recovery (springback) effect, as the simulated results does not consider the springback. Thus, the above procedure is repeated for the entire set of specimens at different test temperatures to determine the ε -WLCs for different temperatures, as shown in Figure 6.9. Distinct symbols and distinct colors were assigned to differentiate the buckled ellipses of different width specimens. It is noticed that an initial slope of ε -WLCs i.e. $d\varepsilon_1/d\varepsilon_2$ is nearly -0.5, which indicates the pure in-plane compression, but further there is change towards the smaller slopes as widths of the specimen decreases. This relates to material flow changes towards increase in thickness before onset of wrinkling. This is responsible for the reduction of original gauge length (L_0) and propagation of plastic instability in the specimen. It is noticed that the true strain is larger, for a specimen with a smaller width (L_1 = 50 mm) compared to other widths. It is also observed that critical wrinkling principal strain values are more scattered at high test temperatures than RT. The resulting WLCs indicate that increasing test temperatures significantly raises the critical wrinkling principal strains for different width specimens and also

slightly increases in the absolute slope value of WLC line. With an increase in the test temperature, wrinkling instability space under WLC line also increases. A comparison of 4 curves indicates that change in slope is 4-6% with increase in the test temperature. Change in the angle of WLC line is observed about 80° to 87° with negative minor principal strains.

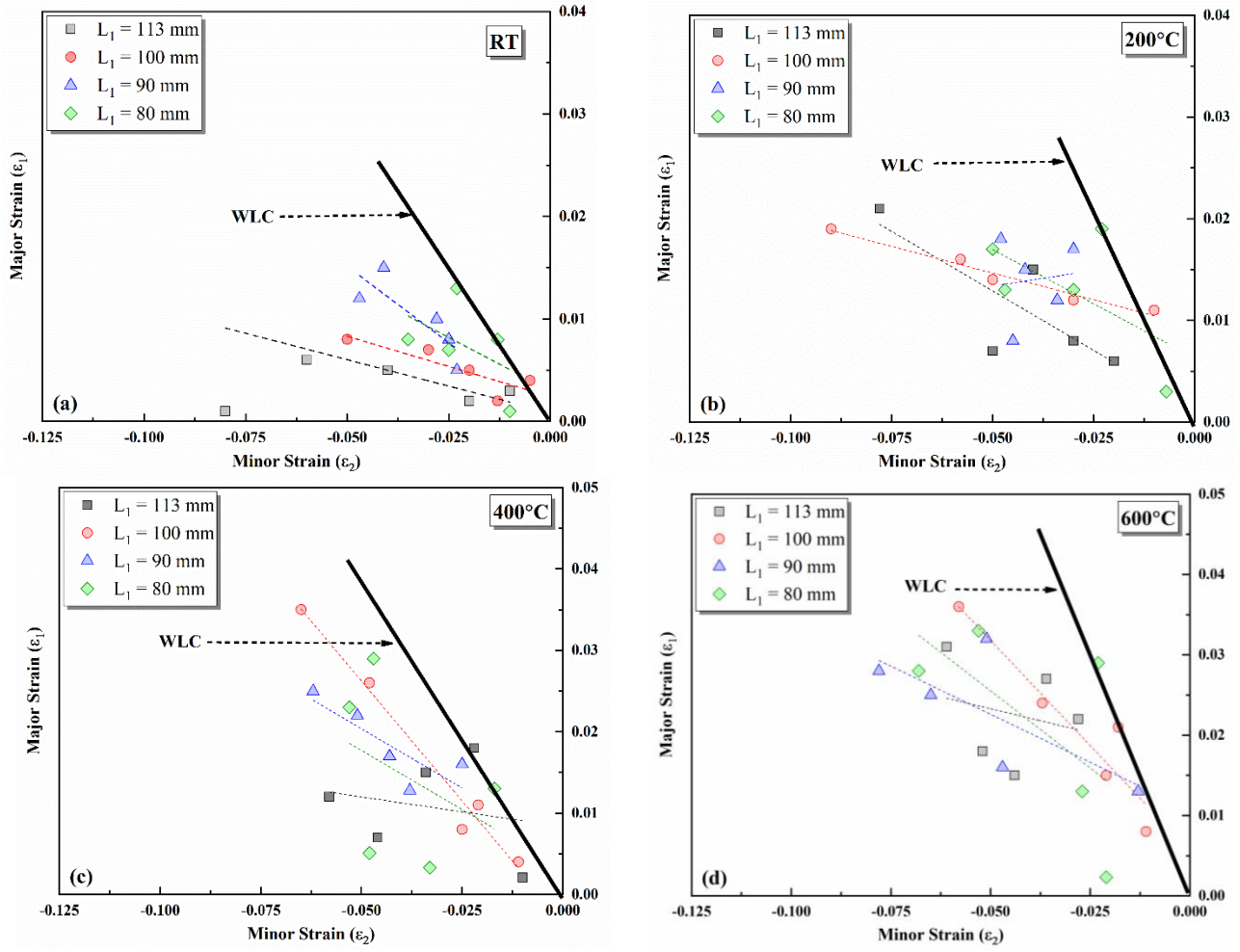

Figure 6.9: Wrinkling limit curves for Inconel 718 alloy at different test temperatures

Figure 6.10 gives WLCs represented in effective plastic strain-stress triaxaility (η) by analytically transferring in-plain plastic strains into the effective plastic strain. It is noticed that each wrinkling curve was separated by a critical effective plastic strain value $(\bar{\varepsilon})_{cr}$. This critical point differentiates the transformation between two strain regions, namely safe and wrinkling instability strain regions. It corresponds to the last permissible critical strain values/pair, which well-matched with the stress boundary conditions similar at the flange edge of the drawn cup. Thus, any strain/ loading path beyond this critical or transition point will lead to the wrinkling instability in the alloy. Further effective plastic strain was more scattered at high test temperatures. Rise in the critical effective plastic strain value $(\bar{\varepsilon})_{cr}$ is observed with rise in test temperatures.

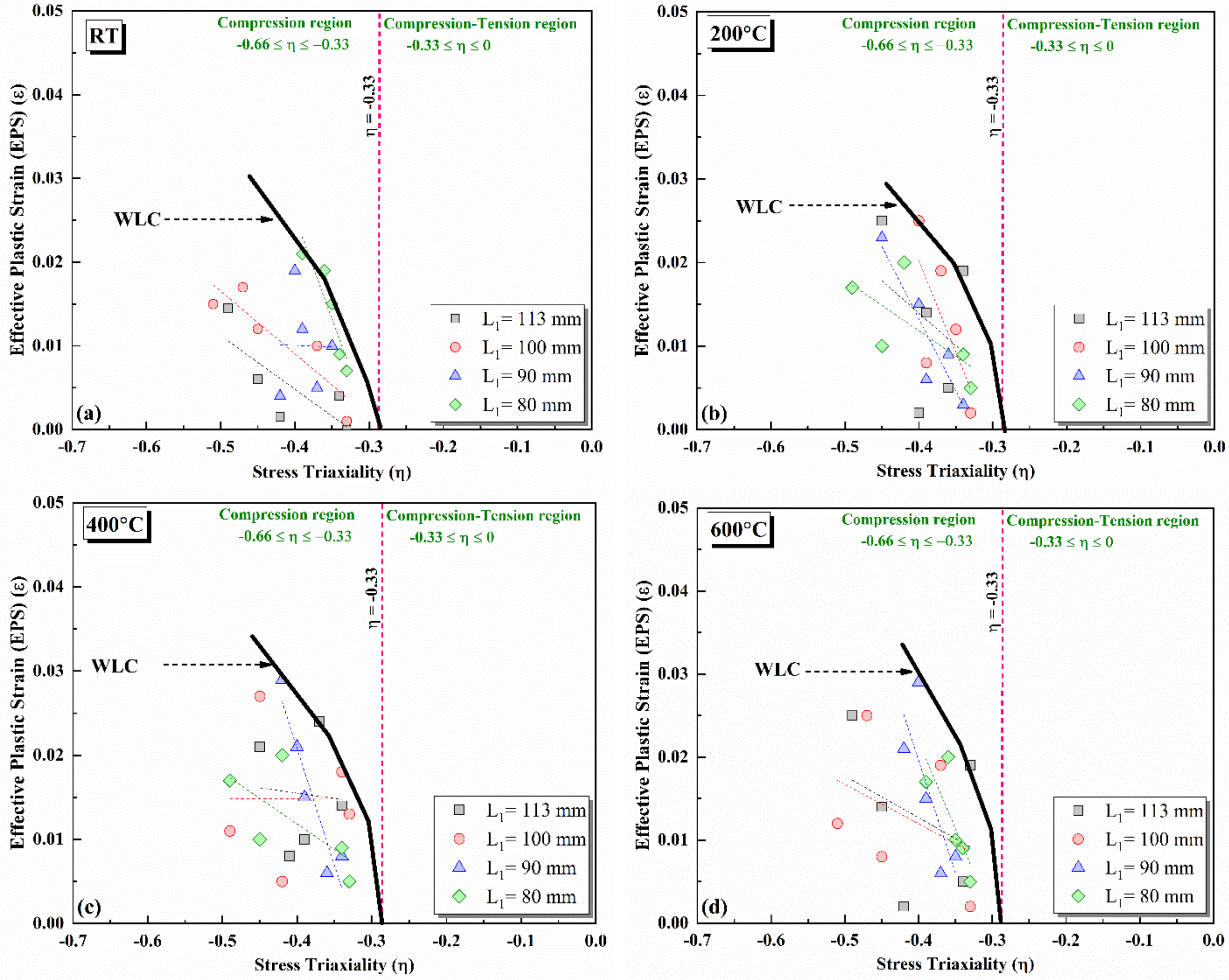

Figure 6.10: Wrinkling-limit curves (WLCs) represented in effective plastic strain vs stress triaxiality space for different test temperatures.

6.5 Post Buckling Analysis

Generally, the YBT specimen first starts contracting, and then it encounters buckling at the center region. Elements located in the buckling area are considered for evaluation. In an attempt to specify bifurcation point of each specimen, measured compression stress verses FE simulation time is plotted (Figure 6.11). Figure 6.11 shows transitions of curves from a negative value to a positive value. When lateral compressive stress suddenly chances to tensile stress, this conforms the occurrence of wrinkling in the specimen (Zheng et al. 2017). It is noticed that value of the bifurcation point of specimen with higher width is greater than that of lower width. For example, specimen with L_1 = 50 mm, the wrinkling occurs at 0.045 s time point, while that of specimens with L_1= 85 mm is 0.03 s. This indicates that the value of the bifurcation point of the specimen increases with an increase in specimen width.

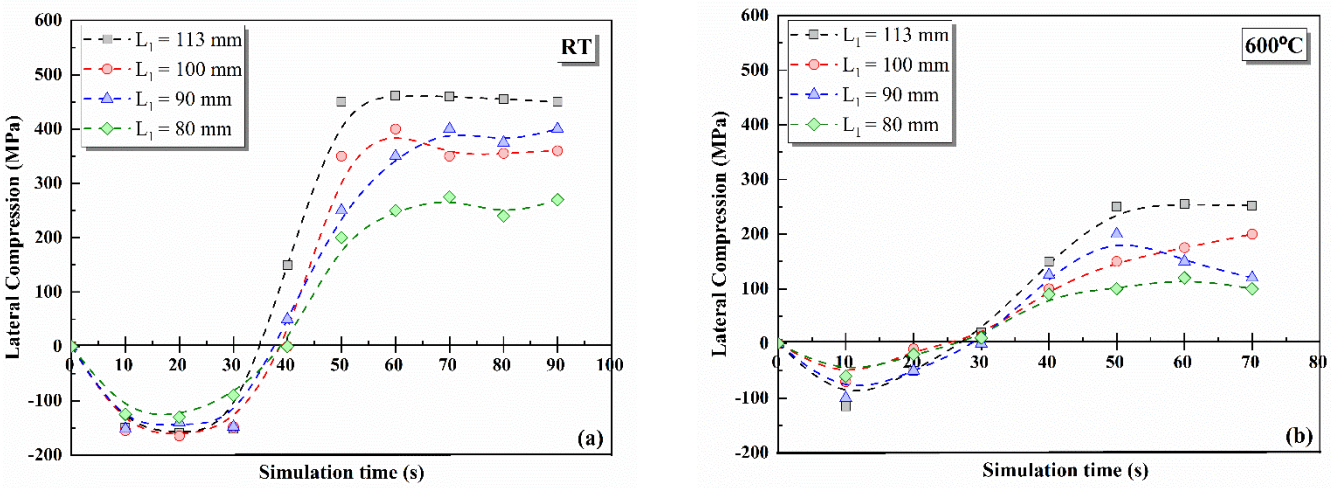

Figure 6.11 Lateral compressive stress vs FE simulation time (a) RT and (b) 600°C

Figure 6.12 gives the variation of buckling heights for YBT specimen with FE simulation time. The curve shows the different trend as in case of the bifurcation point (Figure 6.11). It shows that the buckling height is considerably influenced by specimen width and test temperature. A larger width specimen and higher test temperature lead to a larger buckling height.

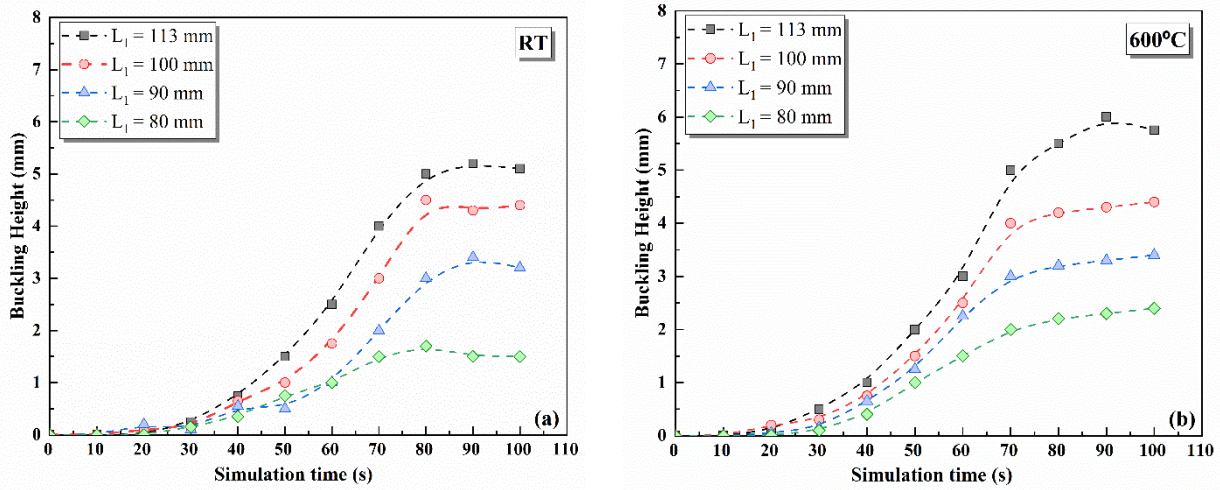

Figure 6.12 Buckling height vs FE simulation time (a) RT and (b) 600 °C

6.6 Assessment by cylindrical deep-drawing

In order to check the wrinkling occurrence in a circular specimen, a deep drawing test without any blank holding pressure was performed. The cylindrical deep drawing test was performed on a hydraulic press (40 Ton capacity) with an induction heating setup. Laboratory-scale deep drawing tooling setup (flat cylindrical punch & die) was used according to the schematic diagram presented in Figure 6.13a. Circular blank specimen, (ϕ = 60 mm, t = 1 mm) for deep drawing test, were wire cut from parent Inconel 718 sheet.

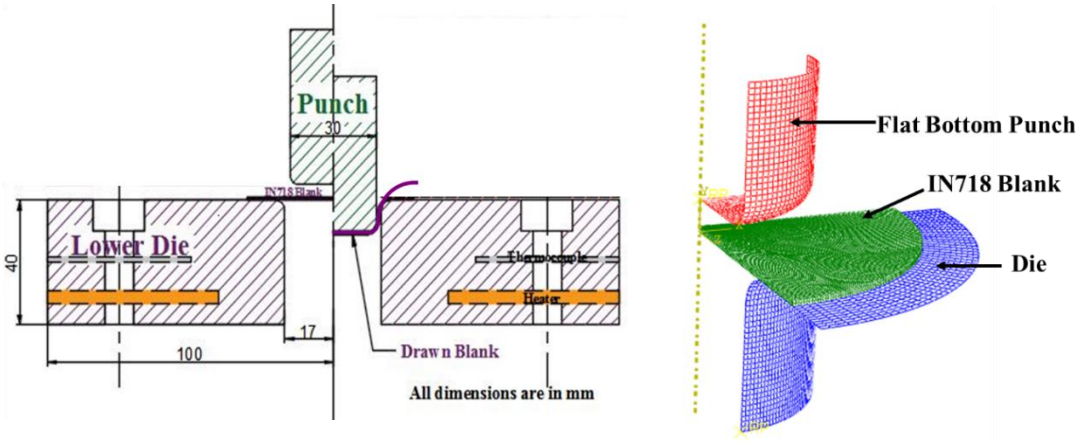

Figure 6.13 (a) Schematic diagram of cylindrical deep drawing setup without the blank holder and (b) FE model used in the numerical simulation

Figure 6.13 (b) shows a typical FE model of cylindrical deep-drawing test cases. A quarter input FE model was developed due to symmetric geometry and to reduce total computational time. Circular blanks were discretized with 16300 shell elements with 5 integrated points across the sheet thickness. Inconel 718 blank was simulated as a deformable body with planar and normal anisotropy properties (Table 6.2 and Table 6.3). The punch and die were modelled as rigid objects and discretized by the spatial triangular and quadrilateral elements. In the FE model, punch is allowed to move downward (y-direction) with a velocity profile (trapezoidal) with a fixed die. Figure 6.14 shows the comparison of the experimental and FE predicted wrinkling instability/profile during the deep drawing using a flat bottom punch on Inconel 718 alloy at different temperatures. It is noticed that the excessive wrinkling instability was initiated on the flange of the drawn cup and alloy consequently fractured within die-punch clearance zone. The experiment was stopped at failure load to study wrinkles progression in terms of numbers of wrinkles. It is noticed that number of the wrinkles predicted is exactly identical as that of experiment. It is observed that the wrinkles are suppressed with increase in test temperature with the same drawing load.

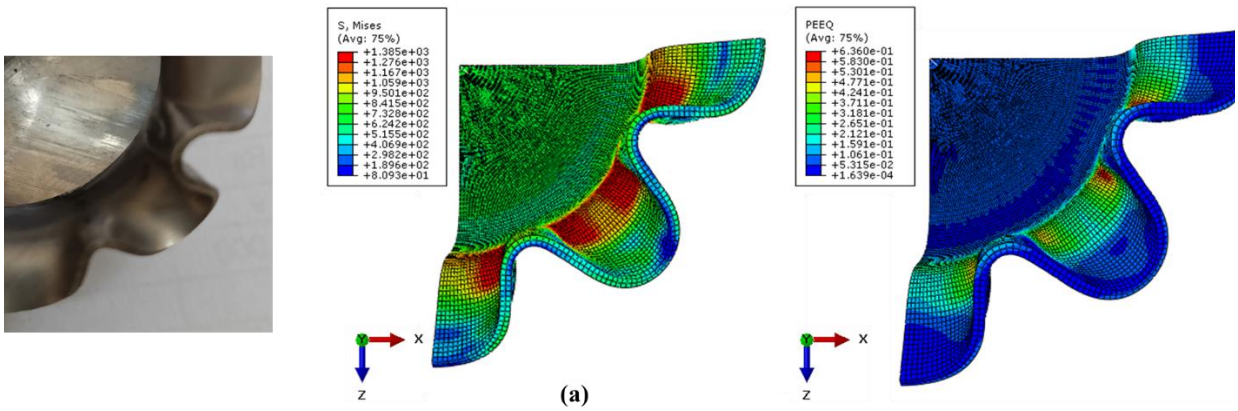

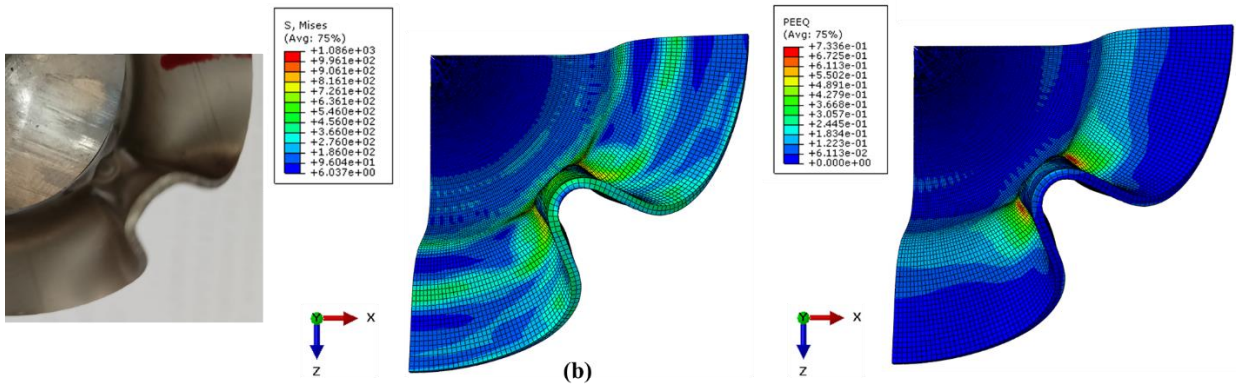

Figure 6.14 Wrinkling instability during deep drawing without blank holder on Inconel 718 alloy at (a) RT and (b) 600°C

Further, it is essential to understand the influence of punch load at the edge of flange of the drawn cup. It is reported in the literature that beyond a critical point, the flange edge will no longer able to undertaking thickening without wrinkling (Kim et al. 2000). Thus, the critical point (defined in section 3) divides the loading path into 2 extreme conditions, one located at the bottom of the valleys and other at top of the hills in drawn cup. Both strain loading paths are result of bending. It is caused by the wrinkling instability in which neutral plane moves towards bending regions.

From another perspective, by referring to analogy between YBT and cylindrical deep drawing in Figure 6.2, the critical point corresponds to maximum initial length L_o of the rectangular test specimen that undergoes wrinkling after previous exclusively the thickening under the pure compression loading. Thus, it can be concluded that it is necessary to identify critical strain pair at which thickening rate increases before wrinkling, i.e. the slope of WLC shifts towards the increasing thickening rate.

6.7 Complete Formability behavior of Inconel 718 Alloy

In order to discover the complete formability behavior of Inconel 718 alloy, forming, fracture, and wrinkling limit curves were plotted at different temperatures. Figure 6.15 (a-b) gives the complete formability behavior of Inconel alloy by differentiating the necking, fracture and wrinkling. The right side, i.e. in the biaxial tension region is safer compared to the left side i.e., tension-compression region as only necking and fracture failure are observed. As limiting strain values exceed the forming limit, necking start and ones reach the fracture limit, failure /fracture occurs. Whereas the compressive in-plane strains are mainly responsible for the wrinkling in the alloy. Figure 6.15 helps to determine safe forming conditions with a relative closeness of neither necking nor fracture nor wrinkling. It is noticed at 600ºC that Inconel 718 alloy shows a higher (~1.5 times) gap between forming and wrinkling limit curve for fixed minor strain value. If gap is

higher, then alloy is more suitable for forming in tension–compression (T-C) region for a particular temperature. This might be due to the high value of strain hardening exponent, anisotropic coefficients, and high strength ratio (σ_{ut}/σ_y), which resists the wrinkling and improves formability of Inconel 718 alloy (Reed 2006). It also confirms the suitability of Inconel 718 alloy for forming application at elevated temperature conditions.

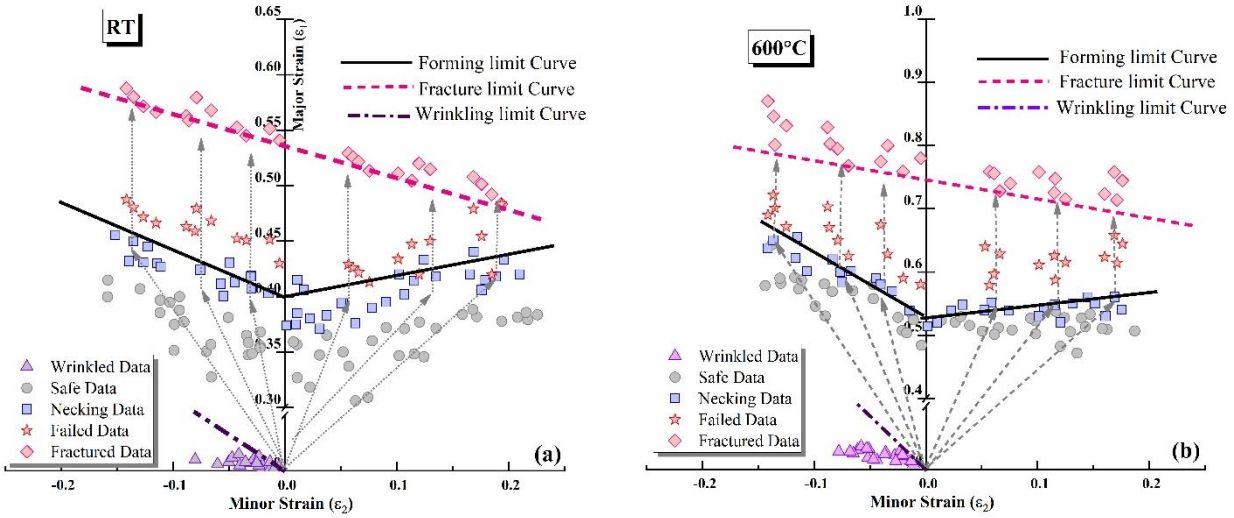

Figure 6.15: Forming, fracture and wrinkling limit curves of Inconel 718 alloy at (a) RT and (b) 600°C

Summary

This chapter described the coupled experimental and numerical approach for the prediction of wrinkling behavior of Inconel 718 alloy at elevated temperature conditions. A coupled experimental (Yoshida buckling test) and numerical approach (FE prediction) is used to determine strain-based wrinkling limit curves (ε-WLCs) of Inconel 718 form RT to 600ºC. the slope of the WLC line changes 4-6% approximately with rise in the test temperature. Further, a critical point by effective plastic strain value $(\bar{\varepsilon})_{cr}$ in triaxiality (η) vs effective plastic strain (EPS) space was traced to differentiate the transformation between safe and wrinkling instability strain regions for all test temperatures.

Further complete forming behavior of Inconel 718 is plotted by means of forming, fracture, and wrinkling limit curves at different test temperatures. The gap between forming limit and wrinkling limit curve increases considerably with a rise in temperature. The next chapter discusses the conclusions and contributions from the present research work.

.

7. Conclusions

This research work mainly focused on experimental and numerical studies of forming, fracture, and wrinkling limit diagrams of Inconel 718 alloy at elevated temperature. Major findings from this research are summarized below:

7.1 Major Conclusions

- Uniaxial tensile flow behavior of Inconel 718 alloy has been investigated at different test temperatures (RT-700°C) and quasi-static strain rate (0.0001-0.1 s^{-1}) conditions.
    - The flow stress and strain hardening behaviors are considerably affected by strain rates and temperatures. The material shows temperature dependency as ultimate tensile strength decreases by ~ 35% (from 1530 MPa at RT to 983MPa at 700°C). Whereas decrease in yield tensile strength observed a drop of ~ 18% (from 505 MPa to 413MPa). The rise in % elongation is noticed around ~15 % (42% at RT to 48% at 700°C).
  - The dynamic strain aging (DSA) phenomena is reported from 400°C-700°C at all the strain rate conditions. Mainly, B and combination of A + B type of serrations are observed at different temperatures and strain rates.
  - Anisotropic material properties have been evaluated at various temperatures and strain rate. Inconel 718 alloy shows an excellent combination of strength and ductility due to improvement in strain hardening capacity. Two-stage work hardening behavior of alloy has been well defined by Voce relationship with the correlation coefficient (>99%) among other empirical relations, namely Hollomon, Ludwik, and Swift.
  - Fracture surfaces of Inconel 718 alloy at various temperatures clearly indicate a ductile-brittle fracture. Nucleation and micro-voids growth are the main fracture phenomena observed in Inconel 718 alloy. From the EBSD study, dynamic recrystallization mechanism seems to start at relatively lower testing temperatures, i.e., 300°C and effect is more pronounced at higher testing temperatures.
- The comparative evaluation of various uniaxial constitutive models namely, m-CS, m-JC, m-ZA, and JC-ZA, anisotropic yield criteria for Inconel 718 alloy, have been investigated at wide range of temperatures and strain rates.
  - Constitutive models (m-JC, m-ZA, and JC-ZA) show good agreement in terms of correlation coefficient (R > 0.96). Among these models, the JC-ZA model shows

best agreement in terms of highest correlation coefficient and least average absolute error.

- Anisotropic yield criteria namely, Hill'48-r, Hill'48-σ and Barlat'89 yield criteria are weighed based on experimental yield strength points, variation in yield stress and anisotropic coefficients. However, Barlat'89 yield criterion exhibited better prediction over a wide range of strain rate, temperature, and sheet orientations.

- The experimental forming and fracture limit diagram of Inconel 718 have been determined at different temperatures using Nakazima test.
  - Limiting and fracture true strains were observed to be increasing with an increase in working temperature for all deformation regions (T-T, plane strain, T-C). The bending strain effect is analyzed, and FLDs are corrected based on the bending correction factor. The corrected FLDs are shifted downward by 3-5% approximately in all strain regions. Fractured forming limit diagrams (FFLDs) for IN718 alloy at different test temperature is also evaluated and significantly influenced by test temperatures.
  - The surface strain distribution (strain signature) indicates that peak major strain has been observed approximately at distance of 7 mm, similar location where stretched specimen fails. Also, Surface strain distribution is mainly depending on strain path change at a particular temperature. The thickness of stretched specimens remained constant initially, and then it started declining. Thickness deviation and maximum thinning rate are comparatively higher at 700°C. The LDH is significantly increased by approximately 33-44% at 700°C as compared with RT.
- Numerical investigations have been carried out for the theoretical prediction of limiting and failure strains for Inconel 718 alloy.
  - Marciniak Kuczynski MK model combined with Hill'48- r and Hill'48–σ model was used to predict FLC theoretically. The MK-FLD with Barlat'89 yield criteria shown a good prediction ability of limiting strains with a least RMSE (<0.058) and AAE (<0.031). Necking strains by the M-K model with Barlat'89 yield criterion showed better predictability in the T-T region than the T-C region.
  - Failure limit strains were prophesied by using Bao-Wierzbicki (B-W) model coupled with Hill'48-r, Hill'48-σ and Barlat'89 yield criteria and compared with the experimental values for onset of fracture. The B-W model with Barlat'89 yield

criterion gives the best prediction of experimental fracture strains with the least RMSE (<0.02) and AAE (<0.028).

- FE analysis of the stretch forming process of Inconel 718 alloy at elevated temperature is studied using ABAQUS-Explicit-SIMULIA^{TM}. Experimental results are validated with FE simulation by incorporating material model, friction, and boundary condition as input. Formability by means of limit dome height (LDH) and thickness distribution of Inconel 718 alloy have been determined.
- An integrated experimental and numerical approach has been discussed for prediction of wrinkling behavior of Inconel 718 alloy at elevated temperature conditions.
  - A coupled experimental (Yoshida buckling test) and numerical approach (FE prediction) is demonstrated for determining the strain-based wrinkling limit curves (ε-WLCs) of Inconel 718 from RT to 600ºC. The safe and wrinkling regions are identified at different temperatures by demarking the critical points $(\bar{\varepsilon})_{cr}$ or limiting permissible strain values in the strain regions.
  - In the post buckling FE analysis, the bifurcation point, buckling height and the section profile distribution has been analyzed. It is noticed that the value of the bifurcation point and buckling heights are considerably influenced by specimen width and test temperatures.
  - The wrinkling tendency in deep-drawn cups have been validated experimentally and numerically at different temperatures. It has been noticed that overall wrinkling tendency has been decreased substantially at higher temperatures. Further, the complete forming behavior of Inconel 718 is plotted by means of forming, fracture and wrinkling limit curves at different temperatures. The gap between forming and wrinkling limit curves increases ~1.5 times from RT to 600°C.

7.2 Specific Contributions to the Research

Through this thesis focused on forming, fracture and wrinkling behavior of Inconel 718 alloy at elevated temperature, the following contributions have been made towards the frontiers of state-of-art research on high strength Ni-based superalloys:

Academic outlooks

- Understanding of thorough deformation behavior and material properties of Inconel 718 alloy at different temperatures and strain rate conditions

- The obtained microstructure and micro-texture were correlated with the mechanical and anisotropic properties of the materials. These studies gave academic insight correlating microstructure with forming performance.
- The estimated material constants and anisotropic coefficient will be helpful for analyzing the forming behavior of Inconel 718 alloy sheet during multi-stage stamping processes.
- A detailed laboratory-scale stretch forming test was designed and developed in order to evaluate the forming process maps of Inconel 718 materials. These setups will be further utilized for evaluating forming limits of different other aerospace-grade sheet materials.
- Development of a systematic experimental plan for the complete determination of forming limit diagram i.e., forming, fracture, and wrinkling limits for Inconel 718 alloy.

Industrial inputs

- The estimated fracture forming limit diagram (FFLD) will provide the guidelines for the successful fabrication of the outer casing of Ni-H2 battery and high-pressure gas bottles.
- The developed FE models can be utilized as diagnostic tools for designing dies, punches and draw beads, and in selecting process parameters for successful fabrication of the above space components.
- The developed models will provide a comprehensive database for selecting the appropriate model as input to the FE code while modeling sheet forming processes.

Augmenting the outcomes given above, the thesis work is documented in the reputed journals, book chapter and conferences.

7.3 Limitations of the Work

The limitation of the present research are mentioned below:

- Extension of analysis of limiting and wrinkling strains for pre-straining and multistage forming processes.
- Incorporation of different uniaxial constitutive models in FE analysis of forming behavior.

7.4 Further Scope of the Work

Few possible directions for enhancing this research further are mentioned below:

- Effect of pre-straining and multistage stamping processes on forming, fracture and wrinkling limits prediction can be analyzed.
- Numerical prediction capabilities can be enhance by using advanced material models.
- Different ductile damage models can be implemented for accurate fracture prediction.

References

Abbasi, M., M. Ketabchi, T. Labudde, U. Prahl, and W. Bleck. 2012. "New Attempt to Wrinkling Behavior Analysis of Tailor Welded Blanks during the Deep Drawing Process." *Materials and Design* 40:407–14.

Afrin, N., D. L. Chen, X. Cao, and M. Jahazi. 2007. "Strain Hardening Behavior of a Friction Stir Welded Magnesium Alloy." *Scripta Materialia* 57(11):1004–1007.

Alves, M. 2000. "Material Constitutive Law for Large Strains and Strain Rates." *Journal of Engineering Mechanics* 126:215–18.

Ameziane-Hassani, H. and K. W. Neale. 1991. "On The Analysis Of Sheet Metal Wrinkling." *International Journal Mechanical Science* 33(1):13–30.

Anderson, D., C. Butcher, N. Pathak, and M. J. Worswick. 2017. "Failure Parameter Identification and Validation for a Dual-Phase 780 Steel Sheet." *International Journal of Solids and Structures* 124:89–107.

ASTM 517-00:2010. 2010. "Standard Test Method for Plastic Strain Ratio r for Sheet Metal." *ASTM Book of Standards* 1–8.

ASTM E2218-15. 2015. "Standard Test Method for Determining Forming Limit Curves." *ASTM Book of Standards* 1–15.

ASTM E3047-16. 2018. "Standard Test Method For Analysis of Nickel Alloys by Spark Atomic Emission Spectrometry." 1–12.

Atkins, A. G. 1996. "Fracture in Forming." *Journal of Materials Processing Technology* 56(1–4):609–18.

Ayres, R., W. Brazier, and V. Sajewski. 1978. "Evaluating the GMR-Limiting Dome Height Test as a New Measure of Press Formability near Plane Strain." *Journal of Applied Metalworking* 1(1):41–49.

Azarbarmas, M., M. Aghaie-Khafri, J. M. Cabrera, and J. Calvo. 2016. "Microstructural Evolution and Constitutive Equations of Inconel 718 Alloy under Quasi-Static and Quasi-Dynamic Conditions." *Materials and Design* 94:28–38.

Banabic. 2010a. "A Review on Recent Developments of Marciniak-Kuczynski Model." *Computer Methods in Materials Science* 10(4):225–37.

Banabic. 2010b. *Plastic Behaviour of Sheet Metal*. Springer Berlin Heidelberg.

Banabic, D. 2000. "Formability of Metallic Materials : Plastic Anisotropy, Formability Testing, Forming Limits." *Engineering Materials*.

Banabic, D., H. Aretz, L. Paraianu, and P. Jurco. 2005. "Application of Various FLD Modelling Approaches." *Modelling and Simulation in Materials Science and Engineering* 13:759–69.

Banabic, D., Ba Carleer, D. S. Comsa, E. Kam, A. Krasovskyy, K. Mattiasson, M. Sester, M. Sigvant, and X. Zhang. 2010. *Sheet Metal Forming Processes: Constitutive Modelling and Numerical*

Simulation. Springer,Berlin, Heidelberg.

Banabic, D., A. Kami, D. S. Comsa, and P. Eyckens. 2019. "Developments of the Marciniak-Kuczynski Model for Sheet Metal Formability: A Review." *Journal of Materials Processing Technology* 287(116446):1–14.

Banabic, D., L. Lazarescu, L. Paraianu, I. Ciobanu, I. Nicodim, and D. S. Comsa. 2013. "Development of a New Procedure for the Experimental Determination of the Forming Limit Curves." *CIRP Annals - Manufacturing Technology* 62(1):255–58.

Bao, Yi and T. Wierzbicki. 2004. "On Fracture Locus in the Equivalent Strain and Stress Triaxiality Space." *International Journal of Mechanical Sciences* 46:81–98.

Barlat, F., J. C. Brem, J. W. Yoon, K. Chung, R. E. Dick, D. J. Lege, F. Pourboghrat, S. H. Choi, and E. Chu. 2003. "Plane Stress Yield Function for Aluminum Alloy Sheets - Part 1: Theory." *International Journal of Plasticity* 19(9):1297–1319.

Barlat, F. and K. Lian. 1989. "Plastic Behavior and Stretchability of Sheet Metals. Part I: A Yield Function for Orthotropic Sheets under Plane Stress Conditions." *International Journal of Plasticity* 5:51–56.

Basak, S. and S. K. Panda. 2019a. "Failure Strains of Anisotropic Thin Sheet Metals: Experimental Evaluation and Theoretical Prediction." *International Journal of Mechanical Sciences* 151:356–74.

Basak, S. and S. K. Panda. 2019b. "Necking and Fracture Limit Analyses of Different Pre-Strained Sheet Materials in Polar Effective Plastic Strain Locus Using Yld2000-2d Yield Model." *Journal of Materials Processing Technology* 267:289–307.

Basak, S., S. K. Panda, and Y. N. Zhou. 2015. "Formability Assessment of Prestrained Automotive Grade Steel Sheets Using Stress Based and Polar Effective Plastic Strain-Forming Limit Diagram." *Journal of Engineering Materials and Technology, Transactions of the ASME* 137:1–12.

Bassoli, E., A. Sola, L. Denti, and A. Gatto. 2019. "Experimental Approach to Measure the Restraining Force in Deep Drawing by Means of a Versatile Draw Bead Simulator." *Materials and Manufacturing Processes* 34(11):1286–95.

Bayraktar, E., N. Isac, and G. Arnold. 2005. "Buckling Limit Diagrams (BLDs) of Interstitial Free Steels (IFS): Comparison of Experimental and Finite Element Analysis." *Journal of Materials Processing Technology* 164–165:1487–94.

Bong, H. J., F. Barlat, M. G. Lee, and D. C. Ahn. 2012. "Surface Roughening of Ferritic Stainless Steel Sheets and Its Application to the Forming Limit Diagram." *Steel Research International* 975–78.

Brozzo, P., B. De Luca, and R. Redina. 1972. "A New Method for the Prediction of Formability Limits in Metal Sheets, Sheet Metal Forming and Formability." Pp. 28–35 in *Proceedings of the 7th biennial Conference of the International Deep Drawing Research group*.

Bruschi, S., T. Altan, D. Banabic, P. F. Bariani, A. Brosius, J. Cao, A. Ghiotti, M. Khraisheh, M. Merklein, and A. E. Tekkaya. 2014. "Testing and Modelling of Material Behaviour and Formability in Sheet Metal Forming." *CIRP Annals - Manufacturing Technology* 63(2):727–49.

Butuc, M. C., C. Teodosiu, F. Barlat, and J. J. Gracio. 2011. "Analysis of Sheet Metal Formability through Isotropic and Kinematic Hardening Models." *European Journal of Mechanics, A/Solids* 48:414–29.

Caliari, F. R., K. C. G. Candioto, D. A. P. Reis, A. A. Couto, C. De Moura Neto, and C. A. Nunes. 2011. "Study of the Mechanical Behavior of an Inconel 718 Aged Superalloy Submitted to Hot Tensile Tests." *SAE Technical Papers* 36:328–37.

Cao, J. and M. C. Boyce. 1997. "Wrinkling Behavior of Rectangular Plates under Lateral Constraint." *International Journal of Solids and Structures* 34:153–176.

Cardoso, R. P. R. and O. B. Adetoro. 2017. "A Generalisation of the Hill's Quadratic Yield Function for Planar Plastic Anisotropy to Consider Loading Direction." *International Journal of Mechanical Sciences* 128–129:253–68.

Charpentier, P. L. 1975. "Influence of Punch Curvature on the Stretching Limits of Sheet Steel." *Metallurgical Transactions A* 6:1665–69.

Che, J., T. Zhou, Z. Liang, J. Wu, and X. Wang. 2018. "An Integrated Johnson–Cook and Zerilli–Armstrong Model for Material Flow Behavior of Ti–6Al–4V at High Strain Rate and Elevated Temperature." *Journal of the Brazilian Society of Mechanical Sciences and Engineering* 40(253):1–10.

Chen, L., G. Zhao, Ji Gong, X. Chen, and M. Chen. 2015. "Hot Deformation Behaviors and Processing Maps of 2024 Aluminum Alloy in As-Cast and Homogenized States." *Journal of Materials Engineering and Performance* 24:5002–12.

Chen, X. M., Y. C. Lin, D. X. Wen, J. L. Zhang, and M. He. 2014. "Dynamic Recrystallization Behavior of a Typical Nickel-Based Superalloy during Hot Deformation." *Materials and Design* 57:568–77.

Cheng, Y. Q., H. Zhang, Z. H. Chen, and K. F. Xian. 2008. "Flow Stress Equation of AZ31 Magnesium Alloy Sheet during Warm Tensile Deformation." *Journal of Materials Processing Technology* 208(1–3):29–34.

Chow, C. L., M. Jie, and S. J. Hu. 2003. "Forming Limit Analysis of Sheet Metals Based on a Generalized Deformation Theory." *Journal of Engineering Materials and Technology, Transactions of the ASME* 125:260–65.

Christopher, J., B. K. Choudhary, E. Isaac Samuel, V. S. Srinivasan, and M. D. Mathew. 2011. "Tensile Flow and Work Hardening Behaviour of 9Cr-1Mo Ferritic Steel in the Frame Work of Voce Relationship." *Materials Science and Engineering A* 528(21):6589–6595.

Clift, S. E., P. Hartley, C. E. N. Sturgess, and G. W. Rowe. 1990. "Fracture Prediction in Plastic Deformation Processes." *International Journal of Mechanical Sciences* 32:1–17.

Cockcroft, M. G. and D. J. Lathan. 1968. “Ductility and the Workability of Metals.” *J. Inst. Met* 33–39. Retrieved October 18, 2019 (https://books.google.co.in/books/about/Ductility_and_the_Workability_of_Metals.html?id=COSPAQAACAAJ&redir_esc=y).

Desu, R. K., N. K. Hansoge, Ad Balu, A. K. Gupta, and S. K. Singh. 2016. “Mechanical Properties of Austenitic Stainless Steel 304L and 316L at Elevated Temperatures.” *Journal of Materials Research and Technology* 5(1):13–20.

Dewang, Y., S. Panthi, and M. Hora. 2019. “Binder Force Effect on Stretch Flange Forming of Aluminum Alloy.” *Materials and Manufacturing Processes* 34(13):1516–27.

Dieter, G. E. 2011. *Mechanical Metallurgy SI Metric Edition;* Mcgraw-Hill Book Company - Koga.

Dilmec, M., H. S. Halkaci, F. Ozturk, H. Livatyali, and O. Yigit. 2013. “Effects of Sheet Thickness and Anisotropy on Forming Limit Curves of AA2024-T4.” *International Journal of Advanced Manufacturing Technology* 67(9–12):2689–2700.

Du, B., J. Xie, H. Li, C. Zhao, X. Zhang, and X. Yuan. 2020. “Thin-Walled Structures Determining Factors Affecting Sheet Metal Plastic Wrinkling in Response to Nonuniform Tension Using Wrinkling Limit Diagrams.” *Thin-Walled Structures* 147:1035–65.

Elangovan, K., C. Sathiya Narayanan, and R. Narayanasamy. 2010. “Modelling of Forming Limit Diagram of Perforated Commercial Pure Aluminium Sheets Using Artificial Neural Network.” *Computational Materials Science* 47:1072–78.

Evangelista, S. H., J. Lirani, and AlQureshi. 2002. “Implementing a Modified Marciniak–Kuczynski Model Using the Finite Element Method for the Simulation of Sheet Metal Deep Drawing.” *Journal of Material Processing Technology,* 130–131:135–44.

Field, J. E., S. M. Walley, W. G. Proud, H. T. Goldrein, and C. R. Siviour. 2004. “Review of Experimental Techniques for High Rate Deformation and Shock Studies.” *International Journal of Impact Engineering* 30:725–75.

Goodwin G M. 1970. “Application of Strain Analysis to Sheet Metal Forming Problems in the Press Shop.” *SAE Technical Paper* 62(8):767–74.

Güler, B. and M. Efe. 2018. “Forming and Fracture Limits of Sheet Metals Deforming without a Local Neck.” *Journal of Materials Processing Technology* 252:477–84.

Gurson, A. L. 1977. “Continuum Theory of Ductile Rupture by Void Nucleation and Growth: Part 1 - Yield Criteria and Flow Rules for Porous Ductile Media.” *Journal of Engineering Materials and Technology, Transactions of the ASME* 99(1):2–15.

Han, Fei and Mathias Liewald. 2014. “A New Method to Enhance the Accuracy of the Buckling Test Using Modified Yoshida Sample.” *Advanced Materials Research* 1018:199–206.

Hazra, S., D. Williams, R. Roy, R. Aylmore, and A. Smith. 2011. “Effect of Material and Process Variability on the Formability of Aluminium Alloys.” *Journal of Materials Processing Technology* 211(9):1516–26.

Hecker, S. S. 1975. “Simple Technique For Determining Forming Limit Curves.” *Sheet Metal Industries* 52(11):671–76.

Hedworth, J. and M. J. Stowell. 1971. “The Measurement of Strain-Rate Sensitivity in Superplastic Alloys.” *Journal of Materials Science* 6(8):1061–69.

Hill, R. 1952. “On Discontinuous Plastic States, with Special Reference to Localized Necking in Thin Sheets.” *Journal of the Mechanics and Physics of Solids* 1(1):19–30.

Hill, R. 1990. “Constitutive Modelling of Orthotropic Plasticity in Sheet Metals.” *Journal of the Mechanics and Physics of Solids* 38(3):405–17.

Hu, Q., X. Li, and J. Chen. 2019. “Forming Limit Evaluation by Considering Through-Thickness Normal Stress: Theory and Modeling.” *International Journal of Mechanical Sciences* 155:187–96.

Huang, L. and M. Shi. 2018. “Forming Limit Curves of Advanced High Strength Steels: Experimental Determination and Empirical Prediction.” *SAE International Journal of Materials and Manufacturing* 11(4):409–18.

Iturbe, A., E. Giraud, E. Hormaetxe, A. Garay, G. Germain, K. Ostolaza, and P. J. Arrazola. 2017. “Mechanical Characterization and Modelling of Inconel 718 Material Behavior for Machining Process Assessment.” *Materials Science and Engineering A* 682:441–53.

Iyer, S. K. and C. J. Lissenden. 2000. “Inelastic Anisotropy of Inconel 718: Experiments and Mathematical Representation.” *Journal of Engineering Materials and Technology* 122:321–26.

Jackson, M. 2000. “Application of Novel Technique to Examine Thermomechanical Processing of near β Alloy Ti-10V-2Fe-3Al.” *Materials Science and Technology* 16(11–12):1437–44.

Jafarian, F., S. Masoudi, H. Soleimani, and D. Umbrello. 2018. “Experimental and Numerical Investigation of Thermal Loads in Inocnel 718 Machining.” *Materials and Manufacturing Processes* 23(9):1020–29.

Jain, M., J. Allin, and D.J. Lloyd. 1999. “Fracture Limit Prediction Using Ductile Fracture Criteria for Forming of an Automotive Aluminum Sheet.” *International Journal of Mechanical Sciences* 41(10):1273–88.

Janbakhsh, M., F. Djavanroodi, and M. Riahi. 2013. “Utilization of Bulge and Uniaxial Tensile Tests for Determination of Flow Stress Curves of Selected Anisotropic Alloys.” *Proceedings of the Institution of Mechanical Engineers, Part L: Journal of Materials: Design and Applications* 227(1):38–51.

Jata, K. V., A. K. Hopkins, and R. J. Rioja. 1996. “The Anisotropy and Texture of Al-Li Alloys.” *Materials Science Forum* 217:647–52.

Jobba, M., R. K. Mishra, and M. Niewczas. 2015. “Flow Stress and Work-Hardening Behaviour of Al-Mg Binary Alloys.” *International Journal of Plasticity* 65:43–60.

Johnson, W. and T. X. Yu. 1982. “The Buckling of Annular Plates in Relation to the Deep-Drawing Process.” *International Journal of Mechanical Sciences* 24(3):175–88.

Keeler, S. and W. Backofen. 1961. “Plastic Instability and Fracture in Sheets Stretched over Rigid Punches.” Massachusetts Institute of Technology.

Kennedy, R. L. 2005. *Allvac 718Plus, Superalloy for the Next Forty Years*.

Khan, A. S., S. Yu, and H. Liu. 2012. “Deformation Induced Anisotropic Responses of Ti-6Al-4V Alloy Part II: A Strain Rate and Temperature Dependent Anisotropic Yield Criterion.” *International Journal of Plasticity* 38:14–26.

Khan, M. Adam, N. Ram Prasad, S. Navaneetha Krishnan, S. Karthic Raja, J. T. Jappes, and Muthukannan Duraiselvam. 2017. “Laser-Treated Austenitic Steel and Nickel Alloy for Human Implants.” *Materials and Manufacturing Processes* 32(1):1635–41.

Kim, J. B., J. W. Yoon, and D. Y. Yang. 2000. “Wrinkling Initiation and Growth in Modified Yoshida Buckling Test: Finite Element Analysis and Experimental Comparison.” *International Journal of Mechanical Sciences* 42(9):1683–1714.

Kim, J. H., M. G. Lee, J. H. Kang, C. S. Oh, and F. Barlat. 2017. “Crystal Plasticity Finite Element Analysis of Ferritic Stainless Steel for Sheet Formability Prediction.” *International Journal of Plasticity* 93:26–45.

Kim, Y. and Y. Son. 2000. “Study on Wrinkling Limit Diagram of Anisotropic Sheet Metals.” *Journal of Materials Processing Technology* 94(1–3):88–94.

Kotkunde, N., G. Krishna, S. K. Shenoy, A. K. Gupta, and S. K. Singh. 2017. “Experimental and Theoretical Investigation of Forming Limit Diagram for Ti-6Al-4 V Alloy at Warm Condition.” *International Journal of Material Forming* 10(2):255–66.

Kotkunde, N., S. Srinivasan, G. Krishna, A. K. Gupta, and S. K. Singh. 2016. “Influence of Material Models on Theoretical Forming Limit Diagram Prediction for Ti − 6Al − 4V Alloy under Warm Condition.” *Transactions Nonferrous Metals Society of China* 26(3):736–46.

Kuhlmann-Wilsdorf, D. 1989. “Theory of Plastic Deformation: - Properties of Low Energy Dislocation Structures.” *Materials Science and Engineering A* 113:1–41.

Kuroda, M. and V. Tvergaard. 2000. “Forming Limit Diagrams for Anisotropic Metal Sheets with Different Yield Criteria.” *International Journal of Solids and Structures* 37(37):5037–59.

Lee, Y. W. 2005. “Fracture Prediction in Metal Sheets.” Massachusetts Institute of Technology, Cambridge,United States.

Leu, D. K. 1997. “A Simplified Approach for Evaluating Bendability and Springback in Plastic Bending of Anisotropic Sheet Metals.” *Journal of Materials Processing Technology* 66(1):9–17.

Li, B., Y. Du, and Z. Peng. 2018. “Investigation on the Hot Deformation Characteristics of Ni-Cr-Fe-Ti Alloy.” *Vacuum* 157:299–305.

Li, D., Q. Guo, S. Guo, H. Peng, and Z. Wu. 2011. “The Microstructure Evolution and Nucleation Mechanisms of Dynamic Recrystallization in Hot-Deformed Inconel 625 Superalloy.” *Materials and Design* 32(2):696–705.

Li, H., H. R. Liu, N. Liu, H. Sun, H. Yang, and B. Y. Liu. 2019. “Towards Sensitive Prediction of

Wrinkling Instability in Sheet Metal Forming by Introducing Evolution of Triple Nonlinearity: Tube Forming." *International Journal of Mechanical Sciences* 161–162(105054):1–16.

Lin, Jianguo, Daniel Balint, and Maciej Pietrzyk. 2012. *Microstructure Evolution in Metal Forming Processes*. Woodhead Publishing Limited.

Lin, Y C, X. M. Chen, D. X. Wen, and M. S. Chen. 2014. "A Physically-Based Constitutive Model for a Typical Nickel-Based Superalloy." *Computational Materials Science* 83:282–89.

Lin, Y. C. and Xiao Min Chen. 2010. "A Combined Johnson-Cook and Zerilli-Armstrong Model for Hot Compressed Typical High-Strength Alloy Steel." *Computational Materials Science* 49(3):628–33.

Lin, Y. C. and Xiao Min Chen. 2011. "A Critical Review of Experimental Results and Constitutive Descriptions for Metals and Alloys in Hot Working." *Materials and Design* 32(4):1733–59.

Lin, Y. C., Xiao Min Chen, and Ge Liu. 2010. "A Modified Johnson-Cook Model for Tensile Behaviors of Typical High-Strength Alloy Steel." *Materials Science and Engineering A* 527(26):6980–86.

Lin, Y. C., Jiao Deng, Yu Qiang Jiang, Dong Xu Wen, and Guan Liu. 2014. "Effects of Initial δ Phase on Hot Tensile Deformation Behaviors and Fracture Characteristics of a Typical Ni-Based Superalloy." *Materials Science and Engineering A* 598:251–62.

Lin, Y. C., Kuo-Kuo Li, Hong-Bin Li, Jian Chen, Xiao-Min Chen, and Dong-Xu Wen. 2015. "New Constitutive Model for High-Temperature Deformation Behavior of Inconel 718 Superalloy." *Materials and Design* 74:108–18.

Lin, Y. C., Fu Qi Nong, Xiao Min Chen, Dong Dong Chen, and Ming Song Chen. 2017. "Microstructural Evolution and Constitutive Models to Predict Hot Deformation Behaviors of a Nickel-Based Superalloy." *Vacuum* 137:104–14.

Lin, Y. C., Dong Xu Wen, Jiao Deng, Guan Liu, and Jian Chen. 2014. "Constitutive Models for High-Temperature Flow Behaviors of a Ni-Based Superalloy." *Materials and Design* 47:115–23.

Lin, Y. C., Hui Yang, Yunchang Xin, and Chang Zheng Li. 2018. "Effects of Initial Microstructures on Serrated Flow Features and Fracture Mechanisms of a Nickel-Based Superalloy." *Materials Characterization* 144:9–21.

Lin, Y. C., Jun Zhang, and Jue Zhong. 2008. "Application of Neural Networks to Predict the Elevated Temperature Flow Behavior of a Low Alloy Steel." *Computational Materials Science* 43(4):752–58.

Liu, D., X. Zhang, X. Qin, and Y. Ding. 2017. "High-Temperature Mechanical Properties of Inconel-625: Role of Carbides and Delta Phase." *Materials Science and Technology* 33(14):1610–17.

Liu, J. and Z. Wang. 2010. "Prediction of Wrinkling and Fracturing in Viscous Pressure Forming (VPF) by Using the Coupled Deformation Sectional Finite Element Method." *Computational Materials Science* 48(2):381–89.

Liu, Nan, He Yang, Heng Li, and Siliang Yan. 2016. "Plastic Wrinkling Prediction in Thin-Walled

Part Forming Process: A Review." *Chinese Journal of Aeronautics* 29(1):1–14.

Luo, J., J. Gao, L. Li, and M. Q. Li. 2016. "The Flow Behavior and the Deformation Mechanisms of Ti–6Al–2Zr–2Sn–2Mo–1.5Cr–2Nb Alloy during Isothermal Compression." *Journal of Alloys and Compounds* 667:44–52.

Luo, S. D. and M. Qian. 2018. "Microwave Processing of Titanium and Titanium Alloys for Structural, Biomedical and Shape Memory Applications: Current Status and Challenges." *Materials and Manufacturing Processes* 33(1):35–49.

Ma, Gao Shan, Song Yang Zhang, Han Ying Wang, and Min Wan. 2011. "Tensile Deformation Behavior of 5A90 Al-Li Alloy Sheet at Elevated Temperature." *Applied Mechanics and Materials* 66–68:70–75.

Magrinho, J. P. G., C. M. A. Silva, M. B. Silva, and Paulo A. F. Martins. 2018. "Formability Limits by Wrinkling in Sheet Metal Forming." *Proceedings of the Institution of Mechanical Engineers, Part L: Journal of Materials: Design and Applications* 232(8):1–12.

Mahalle, G., N. Kotkunde, A. K. Gupta, and S. K. Singh. 2020. "Comparative Assessment of Failure Strain Predictions Using Ductile Damage Criteria for Warm Stretch Forming of IN718 Alloy." *International Journal of Material Forming* 1–14.

Mahalle, G., A. Morchhale, N. Kotkunde, A. K. Gupta, Singh S. K, and Y. C. Lin. 2020. "Forming and Fracture Limits of IN718 Alloy at Elevated Temperatures: Experimental and Theoretical Investigation." *Journal of Manufacturing Processes* 56:482–99.

Mahalle, G., O. Salunke, N. Kotkunde, A. K. Gupta, and S. K. Singh. 2019a. "Anisotropic Yielding Behaviour of Inconel 718 Alloy at Elevated Temperatures." Pp. 1–5 in *ASME International Mechanical Engineering Congress and Exposition, Proceedings (IMECE2019)*. Vol. 2A. Salt Lake City, Utah, USA.

Mahalle, G., O. Salunke, N. Kotkunde, A. K. Gupta, and S. K. Singh. 2019b. "Neural Network Modeling for Anisotropicmechanical Properties and Work Hardeningbehavior of Inconel 718 Alloy at Elevatedtemperatures." *Journal of Materials Research and Technology* 8(2):2130–40.

Marciniak, Z., J. L. Duncan, and S. J. Hu. 2002. *Mechanics of Sheet,Metal Forming*. Linacre House, Jordan Hill, Oxford OX2 8DP 225 Wildwood Avenue, Woburn, MA 01801-2041: Butterworth-Heinemann 2002.

Marciniak, Z. and K. Kuczyński. 1967. "Limit Strains in the Processes of Stretch-Forming Sheet Metal." *International Journal of Mechanical Sciences* 9(9):609–20.

Markandeya, R., S. Nagarjuna, D. V. V. Satyanarayana, and D. S. Sarma. 2006. "Correlation of Structure and Flow Behaviour of Cu-Ti-Cd Alloys." *Materials Science and Engineering A* 428:233–53.

Merklein, M. and Andreas Kuppert. 2009. "A Method for the Layer Compression Test Considering the Anisotropic Material Behavior." *International Journal of Material Forming* 2(1):483–86.

Mishra, N., S. Mishra, and V. Ramaswamy. 1989. "Analysis of the Temperature Dependence of

Strain-Hardening Behavior in High-Strength Steel." *Metallurgical Transactions A* 20(12):2819–29.

Mitchell, A. 2005. "The Precipitation of Primary Carbides in IN718 and Its Relation to Solidification Conditions." *Superalloys 718, 625, 706 and Various Derivatives* 299–310.

Mu, L., Z. Jia, Z. Ma, F. Shen, Y. Sun, and Y. Zang. 2020. "A Theoretical Prediction Framework for the Construction of a Fracture Forming Limit Curve Accounting for Fracture Pattern Transition." *International Journal of Plasticity* (July 2019):102706.

Na, Y. S., J. T. Yeom, N. K. Park, and J. Y. Lee. 2003. "Simulation of Microstructures for Alloy 718 Blade Forging Using 3D FEM Simulator." *Journal of Materials Processing Technology* 141(3):337–42.

Nakazima K, Kikuma T, and Hasuka K. 1989. "Study on the Formabilityof Steel Sheets." *JSME International Journal,* 32(1):142–48.

Narayanasamy, R. and C. Sathiya Narayanan. 2006. "Some Aspects on Fracture Limit Diagram Developed for Different Steel Sheets." *Materials Science and Engineering: A* 417(1–2):197–224.

Nayan, N., N. P. Gurao, S. V. S. Narayana M, A. K. Jha, B. Pant, and K. M. George. 2015. "Microstructure and Micro-Texture Evolution during Large Strain Deformation of Inconel Alloy IN718." *Materials Characterization* 110:256–241.

Nowotnik A, Pędrak P, Sieniawski J, Goral M. 2012. "Mechanical Properties of Hot Deformed Inconel 718 and X750." *Journal of Achievements in Materials and Manufacturing Engineering* 50(2):74–80.

Oyane, M., T. Sato, K. Okimoto, and S. Shima. 1980. "Criteria for Ductile Fracture and Their Applications." *Journal of Mechanical Working Technology* 4(1):65–81.

Panicker, S. S., H. G. Singh, S. K. Panda, and R. Dashwood. 2015. "Characterization of Tensile Properties, Limiting Strains, and Deep Drawing Behavior of AA5754-H22 Sheet at Elevated Temperature." *Journal of Materials Engineering and Performance* 24(11):4267–82.

Park, J., M. C. Jo, H. J. Jeong, S. S. Sohn, J. H. Kwak, H. S. Kim, and S. Lee. 2017. "Interpretation of Dynamic Tensile Behavior by Austenite Stability in Ferrite-Austenite Duplex Lightweight Steels." *Scientific Reports* 7(15726):1–14.

Paul, S. K. 2016. "Prediction of Complete Forming Limit Diagram from Tensile Properties of Various Steel Sheets by a Nonlinear Regression Based Approach." *Journal of Manufacturing Processes* 23:192–200.

Paul, S. K., G. Manikandan, and R. K. Verma. 2013. "Prediction of Entire Forming Limit Diagram from Simple Tensile Material Properties." *Journal of Strain Analysis for Engineering Design* 48(6):386–94.

Pawelski, O. 1967. "Über Das Stauchen von Hohlzylindern Und Seine Eignung Zur Bestimmung Der Formänderungsfestigkeit Dünner Bleche." *Archiv Für Das Eisenhüttenwesen* 38(6):437–42.

Plunkett, B., O. Cazacu, and F. Barlat. 2008. “Orthotropic Yield Criteria for Description of the Anisotropy in Tension and Compression of Sheet Metals.” *International Journal of Plasticity* 24:847–66.

Prakash, V., D. R. Kumar, Al Horn, H. Hagenah, and M. Merklein. 2020. “Modeling Material Behavior of AA5083 Aluminum Alloy Sheet Using Biaxial Tensile Tests and Its Application in Numerical Simulation of Deep Drawing.” *International Journal of Advanced Manufacturing Technology* 106:1133–48.

Prasad, K. S., S. K. Panda, S. K. Kar, S. V. S. N. Murty, and S. C. Sharma. 2018a. “Effect of Solution Treatment on Deep Drawability of IN718 Sheets: Experimental Analysis and Metallurgical Characterization.” *Materials Science and Engineering A* 727:97–112.

Prasad, K. S., S. K. Panda, S. K. Kar, S. V. S. N. Murty, and S. C. Sharma. 2018b. “Prediction of Fracture and Deep Drawing Behavior of Solution Treated Inconel-718 Sheets: Numerical Modeling and Experimental Validation.” *Materials Science and Engineering A* 733:393–407.

Prasad, K. S., S. K. Panda, S. K. Kar, S. V. S. N. Murty, and S. C. Sharma. 2019. “Prediction Capability of Constitutive Models for Inconel 718 Sheets Deformed at Various Elevated Temperatures and Strain Rates.” *Materials Performance and Characterization* 8(5):1–25.

Prasad, S. K., SKumar Panda, S. K. Kar, M. Sen, S. V. S. N. Murty, and S. C. Sharma. 2017. “Microstructures, Forming Limit and Failure Analyses of Inconel 718 Sheets for Fabrication of Aerospace Components.” *Journal of Materials Engineering and Performance* 26(4):1513–30.

Prasad, Y. V. R. K., K. P. Rao, and S. Sasidhara. 2015. *Hot Working Guide—A Compendium of Processing Maps*. edited by S. S. Prasad, Y.V.R.K.Rao K P. ASM International.

Quan, G. z, J. Pan, and X. Wang. 2016. “Prediction of the Hot Compressive DeformationBehavior for Superalloy Nimonic 80A by BP-ANN Model.” *Applied Sciences (Switzerland)* 6(66):1–16.

Reed, R. C. 2006. *The Superalloys Fundamentals and Applications*. New York: Cambridge University Press.

Riks, E. 1979. “An Incremental Approach to the Solution of Snapping and Buckling Problems.” *International Journal of Solids and Structures* 5:529–51.

Roamer, P., C. J. Van Tyne, D. K. Matlock, A. M. Meier, H. Ruble, and F. Suarez. 1997. “Room Temperature Formability of Alloys 625LCF, 718 and 718SPF.” *The Minerals, Metals and Materials Society* 315–29.

Rodriguez, P. 1984. “Serrated Plastic Flow.” *Bulletin of Materials Science* 6:653–63.

Samantaray, D., S. Mandal, and A. K. Bhaduri. 2009. “A Comparative Study on Johnson Cook, Modified Zerilli-Armstrong and Arrhenius-Type Constitutive Models to Predict Elevated Temperature Flow Behaviour in Modified 9Cr-1Mo Steel.” *Computational Materials Science* 47:568–76.

Samantaray, D., S. Mandal, U. Borah, A. K. Bhaduri, and P. V Sivaprasad. 2009. “A Thermo-Viscoplastic Constitutive Model to Predict Elevated-Temperature Flow Behaviour in a

Titanium-Modified Austenitic Stainless Steel." *Materials Science and Engineering A* 526(1–2):1–6.

Satish, F. Feyissa, and D. Kumar. 2017. "Cryorolling and Warm Forming of AA6061 Aluminum Alloy Sheets." *Materials and Manufacturing Processes* 32(12):1345–52.

Satish, D. R. Kumar, and M. Merklein. 2017. "Effect of Temperature and Punch Speed on Forming Limit Strains of AA5182 Alloy in Warm Forming and Improvement in Failure Prediction in Finite Element Analysis." *Journal of Strain Analysis for Engineering Design* 52:258–73.

Satyanarayana, D., G. Malakondaiah, and D. Sarma. 2007. "Analysis of Flow Behaviour of an Aluminium Containing Austenitic Steel." *Materials Science and Engineering: A* 452–453(452–453):244–53.

Schafrik, R. E., D. D. Ward, and J. R. Groh. 2001. "Application of Alloy 718 in GE Aircraft Engines: Past, Present and Next Five Years." *International Symposium on Superalloys and Various Derivatives* 1–11.

Seyedkashi, S. M. H., J. R. Cho, S. H. Lee, and Y. H. Moon. 2018. "Feasibility of Underwater Laser Forming of Laminated Metal Composites." *Materials and Manufacturing Processes* 33:546–51.

Shafaat. 2011. "Investigation into Wall Wrinkling in Deep Drawing Process of Conical Cups," Journal of Materials Processing Technology." *Journal of Materials Processing Technology* 211(11):1783–95.

Shin, H. and J. B. Kim. 2010. "A Phenomenological Constitutive Equation to Describe Various Flow Stress Behaviors of Materials in Wide Strain Rate and Temperature Regimes." *Journal of Engineering Materials and Technology* 132(021009):1–6.

Sieczkarek, P., K. Isik, N. Ben Khalifa, P. A. F. Martins, and A. E. Tekkaya. 2014. "Mechanics of Sheet-Bulk Indentation." *Journal of Materials Processing Technology* 214:2387–94.

Singh, S. K., K. Mahesh, and A. K. Gupta. 2010. "Prediction of Mechanical Properties of Extra Deep Drawn Steel in Blue Brittle Region Using Artificial Neural Network." *Materials and Design* 31(5):2288–95.

Situ, Q., M.K.Jain, and D.R Metzger. 2011. "Determination of Forming Limit Diagrams of Sheet Materials with a Hybrid Experimental–Numerical Approach." *International Journal of Mechanical Science* 53:707–9.

Snedecor, G. W. and W. G. Cochran. 1989. *Statistical Methods*. Iowa State University Press.

Soyarslan, C., B. Klusemann, and S. Bargmann. 2016. "The Effect of Yield Surface Curvature Change by Cross Hardening on Forming Limit Diagrams of Sheets." *International Journal Mechanical Science* 117:53–66.

Su, Y., W. Li, V. Patel, A. Vairis, and F. Wang. 2019. "Formability of an AA5083 Aluminum Alloy T-Joint Using SSFSW on Both Corners." *Materials and Manufacturing Processes* 34(15):1737–44.

Takuda, H., T. Enami, K. Kubota, and N. Hatta. 2000. "Formability of a Thin Sheet of Mg-8.5Li-1Zn

Alloy.” *Journal of Materials Processing Technology* 101(1):281–86.

Tari, D. Ghaffari and M. J. Worswick. 2015. “Journal of Materials Processing Technology Elevated Temperature Constitutive Behavior and Simulation of Warm Forming of AZ31B.” *Journal of Materials Processing Tech.* 221:40–55.

Thaller, Lawrence H. and Albert H. Zimmerman. 2003. *Overview of the Design, Development, and Application of Nickel-Hydrogen Batteries*. NASA Tech. edited by N. G. R. Center. National Aeronautics and Space Administration, Glenn Research Center.

Thomas, A., M. El-Wahabi, J. M. Cabrera, and J. M. Prado. 2006. “High Temperature Deformation of Inconel 718.” *Journal of Materials Processing Technology* 177(1–3):469–72.

Tian, Y., L. Huang, H. Ma, and J. Li. 2014. “Establishment and Comparison of Four Constitutive Models of 5A02 Aluminium Alloy in High-Velocity Forming Process.” *Materials and Design* 54:587–97.

Turetta, A., S. Bruschi, and A. Ghiotti. 2006. “Investigation of 22MnB5 Formability in Hot Stamping Operations.” *Journal of Materials Processing Technology* 177(1–3):396–400.

Venkateswarlu, G., A. K. Singh, J. Davidson, and G. R. Tagore. 2013. “Effect of Microstructure and Texture on Forming Limits in Friction Stir Processed AZ31B Mg Alloy.” *Journal of Materials Research and Technology* 2(2):135–40.

Wallmeier, M., E. Linvill, M. Hauptmann, J. P. Majschak, and S. Östlund. 2015. “Explicit FEM Analysis of the Deep Drawing of Paperboard.” *Mechanics of Materials* 89:202–15.

Wang, C. T., G. Kinzel, and T. Altan. 1994. “Wrinkling Criterion for an Anisotropic Shell with Compound Curvatures in Sheet Forming.” *International Journal of Mechanical Sciences* 36(10):945–60.

Wang, X. and J. Cao. 2000. “On the Prediction of Side-Wall Wrinkling in Sheet Metal Forming Processes.” *International Journal of Mechanical Sciences* 42(12):2369–94.

Wang, X., C. Huang, B. Zou, H. Liu, H. Zhu, and J. Wang. 2013. “Dynamic Behavior and a Modified Johnson-Cook Constitutive Model of Inconel 718 at High Strain Rate and Elevated Temperature.” *Materials Science and Engineering A* 580:385–90.

Wang, Y., W. Z. Shao, L. Zhen, C. Yang, and X. M. Zhang. 2009. “Tensile Deformation Behavior of Superalloy 718 at Elevated Temperatures.” *Journal of Alloys and Compounds* 471(1–2):331–35.

Wen, D. X., Y. C. Lin, J. Chen, Xi-M. Chen, J. L. Zhang, Y. J. Liang, and L. T. Li. 2015. “Work-Hardening Behaviors of Typical Solution-Treated and Aged Ni-Based Superalloys during Hot Deformation.” *Journal of Alloys and Compounds* 618:372–79.

Wen, D. X., Y. C. Lin, J. Chen, J. Deng, X. M. Chen, J. L. Zhang, and M. He. 2014. “Effects of Initial Aging Time on Processing Map and Microstructures of a Nickel-Based Superalloy.” *Materials Science and Engineering A* 620:319–32.

Wen, D. X., Y C Lin, H. B. Li, X. M. Chen, J. Deng, and LT Li. 2014. “Hot Deformation Behavior and Processing Map of a Typical Ni-Based Superalloy.” *Materials Science and Engineering: A*

591:183–92.

Won, C., H. g Kim, S. Lee, D. Kim, S. Park, and J. Yoon. 2019. “Wrinkling Prediction for GPa-Grade Steels in Sheet Metal Forming Process.” *International Journal of Advanced Manufacturing Technology* 102(9–12):3849–63.

Wu, K., G. Liu, B. Hu, F. Li, Y. Zhang, Y. Tao, and J. Liu. 2011. “Hot Compressive Deformation Behavior of a New Hot Isostatically Pressed Ni-Cr-Co Based Powder Metallurgy Superalloy.” *Materials and Design* 32(4):1872–79.

Wu, Y. T. and C. H. Koo. 1997. “Effect of Temperature on the Anisotropic Superplasticity of Textured Ti-25Al-10Nb Alloy.” *Scripta Materialia* 38(2):267–71.

Xiao, R., X. X. Li, L. H. Lang, Y. K. Chen, and Y. F. Yang. 2016. “Biaxial Tensile Testing of Cruciform Slim Superalloy at Elevated Temperatures.” *Materials and Design* 94:286–94.

Xu, S. and K. J. Weinmann. 1998. “Prediction of Forming Limit Curves of Sheet Metals Using Hill’s 1993 User-Friendly Yield Criterion of Anisotropic Materials.” *International Journal of Mechanical Sciences* 40(9):913–25.

Xu, Z. and F. Huang. 2015. “Comparison of Constitutive Models for FCC Metals over Wide Temperature and Strain Rate Ranges with Application to Pure Copper.” *International Journal of Impact Engineering* 79:65–74.

Zhang, J. M., Z. Y. Gao, J. Y. Zhuang, and Z. Y. Zhong. 1999. “Mathematical Modeling of the Hot-Deformation Behavior of Superalloy IN718.” *Metallurgical and Materials Transactions A: Physical Metallurgy and Materials Science* 30:2701–12.

Zhang, R., Z. Shao, and J. Lin. 2018. “A Review on Modelling Techniques for Formability Prediction of Sheet Metal Forming.” *International Journal of Lightweight Materials and Manufacture* 1:115–25.

Zhang, Z. and X. Lu. 2019. “Preparation Process of Magnesium Alloys by Complex Salt Dehydration-Electrochemical Codeposition.” *Materials and Manufacturing Processes* 34(6):591–97.

Zheng, K., J. Lee, D. J. Politis, N. Li, J. Lin, and T. A. Dean. 2017. “An Analytical Investigation on the Wrinkling of Aluminium Alloys during Stamping Using Macro-Scale Structural Tooling Surfaces.” *International Journal of Advanced Manufacturing Technology* 92(1–4):481–95.

Scientific Publications from the Present Research Work

(I) International Journals:

1. **Mahalle G**, Kotkunde N, Gupta AK, Singh SK. An Improved M-K model coupled with different ductile criteria for fracture limit predictions of Inconel 718 alloy, Journal of Materials Research and Technology 2021;11:1162-1174 (IF – 5.289, Elsevier Publisher, SCIE Index). https://doi.org/10.1016/j.jmrt.2021.01.092

2. **Mahalle G**, Kotkunde N, Gupta AK, Singh SK. Comparative Assessment of Failure Strain Predictions using Ductile Damage Criteria for Warm Stretch Forming of IN718 Alloy, International Journal of Material Forming 2020:1-14 (IF – 1.713, Springer Publisher, SCIE Index). https://doi.org/10.1007/s12289-020-01588-3

3. **Mahalle G**, Morchhale A, Kotkunde N, Gupta AK, Singh SK, Lin YC. Forming and Fracture Limits of IN718 Alloy at Elevated Temperatures: Experimental and Theoretical Investigation. Journal of Manufacturing Processes 2020; 56:482–99. (IF – 4.086, Elsevier Publisher, SCIE Index). https://doi.org/https://doi.org/10.1016/j.jmapro.2020.04.070.

4. **Mahalle G**, Kotkunde N, Gupta AK, Sujith R, Singh SK, Lin YC. Microstructure Characteristics and Comparative Analysis of Constitutive Models for Flow Stress Prediction of Inconel 718 Alloy. Journal of Materials Engineering and Performance 2019; 28:3321–3321. (IF – 1.476, Springer Publisher, SCIE Index). https://doi.org/10.1007/s11665-019-04116-w.

5. **Mahalle G**, Salunke O, Kotkunde N, Gupta AK, Singh SK. Neural network modeling for anisotropic mechanical properties and work hardening behavior of Inconel 718 alloy at elevated temperatures. Journal of Materials Research and Technology 2019; 8:2130–40. (IF – 5.289, Elsevier Publisher, SCIE Index). https://doi.org/10.1016/j.jmrt.2019.01.019.

6. **Mahalle G**, Kotkunde N, Gupta AK, Singh SK. Efficacy of semi-empirical models for Prediction of Forming Limit Curve of IN718 alloy at Elevated Temperatures, Advances in Materials and Processing Technologies 2020;1–13. (Taylor & Francis online, Scopus Index). https://doi.org/10.1080/2374068X.2020.1792706

7. **Mahalle G**, Kotkunde N, Gupta AK, Singh SK. Prediction of flow stress behavior by materials modelling technique for Inconel 718 alloy at elevated temperature. Advances in Materials and Processing Technologies 2020;1–8. (Taylor & Francis online, Scopus Index). https://doi.org/10.1080/2374068X.2020.1728649

8. **Mahalle G**, Kotkunde N, Gupta AK, Singh SK. An Integrated Experimental and Finite Element Approach for Wrinkling Limit Prediction of Inconel 718 Alloy at Elevated Temperatures **under review** in The Journal of Strain Analysis for Engineering Design: SAGE Journals 2021. (IF – 1.541, SAGE Publisher, SCI Index).

(II) Book Chapter

1. **Mahalle G**, Kotkunde N, Gupta AK, Singh SK. Analysis of hot workability of Inconel alloys using processing maps, in **Adv. Comput. Methods Manuf., Springer**; 2019; 109–118. https://doi.org/10.1007/978-981-32-9072-3_10.

(III) International Conferences

1. **Mahalle G**, Kotkunde N, Gupta AK, Singh SK, 'Prediction of Hot Deformation Behaviors Under Multiaxial Loading Using Gurson-Tvergaard-Needleman Damage Model for Inconel 718 Alloy Thin Sheet', accepted for ASME Int. Mech. Eng. Congr. Expo. Proc. 2021.

2. **Mahalle G**, Salunke O, Kotkunde N, Gupta AK, Singh SK. Study of Khan-Huang-Liang (KHL) Anisotropic Deformation Model for Deep Drawing Behavior of Inconel 718 Alloy, International Deep Drawing Research Group (IDDRG)-2020, virtual-Korea, Oct. 26-30,2020, **IOP Conf. Ser.: Mater. Sci. Eng**. 967:1, 012054. doi:10.1088/1757-899X/967/1/012054.

3. Mahalle G, Salunke O, Kotkunde N, Gupta AK, Singh SK. Anisotropic yielding behavior of Inconel 718 alloy at elevated temperatures. ASME Int. Mech. Eng. Congr. Expo. Proc., vol. 2A, Salt Lake City, Utah, USA: 2019, p. 1–5. https://doi.org/10.1115/IMECE2019-11126.

4. **Mahalle G**, Kotkunde N, Shah R, Gupta AK, Singh SK. Analysis of Flow Stress Behavior of Inconel Alloys at Elevated Temperatures Using Constitutive Model,11th International Conference and Workshop on Numerical Simulation of 3D sheet metal forming processes (NUMISHEET-2018), Tokyo, Japan, July 30-Augest 3, 2018.IOP

Conf. Series: **Journal of Physics: Conf. Series** 1063 (2018) 012037 http://iopscience.iop.org/article/10.1088/1742- 6596/1063/1/012037

5. **Mahalle G**, Kotkunde N, Gupta AK, Singh SK. Cowper-Symonds Strain Hardening Model for Flow Behavior of Inconel 718 Alloy, International Conference on Materials Processing and Characterization (ICMPC-2019), GRIET-Hyderabad, March 8-9, 2019. **Materials Today: Proceedings** (2019):18(7):2796-2801 https://doi.org/10.1016/j.matpr.2018.06.135

6. **Mahalle G**, Kotkunde N, Gupta AK, Singh SK. Study of Mechanical Properties and Microstructural Analysis for Inconel Alloy sheet at Elevated Temperature, International Conference on Materials Processing and Characterization (ICMPC-2018), GRIET-Hyderabad, March 18-19, 2018.**Materials Today: Proceedings** 5(2018):18016-18023 https://doi.org/10.1016/j.matpr.2018.06.135

7. **Mahalle G**, Kotkunde N, Gupta AK, Singh SK. Comparative Analysis of Constitutive models for flow stress prediction of Inconel 718 Alloy, Sheet Metal Forming (SMF-2018), IIT Madras, December 06-07, 2018.

Brief Biography of the Candidate

Ms. Gauri Rajendra Mahalle has completed her in Mechanical engineering from Government Collage of Engineering, Amravati, Maharashtra, with a CGPA of 7.83 out of 10. She completed her Master of Technology in Design Engineering specialization in 2016 from the Indian Institute of Information Technology, Design & Manufacturing Kancheepuram, Chennai, Tamilnadu, with a CGPA of 8.23 out of 10. She is presently working as an Institute Research Scholar in the Department of Mechanical Engineering, BITS-Pilani, Hyderabad Campus, India. Her research activities primarily focus on sheet metal forming of Inconel alloy sheets, quasi-static strain-rate material behavior, development of different fracture and constitutive models, finite element simulation of different forming operations, microstructure analysis using SEM technique, and micro-texture characterization using EBSD technique. She has already published nine research papers in reputed international Journals and seven in international conferences.

Brief Biography of the Supervisor

Dr. Nitin Ramesh Kotkunde obtained his Ph.D. from BITS-Pilani, Hyderabad Campus in Mechanical Engineering Department, 2015. He is working as an Assistant Professor in the Mechanical Engineering Department, BITS-Pilani, Hyderabad Campus, with 11 years of teaching experience. Before joining BITS Pilani, Hyderabad campus in 2012, he had teaching experience at VIT Vellore. At BITS Pilani Hyderabad Campus, he is an active conveyor of the Department Research Committee since December 2020. He has successfully completed funded projects from DST, BIT-Pilani (RIG), and BITS-Pilani (ACRG). He has 33 publications in international journals and 34 in international conferences. His current research areas include Sheet Metal Forming, Material Testing and Characterization of Metal, Hot Deformation Behavior of Metals, Material Model Development, and Product Design and Development.

Brief Biography of the Co-supervisor

Prof. Amit Kumar Gupta is working as a Professor in the Department of Mechanical Engineering, Birla Institute of Technology and Science (BITS), Pilani, Hyderabad Campus. He obtained his Doctoral degree from Nanyang Technological University (NTU), Singapore, and a Bachelor's degree from the Indian Institute of Technology (IIT), Delhi in Mechanical engineering. For his Ph.D., he has received the prestigious Singapore Millennium Foundation award, and for the excellence in teaching and research at BITS, he has been awarded the Prof. S. Venkateswaran Faculty Excellence Award, 2013. His research interest lies in the area of sheet metal forming, tensile testing and constitutive modeling, production scheduling, manufacturing simulation and modeling, predictive modeling, and optimization of manufacturing processes. He has successfully completed funded projects from BRNS, DST, UGC, DRDO, etc., and authored more than 150 publications in journals and conferences of international repute.